DOCTOR OF PHILOSOPHY

Seasonal modelling of circulation on the Scottish west coast

Pizzamei, Marco

Award date:
2003

Awarding institution:
University of Wales, Bangor

SEASONAL MODELLING OF CIRCULATION ON THE SCOTTISH WEST COAST

A thesis submitted in accordance with the requirements of the University of Wales for the degree of Doctor of Philosophy

by

Marco Pizzamei

University of Wales, Bangor
School of Ocean Sciences
Menai Bridge
Anglesey LL59 5AB
United Kingdom

ABSTRACT

Circulation in the coastal waters to the west of Scotland was investigated using a three-dimensional, primitive equation ocean model. The coastline of this region contains many areas of outstanding natural beauty and over 60 sites of special scientific interest. This, combined with the fact that the area is heavily used for fish farming and shipping and has potential for hydrocarbon exploitation, makes a better understanding of the regional oceanography essential. Particular interest was devoted to the non-tidal circulation, its seasonal development and its interannual variability.

These features were investigated using a version of the Princeton Ocean Model with a spatial resolution of approximately 6 km, and forced with real meteorological data from 1997. Model predictions were compared with observational data (CTD sections and current meter records) collected during the same year. The model was initialised with observational data and was smoothly matched to climatological temperature and salinity data at its open boundaries. It was shown that the model correctly reproduces the development of thermal stratification throughout the heating season. Salinity was reproduced with less success, model results showed less variability than observations; explanations can be found in the different physical mechanisms which control its temporal and spatial evolution.

The model was also used to simulate the baroclinic circulation that develops around a saline intrusion of Atlantic water in the Sea of the Hebrides, causing bifurcation of the northward flow around the Outer Hebrides islands. This feature of the circulation has been previously shown by limited deployments of satellite-tracked drifters. The model reproduced the Scottish Coastal Current and the recirculation in the Sea of the Hebrides showing the importance of the baroclinic component of the flow. Rates of transport were calculated and were in agreement with previous estimates obtained with the help of radioactive tracers.

ACKNOWLEDGEMENTS

I would like to thank Dr. Kevin Horsburgh, Dr. Phil Gillibrand and Dr. Ed Hill for their help and patience throughout my research, without them none of this would have been possible.

The observations I used during my work have been supplied by the British Atmospheric Data Centre (BADC), by the Marine Laboratory, Aberdeen and the Scottish Environmental Protection Agency (SEPA). The bathymetry was kindly supplied by the Proudman Oceanographic Laboratory (POL) together with data I used as boundary conditions for all my simulations.

I would like also to thank my friends and family which supported me and encouraged me. A particular thanks to Jonathan, David, Yener, Carol, Gaynor and Fabienne for the wonderful period I spent in Menai Bridge.

This research was funded by the Marine Laboratory, Aberdeen.

Contents

List of Figures

List of Tables

Chapter 1

Introduction

1.1 General introduction

Coastal regions are the focal point of man's interaction with the marine environment. The coastal seas provide food through fishing and aquaculture, and many industries are sited at coasts to take advantage of the sea as an economical means of transport. Unfortunately the coastal zone is under pressure: the sea is often viewed as an economical dump site for industrial and urban waste; over-fishing is commonplace with an increasing risk of total fisheries collapse (as occurred on the Newfoundland Banks). Oil spills demonstrate how rapidly habitats can be damaged, with long recovery times. Consequently, a good understanding of the physical, biological and environmental behavior of marine coastal system is required for effective management. Accurate and reliable observations are needed to develop theories and increase our understanding of the shelf seas. These observations can also be used to test a new generation of predictive models. Sophisticated numerical models, one of which is employed in this work, have been gradually improved over the last three decades and are now providing reliable predictions and new theoretical insights.

The North-west European Continental shelf is home to several of the world's more powerful and wealthy countries. The shelf seas are heavily used for commercial purposes with many large ports posing environmental risks. Both the United Kingdom and Norway exploit the North Sea for its oil and natural gas. In the same area, overfishing has caused a serious depletion of the cod and mackerel stocks, leading to a temporary suspension of fishing activities. The regional focus of this study - the

Scottish shelf - is an important ground for salmon and shellfish farming and much of the Scottish economy depends on these activities. Any pollution incident in the waters to the west of Scotland would have severe social and economic consequences.

Many aspects of the physical oceanography of the Northwest European Continental shelf are well known. Tides are very energetic and interact strongly with the bottom topography; winds are strong and variable on time scales of atmospheric depressions; there is seasonal variability of sea temperature due to solar heating and freshwater runoff modifies the salinity (and therefore density) of the shelf waters. However, the potentially complex interactions between these factors are less well known and represent a challenge for coastal oceanography. The continental shelf remains an important area for the validation of theories aimed at improving our interdisciplinary knowledge of the marine environment. It is also an ideal site for the application of one of the latest generation of numerical coastal ocean models, with the aim of contributing towards this understanding.

1.2 Physics of shelf seas around the UK

The Northwest European Continental Shelf (see Fig. 1.1 and Fig. 1.2) covers the area roughly between longitude 12°W and 10°E and between latitude 50°N and 62°N. The shelf is divided into two distinct parts by the presence of the British Isles; on the western side is the Celtic Sea, the Irish Sea and the Scottish shelf including the Sea of the Hebrides. The Irish sea is connected to the Malin and Hebridean shelf by the narrow North Channel, to the north of which the Scottish coastline is carved by the presence of numerous fjords. The southern end of the Irish Sea is connected with the Celtic Sea through St.George's Channel. The bathymetry of the whole region is irregular; the Celtic Sea is flat with an average depth of around 100 m whilst the Irish Sea is divided in two by a channel which runs from South to North for almost all its length. The eastern Irish Sea is relatively shallow with depths of 30-40 m whereas the western part is deeper (more than 100 m in places). The narrow North Channel has a maximum depth of almost 300 metres. Between the Outer Hebrides and the Scottish mainland are the Minches where the maximum depth is 170 m in a depression of the Sea of the Hebrides. The North Sea lies between Britain and mainland Europe; it has an almost rectangular shape

with fairly regular coastlines on its western and souther sides but fjords are found on its eastern boundary. Depths range from 25 m in the southern German Bight to deeper waters of 100 m over most of the basin with 500 m in the Norwegian Trench, between Denmark and the Scandinavian Peninsula.

The effect of Earth's rotation has a strong influence on large-scale coastal circulations. Density-driven currents flow with the coastline on the right as in the Scottish coastal current (Simpson and Hill, 1986) or the Norwegian coastal current (Mork, 1981). In other cases rotation combines with topography; Huthnance (1973) showed how the tidal flow can frictionally interact with sandbanks to create a mean circulation. Pingree and Maddock (1979, 1980) demonstrated how islands can induce residual currents when tides interact with the rotation of the earth. Atmospheric forcing also has an impact on shallow coastal seas. Sea level is influenced by atmospheric pressure (the inverse barometer effect) and direct set-up due to the wind which combine to cause storm surges, often with dramatic effects (e.g. the North Sea storm surge of January 1953). The wind can also cause the vertical mixing of surface waters and drives currents that are major constituents of the surface circulation. Transport in the North Channel of the Irish Sea has been found to be highly correlated with wind direction and speed as demonstrated by measurements (Brown and Gmitrowicz, 1995; Knight and Howarth, 1999) and numerical simulations (Davies and Hall, 2000). Wind-driven currents can also interact with baroclinic motions such as the blocking and consequent outbreak of brackish water from the Skagerrak (Mork, 1981). Finally, major rivers can modify the inputs of buoyancy through freshwater runoff as in the Clyde (Rippeth and Simpson, 1996), the Rhine (Sousa and Simpson, 1996) or in Liverpool Bay (Sharples and Simpson, 1995). In all of these examples the buoyancy forcing affects the circulation (e.g. modification of tidal ellipses or straining of stratification over the tidal cycle).

For an understanding and analytical treatment of shelf dynamics it is often easier to separate the various contributions to the circulation. This implies linearity of the system whereas, in fact, the coastal environment is highly nonlinear. Even so, this approach is a reasonable starting point that allows individual forcing mechanisms to be discussed. First it is helpful to introduce the concept of mean circulation (Csanady, 1976), separating periodic and non-periodic motion. Tides have a periodic characteristic with well-defined frequencies and their signals can therefore be averaged to obtain what is defined as the residual (non-tidal) flow (Csanady, 1976).

In this way the picture of motion obtained contains only the net effect of tides (tidal residuals) and the signals of the other forcing factors, mainly the wind-driven circulation but with baroclinic (density-driven) processes having a weaker influence.

1.2.1 Tidal Circulation

The most important dynamical process of shelf seas is the tide. Tides interact in some way with all other processes. They are also an effective way of energy transfer, with tidal energy being dissipated through the bottom friction and the mixing of the water column. Tides on the European continental shelf are not caused by the direct gravitational attraction between the moon, the sun and the earth but by a phenomenon of propagation from the deep ocean to the shelf (Huntley, 1980). (Taylor, 1919) estimated that only 7% of the tidal dissipation in the Irish Sea is due to the direct lunar effect - the main effect being the propagation of the tidal signal on to the shelf as a co-oscillating response with the tidal motion of the Atlantic Ocean. On this particular shelf, tides are strong; maximum elevation can reach up to 3.5 m in the eastern part of the Irish Sea due to amplification by rotation. Currents can reach 1-2 m s^{-1} in the Irish Sea and in the English Channel. Because of these effects the tidal dissipation is high and shelves around the UK are responsible for the loss of the 12.5% of the total energy of the world ocean (Simpson and Bowers, 1981). This fact has implications for several other processes; it plays an important role in the control of seasonal stratification, sediment transport and biological productivity (Simpson, 1998). High velocities and shallow waters mean that the large turbulence generated because of friction in the bottom boundary layer is capable of penetrating the water column for a large portion of its thickness. This availability of kinetic energy may cause mixing throughout the water, working against the stabilizing effect of stratification.

The tide on the European shelf is predominantely semi-diurnal and the main constituents are M_2 and S_2 with periods of 12.42 and 12.00 hours respectively. Figure 1.3 shows the position of an amphidromic point (a point with no tidal elevation) for the M_2 in the Atlantic region with co-tidal lines radiating from it. It is possible to notice the anticlockwise rotation, in this case the tide propagates from the open ocean to the shelf. As soon as it enters the shelf the wave is divided in two, one part turning north and the other propagating eastward inside the English Channel. The

northward component is subsequently divided in two components. The majority of this Kelvin wave follows the west coast of Ireland and propagates on to the Scottish Shelf whilst the part entering the Irish Sea is reflected at its northern end. At this point the wave turns eastward and southward following the profile of the British coast to be reconnected with the wave exiting the English Channel (Howarth and Pugh, 1983). This propagation can be seen in Figure 1.4 which shows the co-tidal and co-range (elevation) lines for the M_2 constituent. There is a degenerate (inland) amphidromic point on the southeast coast of Ireland and another in the vicinity of Islay, west of Scotland. In the North Sea there are three amphidromes, one close to the English Channel, one in the southern North Sea off Denmark and a degenerate amphidrome in southern Norway. The pattern of the S_2 tidal component is similar but, because of the differences in wave propagation due to the different periods, there is a periodical displacement of the total semi-diurnal amphidromic point over the spring-neap cycle (George, 1980). The propagation of tides (neglecting advective and friction terms in the momentum equations) can be expressed as progressive Kelvin waves (see for example Pugh, 1987). Amphidromes result from the interference of an incoming and a reflected wave. The displacement of amphidromes to the left of the inward propagation direction is because there is less energy (or amplitude) in the reflected wave due to friction.

At a given location the tidal velocity can be decomposed (e.g. Soulsby, 1990) into two rotary vector components $\mathbf{R}_+$ and $\mathbf{R}_-$, each with a constant magnitude and rotating anticlockwise and clockwise respectively. A vertical profile of velocity can be obtained and this profile is dependent on the vertical exchange of momentum (through eddy viscosity) which is an intrinsic characteristic of the flow and of the water conditions. Seasonal stratification (because of solar heating) is responsible for changes in the profile of the eddy viscosity, with a reduction of its value in the thermocline (Howarth, 1998) and the possibility of decoupling layers above and below the thermocline. In the Rhine ROFI (Region Of Freshwater Influence) system, high freshwater runoff is responsible for stratification and buoyancy forcing of the top layer of the water column (Simpson and Souza, 1995); in this case the pycnocline causes a reduction of eddy viscosity. Consequently the rotary characteristics of tidal ellipses change below and above the pycnocline, due to the different thicknesses of the boundary layers for clockwise and anticlockwise components (Simpson and Souza, 1995). Other dynamical interactions between stratification and tidal flow can be detected in ROFIs. In the Liverpool Bay a marked semi-diurnal oscillation in the

stability of the water column is observed - "tidal straining" (Simpson, 1998). For one part of the tidal cycle low density water is moved over denser water - increasing stratification - but when dense water is advected over the fresher water the resulting instability destroys stratification.

Tidal energy also plays an important role in governing the seasonal cycle of stratification in some locations of the European Continental Shelf, where competition develops between tidal mixing and the stabilising effect of buoyancy generated by solar heating and fresh water contributions. Tidal mixing fronts are well-observed phenomena around the British Isles (Simpson and Hunter, 1974; Pingree and Griffiths, 1978), where one finds very sharp horizontal gradients of temperature and salinity. They are caused by the differential response of shelf seas to the combination of tidal mixing and solar heating. During spring and summer the water column gains buoyancy due to solar heating but in some areas tidal currents are strong enough to overcome this stratification and the water is well mixed throughout the year. In other areas where tides are weak stratification is established. Tidal fronts mark the boundary of the two different regions.

A parameter which represents the stability of the water column due to stratification is the potential energy anomaly, V (Simpson *et al.*, 1978; Simpson and Bowers, 1981) defined as

$$V = \int_{-h}^{0} (\rho - \overline{\rho}) g z \, \mathrm{d}z \tag{1.1}$$

where ρ is the density, z the vertical coordinate, g the acceleration of gravity and $\overline{\rho}$ the mean density throughout the vertical

$$\overline{\rho} = \frac{1}{h} \int_{-h}^{0} \rho \, \mathrm{d}z \tag{1.2}$$

where h is the depth. Solar heating and fresh water inflow contribute to negative changes in V, increasing the stratification (Simpson and Bowers, 1981). It is possible to relate the rate of change of the potential energy to the power dissipated by wind and tides and the rate of change due to contribution of solar heating (Simpson and Hunter, 1974). Assuming that only local processes are controlling

this balance (i.e. neglecting advective terms), the transition region between mixed and stratified water is where the rate of change of V is zero. When tides dominate over wind and the variations of Q with latitude are negligible, it is possible to obtain the Simpson-Hunter stratification parameter (Simpson and Hunter, 1974)

$$\chi = \frac{h}{u^3} \tag{1.3}$$

where h is the depth and u is the modulus of the tidal velocity. This parameter has been shown to be a good indicator of the position of tidal fronts on the European shelf. The frontal location corresponds to a critical value of the parameter which needs to be deduced from observations (Le Févre, 1986); the critical value on the western part of the European shelf is $\log \chi = 2.7$ (Simpson and James, 1986). Pingree and Griffiths (1978) used a numerical model to estimate the distribution of χ around the British Isles and found the predicted frontal locations agreed well with satellite pictures.

If the wind stress is low, the stability of the water column is modulated by the spring-neap cycle, when tidal velocities in most places change by a ratio of approximately two with consequent modification of the stirring, which is proportional to the cube of the velocity. A fortnightly modulation of the frontal position should be expected to compensate for the change in u. This modulation in reality is not marked and the real frontal movement is only few kilometres (Simpson, 1998), around a third of the predicted displacement. This phenomenon can be explained using models where the efficiency parameters ϵ and δ are not constant but are functions of the existing level of stratification (Simpson and Bowers, 1981; James, 1977); with a constant efficiency model the parameters and can be estimated to be around 0.004 and 0.0007 (Bowers and Lwiza, 1994). Similar values have been obtained from Elliott and Clarke (1991) which used them for the adjustment of the frontal positions in their simulation of the seasonal stratification on the European shelf (Elliott and Clarke, 1991).

Tidal processes are important for the dynamics of the shelf, being a major contributor of the energy balance and cause of mixing processes. The long-term average of tidal currents at a given point is not always zero - there can be a net circulation through tidal residuals. Tidal residuals are generated by the rectification of the oscillatory currents (Robinson, 1983); the flow interacts in a nonlinear way with the bathymetry and with the coastline. The circulation produced is, in general, one or

two orders of magnitude less than the tidal flow but it represents a contribution to the long term circulation as showed by Prandle (1984) in a numerical investigation of the North-West European shelf.

1.2.2 Wind forced circulation

Winds represent the other main source of energy for coastal seas. Momentum is exchanged between the atmosphere and the sea when wind blows over its surface. In the open ocean, where tides are weak, the long term circulation is the combination of the wind-driven circulations and the thermohaline circulation. Winds are the major contribution to the energy budget at the surface, where exchange of momentum between the atmosphere and the ocean take place. In deep water, where the penetration of the wind is negligible, the circulation is mainly driven by density gradients existing between masses of sea water with different thermohaline characteristics. On the continental shelf wind is also responsible for aspects of the circulation where its effects can be even more dramatic because of the size of the system and its relatively shallow depth. Wind exerts a stress on the sea surface and the momentum is transmitted downward through frictional effects; if one considers a constant wind blowing over an infinite ocean and further assumes a constant eddy viscosity then the well-known Ekman spiral solution can be derived from the horizontal momentum equations (see for instance Pond and Pickard, 1978). The Ekman depth, denoted D_e (see (1.10)), is a measure of the penetration of the wind stress down the water column (i.e. it is an estimate of the thickness of the surface layer that is strongly influenced by the wind). In Ekman's theory, surface currents are not parallel to the wind but at an angle of 45 degrees with its direction - a fact which was observed by Nansen during an expedition in the Arctic region at the beginning of the 20^{th} century. The simplifying conditions required for Ekman's solutions are not obtained in reality, but the approach provides a useful understanding of the effects of wind on the sea surface. Observations in fact suggest the angle between surface velocity and wind to be around 15 degrees (Davies and Jones, 1992).

The wind-driven circulation of the northwest European continental shelf has been extensively investigated, both with observations and models. The Celtic and Irish Seas have been modelled by Davies and Jones (1992), whilst the North Channel of the Irish Sea was subject to current measurements by Brown and Gmitrowicz

(1995) and by Knight and Howarth (1999). Xing and Davies (1996c) studied the long term flow on the Malin Shelf and the contributions of winds to it and the North Sea was investigated by Maier-Reimer (1977). Pingree and Griffiths (1980) studied the circulation of the entire shelf using a two-dimensional model forced with a constant wind stress and the M_2 tidal component. Figure 1.5 reproduces their results with constant southwesterly and southeasterly winds: both conditions cause a clockwise circulation around the British Isles and an eastward transport in the English Channel; water enters the North Sea from the north and through the Fair Isle channel, between the islands of Shetland and Orkney. The main differences are found in the North Sea in the area of the Skagerrak where the Baltic Sea outflow is affected by wind direction. This has implications for the Norwegian Coastal Current (Mork, 1981).

1.2.3 Density driven circulation

Density driven currents can play an important role in shelf sea circulation as for example in the exchange between the Black Sea and the Mediterranean. In coastal seas a major factor for the modification of the density structure is the input of buoyancy, due principally to the seasonal cycle of heating and cooling and to lateral input of fresh water by rivers. Heating and cooling processes affect the whole shelf but temperature change is highly dependent on bottom topography and latitude - Elliott *et al.* (1991) compiled a monthly archive of bottom and surface temperature and showed correlation with depth and latitude. It is useful to consider some length scales and non-dimensional parameters which characterise the physics of stratified, rotating fluids. Firstly, it is important to consider the stability of the water column. In a stratified fluid when a vertical displacement takes place, the response of a parcel of water depends on whether the water column is stable, unstable or neutral. A measure of this stability is given by the buoyancy frequency, or Brunt - Väisälä frequency, N defined as

$$N^2 = -\frac{g}{\rho_o}\frac{\partial \rho}{\partial z} \tag{1.4}$$

where ρ_o is a reference density. Physically N represents the adjustment frequency of a parcel of water in purely vertical motion (Gill, 1982). According to the sign of the

expression the fluid is stable, unstable or neutral. In the presence of a strong stable stratification vertical mixing can be inhibited; the parameter that estimates the competition between stratification and mixing is the gradient Richardson Number R_i defined as

$$R_i = \frac{N^2}{\left(\left(\frac{\partial u}{\partial z}\right)^2 + \left(\frac{\partial v}{\partial z}\right)^2\right)^{\frac{1}{2}}} \tag{1.5}$$

For values of $R_i > 0.25$ vertical turbulent exchanges are suppressed.

Another useful parameter is the baroclinic Rossby radius of deformation r_d defined as

$$r_d = \frac{(g'h)^{\frac{1}{2}}}{f} \tag{1.6}$$

where f is the Coriolis parameter, g' and h the reduced gravity and a depth scale respectively. For a simple two-layer fluid g' can be expressed as

$$g' = g\frac{(\rho_2 - \rho_1)}{\rho_2} \tag{1.7}$$

This parameter is the natural length scale for baroclinic processes in a rotating fluid. The Burger number B_u is the ratio between the width of a coastal current L and the Rossby radius defined in (1.6)

$$B_u = \left(\frac{r_d}{L}\right)^2 \tag{1.8}$$

The Ekman number E is defined as

$$E = \left(\frac{D_e}{h}\right)^2 \tag{1.9}$$

where D_e is the Ekman depth defined as.

$$D_e = \sqrt{\frac{K}{f}} \tag{1.10}$$

where K is a coefficient of eddy viscosity and f the Coriolis parameter.

A coastal current is the result of disruption of geostrophic adjustment by the coastline (Hill, 1998). The presence of a coast interferes with this process of spreading and deflection (by Earth's rotation) of a low density mass of fluid. On the North-west European Shelf one finds the Scottish coastal current (Simpson and Hill, 1986) and the Norwegian Coastal Current (Mork, 1981). Both flow northwards along their respective coastlines due to the rotation of the earth, and both are affected by winds. The main difference is related to their Ekman's number. The Scottish current has large E so the mixed layer reaches the bottom and the flow is strongly steered by the bottom topography (Simpson and Hill, 1986; Hill and Simpson, 1989). In the Norwegian case, the current is in relatively deep water and the Ekman's layer does not penetrate the whole water column so a wedge of less salty water flows along the coast. The Norwegian current exhibits baroclinic instabilities due to its Burger number which is less than 1. These instabilities have been observed and also modelled (Oey and Chen, 1992a,b).

Other types of coherent baroclinic structure can be found on the shelf. In some locations, strong horizontal density gradients (fronts) occur both at the sea surface and at the bed, as discussed previously (§ 1.2.1). Two examples of this kind are the seasonal gyre in the western part of the Irish Sea (Hill *et al.*, 1994) and the Islay front on the Malin shelf (Simpson *et al.*, 1979). The first example has been widely studied and modelled (Hill *et al.*, 1994, 1996, 1997a); in this part of the Irish Sea the water column can develop stratification during the year. The spatial variation in topography and tidal currents causes a dome of cold, dense water to form every year which persists until it returns to the mixed state in late autumn because of cooling and strong wind mixing. This lens of dense water triggers a cyclonic circulation which has been observed with satellite tracked drifters (Horsburgh *et al.*, 2000). Modelling studies show unequivocally that this circulation is baroclinic (Horsburgh *et al.*, 2000).

Frontal circulation presents distinctive aspects which can be observed (Simpson *et al.*, 1978, 1979). Fronts are a zone of convergence; debris and foam can be seen at the surface of a front (Simpson and James, 1986) and upwelling can be observed from the temperature minima in the frontal area (Simpson *et al.*, 1978). Baroclinic instabilities such as eddies can be observed in satellite pictures (Simpson *et al.*, 1978). Dynamically fronts are, to a first approximation, in geostrophic equilibrium (Hill

et al., 1993) dominated by the presence of a current parallel to the front (flowing with the stratified water on its left). This along-front jet is one of the most pronounced characteristics of frontal circulation and speeds can reach 0.1-0.2 m s^{-1} (Hill *et al.*, 1993), but it is also one of the most difficult to measure due to the strong tidal background. Some observations were collected for the Islay front (Simpson *et al.*, 1978) and for the Flamborough front, during the North Sea Project (Lwiza *et al.*, 1991); in the first case drouge buoys were employed whilst ADCP instruments were used in the North Sea. Observations of the Flamborough front showed an along-front jet of 0.15 m s^{-1}, much stronger than the cross-front component (Lwiza *et al.*, 1991).

The geostrophic equilibrium is disrupted by friction, which tends to decelerate the along-front jet thus creating an imbalance in the pressure field leading to a secondary cross-frontal circulation (Hill *et al.*, 1993). Various modelling approaches have been undertaken to explain the frontal circulation since observations are difficult to conduct. James (1978) demonstrated the existence of the along-front and cross-front flow with the help of a two-dimensional numerical model. Starting with simple but realistic field of density, he obtained a two cell circulation in the plane normal to the front with associated convergence in the frontal zone and upwelling of cold water (James, 1978). The importance of frictional effects on frontal circulation was investigated by Garrett and Loder (1981); their study showed the relationship between the Ekman number and the strength of the cross-frontal flow. With their diagnostic model they achieved results similar to those of James (1978). Their predictions showed the upwelling of cold water on the well mixed side in accordance with the observations carried out by Simpson *et al.* (1978). Other mechanisms for cross-frontal exchange of properties were analysed in this investigation showing that wind could play a secondary role in the transfer along with barotropic and baroclinic eddies.

1.2.4 Long term circulation

Long term circulation may be defined as the shelf circulation averaged over a long period of time so that periodical contributions (such as tides and any high frequency signals) are minimised or eliminated. Historically, many studies of the circulation, transport pathways and residence times in the Irish Sea and on the Scottish Shelf

have been based on the transport of radioactive caesium ^{137}Cs released into the Irish sea from the Sellafield nuclear reprocessing plant (Jeffrey *et al.*, 1973; McKinley *et al.*, 1981; McKay *et al.*, 1986). A model study (Prandle, 1984) covered the whole shelf with a two-dimensional hydrodynamic model to reproduce the horizontal mixing of ^{137}Cs; the model was forced for 17 years with the M_2 tidal component and with annual wind stress. The model runs covered different combinations of wind stress and were used to infer the residual circulation. The results agree qualitatively with fig. 1.6. The pattern is for a clockwise circulation around the British Isles; water flows from the Celtic sea into the Irish Sea and the Sea of the Hebrides and later turns eastward inside the North Sea. The residual flow in the North Channel is around 0.02-0.03 m s^{-1} (Knight and Howarth, 1999) and can be correlated with the wind but cannot be fully described as a wind-driven motion (Brown and Gmitrowicz, 1995). Density gradients also play an important role as a driving mechanism (Brown and Gmitrowicz, 1995). Irish Sea water moving on to the Malin Shelf mixes with water exiting the Clyde Sea, which is less dense due to fresh water inflow (Poodle, 1986). On the Scottish shelf the flow remains northward consistent with the existence of a coastal current (Simpson and Hill, 1986).

Fig. 1.6 illustrates that shelf circulation is not a closed system but is significantly influenced both dynamically and in terms of exchanges with the ocean. Tides propagate from the deep ocean into the shelf, generating the co-oscillating response (Huntley, 1980) and in the process undergoing amplification in both elevation and currents (Clarke and Battisti, 1981). Because the continental slope is usually parallel to the coast and the Taylor-Proudman theorem states that geostrophic flow cannot cross isobaths (Brink, 1998), the slope could act as an insulator between the shelf and the deep ocean and prevent exchange. In reality, friction and baroclinic instability ensure shelf-ocean exchanges. Hill (1995) has demonstrated that leakage of barotropic slope currents on the shelf is possible when there is an increase of slope in the direction of the current flow. This fact is directly applicable to the Northwest European Shelf; a slope current has been extensively observed and studied (Ellett and Martin, 1973; Booth and Ellett, 1983; Dickson *et al.*, 1986; Huthnance, 1986). These measurements show the existence and the persistence of a slope current which flows northward along the shelf edge with a velocity of typically 0.16 m s^{-1} (Booth and Ellett, 1983) driven by an along-slope pressure gradient (Huthnance, 1981). There is evidence which suggests that the Scottish slope current spreads over the shelf, especially in winter and autumn (Booth and Ellett, 1983; Ellett *et al.*,

1986). Xing and Davies (2001) employed a three-dimensional model with realistic topography and bathymetry and showed that the slope current can intrude onto the continental shelf and in the Irish Sea through the North Channel. Several other dynamical processes (e.g. internal tides and internal waves) occur at the shelf edge which permit an exchange of properties with the ocean (for a review of these shelf exchange properties see Huthnance, 1981). These complex exchange processes are difficult to quantify and, consequently, to model in a realistic way.

1.3 The role of 3D baroclinic models in the simulation of shelf seas circulation

A large number of three-dimensional hydrodynamic ocean and coastal models are now available to the scientific community. Due to the non-linearity of the equations describing fluid motion, in general analytical solutions are rarely available and numerical solutions are required. For this purpose various techniques have been created: equations have to be transformed in a discrete form and then numerically integrated in a number of different ways. Finite difference methods are used in the Princeton Ocean Model (Blumberg and Mellor, 1987) and also in so-called spectral models (Davies *et al.*, 1997a). Recently the finite element approach has been utilized for its ability to cope with fine resolution and convoluted coastlines together with boundary fitted co-ordinates, as for example in the QUODDY (Ip and Lynch, 1994) or SCRUM (Song and Haidvogel, 1994) models but this approach is still under investigations and testing and there are still few case studies to allow a complete evaluation of their performances in three-dimensional baroclinic problems.

The coastal environment represents a big challenge for these tools. Shelf seas are highly baroclinic and the temporal and length scales of physical processes cover various order of magnitude. Eddies and frontal systems have a length scale of tens of kilometres and span days or even months whilst turbulent dissipation occurs on scales of the order of the centimeter or less and has a characteristic timescale of seconds. On a larger scale, the continental shelf is subjected to different barotropic motions like storm surges or tides which contain most of the energy on the shelf. All these processes need to be resolved (or parameterised) and this make their simulation demanding from a computational and theoretical point of view.

Coastal modelling is a valuable mathematical tool for the understanding of the physics of shelf seas and many coastal theoretical problems have been investigated with models. (Tee, 1994) studied the process of topographic rectification with the help of a two-dimensional model and he was able to investigate the contributions of various forcings and the effects of upwelling and downwelling on the residual circulation. Xing and Davies (1999) investigated the behaviour of a river plume under the action of wind with a variety of turbulence closure schemes, wind stresses and bathymetries. Kourafalou *et al.* (1996a,b) described the fate of a river plume and its transport due to meteorological forcing. Zavatarelli and Mellor (1995) studied the seasonal dynamics of the Mediterranean Sea and the formation of deep water in the same basin. Davies (1997) and Davies and Kwong (2000) investigated tidal mechanisms such propagation and dissipation with the help of a spectral model covering the whole European shelf, with results in agreement with observations.

Early models of the physics of the shelf were primarily concerned with barotropic processes. Due to their two-dimensional nature, shallow-water linear equations could be used. These models were employed to investigate storm surges on the European shelf (Heaps, 1969) or the propagation of tides (Flather, 1976). Results were in good agreement with observations but their resolutions were coarse and other important phenomena were not simulated. With the increase of computer power and its availability, these models developed allowing three-dimensional equations of motion to be used (Davies, 1987). Density gradients and stratification were included in simulations and the models became more realistic. With three-dimensional models it is possible to investigate the vertical profile of coastal currents that had previously been described by depth average velocities. Such models also allow surface and seabed boundary layers, or Ekman's layers. In coastal waters, density evolves in time both horizontally and vertically and driven-density currents are an important component of shelf sea flow, so a prognostic description of the salinity and temperature fields is needed for realistic simulations. The correct simulation of density-driven features like those previously described (§ 1.2.3) is a stern test for coastal ocean models. These features are highly non-linear and require an accurate specification of buoyancy fluxes at the surface and later boundaries so that sources of fresh water must be accounted for modelled in a realistic way with the help of observations; moreover it relies on the correct description of processes such advection and diffusion which are not easily reproduced numerically.

A key factor in the accuracy of coastal simulations is the resolution of the model. The typical length scale for some baroclinic processes (Gill, 1982) is the baroclinic Rossby radius r_d as defined in (1.6). The internal Rossby radius is the appropriate length scale for coastal modelling (James, 1990) and it is the minimum scale required for resolving baroclinic phenomena like frontal and coastal current instabilities. This has implications for the computer power needed, especially if a simulation of the whole continental shelf is required at middle-northern latitude where r_d is of the order of 10 km or less.

A grid chosen with this parameter in mind could still be too coarse if the spatial variability of currents is of the order of 1 km as, for example, in the North Channel (Davies and Hall, 2000). The spatial resolution can automatically define a constraint on the temporal resolution of the model, when using explicit algorithms; for example the CFL (Courant-Friedrichs-Levy) condition determines the maximum time step to obtain a stable solution (see for instance Kowalik and Murty, 1993). When high resolution is only required in a local region, or subsection of the domain, then it is possible to use a nested grid in which a fine resolution grid is placed inside a coarser resolution grid. This approach was implemented for the Norwegian Coastal Current (Oey and Chen, 1992a), although there was no two-way coupling between the grids. Resolution constraints can also be overcome by the use of finite element methods, which have finer resolution on the area of interest, or by using implicit algorithms which are stable for every time step. Coastal models must also generate and maintain sharp density gradients. When the dynamical equations are transformed to allow their numerical integration, errors are introduced into the solution especially in that part responsible for the advection of scalars such as salinity and temperature. This can result in unphysical smoothing or overshooting (ripples) in the scalar fields (Kowalik and Murty, 1993). Numerical schemes designed to correct or minimize these problems will be discussed in detail later. The drawback of these corrective schemes is the large increase in computational time required.

A major uncertainty in the accurate modelling of the vertical structure of the flow is the specification of vertical momentum exchange. Shelf sea flows are turbulent and Reynolds stresses are the manifestation of turbulence in the governing equations (Gill, 1982). The Reynolds stresses can be related to the characteristics of the mean motion through various closure hypotheses (see Jaw and Chen, 1998, for an overview). However the theoretical formulation of these closure schemes, and

their application in models, is complicated and demands computational effort. A variety of such schemes have been tested against measurements in laboratories and in situ (Burchard *et al.*, 1998). In models, eddy coefficients can be explicitly defined through an algebraical formulation (e.g. Proctor and Davies, 1996) or they can be calculated with the Mellor-Yamada 2.5 closure scheme (Mellor and Yamada, 1982) which is implemented in various coastal models including the Princeton Ocean Model (Blumberg and Mellor, 1987).

Models are valuable for testing theories and for providing the temporal and spatial coverage unobtainable by observations. They can also provide insight into processes that are intrinsically difficult to measure due to the spatial or temporal scales involved or simply because the observations required are expensive or difficult to carry out. Frontal systems are one example where long-term observations are difficult for a variety of practical reasons and the controlling physics are complicated. Yet understanding of the mechanics of fronts, including convergence and cross or along-frontal flows can be helpful for a variety of environmental reasons (Hill *et al.*, 1993). In cases like these, coastal models are useful tools provided that they are validated at the same time with observations. Ideally these observations should be collected on a very fine temporal and spatial grid so to have a huge ensemble of data for the validation but this approach is not always viable for economical and technical reasons. Careful thinking must be given to locations and temporal length of deployment; a comprise could be reached if the boundaries of the regions are sampled. In this case these data would be a twofold purpose, to be used for validation and also as driving forcing for simulations. For coastal simulations, such the one presented in this work, these locations should be close to the coast to take into account and to measure the effects of sources of fresh water on the circulation. Another critical region is the area between open ocean and shelf sea so that is possible to determine and later incorporate the exchanges at the open boundaries (see later discussion). The temporal deployment should at least annual, to resolve the seasonal development of the area of interest.

1.4 Aim of the study and layout of the thesis

The Scottish Shelf is the main object of investigation in this modelling study and the main tool is an application of the Princeton Ocean Model (POM). In this chapter

a brief description of the dynamical processes affecting the circulation of shelf seas has been given, with a focus on the northwest European continental shelf. The European shelf has undergone fairly extensive study but the Scottish Shelf has been relatively neglected. Observations there are sparse and sporadic and models have been applied only for tidal or wind-driven simulations (Proctor and Davies, 1996; Xing and Davies, 1996c). No full baroclinic seasonal simulation of the area has been attempted to date. This study makes a contribution towards understanding of the full seasonal dynamics of this region. Seasonal cycles of salinity and temperature will be simulated and their contribution to the density structure will be investigated. The annual variability of circulation and transport in the region will also be modelled. Particular attention will be given to well-observed features - the tidal mixing front on the Malin Shelf and the recirculation in the Sea of the Hebrides.

The influence of wind direction and strength, inflow from the Scottish Shelf and local density structure on the recirculation in the Sea of the Hebrides will all be investigated. The variability of transport through this particular region will be also studied for its importance and implications for the biology of the region (e.g. Nephrops larval retention, fish farming and the potential management of oil spills or waste dispersion). A model investigation into the development of the Islay front will also be carried out, from its establishment in spring until its breakdown in autumn due to the seasonal cooling. As previously mentioned, observations (Hill and Simpson, 1989) show that a distinct salinity front coexists with the thermal front. One of the aims of this study is to study their interaction during the seasonal development. A final aim of this study is to assess the feasibility using the Princeton Ocean Model for coastal simulations where baroclinic effects make an important contribution to the general circulation.

- This introductory chapter provides a brief summary of the physics of the coastal sea with special attention to the processes operating on the northwest European shelf, including density-driven effects.
- The second chapter will deal with the regional oceanography of the area under examination. Its seasonal cycles of thermal and haline stratification, and their interaction, will be described. The regional circulation will also be described on the basis of the available observations.

- The third chapter will give a thorough description of the Princeton Ocean Model, including a discussion of previous applications and results from the literature. Then its configuration for the region will be outlined along with descriptions of the initial and boundary conditions, meteorological forcing and temperature and salinity fields at the open boundaries. Modifications to the original code will be highlighted.

- The fourth chapter will be concerned with validation of the model, especially the comparison between observed and modelled tidal currents and elevations. As previously stressed, tides are the major source of kinetic energy on the shelf and are also responsible for other effects such as the position of tidal mixing fronts. In this study, accurate reproduction of the tidal characteristics is a necessary condition for the correct simulation full seasonal cycles of the other properties.

- The fifth chapter will present detailed results from a full seasonal simulation and will make comparisons with observations in the area, to evaluate the overall performances of the model when simulating the seasonal cycle of temperature and salinity.

- The sixth chapter will concentrate on the Islay front, and the model performance regarding the simulation of this important baroclinic structure. Observations and model results will be compared and discussed, with particular interest in the long term circulation present in the Sea of the Hebrides. The seasonal variation of the transport through the Minch will be described and results will be compared with the few observations available.

- The seventh chapter will recap and discuss the overall work produced within this study. The performances of the model will be evaluated. There will follow a general discussion which will include directions for future work.

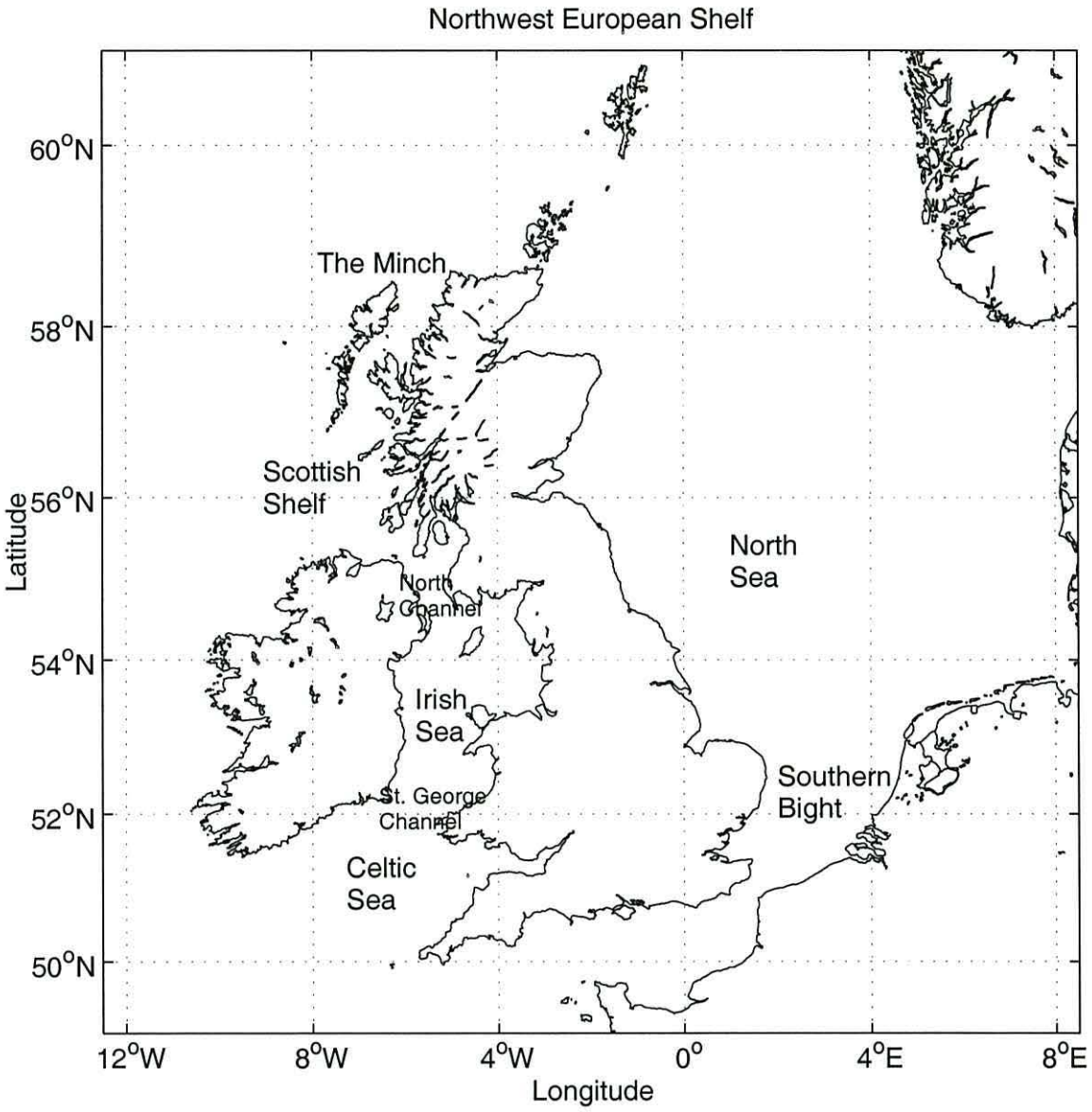

Figure 1.1: The North-west European Continental Shelf: Locations and Names.

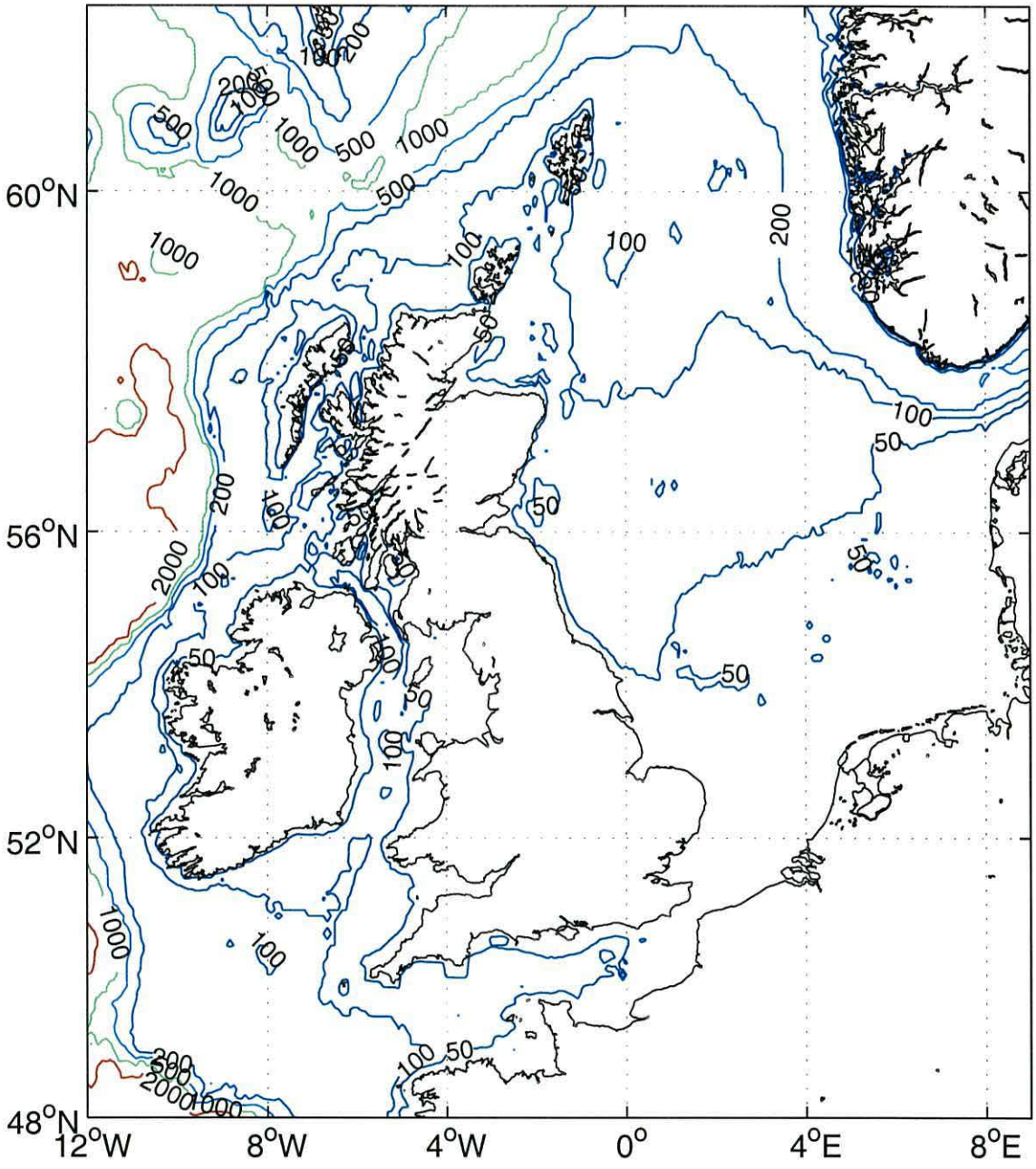

Figure 1.2: Bathymetry of the North-west European Continental Shelf: countour levels at 50, 100, 200, 500, 1000 and 2000 m.

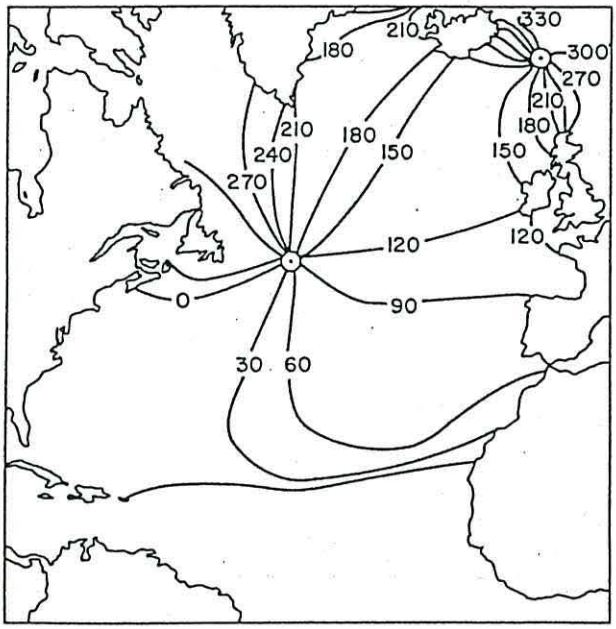

Figure 1.3: Estimated position of the North-Atlantic amphidromic point for M_2 (from Huntley, 1980).

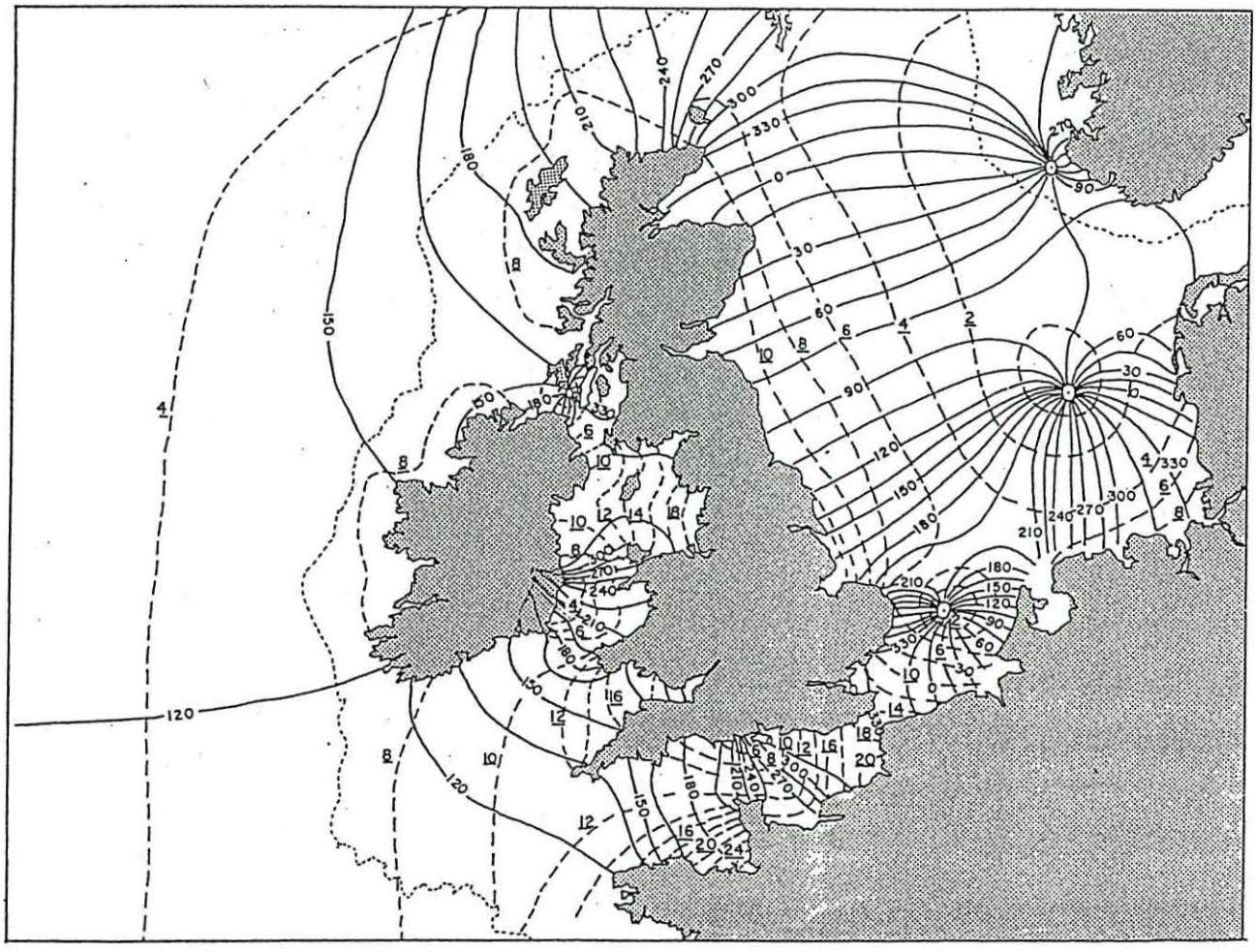

Figure 1.4: Co-tidal and co-range chart for M_2 in the North-west European Continental Shelf. Solid lines: co-tidal lines showing phase lag in degrees relative to passage of the moon over Greenwich; dashed lines: co-range, underlines numbers show range in feet (~ 0.3 m) (from Huntley, 1980).

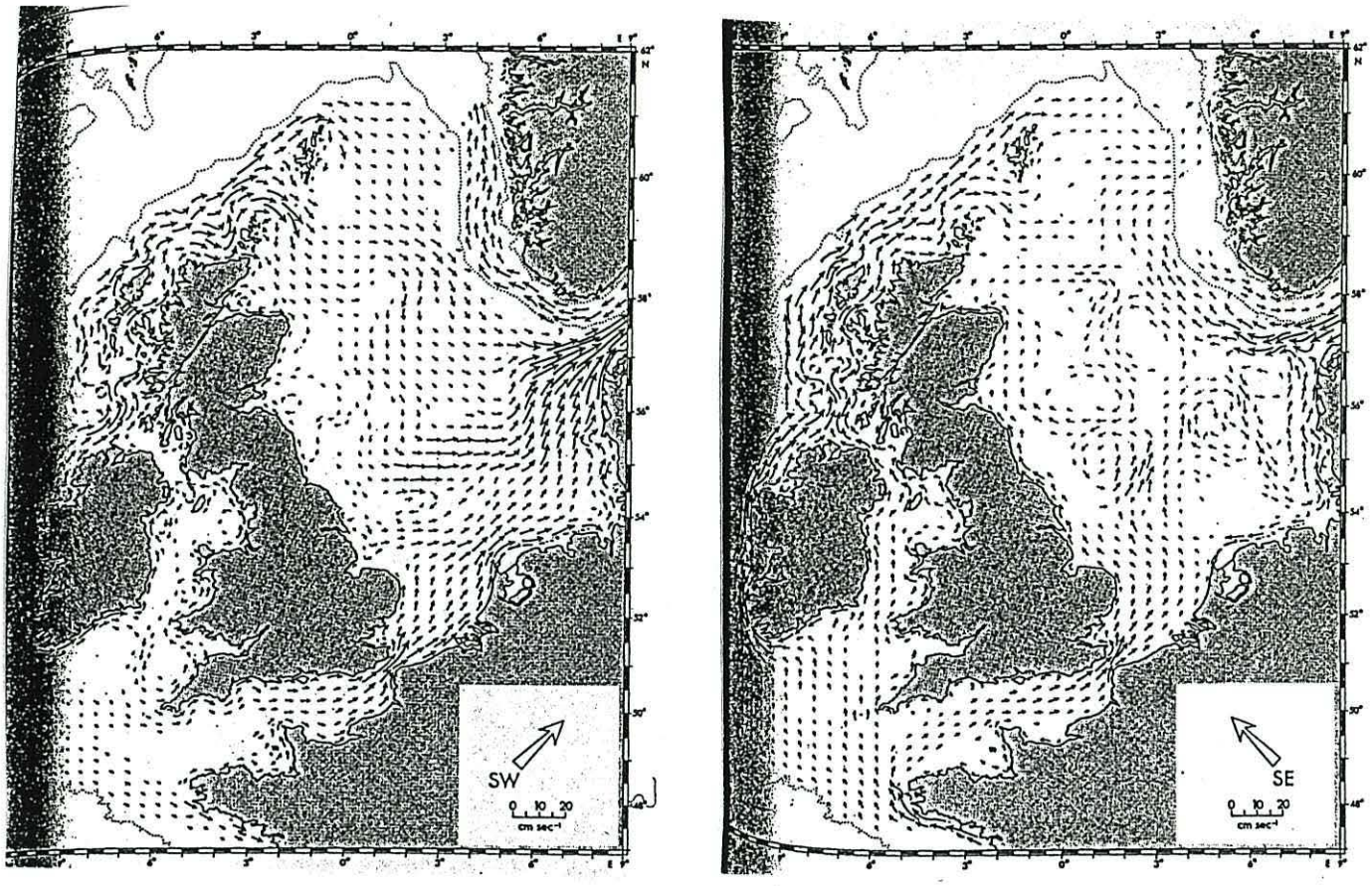

(a) (b)

Figure 1.5: Simulated residual flows on the North-west European Continental Shelf for a) constant southwesterly and b) southeasterly winds (from Pingree and Griffiths, 1980).

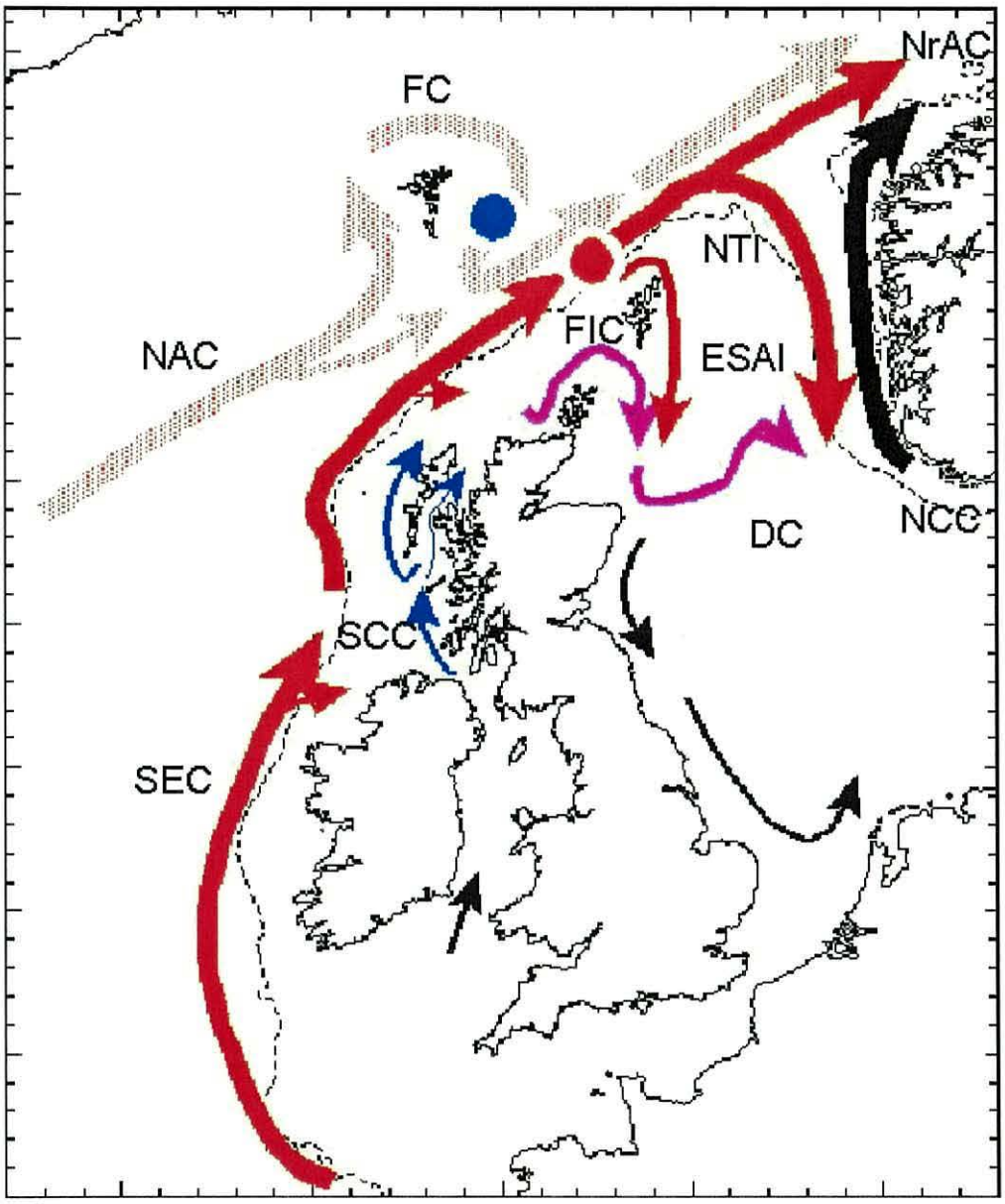

SEC	Slope Edge Current
SCC	Scottish Coastal Current
NAC	North Atlantic Current
FC	Faroe Current
FIC	Fair Isle Current
DC	Doodley Current
ESAI	East Shetland Atlantic Inflow
NTI	Norwegian Trench Inflow
NCC	Norwegian Coastal Current
NrAC	Norwegian Atlantic Current

Figure 1.6: Long term circulation on the North-west European Continental Shelf (from Turrell, 2000).

Chapter 2

Regional Oceanography

2.1 Introduction

The Scottish shelf is located between latitude 55°N and 59°N and longitude 4°W and 8°W (Figure 2.1) and includes the Malin Shelf in the South and the Hebridean shelf to the north. This region includes a part of the Scottish mainland and some islands: in particular the chain of the Outer Hebrides and Inner Hebrides. Together they form the area known as Hebridean waters which include the Sea of the Hebrides, the Little Minch and the North Minch (the channel formed by the Outer Hebrides and the mainland). It has been shown that several distinct masses of water meet on this shelf, with different thermohaline characteristics (see for example McKay *et al.*, 1986). Interactions of these waters with the topography and the seasonal cycle of heating and cooling give origin to the seasonal pattern and circulation observed in the region. As discussed in the previous chapter there is a weak northward residual circulation which follows the Scottish coast and there are two major coherent structures observed in the region: the recirculation cell in the Sea of the Hebrides and the tidal mixing front on the Malin Shelf, between Malin Head and Islay. The former is a constant feature which consists in the diversion of part of the northward flow when it reaches the Sea of the Hebrides while the latter is, in part, a seasonal feature which is observed mainly in spring and summer.

The aim of this section is to supply some background on the physical oceanography of the area and describe its seasonal variability. Some observations are presented together with some regional studies but it remains important to stress that there

are few observations available in the region and that temporal and spatial coverage is sparse and discontinuous. Knowledge of the long term circulation comes largely from radioactive tracers released from the reprocessing nuclear plant at Sellafield (Cumbria) on the English coast of the Irish Sea. Observations (McKinley *et al.*, 1981; McKay *et al.*, 1986) and models (Prandle, 1984) enabled features of the flow and residence time to be estimated. Temperature and salinity fields were also measured during these cruises but detailed seasonal coverage is lacking. One of the aims of this numerical investigation is to clarify important physical aspects of this region which contains 11 designated National Scenic Areas, (NSAs) and many other areas of great importance for animals, especially birds, and plants (Bryan, 1994). The region of the Minch is also important for the whole Scottish economy, being the location of most of the Scottish fish farming operators and of important fishing ports (Bryan, 1994).

2.2 Topography and bathymetry

The eastern boundary of the area is the Scottish mainland where the coastline is very complicated (Fig. 2.2), due to the presence of glacial valleys that have become fjords and sea lochs. These lochs have typical depth from 100 m to 200 m with the deepest reaching 316 m (Ellett and Edwards, 1983). This complex bathymetry can affect dynamical processes such as tides: each basin can respond in a different way when tidal waves propagate inside lochs. The different wave propagation routes, phases and ranges causes sea level variations which drive currents. In addition, topographic features are sources of enhanced turbulence and can interact with tidal flow (Huthnance, 1973). The western boundary to the region is open; both the Hebridean and the Malin shelves are in direct contact with the Atlantic Ocean. The continental slope is situated in this area, where there is a sharp change in bathymetry and a continuous slope current as discussed in the previous chapter. At about 58°N the continental slope changes orientation from north-south to northeast-southwest, which is the maintained for about 900 km (Jones *et al.*, 1986). This is reflected also in a change of the morphology of the continental margin and of the orientation of the Outer Hebrides which run parallel to the new slope direction. To the south, the Hebridean region is bounded by Ireland and the narrow North Channel (20 kilometres wide in its narrowest). The depth of this channel ranges from

20 m to about 250 m. Finally the northern boundary is completely open and allows exchanges of properties between inner shelf and outer shelf water. In conclusion the Scottish shelf is a region bounded by one rigid and three open boundaries which are responsible for the interaction with the Atlantic ocean and the Irish Sea.

2.3 Tides

The area is subject principally to the action of tides of the Atlantic ocean, as explained in the previous chapter. Tidal motion inside the region is not related directly to the action of gravitational forces but due to a co-oscillating response of the shelf seas to the tides generated in the ocean (Huntley, 1980; Ellett and Edwards, 1983). Inside the Hebridean Shelf the tide can be described by a standing long wave (Ellett and Edwards, 1983) with a semidiurnal period and a wavelength of 1300 km so that a bulge or a trough alternately covers the Inner Hebrides region which extends for almost half a wavelength. A large difference in the spring-neap cycle characterises the southern part of the region. Adjacent to the island of Skye the neap range is 1.6 m while the spring one is 4.5 m, whereas near Kintyre the respective elevation values are 0.5 m and 1.6 m (Ellett and Edwards, 1983). From observation (George, 1980) it is possible to infer the presence of an amphidromic point between Islay and the coast of Ireland, at the northern end of the North Channel. Here, tidal amplitudes are small compared with other areas within the shelf. Generally, shelf tides are dominated by semi-diurnal constituent and elevations of this component are normally ten times greater than those of diurnal components (Huthnance, 1986). Near the shelf edge other characteristics are seen: in the area of St. Kilda and the Outer Hebrides diurnal currents are comparable with semi-diurnal currents because of the properties of propagation of continental shelf waves (Cartwright *et al.*, 1980a,b).

The water in the North Channel is well mixed all the year round, due to the strong tidal current there, whereas further west on the Malin shelf seasonal stratification due to solar heating develops. The sharpest gradient (front) between the stratified and mixed waters is observed near the island of Islay and is clearly visible in satellite pictures (Simpson *et al.*, 1978). There are two distinct aspects to the Islay front (Hill and Simpson, 1989); the haline front is generated by the difference of salinity between the Atlantic and the coastal waters. This feature is present throughout the

year although it is not static and a seasonal adjustment can be observed (Hill and Simpson, 1989). The thermal signature of the front is typically seasonal (Simpson *et al.*, 1979; Hill and Simpson, 1989) and can be interpreted as the interplay between the seasonal cycle of stratification and the turbulence generated by tides, as already discussed in the previous chapter.

2.4 Mean Circulation

Composite observations show that the mean circulation on the Scottish shelf is mainly northward. Craig (1959) used drifting bottles, and salinity and temperature measurements, to sketch the main features of the surface circulation (figure 2.3). The Irish Sea water flows northward, exiting the North Channel; on the Malin shelf it encounters Atlantic water establishing the haline front. When the flow reaches the chain of the Outer Hebrides there is a diversion; part of the flow passes through the Sea of the Hebrides and the Little and North Minches. The other part is deviated westward and circulates around Barra Head to continue northward, on the western side of the Outer Hebrides as illustrated in Fig. 2.4. At the north end of the chain the flow rejoins, after an Atlantic intrusion in the North Minch (Craig, 1959), and proceeds around the Scottish coast. The overall picture is compatible with the flow of a coastal current under the influence of the Coriolis force (Simpson and Hill, 1986). Several mechanisms combine to give this flow. Wind driven currents and (with a minor contribution) tidal residual currents play an important role as generating mechanisms for the observed pattern; it is possible to distinguish between local effects (such tidal rettification and local wind induced currents) and far field effects where there is a contribution from regions far from the Scottish shelf. Xing and Davies (1996c) investigated the importance far field effects generated by winds in the dynamics of this particular shelf, showing their importance in the region. Brown and Gmitrowicz (1995) also discussed the importance of this effects in controlling fluxes through the North Channel. The other important contribution is given by buoyancy driven flow which add and interacts with the previous components, to generate what is known as the Scottish coastal current (Simpson and Hill, 1986). The density driven flow is created by coastal water that is less saline than the oceanic water. There are major contributions of buoyancy through fresh water inflow in the Clyde sea, loch Linnhe and the Firth of Lorne. Finally Xing and Davies (1996c)

also showed the effect of the configuration of the topography (where isobaths are roughly parallel to the coastline) in steering the long term circulation, demonstrating its importance in controlling the direction of the flow.

For the Hebridean and Malin shelves there are few direct observations of currents. Craig (1959) estimated a flow of 5 km d^{-1} or 5.7 cm s^{-1} for the area from the North Channel to the Minches. Having noticed the existence of the recirculation cell in the Sea of the Hebrides, he calculated the strength of the two main branches. According to these estimates (Craig, 1959) the water in the central Minch accounted for two-fifth of the total flow, leaving the remaining three-fifth flowing on the western side of the Hebridean chain. In the same way he estimated the exiting flow in the North Minch. He split the water in this region into three different bodies: West Hebrides water, Central Minch water and Coastal stream. Craig (1959) compared the movement of the first body to the counter current in the North Channel and estimated its velocity to be between 0.5-0.75 km d^{-1}, leaving the main body with a velocity of 1-1.5 km d^{-1}. These values were calculated accounting for the freshening of water in the area and they represent a crude but effective estimate of the real circulation.

More recently, McKinley *et al.* (1981) analysed the results of two cruises which took place in the summers of 1976 and 1977 and used the properties of radioactive tracers ^{134}Cs and ^{137}Cs and their differential decay constants. During the first cruise it was possible to show that mean velocities were of the order of 1.6 km d^{-1} in the North Channel and 5 km d^{-1} in the region between it and the Minches. Current meters deployed in the proximity of Tiree and Coll showed a mean velocity of 11.8 km d^{-1} but the instruments were deployed for only 5 days at the end of May and soon after a period of strong southerly winds (McKinley *et al.*, 1981). The second cruise showed a different picture of the area with the radioactive plume from the the Windscale plant being spread more westward. This pattern was reflected in the salinity distribution (see Fig. 5, McKinley *et al.*, 1981). In this case mean velocities were lower than the previous estimates. For the region from the North Channel to the isle of Coll, they were of the order of 1.5 km d^{-1} while currents in the area approaching the Little Minch were estimated at 0.5 km d^{-1}. In July 1981 a further cruise (McKay *et al.*, 1986) was undertaken to investigate the distribution of ^{134}Cs and ^{137}Cs on the Scottish shelf. Here, two current meters were deployed for the entire duration of the cruise, but not in the same position as previously. One was

deployed close to Coll while the other was deployed near South Uist. The radiotracer data collected gave an estimate for mean velocity in the Sea of the Hebrides of the order of 1.9 km d^{-1}, slightly above the value measured in 1977. The current meters detected a northward residual of 2.6 km d^{-1} so that this cruise was more similar to the one undertaken in 1976 than in 1977 when, probably, there was a relaxation of the coastal current due to the Atlantic flushing (McKay *et al.*, 1986).

A program of observations was undertaken during 1983 with the aim of directly establishing the existence of a mean northward flow close to the Scottish coasts and to assess its variability (Simpson and Hill, 1986; Hill and Simpson, 1989). Three currents meters were deployed for a long period in different points of the Scottish shelf and at different depths (see table 1, Hill and Simpson, 1989). Two were deployed on the Malin shelf, southward and eastward of Tiree and Coll. The remaining one was moored inside the Little Minch, to measure current in this previously unobserved area. The results obtained mainly confirmed the exiting picture; on the Malin shelf the flow is predominantly northward with velocities of the order of 5-10 cm s^{-1} but with peaks of 40 cm s^{-1} and also events where the flow reverses (Simpson and Hill, 1986). In the Minch, low frequencies currents flow northward, especially in the autumn (Simpson and Hill, 1986) but again reversal events are present in the summer months.

A major feature of the Scottish coastal current is its interaction with the Outer Hebrides ((Simpson and Hill, 1986). Previous calculations predict almost the same total transport reaching the Sea of the Hebrides of 11.0×10^4 m^3 s^{-1} (McKay *et al.*, 1986) and 11.5 $\times 10^4$ m^3 s^{-1} (Craig, 1959) but there is disagreement regarding the partition of the flow. Craig (1959) was aware of the recirculation in the Sea of the Hebrides (Fig. 2.4), yet his estimate that 2/5 of the flow passes inside the Minch (with the remaining 3/5 passing on the Atlantic side of the Outer Hebrides) differs from that of McKay *et al.* (1986) who put the ratio at 9/11 and 2/11 respectively. More insight into the recirculation cell was gained during a series of two cruises undertaken during April and May 1995 (Hill *et al.*, 1997b) when five satellite-tracked drifters were released inside the Sea of the Hebrides (fig. 2.5). These drifters gave a direct proof of the existence of a near surface, cyclonic flow in that area of the Scottish shelf (Hill *et al.*, 1997b). This coherent residual flow is associated with an intrusion of Atlantic water at depth. The tongue of saline water is present throughout the year. The drifter tracks showed that at the entrance of the Minches

the flow bifurcates, one part following the channel northward while the other flows to the west of the Outer Hebrides. Since previous models results (Proctor and Davies, 1996; Xing and Davies, 1996c) show a negligible barotropic circulation due to tidal rectification and wind-driven residuals, this seems to suggest a baroclinic interpretation of the feature.

2.5 Seasonal evolution and observations

Observations of temperature and salinity fields are mainly available for the summer period. The summer of 1976 and 1977 (months of May and July, respectively) have been described in McKinley *et al.* (1981) and the summer of 1981 (July) in McKay *et al.* (1986). There are data from a CTD transect which covers the year from 1982 to 1986 (Hill and Simpson, 1989) but in general the area lacks a full and coherent coverage. In addition, the spatial resolution and stations visited vary according to the aim of the individual cruise. Recent measurements made by the Marine Laboratory Aberdeen represents an attempt to monitor the development of salinity and temperature throughout the seasonal cycle in the Sea of the Hebrides and the Minches. Four cruises were made in the period from 1996 to 1998, one during each of the four different seasons. Some of these data will be presented and discussed later.

A major feature of this region is the intrusion of Atlantic water in the Sea of the Hebrides, which can be detected during the whole year and it is persistent from year to year (Hill *et al.*, 1997b). From the earliest observations of Craig (1959) to the more recent cruises, carried out by the Marine Laboratory Aberdeen from 1996 to 1998, this intrusion is regularly observed. There is a similar intrusion in the northern part of the Minch, near the Butt of Lewis. In both cases the intrusion has a signal throughout the water column with, usually, an increase of density with depth. The strength of this saline intrusion changes seasonally as observed by Hill *et al.* (1997b) with maximum density difference in spring. The dome-like structure is also present during summer but the isopycnals tend to be more horizontal and in Autumn the structure strengthens again. The intrusion is flanked on both sides by fresher and usually colder coastal waters. On the eastern side this can be explained as advection of the Scottish Coastal Current and on the western flank this results

from the recirculation described. The input of fresh water coming from the Outer Hebrides, estimated at 32 m^3 s^{-1} by Craig (1959), is not sufficient to explain the presence of coastal water in this area which points to a non-local source as its cause (Hill *et al.*, 1997b). The saline dome provides a dynamical explanation of the recirculation pattern observed. Barotropic tidal models applied in this region (Xing and Davies, 1996c; Proctor and Davies, 1996) show very small residual currents in the Sea of the Hebrides so that the observed southward flow can not be explained by tidal rectification, instead a baroclinic component needs to be taken into account. If the dome is static, as shown by observations, the surface flow is expected to be cyclonic to maintain the density field in geostrophic equilibrium (Hill *et al.*, 1997b). This recirculation cell has also biological implications similar to the ones observed in the western Irish Sea (Hill *et al.*, 1994) where it acts as a mechanism for larval retention for the Norway lobster (Hill *et al.*, 1997a). A similar mechanism is at work in the Sea of the Hebrides as indicated in Fig. 2.6 which shows the Norway lobster grounds at both entrances to the Minch region. The cyclonic recirculation ensures that enough larvae are trapped inside the area to maintain a population.

On the inner areas of the Scottish shelf the salinity field is dictated by the coastal plume flowing northward from the North Channel to Cape Wrath (McKinley *et al.*, 1981; McKay *et al.*, 1986). Seasonal changes in salinity can be ascribed to the coastal fresh water discharge. The Firth of Clyde and the Firth of Lorne represent the two main sources of buoyancy in the area, and the rest can be thought as uniformly distributed along the Scottish Coast. Fig. 2.7 shows the fresh water outflow for the year 1997 for these location. Maxima in flow for all sources are reached between December and February. In spring and summer the outflow is negligible. However these data could underestimate the extent of the real outflow since rivers are often gauged long way upstream so that eventual contributions from tributaries are missing from the total budget. This pattern was discussed by Simpson and Hill (1986) who correlated these values with the mean current measured in the Tiree passage during 1983; they suggested a strong link between the strength of the mean current and the strength of the runoff (see Fig. 5, Simpson and Hill, 1986) but this picture did not take into account the wind field which may have followed a similar season pattern as suggested in Fig. 2.8 for 1997.

Seasonal variation in salinity is evident in Hill and Simpson's study of the Islay front (Hill and Simpson, 1989). The haline front is a 'surface to bottom' front (Hill and

Simpson, 1989), referred to as a type 1 frontal interface by Csanady (1978). Figs. 2.9a-e and 2.10a-e show a series of vertical sections taken during five different months spanning the years 1983 to 1986. They show the same line (Latitude 56° 10′ N) so that is possible to follow the seasonal development of salinity and temperature. Concentrating on salinity for now, in February (Fig.2.9a) the isohalines (and isotherms) are vertical showing that the water is well mixed in this period of the year. Salinity increases from east to west as expected and as the year progresses the front tends to strengthen (Figs 2.9b and 2.9c relative to May and April). The coastal water with salinity less than 34.0 is present at this stage and this indicates the freshest part of the plume. In summer the haline front shows a distortion (Fig. 2.9d relative to July) where the interface resembles an 'S' (Hill and Simpson, 1989) with a strong vertical stratification on the inner part of the shelf. In November (Fig. 2.9e) the situation returns toward a winter condition where isohaline are again almost vertical, before the water column reverts to a state of vertical homogeneity.

The seasonal cycle of the temperature in this region follows the pattern of the other parts of the North West European continental shelf (Elliott and Clarke, 1991; Elliott *et al.*, 1991). Temperature minima are reached on the whole shelf around February-March (Ellett and Edwards, 1983) and close to the coast temperature reaches $6-7$°C (Craig, 1959) as shown in figure 2.10a. The Scottish shelf is subject to the mitigating influence of the Atlantic so that on the Outer Hebridean Shelf temperature is around 8°C. In this period the water column is mostly vertically mixed (Craig, 1959), but there are some areas, where tidal mixing is weak, where the bottom water can be warmer than the surface (Craig, 1959) with salinity compensating for thermal instability. With the onset of the spring the entire shelf starts to gain heat and buoyancy at the surface through the heat flux. A thermocline develops, particularly where the water is deep and the tidal mixing is not strong enough to maintain homogeneity. Surface temperature maxima are reached in August with values around 15°C (Ellett and Edwards, 1983) near the coast. On the oceanic side of the Hebridean maxima are slightly lower, around 13°C (Ellett, 1979). In this deeper area surface water heats faster and there is a delay in the transmission of heat downward so that temperature maxima at depth are reached later in Autumn (Ellett and Edwards, 1983). As with salinity, an intrusion of warmer Atlantic water with oceanic characteristics can be detected in the Sea of the Hebrides and to the North of the Isle of Lewis. This is seen in a satellite picture of the sea surface temperature of the 26th April 1999, (fig. 2.11) which shows warmer water at both extremities of the Minch.

These intrusions are still present in July (Ellett, 1979; Ellett and Edwards, 1983) with relatively cool water in the central part of the Minches.

The seasonal development of the Islay front can be followed in Figs. 2.10a-e. In winter (Fig. 2.10a) the water column is thermally homogenous as in the case of salinity. Isotherms are vertical and temperature varies from less than 7°C close to the coast to more than 8.5°C on the Atlantic side. The sharp vertical front is found around 7° 20′ W, which mirrors the haline front and divides the fresher, colder coastal water from the ocean. With the increase of the heat flux the water slowly warms, Fig 2.10b illustrating a May condition where stratification has not fully developed; the coastal water remains colder and almost vertically mixed in contrast to the Atlantic side where stratification is detectable. Temperature ranges from 7°C to 9.5°C at this time. Fig. 2.10c (April) shows almost the same picture but with temperature slightly higher (8° to 10°C), illustrating interannual differences. In July (Fig. 2.10d) stratification is distinctly present on the western side where the thermocline is clearly visible while on the eastern side the water is less stratified, exhibiting the typical structure of a tidal mixing front (Simpson and Hill, 1986). The thermocline separates warm surface water (greater than 13°C from cool bottom water (less than 10°C). In November (Fig. 2.10e) homogeneity is already visible on the wester side where isotherms are now vertical, but weak stratification remains near the coast.

2.6 Recent observations in the Sea of the Hebrides

A recent series of cruises was conducted by the Marine Laboratory (FRS), Aberdeen, with the aim of obtaining detailed coverage of the Scottish shelf, with focus on the region of the Minches. During the four cruises CTD measurements were collected using a Seabird SBE 25 CTD calibrated for conductivity against collected water samples, which were analysed on a 'Portsal' salinometer; at the same time chemical samples were also taken. Table 2.1 shows detail of the cruises whilst Fig. 2.12 presents the spatial coverage for each cruise.

Cruise	Season	Period
CU199610	Summer	6 - 12 July 1996
CU199689	Winter	19 November - 15 December 1996
CU199706	Spring	6 - 20 April 1997
CU199815	Autumn	5 - 19 September 1998

Table 2.1: Durations of the cruises undertaken in the Minch by the Marine Laboratory, Aberdeen.

Throughout this work these cruises will be mentioned either with the cruise designator (column 1) or with the 'season' name (in italics to distinguish it from the proper season). Here, for simplicity, only bottom and surface salinity and temperature (and hence density) data will be presented and discussed although full profile data were taken and they will be discussed when compared with model's results.

2.6.1 Salinity

Figures 2.13a-d and 2.14a-d show the surface and bottom salinity obtained from the CTD stations. In the nearbed *spring* (Fig. 2.14a) the dome of high salinity is clearly visible with a maximum in the core of 35.4 and the isohaline of 35.0 almost entering the Minch. The northern part shows the intrusion of more saline water of Atlantic origin. Surface salinity (Fig. 2.13a) follows roughly the same pattern - the southern intrusion is visible and the coastal water is attached to the west coast. The *summer* data presented in Fig. 2.13b and Fig. 2.14b shows a slightly different picture; surface salinity is largely homogenous with only a limited southern intrusion and a limited plume of coastal fresher water. Bottom salinity still reveals the dome but in this case the 35.0 isohaline extends less far and does not reach the entrance of the little Minch. The norther intrusion is absent, both in surface and bottom. The *autumn* situation (Fig. 2.13c and Fig. 2.14c) resembles the *spring* condition. The dome in the Sea of the Hebrides is again well developed although not with same strength; the 35.0 isohaline at the seabed reaches the entrance of the little Minch. At the northern end of the Minch, the Atlantic intrusion is again present. The surface salinity shows a similar picture and it is possible to see the effect of the

freshening due to the coastal water and runoff. The maximum measured surface intrusion does not exceed 34.6. Finally the *winter* measurements (Fig. 2.13d and Fig. 2.14d) present a picture of the bottom salinity similar to the conditions found during the *summer* cruise; the intrusion in the South seems to weakened compared to the previous observations. The 35.0 isohaline does not intrude deeply into the Sea of the Hebrides but near the coast the fresh water signal retains the autumn characteristics with a well detectable gradient.

2.6.2 Temperature

Fig. 2.15a-d and Fig. 2.16a-d present the seasonal cycle of temperature which agrees with the pattern already discussed in Craig (1959) and Elliott *et al.* (1991). In the *spring* observations (Fig. 2.15a and Fig. 2.16a) temperature has its lower value and the warmer Atlantic intrusion is clearly visible with temperature reaching 9.5°C in its centre whilst the coastal values are lower due to shallower waters and fresh water influence. It is interesting to note that some weak stratification is present not only as a result of coastal inflow but also due to the intrusion, where deep water is warmer than the sea surface. Water is also weakly stratified in the Little Minch, away from the intrusion. Fig. 2.15b and Fig. 2.16b illustrate the results collected in July when the water is warmer and the area starts to stratify - especially in its deepest regions. Both northern and southern oceanic inflows are detectable at the surface while the bottom temperature intrusion shows up most clearly in the North Minch. Surface observations agree with data collected previously at coarser resolution (Craig, 1959; McKay *et al.*, 1986). Further evolution of the temperature can be seen in Fig. 2.16c and Fig. 2.16c, which show the *autumn* data set. Bottom temperatures have increased by almost 2°C in the northern region of the Minch. At the southern end values are similar to those in the previous *summer* measurements. The intrusion is again clearly defined with a horizontal gradient showing the contrast with coastal water, and stratification remains developed. Fig. 2.15d and Fig. 2.16d shows a return to almost vertically mixed conditions after cooling and the breakdown of stratification.

To recap, the seasonal cycle of heating and cooling in the region results in temperature minima being obtained in late winter and maximum values in August, after which there is an overall cooling due to decreasing solar radiation and increased

winds which promote convective overturning and the breakdown of stratification. This cycle differs from other parts of the European Shelf because of the mitigating effects of the Atlantic ocean (Elliott and Clarke, 1991). This influence is noticeable in the intrusion of generally warmer (and saltier) water at both ends of the Minch. The persistent intrusions are located in deep depressions (see Fig. 2.2) where the Atlantic water remains trapped. Just as for salinity, temperature stratification is always present over most of the area, weakly in the period from December to April and fully developed throughout the summer period. The presence of thermal stratification in the winter is probably due to oceanic inflow. The local coastal influence seems to be negligible due to the very low amount of fresh water discharge in the region of the Minch.

2.7 Summary

The region of interest for this study is located on the Scottish shelf, to the west of Scotland and to the north of Ireland. The topography is convoluted with the presence of fjords and sea lochs and these features, along with bathymetry, influence the regional circulation . The local non-tidal circulation is generally northbound and it is compatible with the weak circulation on the European shelf; a coastal current can be observed flanking Scotland throughout the year, with some seasonal variability. This part of the shelf is tidally energetic which explains some of the features present in the area, such as the tidal mixing front on the Malin shelf. Tidal residual currents are weak, as shown in previous model studies of the area (Proctor and Davies, 1996; Xing and Davies, 1996c) so that baroclinic effects must be taken into account to explain the measured regional circulation. The most likely forcing mechanism for the recirculation cell in the Sea of the Hebrides is the horizontal density gradient in the dome-like intrusion. The bathymetry plays an important role since the dome is located in a deep depression. Hydrographic measurements shows an analogous but weaker intrusion in the northern part of the North Minch. Salinity measurements show an influence of the freshwater runoff which peaks in winter and spring. The most recent measurements show the persistence of the haline dome and its variability.

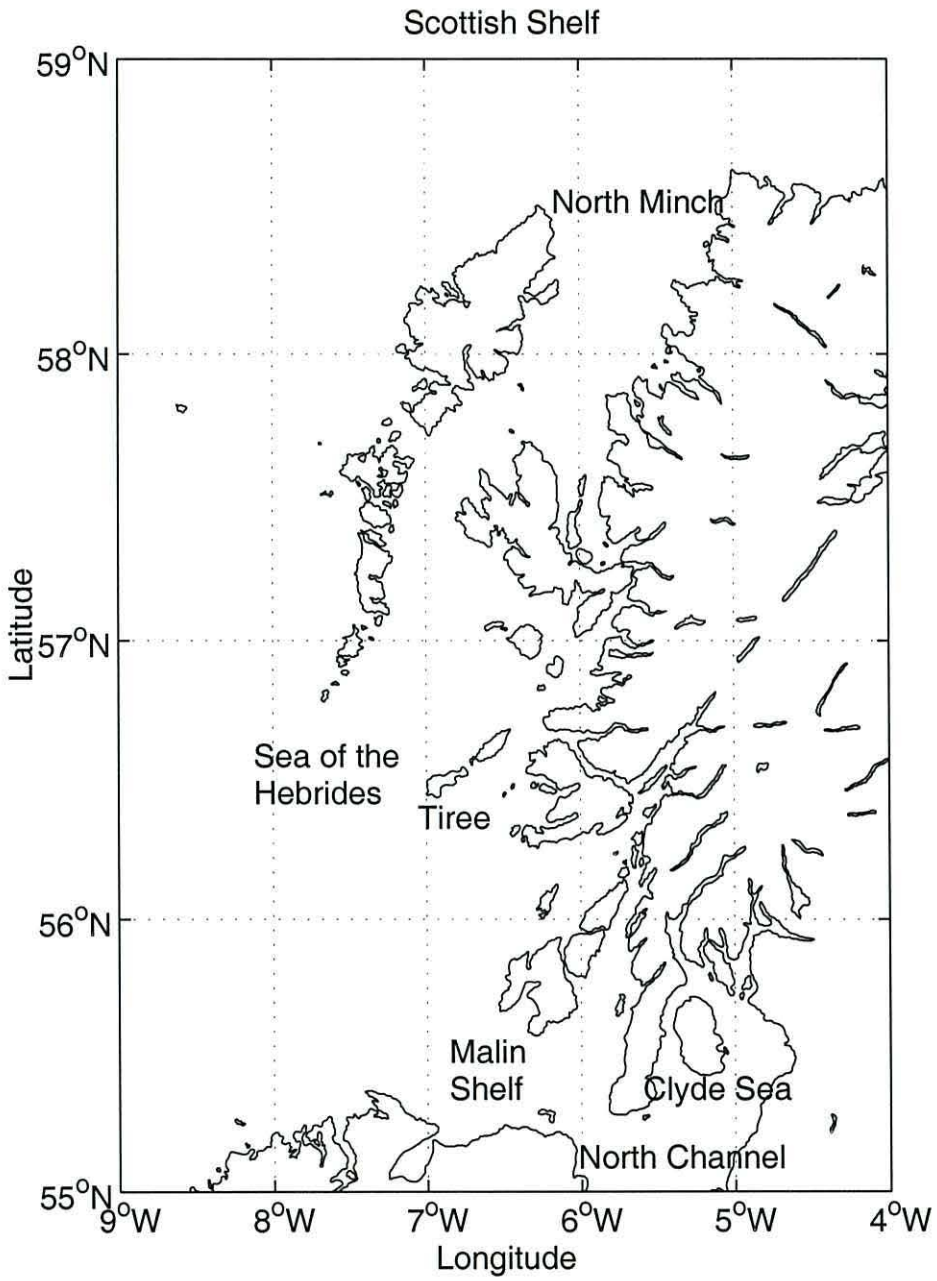

Figure 2.1: Location and region mentioned in this work.

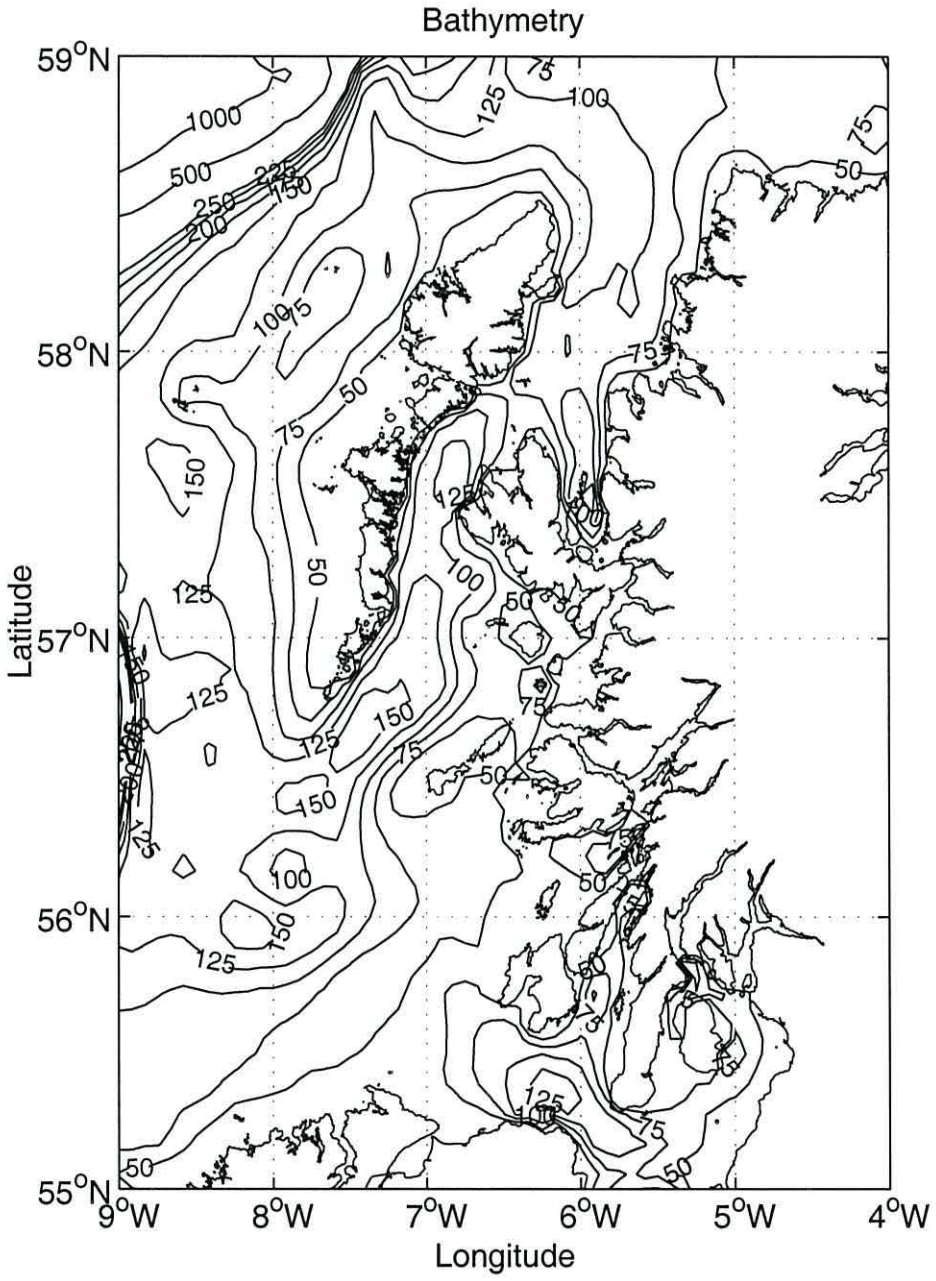

Figure 2.2: Bathymetry (from the model grid).

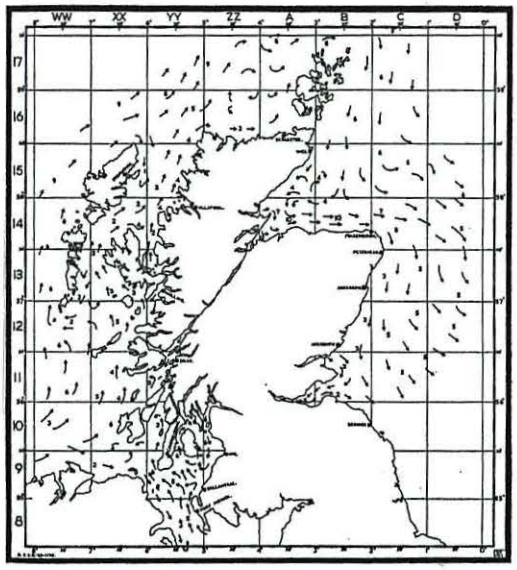

Figure 2.3: Surface circulation in the Minch (from Craig, 1959).

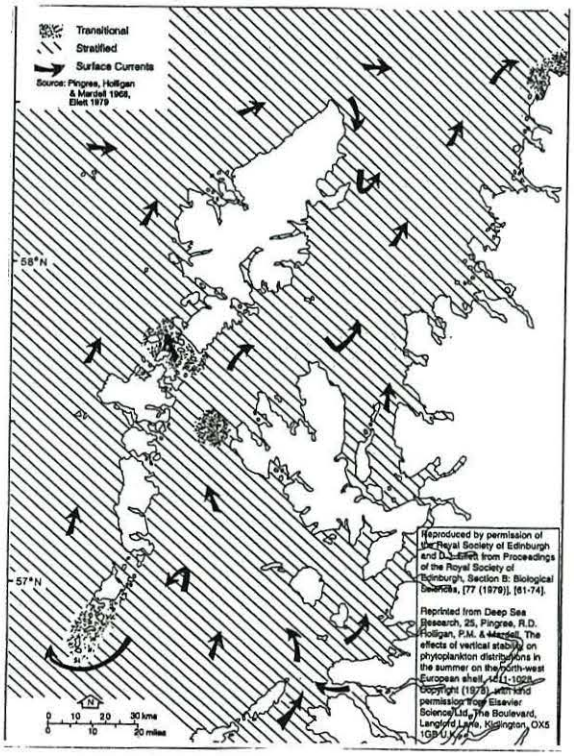

Figure 2.4: Recirculation in the Sea of Hebrides (from Bryan, 1994).

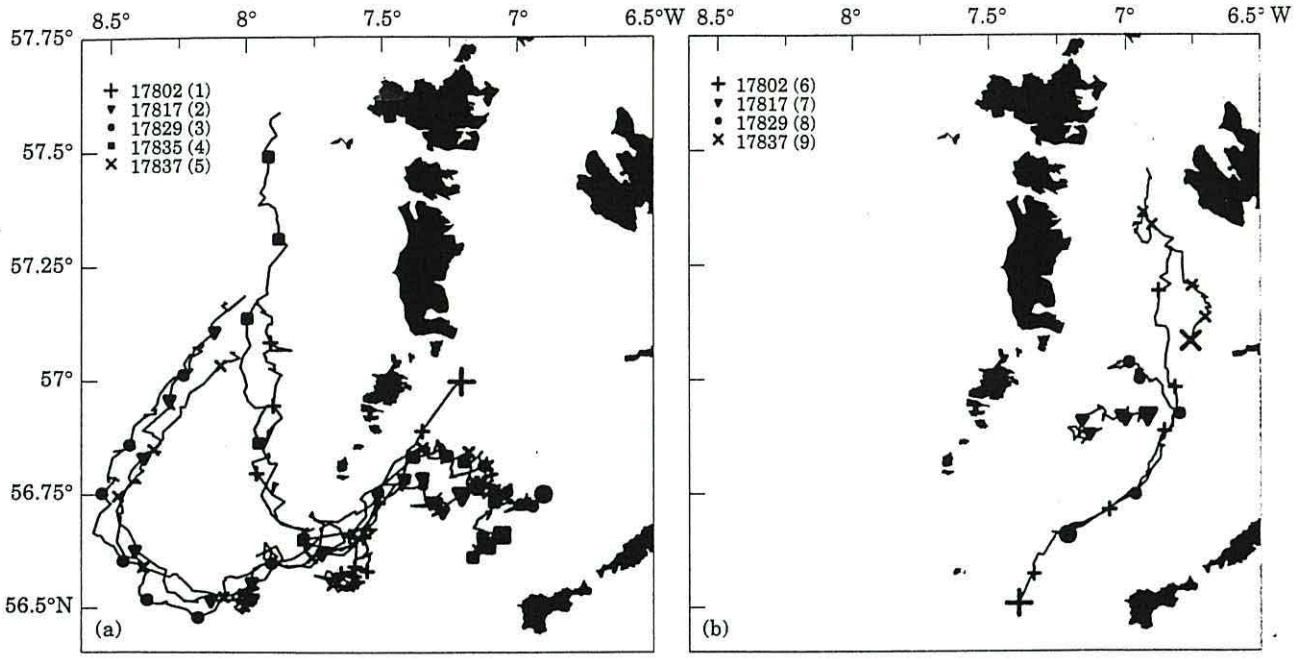

Figure 2.5: Tracker buoys trajectories (from Hill *et al.*, 1997b)

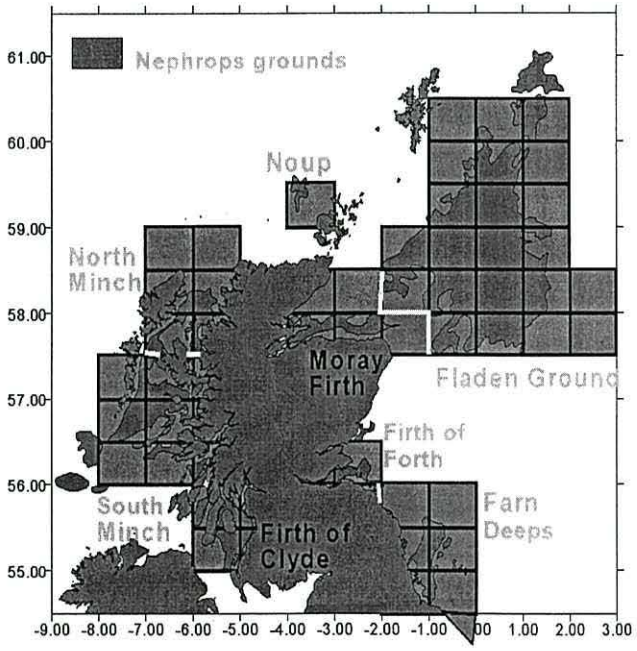

Figure 2.6: Nephrops Grounds (from Gillibrand, *pers. comm.*)

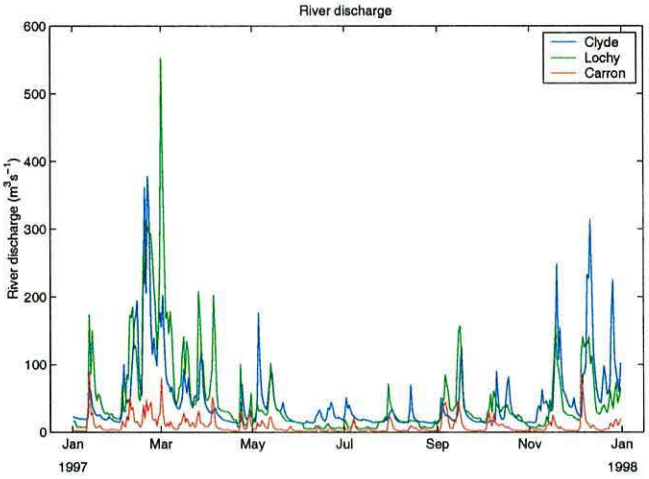

Figure 2.7: Fresh water outflow for the year 1997 for the rivers Clyde, Lochy and Carron (data from the Scottish Environment Protection Agency).

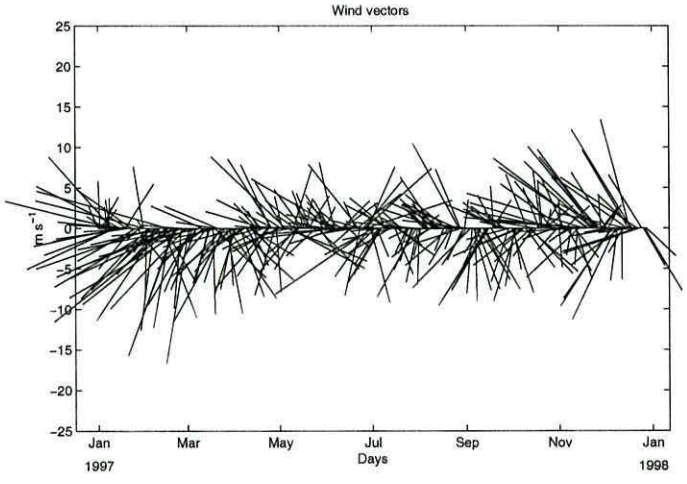

Figure 2.8: Vectors showing direction and intensity for the wind at the Tiree weather station for the year 1997 (data from the British Atmospheric Data Centre).

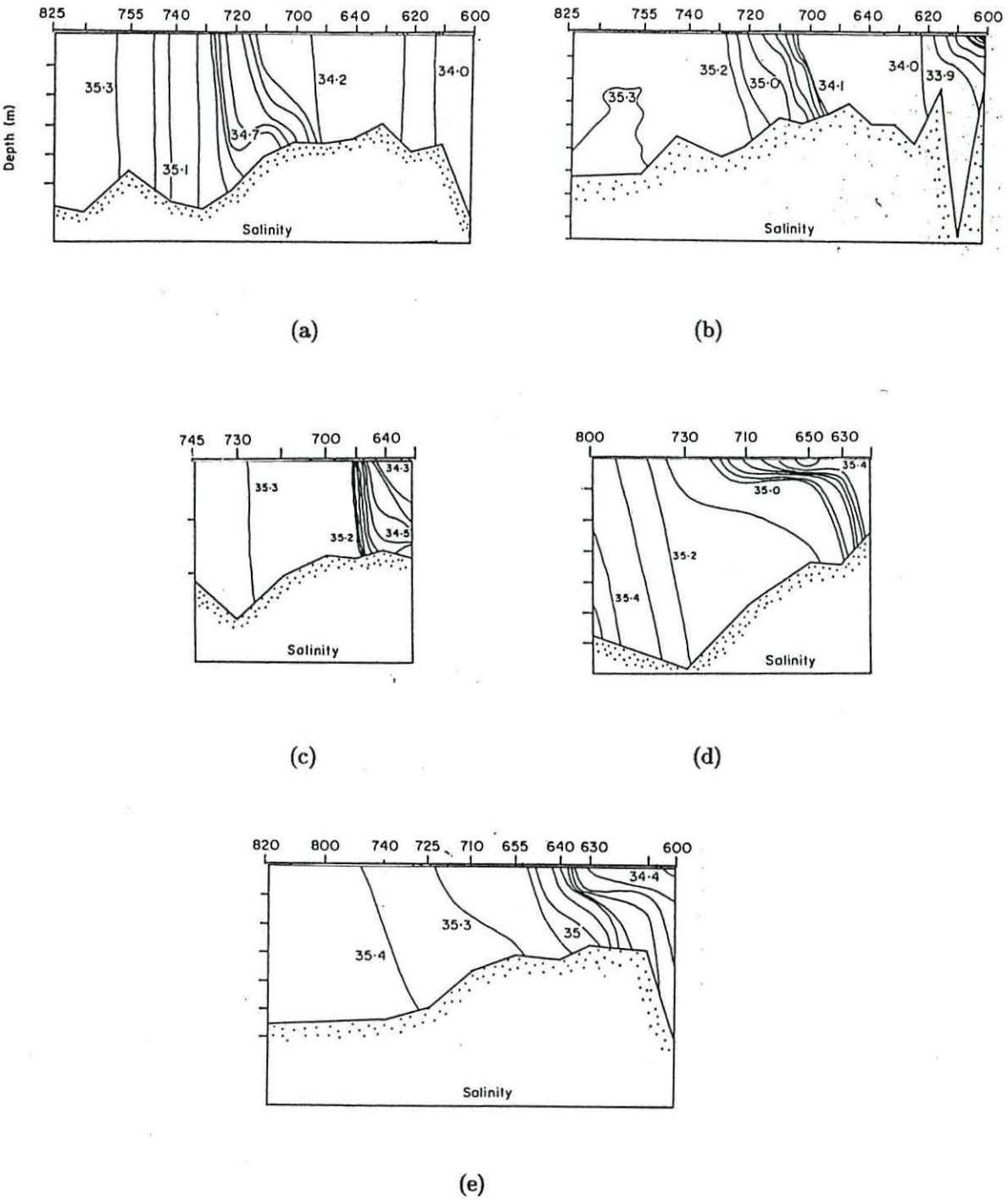

Figure 2.9: Islay front structure. Salinity (from Hill and Simpson, 1989). Sections at 56°10′ N, (a) February 1985, (b) May 1986, (c) April 1984, (d) July 1983, (e) November 1983.

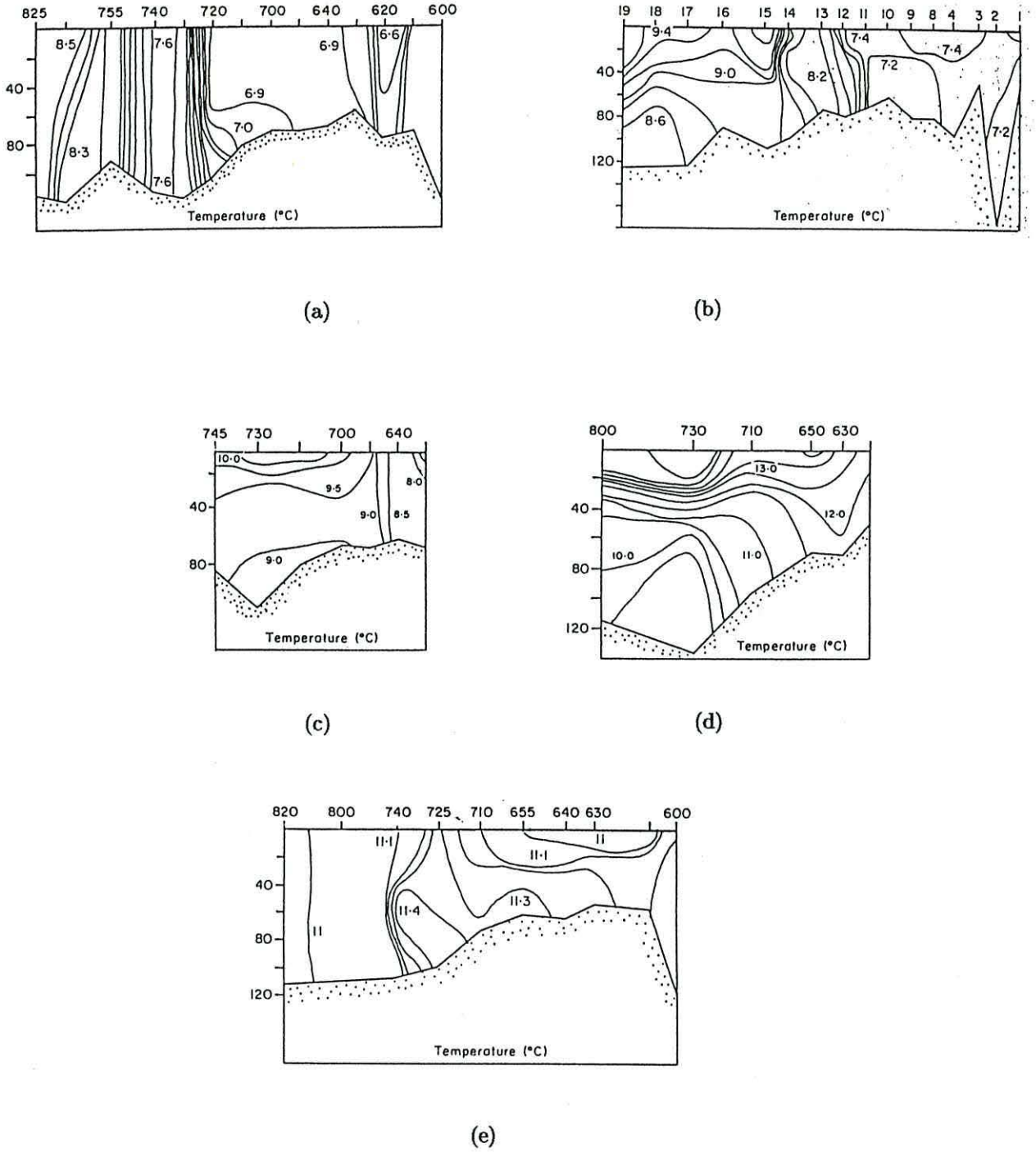

Figure 2.10: Islay front structure. Temperature ((from Hill and Simpson, 1989). Sections at 56°10′ N, (a) February 1985, (b) May 1986, (c) April 1984, (d) July 1983, (e) November 1983.

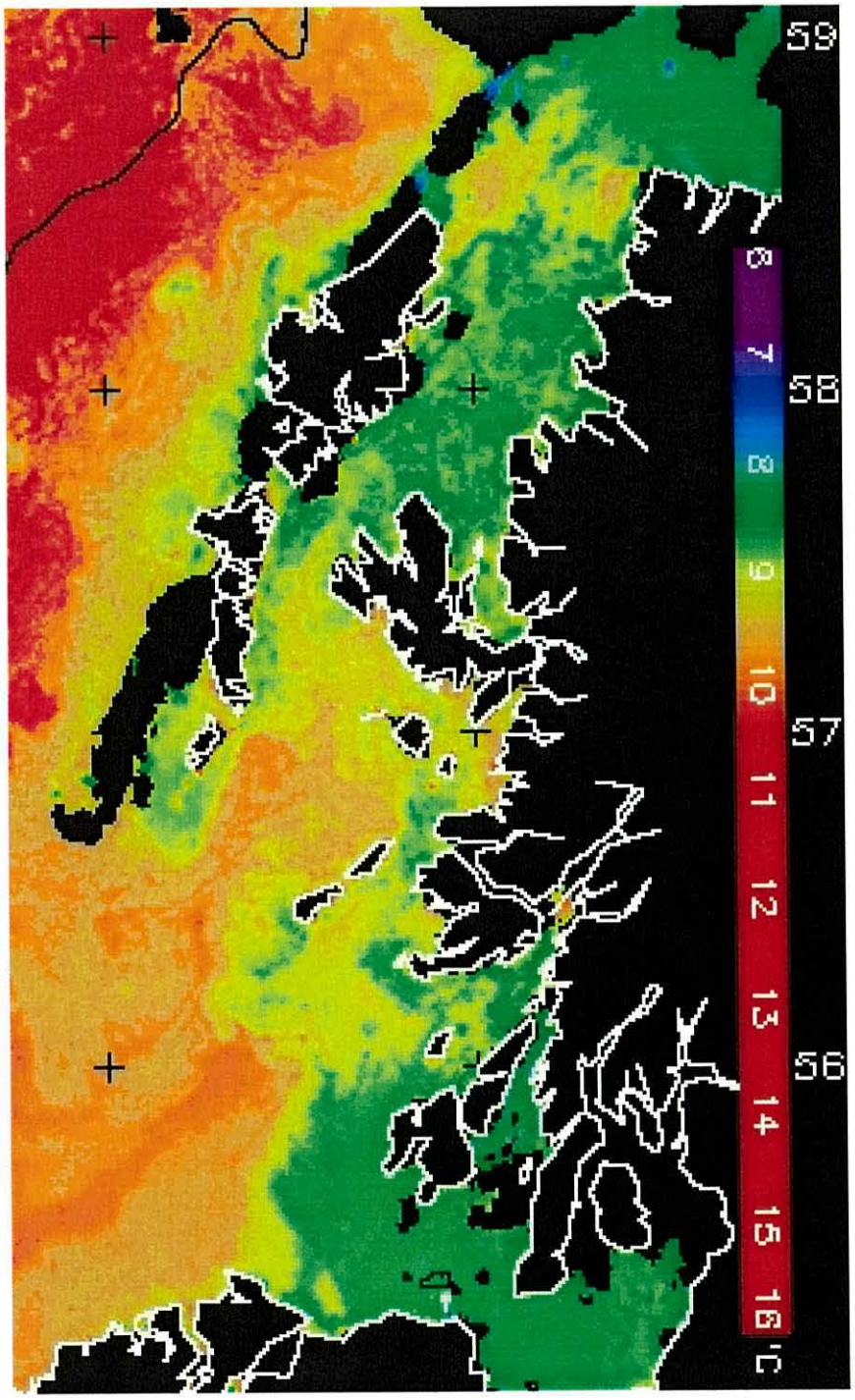

Figure 2.11: Sea Surface temperature for the 26th April 1999 (Satellite image from the British Atmospheric Data Centre).

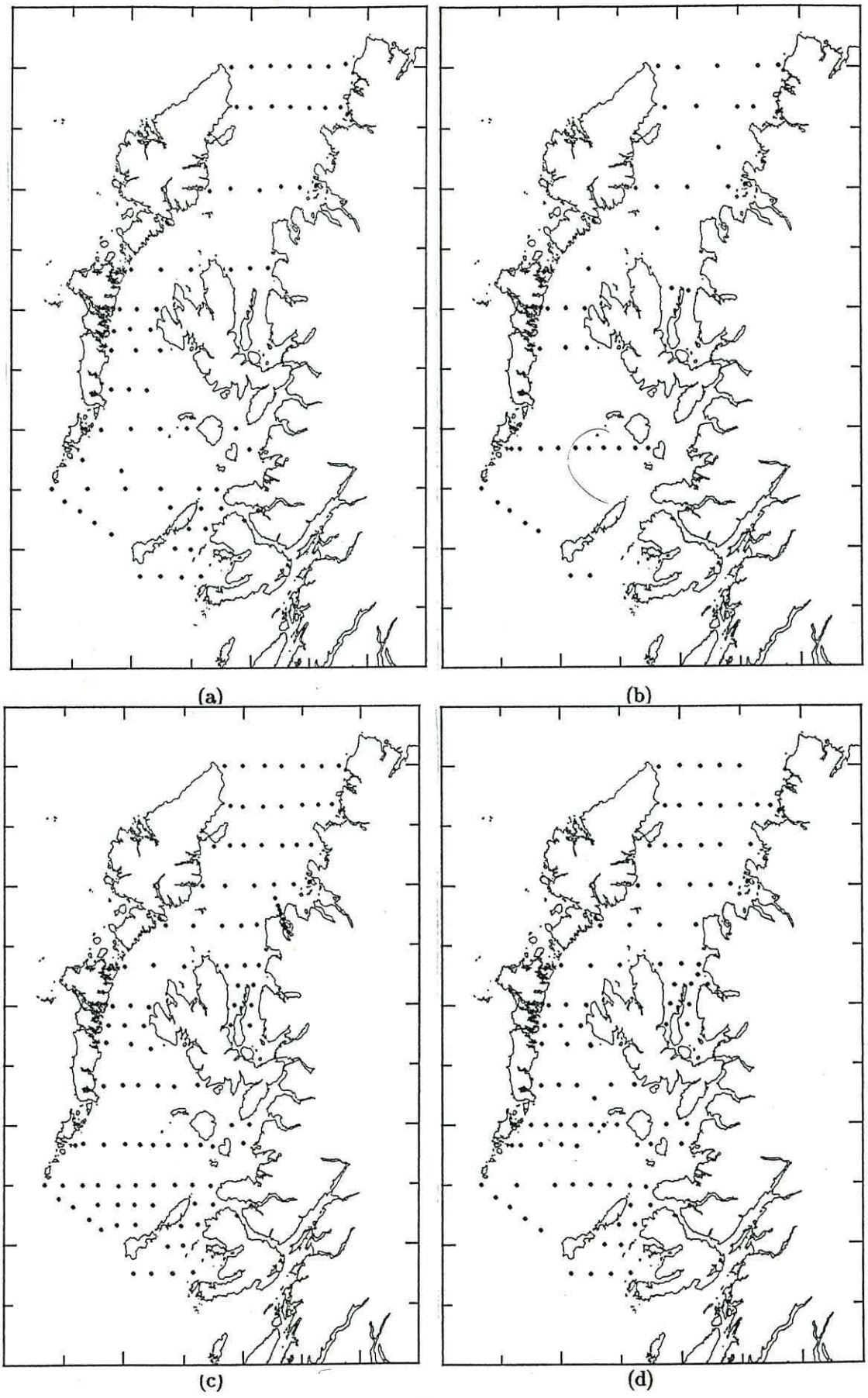

Figure 2.12: Spatial coverage for each cruise. (a) *Spring* (6-20 April 1997), (b) *Summer* (6-12 July 1996), (c) *Autumn* (5-19 September 1998), (d) *Winter* (19 November-15 December 1996).

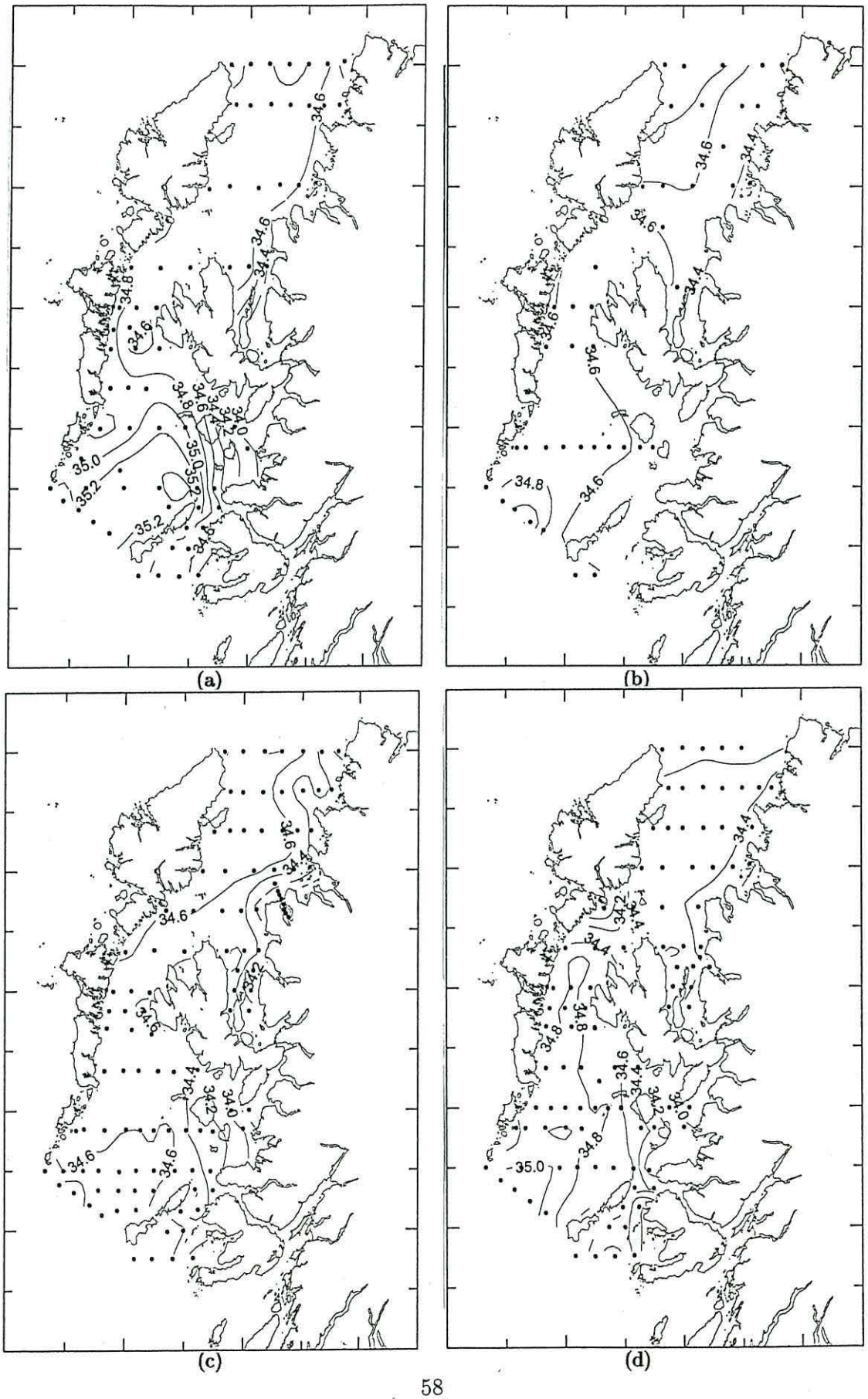

Figure 2.13: Surface Salinity. (a) *Spring* (6-20 April 1997), (b) *Summer* (6-12 July 1996), (c) *Autumn* (5-19 September 1998), (d) *Winter* (19 November-15 December 1996).

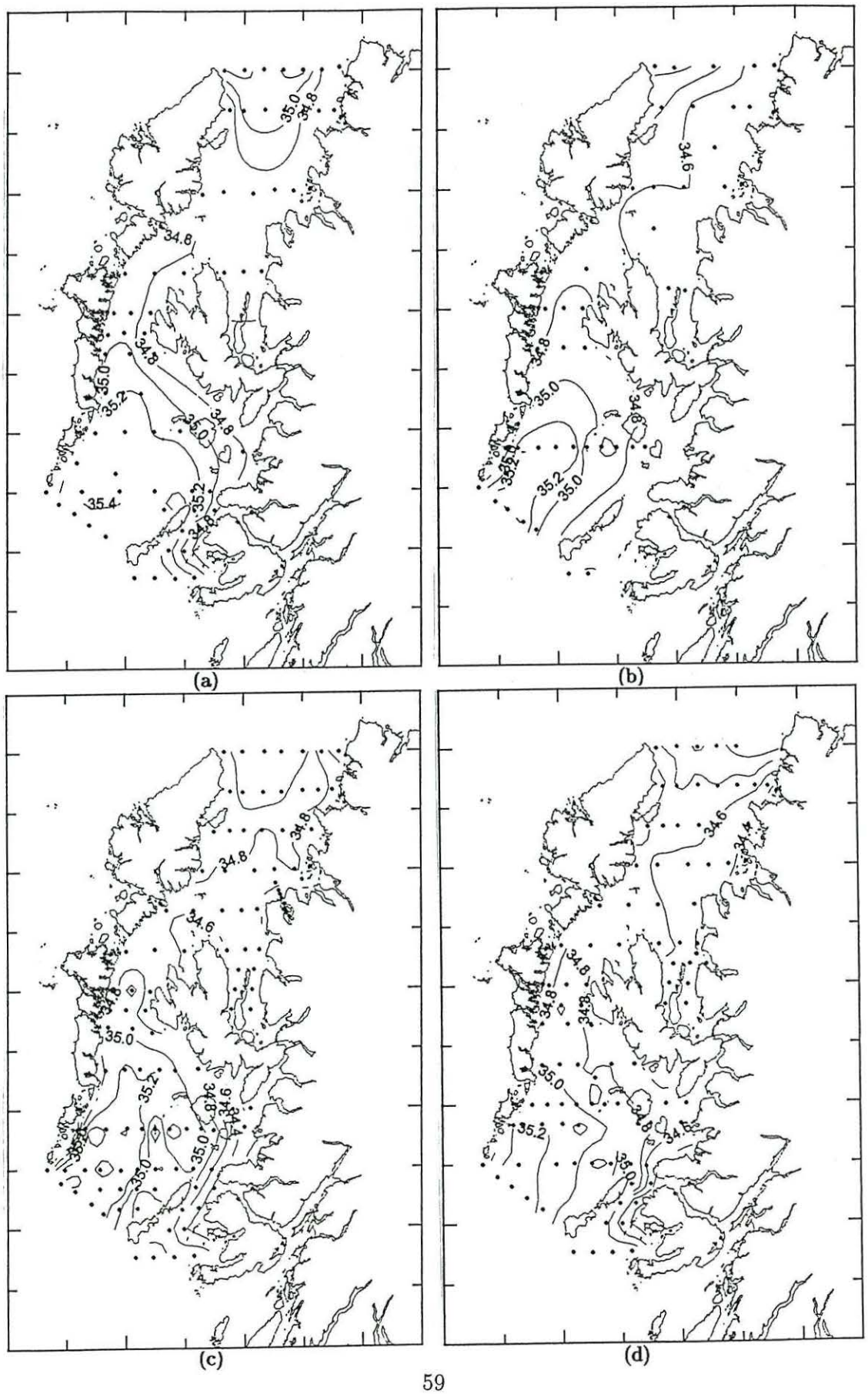

Figure 2.14: Bottom Salinity. (a) *Spring* (6-20 April 1997), (b) *Summer* (6-12 July 1996), (c) *Autumn* (5-19 September 1998), (d) *Winter* (19 November-15 December 1996).

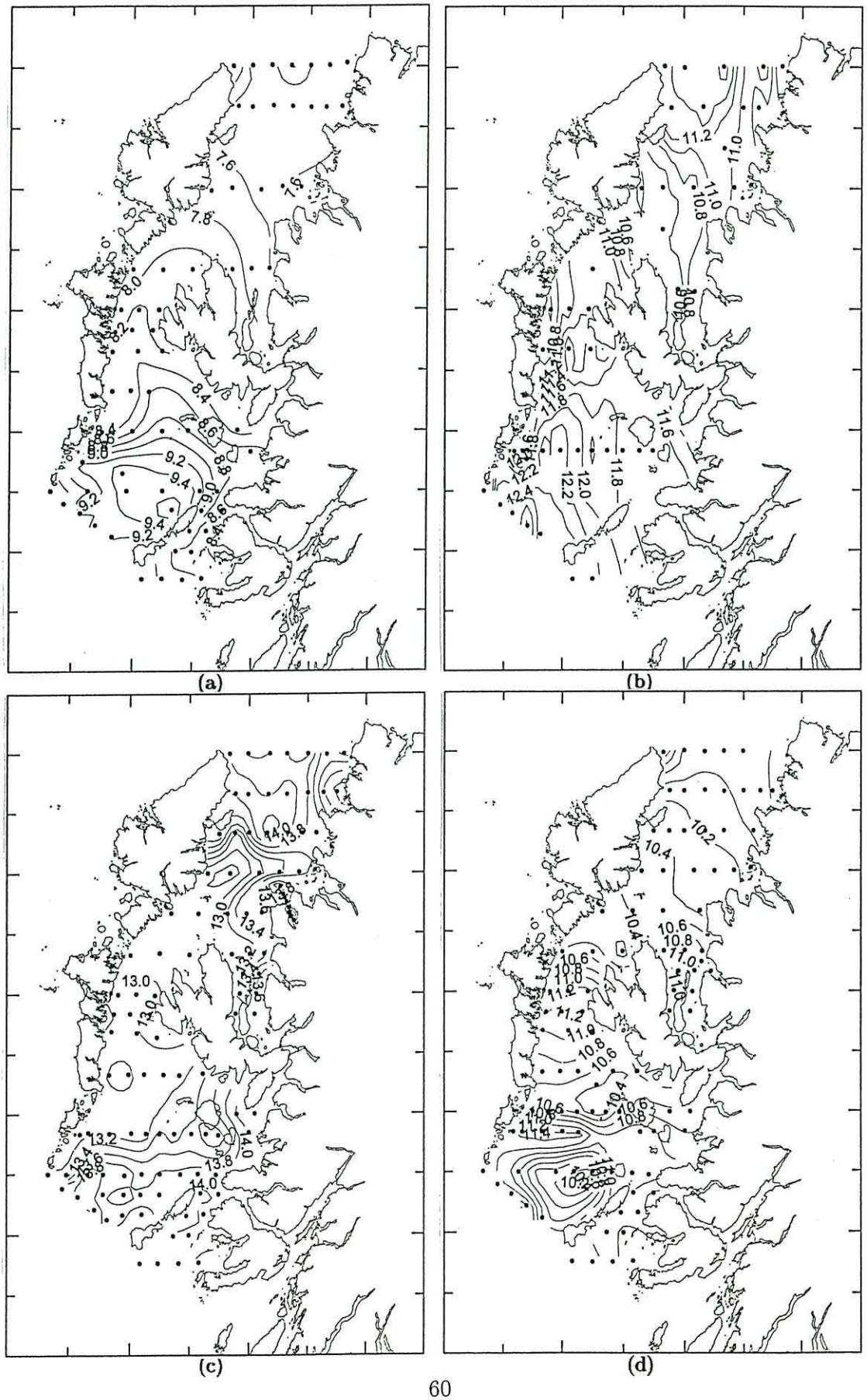

Figure 2.15: Surface Temperature. (a) *Spring* (6-20 April 1997), (b) *Summer* (6-12 July 1996), (c) *Autumn* (5-19 September 1998), (d) *Winter* (19 November-15 December 1996).

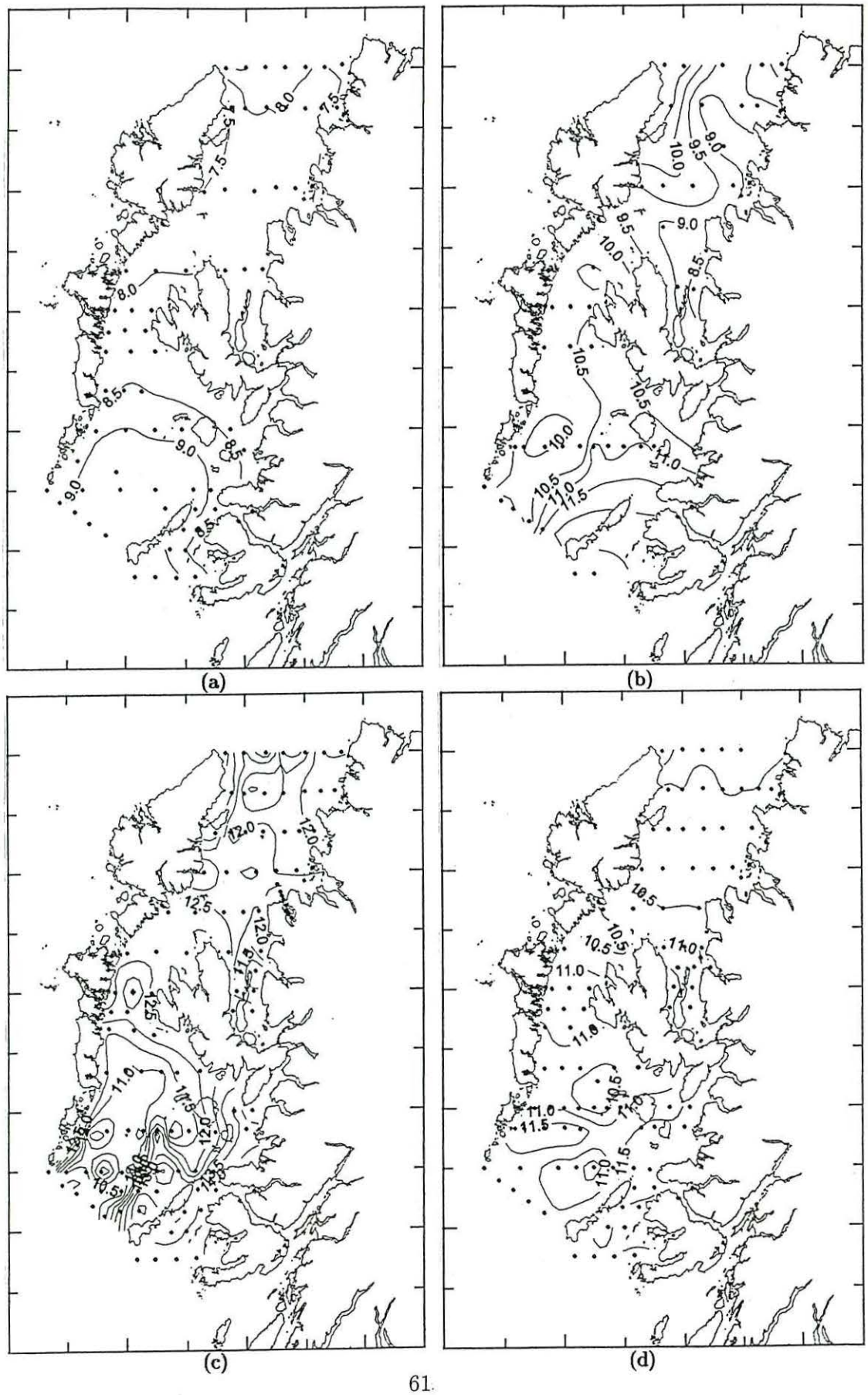

Figure 2.16: Bottom Temperature. (a) *Spring* (6-20 April 1997), (b) *Summer* (6-12 July 1996), (c) *Autumn* (5-19 September 1998), (d) *Winter* (19 November-15 December 1996).

Chapter 3

The Princeton Ocean Model

3.1 Introduction

Coastal regions represent one of the major challenges for numerical models. Buoyancy is modified by the seasonal heating-cooling cycle and by fresh water inputs (Hill, 1998); tidal and wind driven currents are strong and surface and bottom friction play an important role in the generation and maintenance of turbulence (Simpson, 1998). Boundary effects are equally important due to presence of the coastline and shallow regions (Huthnance, 1973). The baroclinic component of the motion is often not negligible and needs to be taken into account in coastal numerical simulations.

Many different numerical models are available for these kind of studies; they solve the fully non-linear "primitive equations" (Haidvogel and Beckmann, 1998) but different mathematical techniques are used to numerically solve this set of differential equations. A recent thorough review of some of the available models has been presented by Haidvogel and Beckmann (1998). The main differences are the treatment of the spatial and temporal discretisation. Typically the equations of motion are integrated using finite differences in models such as POM (Blumberg and Mellor, 1987), DieCAST (Dietrich *et al.*, 1987) or POLCOMS (Holt and James, 1999) but recently finite elements have been successfully employed for example in QUODDY (Ip and Lynch, 1994) and SCRUM (Song and Haidvogel, 1994) models. Horizontal and vertical coordinates may differ from model to model; in the vertical domain Cartesian geopotential z-coordinates are employed in GFDLM (Bryan, 1969; Cox, 1984) and σ-coordinates (e.g. POM) are popular choices but representation with

isopycnal surfaces is also possible - for example the MICOM model (Bleck *et al.*, 1992). Horizontal coordinates can be orthogonal or curvilinear to accommodate different needs in resolution. Differences can be also found in the parameterization of unresolved physical processes.

The model used in this work, the Princeton Ocean Model, is a fully non-linear three-dimensional model with a turbulence closure scheme which allows a realistic parameterisation of mixing processes (Blumberg and Mellor, 1987). It has been employed in a wide series of coastal simulations and also for large-scale modelling, as will be discussed later on in this section; it has been chosen for this particular regional application for its reliability and availability.

3.2 Governing Equations

The non-linear Reynolds equations of motion for a parcel of fluid are cast in an orthogonal Cartesian frame of reference where the horizontal coordinates x and y increase in the eastward and northward direction respectively whilst the vertical coordinate z increases upward. Defining the free surface as $z = \eta(x, y, t)$, the bottom as $z = -H(x, y)$ and the three components of the velocity vector u, v and w where u and v represent the horizontal components and w the vertical component, the momentum equations can be written as

$$\frac{\partial u}{\partial t} + u\frac{\partial u}{\partial x} + v\frac{\partial u}{\partial y} + w\frac{\partial u}{\partial z} - fv = -\frac{1}{\rho_0}\frac{\partial p}{\partial x} + \frac{\partial}{\partial z}\left(K_m\frac{\partial u}{\partial z}\right) + F_x \tag{3.1}$$

$$\frac{\partial v}{\partial t} + u\frac{\partial v}{\partial x} + v\frac{\partial v}{\partial y} + w\frac{\partial v}{\partial z} + fu = -\frac{1}{\rho_0}\frac{\partial p}{\partial y} + \frac{\partial}{\partial z}\left(K_m\frac{\partial v}{\partial z}\right) + F_y \tag{3.2}$$

$$\frac{\partial p}{\partial z} = -g\rho \tag{3.3}$$

with the continuity equation for incompressible fluids

$$\frac{\partial u}{\partial x} + \frac{\partial v}{\partial y} + \frac{\partial w}{\partial z} = 0 \tag{3.4}$$

where f is the Coriolis parameter, K_m is the coefficient of vertical eddy viscosity and p is the pressure calculated by integrating (3.3) from z to the free surface so that

$$p(z) = p_{atm} + g\int_z^0 \rho_0 dz + g\rho_0\eta + g\int_z^\eta \rho' dz \tag{3.5}$$

In writing these equations two approximations have been used: the hydrostatic approximation so that the pressure is balanced by the weight of the column of fluid (3.3) and the Boussinesq approximation where differences of density are neglected unless they are multiplied by the acceleration of gravity g. In this case the density ρ is expressed as

$$\rho(x, y, z, t) = \rho_0(z) + \rho'(x, y, z, t) \tag{3.6}$$

with ρ_0 chosen as a reference density and ρ' as the departure from this value. In the Princeton Ocean Model the density is explicitly calculated from temperature and salinity using an equation of state derived from an polynomial expansion (Mellor, 1991) so that

$$\rho = \rho(T, S) \tag{3.7}$$

The terms F_x and F_y represent the parameterisation of the turbulent diffusion of momentum in the horizontal which is not resolved by the model grid. Due to the large scale of coastal simulations viscous effects are negligible so that these frictional terms can be expressed as

$$F_x = \frac{\partial}{\partial x}\left(2A_m\frac{\partial u}{\partial x}\right) + \frac{\partial}{\partial y}\left(A_m\left(\frac{\partial u}{\partial y} + \frac{\partial v}{\partial x}\right)\right) \tag{3.8}$$

$$F_y = \frac{\partial}{\partial y}\left(2A_m\frac{\partial v}{\partial y}\right) + \frac{\partial}{\partial x}\left(A_m\left(\frac{\partial u}{\partial y} + \frac{\partial v}{\partial x}\right)\right) \tag{3.9}$$

The conservation equations for salinity S and temperature T complete the set, and are formulated as

$$\frac{\partial S}{\partial t} + u\frac{\partial S}{\partial x} + v\frac{\partial S}{\partial y} + w\frac{\partial S}{\partial z} = \frac{\partial}{\partial z}\left(K_h \frac{\partial S}{\partial z}\right) + QP_S + QN_S + F_S \tag{3.10}$$

$$\frac{\partial T}{\partial t} + u\frac{\partial T}{\partial x} + v\frac{\partial T}{\partial y} + w\frac{\partial T}{\partial z} = \frac{\partial}{\partial z}\left(K_h \frac{\partial T}{\partial z}\right) + QP_T + QN_T + F_T \tag{3.11}$$

By analogy with (3.1) and (3.2) K_h represents the eddy diffusivity for the turbulent diffusion of these two scalars in the vertical. $QP_{S,T}$ and $QN_{S,T}$ represent the sources and sinks whilst the terms F_S and F_T describe the unresolved processes of horizontal mixing and are written, following (3.8) and (3.9), as

$$F_{S,T} = \frac{\partial}{\partial x}\left(A_h \frac{\partial (S,T)}{\partial x}\right) + \frac{\partial}{\partial y}\left(A_h \frac{\partial (S,T)}{\partial y}\right) \tag{3.12}$$

In POM the coefficient of horizontal eddy viscosity A_m follows the formulation due to Smagorinski (1963)

$$A_m = C_m \triangle x \triangle y \frac{1}{2}\left[\left(\frac{\partial u}{\partial x}\right)^2 + \frac{1}{2}\left(\frac{\partial u}{\partial x} + \frac{\partial v}{\partial x}\right)^2 + \left(\frac{\partial v}{\partial x}\right)^2\right]^{\frac{1}{2}} \tag{3.13}$$

where $\triangle x$ and $\triangle y$ are the grid spacing and C_m is a non-dimensional coefficient which depends on the application. This device allows an explicit diffusivity to decrease any computational noise. In the limit of a very fine resolution simulation its value become negligible. The value of A_h can be chosen to be equal to A_m or related to the latter through the horizontal turbulent Prandtl number defined as

$$P_r = \frac{A_m}{A_h} \tag{3.14}$$

which determines the efficiency of the horizontal turbulent exchanges of momentum and heat or salt flux (Kundu, 1990).

3.2.1 Turbulence Closure

The correct description of the vertical turbulent exchanges is particularly important in shelf seas studies. Primary production and fluxes of organic matter are mainly controlled by vertical mixing (Burchard *et al.*, 1998) so that turbulent motion needs to be realistically simulated in coastal modelling. In the Reynolds decomposition of velocity (see for example Kundu, 1990) the instantaneous velocity is decomposed in a mean part u and in a deviation from the mean u'. After time-averaging, the additional turbulent stresses acting on the mean flow can be expressed as

$$-\rho_0\overline{u_i'u_j'} = \begin{vmatrix} -\rho_0\overline{u'^2} & -\rho_0\overline{u'v'} & -\rho_0\overline{u'w} \\ -\rho_0\overline{u'v'} & -\rho_0\overline{v'^2} & -\rho_0\overline{v'w'} \\ -\rho_0\overline{u'w'} & -\rho_0\overline{v'w'} & -\rho_0\overline{w'^2} \end{vmatrix} \tag{3.15}$$

By analogy with viscosity in laminar flows, and relating the turbulent exchange to the mean velocity gradient, it is possible to write

$$-\overline{u'w'} = K_m\frac{\partial u}{\partial z} \tag{3.16}$$

$$-\overline{v'w'} = K_m\frac{\partial v}{\partial z} \tag{3.17}$$

for the turbulent exchange of momentum in the equations of motion. Similar relations can be written for the turbulent exchange of heat and salt. These coefficients are not a property of the fluid but a property of the state of motion.

Various formulations for K_m have been attempted. The simplest solution is to consider the parameter a constant; this approximation is easy to handle mathematically but it does not take into consideration turbulent evolution in the motion of the fluid. Other analytical representations have been employed for the study of vertical profiles in tidal currents and a brief summary is presented in Soulsby (1990). These theoretical distributions of eddy viscosity are also physically unrealistic since, although allowing for spatial variation, they are time-invariant.

Other parameterisations relate K_m directly to characteristics of the motion. In the logarithmic boundary layer (e.g. Howarth, 1998)

$$K_m = \kappa |\mathbf{u}_*| z \tag{3.18}$$

where z is the vertical coordinate, κ the von Karman's constant ($\kappa = 0.4$) and u_* the friction velocity defined as $|\mathbf{u}_*|^2 = |\boldsymbol{\tau}_0|/\rho$, being $\boldsymbol{\tau}_0$ the stress acting on the bed. Predicted vertical profiles were in agreement with observations near the sea bed but surface values of K_m became unrealistically large in water deeper than 10 m. In the work of Bowden *et al.* (1959) the eddy viscosity was calculated directly from the depth averaged tidal velocity $\mathbf{V}$ as

$$K_m = 0.0025 |\mathbf{V}| h \tag{3.19}$$

where h is the water depth. In the formulation of Davies and Furnes (Davies and Furnes, 1980) for deep water the turbulent parameter was taken to be equal to

$$K_m = 2 \times 10^{-5} \frac{|\mathbf{V}|^2}{\omega} \tag{3.20}$$

with ω being the frequency of the long period waves of the order of 10^{-4}s .

All the above descriptions fail to consider the density stratification of the water column and its effect (since vertical exchanges of properties are inhibited by the presence of stable stratification). An indication of the stability in relation to stratification is given by the gradient Richardson Number, R_i (1.5). Munk and Anderson (1948) used a parameterisation involving functions of R_i as below

$$K_m = K_{m0}(1 + \alpha R_i)^{-\beta} \tag{3.21}$$

$$K_h = K_{h0} \left(1 + \frac{\alpha \beta R_i}{\beta - 1}\right)^{-(\beta - 1)} \tag{3.22}$$

where K_{m0} ad K_{h0} are the eddy coefficients in neutral conditions and α and β are adjustable problem-dependent constants; James (1978) studied the dynamics of a shallow-sea front with this particular formulation.

The turbulent eddy viscosity and diffusivity in the Princeton Ocean Model are calculated using a turbulent closure model developed by Mellor and Yamada (1982) which is based on turbulence hypotheses formulated by Rotta and Kolmogorov, extended to stratified flows (Mellor, 1998). Further modifications and simplifications were introduced by Galperin *et al.* (1988). Following this approach, the coefficients are directly related to two additional turbulent quantities, namely the turbulent kinetic energy (TKE) and the turbulent length scale. Mellor and Yamada (1982) proposed a family of turbulence closure schemes with increasing levels of complexity depending on the degree of anisotropy in the turbulence due to its advection and diffusion. POM incorporates the level 2.5 model (see Mellor and Yamada, 1982, for further details) so that it is possible to write two prognostic equations for the TKE $q^2/2$ and the quantity $q^2 l$ which yield

$$\frac{D}{Dt}\left(\frac{q^2}{2}\right) = \frac{\partial}{\partial z}\left(K_q \frac{\partial}{\partial z}\left(\frac{q^2}{2}\right)\right) + K_m\left(\left(\frac{\partial u}{\partial z}\right)^2 + \left(\frac{\partial v}{\partial z}\right)^2\right) + \frac{g}{\rho_0} K_h \frac{\partial \rho}{\partial z} - \frac{q^3}{B_1 l} \quad (3.23)$$

$$\frac{D}{Dt}\left(q^2 l\right) = \frac{\partial}{\partial z}\left(K_q \frac{\partial}{\partial z}\left(q^2 l\right)\right) + l E_1 K_m\left(\left(\frac{\partial u}{\partial z}\right)^2 + \left(\frac{\partial v}{\partial z}\right)^2\right) + \frac{l E_1 g}{\rho_0} K_h \frac{\partial \rho}{\partial z} - \frac{q^3}{B_1}\tilde{W} \quad (3.24)$$

(3.23) represents the transport of the turbulent kinetic energy and the balance between its production (including buoyant production), diffusion and dissipation. l is the turbulent length scale and B_1 is an empirical constant. (3.24) represents the transport of the quantity $q^2 l$, which is linked to the turbulent length scale. One of the weaknesses of this approach is the difficulty in defining such a quantity (Mellor and Yamada, 1982). $\tilde{W}$ is the wall proximity function

$$\tilde{W} = 1 + E_2\left(\frac{l}{\kappa L}\right)^2 \quad \text{with} \quad \frac{1}{L} = \frac{1}{\eta - z} + \frac{1}{H + z} \quad (3.25)$$

which includes an empirical non local length scale L so that for simulation with infinite depth $L = \kappa z$ (Burchard, 2001); E_1 and E_2 are empirical constants (Mellor and Yamada, 1982). Other schemes prefer to close the set of equations using dissipation of TKE, ϵ, rather then l, where

$$\epsilon = \frac{q^3}{B_1 l} \tag{3.26}$$

and it is possible to relate the two formulations (Burchard *et al.*, 1998).

Turbulence closure schemes may also use algebraic definitions of the length scale. For instance, Blackadar (1962) relates l to the integral of the turbulent intensity q

$$l = \frac{\kappa z}{1 + \kappa z / l_0} \qquad l_0 = \gamma \frac{\int_{z_0}^{h} q z dz}{\int_{z_0}^{h} q dz} \tag{3.27}$$

where κ is von Karman's constant, z_0 is the roughness length at the boundary and γ is an empirical constant. This approach was used by Martin (1985) to simulate changes in the mixed layer at the ocean stations November and Papa for the year 1961. Another algebraic parameterisation of the turbulent length scale has been employed in tidal simulations (see for example Xing and Davies, 1995, 1996c). In their case the length scale is given by the expression

$$l = \frac{1}{l_1^{-1} + l_2^{-1}} \tag{3.28}$$

$$\text{with} \qquad l_1 = \kappa(\sigma H + z_0) e^{(\beta_1 \sigma)} \qquad \text{and} \qquad l_2 = \kappa(H - \sigma H + z_s) \tag{3.29}$$

where β_1 is an adjustable parameter, σ is the value of the normalized vertical coordinate, H is the total depth of water and z_0 and z_s are roughnesses of the bottom and surface respectively.

Following the integration of the equations for $q^2/2$ and $q^2 l$ the vertical exchange coefficients are given by 3.16 and 3.17 with a further equation for the density transport

$$\overline{\rho' w'} = -K_h \left(\frac{\partial \rho}{\partial z} \right) \tag{3.30}$$

where eddy viscosity and diffusivity are related to the TKE and length scale through

$$K_m = q l S_m \tag{3.31}$$

$$K_h = qlS_h \tag{3.32}$$

$$K_q = qlS_q \tag{3.33}$$

S_m, S_h and S_q represent stability functions which are related to the Richardson number so that the stabilising effect of stratification is taken into consideration during the calculation of the coefficients. Following Mellor and Yamada (1982) their analytical expression yields

$$S_m = A_1 \frac{1 - 3C_1 - (6A_1/B_1) - 3A_2G_h[(B_2 - 3A_2)(1 - 6A_1/B_1) - 3C_1(6A_1 + B_2)]}{[1 - 3A_2G_h(6A_1 + B_2)](1 - 9A_1A_2G_h)} \tag{3.34}$$

$$S_h = A_2 \frac{1 - (6A_1/B_1)}{1 - 3A_2G_h(6A_1 + B_2)} \tag{3.35}$$

where G_h is the stability function defined as

$$G_h = \frac{l^2}{q^2} \frac{g}{\rho_0} \frac{\partial \rho}{\partial z} \tag{3.36}$$

Table 3.1 contains the values of all the empirical constants listed in the above equations which were obtained from laboratory experiments with fluids in neutral conditions (Mellor and Yamada, 1982).

A_1	A_2	B_1	B_2	C_1	E_1	E_2	S_q
0.92	0.74	16.6	10.1	0.08	1.8	1.33	0.2

Table 3.1: Values of the empirical constants used in the Mellor-Yamada scheme

3.2.2 Boundary conditions

The equations of motion together with the prognostic equations describing the turbulent evolution of the mixing coefficients need boundary conditions to be integrated forward in time. In POM there are two sets of boundary conditions; at the free surface $z = \eta(x, y, t)$ they read

$$\rho_0 K_m \left(\frac{\partial u}{\partial z}, \frac{\partial v}{\partial z} \right) = (\tau_{sx}, \tau_{sy}) \tag{3.37}$$

$$\rho_0 K_h \left(\frac{\partial T}{\partial z}, \frac{\partial S}{\partial z} \right) = \left(\frac{dQ_s}{dt}, \frac{dS_s}{dt} \right) \tag{3.38}$$

$$q^2 = B_1^{\frac{2}{3}} |\mathbf{u}_*|^2 \tag{3.39}$$

$$q^2 l = 0 \tag{3.40}$$

$$w = u \frac{\partial \eta}{\partial x} + v \frac{\partial \eta}{\partial y} + \frac{\partial \eta}{\partial t} \tag{3.41}$$

where τ_{sx} and τ_{sy} represent the Cartesian components of the surface wind stress, $\frac{dQ_s}{dt}$ and $\frac{dS_s}{dt}$ are the heat flux and the salt flux rates at the surface and $\mathbf{u}_*$ is the surface friction velocity ($|\mathbf{u}_*|^2 = |\boldsymbol{\tau}_s|/\rho$). The assumptions for the boundary conditions on q^2 and l derive from the turbulence closure scheme (Blumberg and Mellor, 1987). In the same fashion at the bottom $z = -H(x, y)$

$$\rho_0 K_m \left(\frac{\partial u}{\partial z}, \frac{\partial v}{\partial z} \right) = (\tau_{bx}, \tau_{by}) \tag{3.42}$$

$$\rho_0 K_h \left(\frac{\partial T}{\partial z}, \frac{\partial S}{\partial z} \right) = (0, 0) \tag{3.43}$$

$$q^2 = B_1^{\frac{2}{3}} |\mathbf{u}_*|^2 \tag{3.44}$$

$$q^2 l = 0 \tag{3.45}$$

$$w_b = -u_b \frac{\partial H}{\partial x} + v_b \frac{\partial H}{\partial y} \tag{3.46}$$

where τ_{bx} and τ_{by} are the components of the bottom frictional stress

$$\boldsymbol{\tau}_b = \rho_0 C_d |\mathbf{u}_b| \mathbf{u}_b \tag{3.47}$$

and $\mathbf{u}_*$ the frictional velocity at the bed. The logarithmic law of the wall can be combined with the nearest velocity point in the model to give

$$\mathbf{u}_b = \frac{\mathbf{u}_*}{\kappa} \ln \left(\frac{z_b}{z_0} \right) \tag{3.48}$$

and the drag coefficient C_d is defined as

$$C_d = max \left[0.0025, \frac{\kappa^2}{(\ln(z_b/z_0))^2} \right] \tag{3.49}$$

with z_b being the distance of the nearest velocity grid point to the bottom, z_0 a roughness length and κ is von Karman's constant. (3.48) together with (3.49) allow for a matching between the quadratic frictional stress defined with (3.47) and a logarithmic profile for the velocity near the bottom; z_0 is set to 0.001 m when further details about the topography and composition of the sea bed are lacking (Weatherly and Martin, 1978). The constant allows for situations where the bottom is not well resolved and in shallow areas.

3.2.3 Coordinate system

In the Princeton Ocean Model the σ-coordinate system is the choice for the vertical coordinate whilst the horizontal coordinates can be orthogonal Cartesian (as in this particular regional study,) or curvilinear - for the use of the latter see a review by Blumberg and Herring (1987). The σ-coordinate is a terrain following system in which the vertical coordinate is scaled on the water column depth (Mellor, 1998). Unlike z-coordinates this system allows the representation of topographic features even when the resolution is coarse (Gerdes, 1993). Another advantage is the treatment of flows in the boundary layer (Mellor and Blumberg, 1985) and the definition of the boundary conditions in the vertical equation of motion.

The new coordinate is obtained from the z-coordinate through a transformation following the work of Phillips (1957)

$$\sigma = \frac{z - \eta}{H + \eta} \tag{3.50}$$

so that $\sigma = 0$ at the free surface where $z = \eta(x, y, t)$ and $\sigma = -1$ at the bottom where $z = -H(x, y)$. Indicating the total depth with $D = H + \eta$ it is possible to rewrite the equations of motions in flux form

$$\begin{aligned} &\frac{\partial uD}{\partial t} + \frac{\partial u^2 D}{\partial x} + \frac{\partial uvD}{\partial y} + \frac{\partial u\omega}{\partial \sigma} - fvD + gD\frac{\partial \eta}{\partial x} = \\ &\frac{\partial}{\partial \sigma}\left(\frac{K_m}{D}\frac{\partial u}{\partial \sigma}\right) - \frac{gD^2}{\rho_0}\frac{\partial}{\partial x}\int_\sigma^0 \rho d\sigma + \frac{gD}{\rho_0}\frac{\partial D}{\partial x}\int_\sigma^0 \sigma\frac{\partial \rho}{\partial \sigma}d\sigma + F_x \end{aligned} \tag{3.51}$$

$$\begin{aligned} &\frac{\partial vD}{\partial t} + \frac{\partial V^2 D}{\partial y} + \frac{\partial uvD}{\partial x} + \frac{\partial v\omega}{\partial \sigma} + fuD + gD\frac{\partial \eta}{\partial y} = \\ &\frac{\partial}{\partial \sigma}\left(\frac{K_m}{D}\frac{\partial v}{\partial \sigma}\right) - \frac{gD^2}{\rho_0}\frac{\partial}{\partial y}\int_\sigma^0 \rho d\sigma + \frac{gD}{\rho_0}\frac{\partial D}{\partial y}\int_\sigma^0 \sigma\frac{\partial \rho}{\partial \sigma}d\sigma + F_y \end{aligned} \tag{3.52}$$

with the continuity equation written as

$$\frac{\partial \eta}{\partial t} + \frac{\partial uD}{\partial x} + \frac{\partial vD}{\partial y} + \frac{\partial \omega}{\partial \sigma} = 0 \tag{3.53}$$

where ω represents the new vertical velocity orthogonal to σ-surfaces and scaled by the total depth D

$$\omega = w - u\left(\sigma\frac{\partial D}{\partial x} + \frac{\partial \eta}{\partial x}\right) - v\left(\sigma\frac{\partial D}{\partial y} + \frac{\partial \eta}{\partial y}\right) - \left(\sigma\frac{\partial D}{\partial t} + \frac{\partial \eta}{\partial t}\right) \tag{3.54}$$

F_x and F_y are the horizontal diffusion terms, parameterised as

$$F_x = \frac{\partial}{\partial x}\left(2DA_m\frac{\partial u}{\partial x}\right) + \frac{\partial}{\partial y}\left(DA_m\left(\frac{\partial u}{\partial y} + \frac{\partial v}{\partial x}\right)\right) \tag{3.55}$$

$$F_y = \frac{\partial}{\partial y}\left(2DA_m\frac{\partial v}{\partial y}\right) + \frac{\partial}{\partial x}\left(DA_m\left(\frac{\partial u}{\partial y} + \frac{\partial v}{\partial x}\right)\right) \tag{3.56}$$

These use the formulation of Mellor and Blumberg (1985) and do not use the transformed quantity in order to obtain better resolution of horizontal diffusivity in the presence of large topographic slopes. The conservation equations for salinity and temperature are

$$\frac{\partial SD}{\partial t} + \frac{\partial uSD}{\partial x} + \frac{\partial vSD}{\partial y} + \frac{\partial \omega S}{\partial \sigma} = \frac{\partial}{\partial \sigma}\left(\frac{K_h}{D}\frac{\partial S}{\partial \sigma}\right) + F_S \tag{3.57}$$

$$\frac{\partial TD}{\partial t} + \frac{\partial uTD}{\partial x} + \frac{\partial vTD}{\partial y} + \frac{\partial \omega T}{\partial \sigma} = \frac{\partial}{\partial \sigma}\left(\frac{K_h}{D}\frac{\partial T}{\partial \sigma}\right) + F_T \tag{3.58}$$

Finally the equations for the turbulence intensity and length scale become

$$\begin{aligned}\frac{\partial q^2 D}{\partial t} + \frac{\partial uq^2 D}{\partial x} + \frac{\partial vq^2 D}{\partial y} + \frac{\partial \omega q^2}{\partial \sigma} &= \frac{\partial}{\partial \sigma}\left(\frac{K_q}{D}\frac{\partial q^2}{\partial \sigma}\right) \\ + \frac{2K_m}{D}\left(\left(\frac{\partial u}{\partial \sigma}\right)^2 + \left(\frac{\partial u}{\partial \sigma}\right)^2\right) + \frac{2gK_m}{\rho_0}\frac{\partial \rho}{\partial \sigma} - \frac{2Dq^3}{B_l l} + F_{q^2}\end{aligned} \tag{3.59}$$

$$\frac{\partial q^2 lD}{\partial t} + \frac{\partial u q^2 lD}{\partial x} + \frac{\partial v q^2 lD}{\partial y} + \frac{\partial \omega q^2 l}{\partial \sigma} = \frac{\partial}{\partial \sigma}\left(\frac{K_q}{D}\frac{\partial q^2 l}{\partial \sigma}\right)$$
$$+E_1 l\left(\frac{K_m}{D}\left(\left(\frac{\partial u}{\partial \sigma}\right)^2 + \left(\frac{\partial u}{\partial \sigma}\right)^2\right) + \frac{g}{\rho_0}K_h\frac{\partial \rho}{\partial \sigma}\right) - \frac{Dq^3}{B_l}\tilde{W} + F_{q^2 l} \tag{3.60}$$

In equations (3.57) to (3.60) the terms describing the horizontal turbulent diffusivity are given by

$$F_\phi = \frac{\partial}{\partial x}\left(DA_h\frac{\partial \phi}{\partial x}\right) + \frac{\partial}{\partial y}\left(DA_h\frac{\partial \phi}{\partial y}\right) \tag{3.61}$$

where ϕ is one of the previous scalars S,T,q^2 and $q^2 l$.

Boundary conditions in the transformed system of coordinates are not materially different, with the exception of (3.41) which becomes

$$\omega(0) = 0 \tag{3.62}$$

and (3.46) which becomes

$$\omega(-1) = 0 \tag{3.63}$$

There are no salt or heat fluxes through the sea bed and the new velocity ω is zero at both surface and bottom boundary.

Bathymetry is the main source of error in this terrain following system of coordinates, especially in the presence of steep topographic gradients and large density gradients (Kliem and Pietrzak, 1999). The problem is related to the horizontal pressure gradient when expressed in σ-coordinates (Haney, 1991; Mellor *et al.*, 1994)

$$\nabla p\Big|_z = \nabla p\Big|_\sigma - \frac{\sigma}{D}\frac{\partial p}{\partial \sigma}\nabla H \tag{3.64}$$

which is the sum of two terms, the second depending on the tilt of the coordinate

surface which introduces a truncation error not present in the z-coordinates system (Haney, 1991). This imposes a limitation on the topographic slope which can be resolved by the model with a given resolution (Gerdes, 1993) and this could lead to errors in the calculation of the geostrophic flow (Kliem and Pietrzak, 1999). Various solutions to this problem have been attempted; the removal of a horizontally uniform reference density as suggested by Gary (1973) is also used in atmospheric modelling; other methods involve the use of z-coordinates pressure calculations which are later interpolated into σ-coordinates (Kliem and Pietrzak, 1999). Together with the truncation error problem, σ-coordinates models can be affected by "hydrostatic inconsistency" (Haney, 1991); a finite difference scheme is said to be consistent if the relation

$$\left| \frac{\sigma}{D} \frac{\partial D}{\partial x} \right| \triangle x < \triangle \sigma \tag{3.65}$$

is satisfied, where $\triangle x$ and $\triangle \sigma$ are the horizontal and vertical grid size. This ensures that σ surfaces remain in the same relative position to each other within the distance of a horizontal grid cell (Haney, 1991). Equation (3.65) can put big constraints on vertical and horizontal resolutions, Mellor *et al.* (1994) who investigated this problem concluded that pressure gradient error is non divergent and that it is eliminated through advection. In their study the error was reduced by subtracting an area-averaged density gradient before its calculation using σ-coordinates.

3.3 Description of the model

The complete technical details of the Princeton Ocean Model are described in Blumberg and Mellor (1987) and O'Connor (1991) and they will not be repeated here. The numerical integration is carried out using a finite difference method on a discrete grid and is based on the concept of mode splitting (Simons, 1974; Madala and Piacsek, 1977) where barotropic and baroclinic motions are treated separately. It is then possible to calculate the surface elevation and the vertical shear without compromising the choice of the time step for the simulation. The two modes are called external and internal modes respectively following Blumberg and Mellor (1987); the former is obtained from the vertical integration of the continuity equation (3.53) and momentum equations (3.51) and (3.52) which return

the shallow water equations for the vertically averaged velocity components $\overline{U}$ and $\overline{V}$. The numerical strategy consists of resolving this mode with a time step $\triangle t_e$ which is subject to the Courant-Friedrics-Levy (CFL) criterion of stability given by

$$\triangle t_e \leq \frac{1}{C}\left(\frac{1}{\triangle x^2}+\frac{1}{\triangle y^2}\right)^{-\frac{1}{2}} \qquad \text{with} \quad C = 2\sqrt{gH}+\overline{U}_{max} \tag{3.66}$$

where $\triangle x$ and $\triangle y$ are the grid size, g the acceleration of gravity, H the maximum depth of the domain and $\overline{U}_{max}$ the maximum depth averaged velocity. The value of the surface elevation gradient is then used to carry out the integration of the baroclinic internal mode with a longer time step $\triangle t_i$, for convenience an integer multiple of $\triangle t_e$. In this way it is possible to save computational time since the constrain on the internal time step is less stringent and the ratio $\triangle t_i/\triangle t_e$ can be of the order of 100.

The model uses an Arakawa "C " grid (Arakawa and Lamb, 1977) - see Fig. 3.1 - which has been widely used in coastal and ocean modelling (see for instance Backhaus, 1985; Haidvogel and Beckmann, 1998); other finite difference grids are possible, namely the "A " and the "B ", the latter was used by James (1987) and in the GFDLM model (Cox, 1984). The integration is carried out using a leap-frog scheme and is second order accurate in time and space to conserve energy, momentum, mass, salinity and temperature (Blumberg and Mellor, 1987); the leap-frog scheme can cause the solution at odd time steps to diverge from the solution at even time steps. Time splitting is smoothed with a weak filter (Asselin, 1972) given by

$$\Psi_s^n = \Psi^n + \frac{\alpha}{2}\left(\Psi^{n+1} - 2\Psi^n + \Psi^{n-1}\right) \tag{3.67}$$

where Ψ_s^n is the new smoothed solution at time n, a function of the old solutions Ψ at time $n-1$, n and $n+1$. The coefficient α is usually set to be equal to 0.05.

3.3.1 Advection schemes

Numerical diffusion is a concern for the solution of the advection equation for scalars, such as salinity and temperature. In shelf sea simulations it is important that

sharp gradients of density are reproduced in a realistic way. Various advection schemes have been devised; all should ideally fulfill the requirements of conservation of mass, being positive definite, preserving monotonicity and with negligible phase and amplitude errors (Pietrzak, 1995). Unfortunately it is difficult for a single scheme to have all these characteristics especially in the presence of strong gradients (James, 1996).

The simplest solution is the upstream advection scheme; it is easy to implement numerically, efficient and it preserves monotonicity. However, because of the amplitude truncation related to first order schemes, it is the most numerically diffusive scheme (Pietrzak, 1995). An alternative solution is to use a central difference scheme which is not as diffusive but lacks the preservation of the monotonicity; it is not positive definite and tends to cause numerical ripples (Pietrzak, 1995). Other schemes have been developed and used with success in coastal simulations. A review is presented in Pietrzak (1995) where a series of scheme were tested with the Princeton Ocean Model and the results compared; they included hybrid schemes such as the total variation diminishing method (TVD) and the MPDATA (Multidimensional Positive Definite Advection Transport Algorithm) family of schemes developed by Smolarkiewicz (1983, 1984).

This work uses the MPDATA scheme which is based on the upstream method of solution, and is corrected iteratively. It is possible to show that the upstream scheme adds an implicity numerical diffusion (see for example Kowalik and Murty, 1993). For a one dimensional case the advection equation becomes

$$\frac{\partial \psi}{\partial t} + \frac{\partial}{\partial x}(u\psi) = \frac{\partial}{\partial x}\left(K_{imp}\frac{\partial \psi}{\partial x}\right) \tag{3.68}$$

where ψ is the scalar to be advected and K_{imp} is the implicit diffusion given by

$$K_{imp} = \frac{1}{2}(|u|\triangle x - \triangle t u^2) \tag{3.69}$$

The MPDATA approach applies the upstream scheme with a successive iteration where the diffusion is corrected using an upstream method but with an antidiffusive velocity u_{ad} defined by

$$u_{ad} = -\frac{K_{imp}}{\psi}\frac{\partial \psi}{\partial x} \quad \text{for} \quad \psi > 0 \quad \text{otherwise} \quad u_{ad} = 0 \tag{3.70}$$

MPDATA has small implicit diffusion but the numerical integration requires more computational time due to the iterations. This problem is common to all higher order schemes.

3.3.2 Imposed boundary conditions

Particular care must be paid to the meteorological forcing which goes into the boundary conditions. In this application the salinity flux on the surface has been taken as zero but it can be specified if data regarding evaporation and precipitation are available (Blumberg and Mellor, 1987). The discharge of fresh water was included because of its importance in the dynamics of the Malin-Hebridean region (Simpson and Hill, 1986; Hill and Simpson, 1989). The code was modified following the approach of Kourafalou *et al.* (1996a) so that the fresh water runoff was modelled through the continuity equation (3.53), taking the momentum associated with the river discharge to be negligible. The salinity of the source was considered to be zero and it was possible to specify also the temperature of the discharge.

The heat flux was modelled using observations and following a standard approach used in other studies (Rosati and Miyakoda, 1988; Zavatarelli and Mellor, 1995). The net surface heat flux Q_n can be expressed as the sum of two terms: the flux received from the sun Q_s and the flux released from the water column Q_{wc} so that

$$Q_n = Q_s - Q_{wc} \tag{3.71}$$

Q_s can be obtained either from observations or from bulk formulae that can be found in literature (see for instance Reed, 1977). Here, observations have been obtained from the British atmospheric Data Centre (BADC) for the station of Stornoway and cover the year 1997. The heat loss, Q_{wc}, comprises three terms

$$Q_{wc} = Q_{lw} - Q_{se} + Q_{la} \tag{3.72}$$

where Q_{lw} is the long wave radiation and Q_{se} and Q_{la} are respectively the sensible and latent heat from the surface to the atmosphere. Established bulk formulae have been used for these simulations (Rosati and Miyakoda, 1988; Holt and James, 1999); the net long wave radiation flux is written as

$$Q_{lw} = \varepsilon\sigma T_s^4 \left(0.39 - 0.05 e_a^{\frac{1}{2}}\right)(1 - 0.8C) - 4\sigma T_s^3 (T_s - T_a) \tag{3.73}$$

where σ is the Stefan-Boltzmann constant ($\sigma = 5.67 \times 10^{-8}$ W m^{-2} K^{-4}) and ε is the emissivity of the ocean (a correction for the emission of the black body, $\varepsilon = 0.97$), T_s is the absolute temperature of the water, e_a is the atmospheric vapour pressure and C is the cloud cover. This formula takes into account the difference in temperature between sea and air with the second term where T_a is the air temperature. The vapour pressure is computed from the saturation vapour pressure, e_w, at the air temperature just above the sea (taken as T_s) and relative humidity, R_h, using the polynomial approximation

$$e_a = R_h e_w \qquad \log e_w = \left(\frac{0.7859 + 0.03477\,(T_s - 273.14)}{1 + 0.0042\,(T_s - 273.14)}\right) \tag{3.74}$$

The sensible heat flux is a function of the air-sea temperature difference and the wind speed so that

$$Q_{se} = c_h \rho_a c_p |\mathbf{W}|\,(T_s - T_a) \tag{3.75}$$

In this case c_h is the Stanton number, ρ_a (1.25 kg m^{-3}) is the density of the air, c_p the specific heat of air (1004 J kg^{-1} K^{-1}), $|\mathbf{W}|$ is the wind speed and T_a is the absolute air temperature. Finally the latent heat flux can be written as

$$Q_{la} = L_t c_e \rho_a |\mathbf{W}|\,(q_s - q_a) \tag{3.76}$$

where L_t is the latent heat of vapourisation ($2.5 \times 10^6 - 2.3 \times 10^3 T_s$) and c_e is the Dalton number. The quantities q_s and q_a represent the specific humidity of the air and are related to the vapour pressure, e_t, at temperature t with the expression

$$q_t = \frac{0.62 e_t}{(p - 0.38 e_t)} \qquad \text{where } p \text{ is the the atmospheric pressure in mb} \qquad (3.77)$$

During these simulations the heat flux derived from (3.71) - (3.77) was used directly in (3.38) for the calculation of this value at the boundary. Other methods have been used for the surface heat flux, for example Oey and Chen (1992a) employed a relaxation term which was function of the difference between simulated and climatological temperature to improve the overall result.

Lateral boundary conditions need to be specified very carefully since they can strongly influence the solution inside the domain. Ideally an open boundary condition should be totally transparent to outgoing disturbances without any reflection, to avoid the propagation of spurious signals inside the region of interest (Chapman, 1985). In this work a radiation condition was implemented for the external mode, following the work of Flather (1976). This was found to be the best option after extensive testing. Due to the tidal characteristics of the area under investigation the major energetic contribution to the signal propagating inside the domain is known to be Kelvin waves. A simple radiation condition for this kind of wave has been selected, which yields

$$u_n = \hat{u}_n + \frac{c}{H}(\eta - \hat{\eta}_n) \qquad c = \sqrt{gH} \qquad (3.78)$$

where u_n is the velocity component orthogonal to the boundary; the component parallel was set to zero. The quantities $\hat{u}_n$ and $\hat{\eta}_n$ represent prescribed values at the open boundaries. In this case these values came from a larger scale simulation of the North-West European Continental Shelf, run at the Proudman Oceanography Laboratory. For the tidal constituents of interest the total prescribed signal can be written as

$$\hat{u}_n = \sum_i u_{ai} \cos(\omega_i t - \varphi_{ui}) \qquad \hat{\eta}_n = \sum_i \eta_{ai} \cos(\omega_i t - \varphi_{\eta i}) \qquad (3.79)$$

Open boundary conditions for the horizontal component of the baroclinic velocity were an upstream radiation condition. Salinity and temperature were also modelled with an upstream scheme at the open boundaries with the exterior value supplied

by climatological data (Levitus, 1982) and then interpolated onto the model grid.

3.4 Previous applications of the Princeton Ocean Model

Some previous applications of POM will be discussed briefly. Since its formulation POM has been widely used in a range of applications from coastal and regional simulations to oceanic and climate studies.

3.4.1 Oceanic applications

Here two applications of the Princeton Ocean Model will be discussed, one simulation covering the entire Atlantic Ocean from 80°N to 80°S (Ezer and Mellor, 1997) and another covering only the northern part of the same ocean (Ezer and Mellor, 1994). The former work represents the first time that decadal simulations have been executed with this type of model. Horizontal orthogonal curvilinear coordinates were used and the resolution varied from 20 km to 100 km with a mesh grid of 50 km covering the Gulf Stream. In the vertical 16 layers were used with high resolution near the surface. The time steps were chosen as 44 s for the external barotropic mode and 2000 s for the internal baroclinic mode. The Mediterranean basin was included in the domain of simulation because it could affect the pattern of the thermohaline circulation. The model was run for 30 years run with monthly forcing and was able to reproduce all the main features of the Atlantic circulation.

For the North-Atlantic model the grid mesh varied from 20-30 km in the western Atlantic to 80-100 km in the east. The vertical structure used 15 layers and topography was smoothed to minimise numerical errors in regions where bathymetry is steep. The results of their simulations were compatible with observational data both for circulation and thermodynamics. This work also analysed the differences between diagnostic and prognostic runs and the subsequent adjustment from one regime to the other. Purely diagnostic simulations suggested inconsistency between the hydrographic variables and the bottom topography; with a subsequent short prognostic run physical and realistic results are obtained due to dynamic adjustment.

3.4.2 Coastal Applications

South Atlantic Bight (Blumberg and Mellor, 1983)

This was one of the first uses of the Princeton Ocean Model. The model employed a Cartesian reference frame with a mesh of 23.6 km× 27.8 km; the vertical structure was resolved using 21 σ layers and internal and external time steps were 24 s and 40 min respectively. Forcing boundary conditions were obtained from observational data and velocities at open boundaries were evaluated through a geostrophic calculation called the characteristic tracing model (CTM), relating total transport between different points of the grid. Several model runs were made reproducing realistic circulation including the Gulf Stream.

Delaware Bay and River System (Galperin and Mellor, 1990a,b)

A coupled shelf-estuarine model was developed in this work. To cover the domain of interest a grid with two different meshes was used, the estuarine system was covered with a grid with $\triangle x = \triangle y = 1$ km while a grid with $\triangle x = 5$ km and $\triangle y = 4$ km covered the shelf area. The thermohaline properties of the region were predicted reasonably well, with some discrepancy due to errors in the forcing climatologies at the open shelf. Results indicated the presence of a typical two-layer estuarine system that interacts with wind stress. Numerical evaluations were compatible with observations and the model was able to reproduce tidal propagation inside the bay, taking into account non-linear effects and amplification of high-frequency constituents.

Northeast Atlantic Shelves and Seas Circulation (Oey and Chen, 1992b,a)

This simulation employed a 20 km grid with 11 σ levels. Particular care was taken to describe fresh water runoff in the area under investigation. Tides and mean transports were derived from observational data. Simulations lasted 300 days and showed a good agreement with observations, failing to reproduce some thermodynamical features. Unfortunately the grid was unable to resolve the Minches area due to the coarse grid, only few points falling inside the area.

Mediterranean Sea Circulation (Zavatarelli and Mellor, 1995)

This was a study of the circulation inside the Mediterranean Basin and the water exchange between the enclosed sea and The North-Atlantic Ocean. The size of the mesh ranged from 8-15 km near the Gibraltar region to 50-60 km in the northernmost area of the domain of simulation. With a run of 10 years the exchange in the strait of Gibraltar was evaluated together with the seasonal pattern inside the whole basin. Deep water formation was investigated finding the location of deep water sources for the different parts of the Mediterranean to be in agreement with observations.

East River, New York (Blumberg and Pritchard, 1997)

This model was developed for water quality purposes. The resolution was given by 10 equally spaced sigma levels and was high because the whole system covered a length of only 25 kilometres with an average depth of 10 metres. Forcing was described using observational climatology with particular attention to the tidal forcing, the system being tidally dominated. The tidal regime was well reproduced; at every depth the model result showed an agreement with a confidence of 90%. Some computed phases differed from observations by up to 40° but this could have been due to the boundary conditions specified. The same problem also affected the thermohaline fields (the lack of a good set of observational data). Surface elevations calculated with the model showed an accuracy of 99%.

Tides and storm surges in Seto Inland Sea (Minato, 1996, 1998)

In this study an air-sea coupled system was under investigation. The aim was to simulate short term variations of elevation inside the Seto Inland sea in Japan. These changes in sea level are principally due to tides and storm surges. A set of 40 tidal components and the barotropic 2D version of the model was used to simulate the tides in the area. Results were in general agreement with observational data although there were some inaccuracies due to a poor resolution in some parts of the inland sea. A simulation of the passage of typhoon was carried out to evaluate the effects of the resulting storm surge but the simulation showed some discrepancy with observational data, probably arising from an inaccurate representation of the

real wind field and lack of resolution. The results showed also that it is possible to consider the total effect on the sea level as the superposition of the separate effects of tide and storm surge. Another similar experiment was carried out in the Tosa Bay, with a slightly coarser grid (4 km-4.6 km) and different vertical resolution.

3.5 Modelling of the Hebridean Shelf

The Hebridean Shelf has received little attention from researchers and this is one of the reasons for the present work. In this section previous models of the area are described. The models are all homogeneous so baroclinic and thermodynamical aspects (e.g. seasonal stratification or the presence of the Islay front) are not reproduced; however a good description of the tidal circulation is achieved.

3.5.1 Models of tides in the Hebridean area

The region covered by these studies extended from 55° N to 59° N and from 4° W to 12° W (Proctor and Davies, 1996; Xing and Davies, 1996b,c). The equations of motion were expressed in spherical polar co-ordinates and σ coordinates in both models but they differed in the method of dealing with the vertical structure. The Proctor and Davies model used a Galerkin approach where the components of the horizontal velocity were expanded in terms of basis functions of the vertical coordinate with coefficients that are functions of time and of horizontal position. This approach allows a 3-D model to be integrated on a 2-D grid reducing computational efforts. Vertical eddy viscosity was expressed as a function of horizontal position and time and a fixed function which gives the vertical profile of viscosity.

In the Xing and Davies models the eddy viscosity was calculated using the level 2.5 turbulence closure sub-model with two different specification for the length scale; one involving the prognostic equation for $q^2 l$ (3.24) and the other involving the trigonometric profile (3.28) - (3.29). Both models employed a grid with mesh 1/12° of latitude × 1/12° of longitude. The results for the M_2 constituent will be briefly discussed later, in comparisons with the results obtained from this work. Both models resolved the amphidromic point situated close to the North Channel. Cotidal lines showed that phase and amplitude both increase northward, the typical pattern

of a Kelvin wave travelling along a coast. The different choice of turbulence closure sub models did not affect results in a significant way.

3.5.2 Long term flow along the Malin-Hebrides shelf

This study was concerned with the long term circulation in the area (Xing and Davies, 1996c). Equations were expressed in polar coordinates and two different turbulence closure sub models were used. Wind stress and radiation conditions were prescribed at open boundaries. In particular the wind-forced circulation and tidal residual circulation were investigated. Two different wind fields were chosen, westerly and southerly with a stress of 1 N m^{-2} (corresponding to a velocity of 20 m s^{-1}). For the calculation of the tidal residual circulation the wind stress was set to zero and the model was forced with an M_2 tidal input as in the model used by Xing and Davies (1996b). Finally a flow through the North Channel was simulated. Wind forcing was removed and a 0.2 m s^{-1} depth mean current was used as input at the North Channel open boundary. In this simulation it is possible to see some recirculation in the southern end of the Minches but not of sufficient magnitude to explain the observations (Hill *et al.*, 1997b).

3.6 Summary

The Princeton Ocean Model is a three-dimensional, non-linear primitive equation coastal model and it has been described in this chapter. Its main attributes are:

- Terrain following coordinates in the vertical (σ-coordinates) which allows a better representation of the bottom topography. The horizontal coordinates may be curvilinear or rectangular.
- The vertical turbulent exchange parameters (eddy viscosity and diffusivity) are calculated using a second moment turbulence closure scheme (the Mellor-Yamada 2.5 closure scheme).
- The horizontal turbulent exchange parameters are calculated using the Smagorinsky formulation so that they are related to the mesh grid and to the local shear in velocity.

- The numerical integration is carried out using finite differences on an "Arakawa C" grid. The external mode is two-dimensional and is integrated explicitly with a short time subject to the CFL constraint. The internal mode is three-dimensional, and uses a longer time step to minimise computational effort.

POM has been widely used for both ocean and coastal simulations and some of its uses have been reviewed in this section. The next chapters will be devoted to its application on the Hebridean-Malin shelf to study tidal structure and seasonal evolution of temperature and salinity and to investigate the dynamical response of the shelf to these changes.

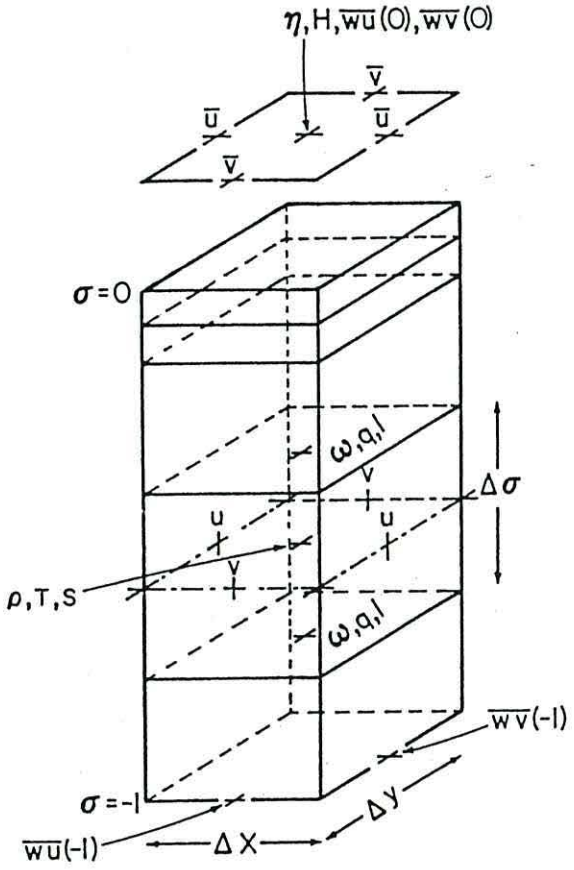

Figure 3.1: Location of the variables on the Arakawa "C" grid (from Blumberg and Mellor, 1987).

Chapter 4

Tidal validation of POM

4.1 Introduction

The ability to correctly reproduce the tides is the first test to assess the capabilities of the Princeton Ocean Model. As discussed in the previous chapters tides are important on the European Shelf; they strongly interact with the seasonal heating-cooling cycle (Simpson, 1981, 1998; Hill and Simpson, 1989), modulating stratification in areas such as the Malin shelf (Hill and Simpson, 1989) and Flamborough Head (Hill *et al.*, 1993). Interactions are also possible with density structures generated by freshwater runoff as in Liverpool Bay (Sharples and Simpson, 1995) and in the German Bight (Simpson and Souza, 1995). Tides are also responsible for production of turbulence in the water column via dissipation of their energy. For these reasons, if a large time-scale simulation is to be carried out the realistic simulation of the tide is a necessary prerequisite. For this regional study only two constituents will be considered, namely M_2 and S_2. They are both semi-diurnal and they account for the majority of the energy dissipation on the shelf, with M_2 being the largest contributor in the balance.

This chapter will deal with the setting of bathymetry and boundary conditions for POM for a tidal study of the Scottish shelf. Results will be compared with observations from tidal gauges and current meters deployed in the area during previous studies. The results will also be compared with those from other models used for tidal simulations on this shelf (Proctor and Davies, 1996; Xing and Davies, 1996c; Young *et al.*, 2000).

4.2 Model setting for the tidal simulations

Fig. 2.2 illustrates the bathymetry of the area under investigation. It extends from 9° 5′ W to 2° 45′ W and from 52° 24′ N to 60° 10′ N; the resolution is 1/18 degree of latitude and 1/12 degree of longitude so that there are 141 × 77 elevation and velocity points. The grid mesh is 6.1 km×5.6-4.6 km (depending on latitude) and it is fine enough to resolve baroclinic processes because the Rossby radius of deformation, r_d, defined in (1.6), is of the order of 10 km on this part of the European shelf (James, 1990). This bathymetry was obtained by interpolation from a coarser bathymetry, covering the whole European Shelf in use at the Proudman Oceanographic Laboratory. It has already been used in various studies concerning tidal processes, see for example Davies *et al.* (1997b) and Davies and Kwong (2000). The aim of the simulation was to reproduce tidal patterns on the Scottish shelf but the domain chosen was larger, to include the Irish Sea. This approach was followed mainly for two reasons, one numerical and the other related to the dynamics of the area. The first aim was to have the modelled area relatively far from the influences of the boundaries (where boundary conditions can influence the interior of the domain as previously discussed); secondly, far field effects play an important role in determining the dynamics of the region, especially the exchange between the Irish Sea and the Malin Shelf (Brown and Gmitrowicz, 1995). Young *et al.* (2000, 2001) followed the same approach in her modelling study of fluxes in the North Channel of the Irish Sea.

In the vertical 21 σ layers were used. Resolution was increased at the surface and at the bottom, to better resolve the associated boundary layers. Table 4.1 illustrates the thickness of each single σ layer; resolution varies from 5-10 metres in a water depth of 100 metres to 100 metres where the depth is 1500 metres. The minimum depth was set to be 10 metres in all the domain to avoid the wetting-drying of cells. A major problem with this bathymetry was the presence of the shelf-break in the domain of simulation (see Fig. 2.2). This could bring about errors in the determination of the baroclinic pressure gradient (and hence velocities) because of the use of σ-coordinates (Haney, 1991). As seen in the previous chapter this problem is intrinsically linked with the the definition of the terrain-following coordinates. As demonstrated in various works (Mellor *et al.*, 1994; Kliem and Pietrzak, 1999) there are several methods to try to reduce the influence of steep bathymetry on simulations. In this work the method chosen to minimise the errors was to subtract an area

mean density field before the calculation of the pressure gradient terms in the model (Mellor *et al.*, 1994). The problem generated by the so-called "hydrostatic consistency" (§ 3.2.3) was thought not to cause particular problems, as already discussed in Xing *et al.* (1999), since inconsistencies are reduced by advective adjustment of the density field, as shown in Mellor *et al.* (1994). Furthermore inconsistencies are mainly concentrated in the region with steep topography (see (3.65)) far from the area of interest (the Scottish shelf and the Minch) and a steep continental shelf break acts as an insulator (Hill, 1995). The resolution used in this work is consistent with other studies (Ezer and Mellor, 1994; Zavatarelli and Mellor, 1995; Ezer and Mellor, 1997) where errors in the velocities were minimal.

k (layer)	σ (coor.)
1	0.000
2	-0.005
3	-0.025
4	-0.050
5	-0.075
6	-0.100
7	-0.150
8	-0.200
9	-0.250
10	-0.300
11	-0.400
12	-0.500
13	-0.600
14	-0.700
15	-0.800
16	-0.900
17	-0.925
18	-0.950
19	-0.975
20	-0.995
21	-1.000

Table 4.1: Distribution of vertical σ layers for tidal simulations.

Initial conditions for velocity and elevation were set to zero and their values were ramped in the first day of simulation. Salinity and temperature were kept constant throughout the tidal validation run with values of T = 10°C and S = 35. The model

was forced on all 4 open boundaries with depth-mean velocities and elevations for M_2 and S_2 tidal constituents. Their values were obtained from a large scale model which provided the bathymetry (the CS3 model from the Proudman Oceanographic Laboratory). These data were interpolated on the model's grid and the results presented here represent the best results collected over various tests carried out to optimise boundary conditions for this particular domain. Performances of models are highly sensitive to the prescription of inputs at boundaries as shown by Davies and Aldridge (1993) and Xing and Davies (1996a) in the case of the Irish Sea.

The lateral diffusivity of momentum A_m was calculated with the Smagorinsky approach, as discussed in section 3.2; the horizontal diffusivity of scalars was related through the turbulent Prandtl number chosen to be 0.5. The background eddy viscosity was set to 2×10^{-5} m^2 s^{-1}; the roughness of the bottom, z_0, was 0.001 m and finally the constant α in the Asselin filter was taken to be 0.2.

Radiation boundary conditions were used in this set of simulations following the work of Flather (1976). This approach has been successfully used in tidal simulations (see for example Davies, 1997; Young *et al.*, 2000, 2001) and it allows the propagation of strong tidal forcing from outside the domain of simulation. Other types of radiation condition were attempted but they all resulted in instability of the model. Temperature and salinity were not a problem since they were constant and there was no advection of these two scalars inside or outside the domain of simulation.

4.3 M_2 tidal elevations and currents

Fig. 4.1 and Fig. 4.2 show the calculated amplitude and phase respectively for the Scottish region. As expected, the semidiurnal tide behaves as a Kelvin wave travelling northward, along the coast. The amplitude varies from 0 m in the amphidromic point to 1.4 m in the Minch region, close to the isle of Skye. The presence of the amphidromic point is also confirmed by the co-tidal chart, its position is in good agreement with observations (George, 1980) and with results of other simulations (Proctor and Davies, 1996; Young *et al.*, 2000). Elevations and phases are also in good agreement with these previous modelled studies.

For a quantitative assessment, observations from various sources were compared with the computed results (see appendix A for the tables mentioned in this chapter). Elevations and phases for the semidiurnal constituent M_2 were calculated using harmonic analysis; the model was integrated forward in time for 20 M_2 tidal cycles with all values ramped for the first day of simulations. The last 4 tidal cycles were used for the analysis; this long simulation allowed the two semidiurnal constituents to be better separated as discussed in Proctor and Davies (1996) when starting from a state of rest. These modelled results were compared with the same observations used in Proctor and Davies (1996) for their assessment; Fig. 4.3 shows the position of these tidal gauges whilst Table A.1 contains the observed and computed values together with estimates of absolute and percentage errors. Fig. 4.4a and Fig. 4.4b picture the comparison between model results and observations for amplitude and phase; in general there is a slight tendency to underestimate the elevation while phases are well reproduced apart from a few points. One of these points (No. 20) is close to the amphidromic point so that even small errors in the model are amplified, as noticed in Young *et al.* (2000), due to the inability of the model to correctly locate this point at coarse resolution. Errors in the other three points (No. 10, 16 and 17) are probably due to a combination of the previous cause and topographic effects which cannot be resolved by the model's grid (Proctor and Davies, 1996).

Table A.2 and Table A.3 show the distribution of errors for the amplitude and phase of M_2. This confirms the tendency to underestimate by the model and the presence of few points which are responsible for the overall error. Finally the RMS errors in amplitude and phase were 9 cm ($r^2 = 0.94$) and 42° ($r^2 = 0.70$) respectively, with the error in phase due principally to the 4 points mentioned. To validate this last statement, the statistical analysis was repeated not considering these locations and the new results for the RMS error on the phase was 8° ($r^2 = 0.99$) which proves this assertion. These values of RMS errors are comparable with the errors obtained in other simulations in the same region; Proctor and Davies (1996) give 13.3 cm and 13° for the RMS errors for amplitude and phase respectively whilst a range of different values, from 11.93 cm to 7.85 cm and from 3.58° to 8.33°, are reported by Young *et al.* (2000) but that simulation was more concerned with the Irish Sea and the North Channel.

Fig. 4.5 shows the location of the current meters used for the comparison between observations and computed results. They are a subset of the current meters used

in the work of Young *et al.* (2000) for the assessment of their model of the North Channel. They are distributed over the shelf, from the coastal shallow waters to the shelf break. Table A.4 and Table A.5 contain positions, observed and calculated values and absolute and percentage errors for both components of the tidal velocity. For a quantitative assessment of the performance in reproducing tidal velocities, Figs. 4.6a,b and Figs. 4.7a,b show graphically the comparison between observations and modelled results for the u and v components. Table A.6 and Table A.7 give the distribution of errors for amplitude and phase for both components. The agreement for the two components is fairly good; the model can reproduce strong currents in the proximity of the North Channel (No. 23 and 25) but with some overprediction. The reduction in speed due to the increased depth at the shelf edge is also present in the results (No. 5, 6 and 7). Phases for the u and v components are also in good agreement with the observations. However the phase of the meridional component was simulated with errors larger than 70° in some location (No. 9, 22 and 24); these errors are probably caused by topographic effects not resolved by the model because of the coarse resolution. The modelled u component shows a RMS error in elevation of 11 cm s^{-1} ($r^2 = 0.85$) and in phase of 23° ($r^2 = 0.73$). The v component, instead, has a RMS error of 9 cm s^{-1} ($r^2 = 0.81$) on the elevation and 37° ($r^2 = 0.64$) on the phase.

Finally tidal ellipse characteristics were calculated. Following the decomposition presented in Sousa and Simpson (1996) predicted values for these parameters were compared against the values calculated from observations for the same position, namely the semi-major axis r_{max}, semi-minor axis r_{min}, orientation α and phase β. Table A.8 illustrates this comparison. RMS errors of 13 cm s^{-1} ($r^2 = 0.88$) and 5 cm s^{-1} ($r^2 = 0.59$) were obtained for the semi-major and semi-minor respectively. Orientation and phase are computed with an RMS error of 28° ($r^2 = 0.66$) and 31° ($r^2 = 0.55$) respectively showing reasonable agreement with observations as does the sense of rotation, which is correctly reproduced in the majority of the locations.

4.4 S_2 tidal elevations and currents

The analysis for this constituent follows the same pattern used for M_2. Figs. 4.8 and 4.9 illustrate calculated elevations and phases for the S_2; they are similar to

Figs. 4.1 and 4.2 showing the characteristic behaviour of a Kelvin wave travelling northward along the Scottish coast. Amplitudes of this constituent are smaller than for M_2, reaching 0.6 m inside the Minch. There is an amphidromic point close to the North Channel, as previously seen for M_2. Fig. 4.10 shows the positions of the tidal gauges used for the validation of elevation and phase (data supplied by the Proudman Oceanographic Laboratory) whilst Table A.9 contains the values of observations. Figs. 4.11a and 4.11b show graphically these results; fewer points were used for the validation of S_2 because of availability of observations in the area but the agreement is good with an RMS error of 2 cm ($r^2 = 0.94$) and 1° ($r^2 = 0.99$) for elevation and phase respectively. In this case all the points used for the comparison are well away from the coastline and the boundaries where errors are more likely to appear. Finally Tables A.10 and A.11 illustrate the distribution of the errors between observations and predicted values mirroring the fact the agreement is good.

The u and v components of the velocity were validated using the same data utilised for M_2; Fig. 4.5 presents the locations of the current meters deployed. Results for the u and v components are shown in Table A.12 and Table A.13. Figs. 4.12a, 4.12b, 4.13a and 4.13b graphically describe them while Tables A.14 and A.15 give the histograms with the distributions of the errors for amplitude and phase. The u component is predicted with a RMS error of 3 cm s^{-1} ($r^2 = 0.82$) for amplitude and 42° ($r^2 = 0.13$) for phase; meanwhile the v component shows RMS errors of 3 cm s^{-1} ($r^2 = 0.82$) and 31° ($r^2 = 0.26$) for amplitude and phase respectively. It is interesting to notice the difference in the prediction of amplitude and phase for both components. The amplitude is reasonably reproduced whilst the phase suffers from large errors. Looking at Figs. 4.12a,b and 4.13a,b the inconsistencies are located in a few points; for the u component points 3, 5, 11 and 20 show errors larger than 70° in absolute value; similarly points 3, 5, 9, 10 and 24 have errors between 60° and 90°. As previously seen they are located near the shelf break (see Tables A.11 and A.12) where large errors are expected; also the model does not predict shear well in the deepest part of the domain and the effect seems to be more pronounced in the case of S_2 than M_2.

Tidal ellipses characteristics were calculated as previously and Table A.16 shows the comparison between observation and predicted values for S_2. As before there is a close resemblance between the behaviour of the currents and that of the tidal ellipses; there is no shear in the deep ocean whilst there is a reasonable agreement

on the continental shelf; the RMS error for amplitude of the semi-major axis is 4 cm s^{-1} ($r^2 = 0.89$), the semi-minor axis shows an error of 2 cm s^{-1} ($r^2 = 0.51$). The angular values, orientation and phase, exhibit a RMS error of 43° ($r^2 = 0.41$) and 39° ($r^2 = 0.44$) respectively.

4.5 Residual Circulation

The sub-tidal circulation was examined with the same model set-up; tidal residual velocities were calculated from the previous data by subtracting the harmonic motion predicted by the model. The model was forced with both constituents so residuals contain contributions from S_2 and M_2. Figs. 4.14 and 4.15 illustrate the predicted surface and bottom residual velocities. These results show that the tidal residual circulation is weak, velocities are of the order of 1-3 cm s^{-1} over most of the Scottish Shelf. There is a general northward motion, the flow tends to be steered along the bathymetry. Exceptions are the area of the North Channel and the Minch where strong tidal residuals are present with velocities up to 15 cm s^{-1} at the surface. In both areas the topography changes rapidly and strong non-linear interactions between tides and bathymetry are generated, creating the residual circulation observed in the model. Another example of such interaction is in the area of Tiree and Coll where tides interact with these two islands. Unfortunately in these areas the resolution of the model is also coarse (few grid points across each location) and this probably contributes to the overall picture since a fine resolution is needed to predict correctly the tidal flow in this region of the shelf (Young *et al.*, 2000, 2001). There is agreement with previous studies, Xing and Davies (1996c) also show a weak residual circulation, and there is almost no recirculation in the region of the Minch so that the pattern observed in reality must include baroclinic effects since that simulation used constant density throughout all the simulations.

To complete these simulations on the sub-tidal circulation, two further runs were completed to study the contribution of the wind on the general circulation. Following previous works (Xing and Davies, 1996c; Young *et al.*, 2001) the model was forced with a southerly and a westerly wind; there was no tidal forcing and boundary conditions and other adjustable parameters were kept constant. The wind stress $\boldsymbol{\tau}_w$ acting on the sea surface was calculating using a quadratic function

of the wind velocity $\mathbf{U}_w$, of the form

$$\boldsymbol{\tau}_w = \rho_{air} C_d |\mathbf{U}_w| \mathbf{U}_w \tag{4.1}$$

and in this case the wind speed was set equal to 10 m s^{-1} in both cases for a direct comparison with the work of Young *et al.* (2001). Simulations lasted for 12 days so that the model was able to reach a state of dynamical equilibrium; elevation and circulation were extracted from the model's output for the last 24 hours. Results for the case of southerly wind forcing are shown in Fig. 4.16 for the elevation and Figs. 4.17 and 4.18 for the surface and bottom velocities, respectively. As for the tidal simulation, the topography plays a role in the wind-induced circulation. Contours of surface elevation closely follow the bathymetry, and range from 0 to 5 cm at the coast - these values are smaller than the ones predicted in Young *et al.* (2001). Surface velocities are of the order of 20 cm s^{-1} in the shallow parts of the region (the same order of magnitude found by Young *et al.*, 2001), with a decrease toward the open ocean, as expected. Peaks of 40 cm s^{-1} are present in some of the shallowest areas. The effect of the rotation of the earth is noticeable, especially in the deepest regions, away from the coastal boundary and from the perturbing effects of topography. The bottom circulation shows the bathymetric steering; the flow is mainly northward with magnitudes of the order of 5-10 cm s^{-1} and mirrors the isobaths. In this simulation there is recirculation at both entrances of the Minch, so wind may contribute to the observed circulation but it is very unlikely that a real wind field would maintain direction and strength as in the simulation.

The simulation with westerly forcing shows a different picture, especially in the case of coastal elevation (Fig. 4.19). Values are smaller, reaching a maximum of 3 cm inside the Clyde sea showing a better agreement with Young *et al.* (2001) probably because these simulations had a bias in the long term wind field. The bathymetric steering is less noticeable but is present. Surface circulation (Fig. 4.20) shows very little topographic effect and velocity peaks of 30 cm s^{-1} in the proximity of the northern Irish coast and in some shallow regions. Otherwise velocities were around 15 cm s^{-1} in the majority of the domain. In this case the Coriolis effect contributes, deflecting the vectors towards the right as expected. The bottom circulation (Fig. 4.21) is very weak, of the order of 1 cm s^{-1}, but showing the same pattern observed in the previous simulation; there is tendency of the water to flow northwards following

the bathymetry. In this case there is almost no recirculation at the entrance of the Minch, in the Sea of the Hebrides. A weak intrusion is, instead, located in the North Minch confirming observations of a Atlantic intrusion in this region.

4.6 Summary

The tidal validation of the Princeton Ocean Model for the Scottish shelf was accomplished in this chapter. To take into consideration far field effects and to minimise the numerical influence of boundaries on solutions, a larger domain than the area of interest was used covering the Irish Sea and North Channel. The bathymetry was obtained from another model (CS3 from the Proudman Oceanographic Laboratory) with interpolation to increase the resolution. The same model also supplied boundary conditions for these tidal studies. In this case only semidiurnal constituents were utilised, namely M_2 and S_2. The model was forced for 20 tidal cycles and the last 4 were used for statistical analysis. Although this period of time was shorter than the limit imposed by the Rayleigh's criterium to separate these two tidal signals, results demonstrated good agreement with observations, both for elevation and velocity components, showing small leakage between the constituents. Large errors are present in a few locations, due to local topographic effects not resolved by the model's grid or proximity to the amphidromic point, this last factor influencing especially the phase of the M_2 elevations. Fewer observations were available for the S_2 but the agreement was reasonable. Velocity components were reproduced with a small overestimation for the amplitude; 28 locations were used for comparison and predicted values were in reasonable agreement with current meter data with S_2 showing larger errors. Tidal ellipse characteristics were also reproduced within acceptable limits. In deep water and on the shelf break there was no vertical variability in the modelled currents. It is probable that the forcing contributed to this lack of vertical variability; the model was forced on the boundaries with a depth-mean component of velocity acting on the whole water column. This could act as a constraint on the velocities in the proximity of the boundaries, limiting the vertical development of the shear. Finally a poor resolution of the vertical velocity profile due to the σ-coordinates may also contribute to the overall picture. Tidal residual circulation shows the same patterns displayed in previous work (Proctor and Davies, 1996; Xing and Davies, 1996c; Young *et al.*, 2000) with a weak northward

flow, steered along the bathymetry. Predicted values cannot justify the presence of the bifurcation of the flow in the Sea of the Hebrides, pointing toward a large baroclinic contribution.

For its importance in the overall dynamics of the shelf, wind-driven circulation was simulated. Two cases were studied - the effect of a constant southerly and westerly wind forcing. Results were in agreement with previous studies (Xing and Davies, 1996c; Young *et al.*, 2001). Surface flow follows the forcing with a deflection due to rotation whilst bottom velocities show the same pattern of a northward flow, steered by bathymetry. As observed by Xing and Davies (1996c), the independence of the bottom flow structure from the direction of the wind suggests a strong interplay between flow and bathymetry so that locations of baroclinic effects such as the bifurcation of the flow may also be influenced by the topography of the region. For all these studies density was kept constant. In the next chapter, baroclinicity is introduced to take into account all the factors which may influence the circulation and to explain the observations.

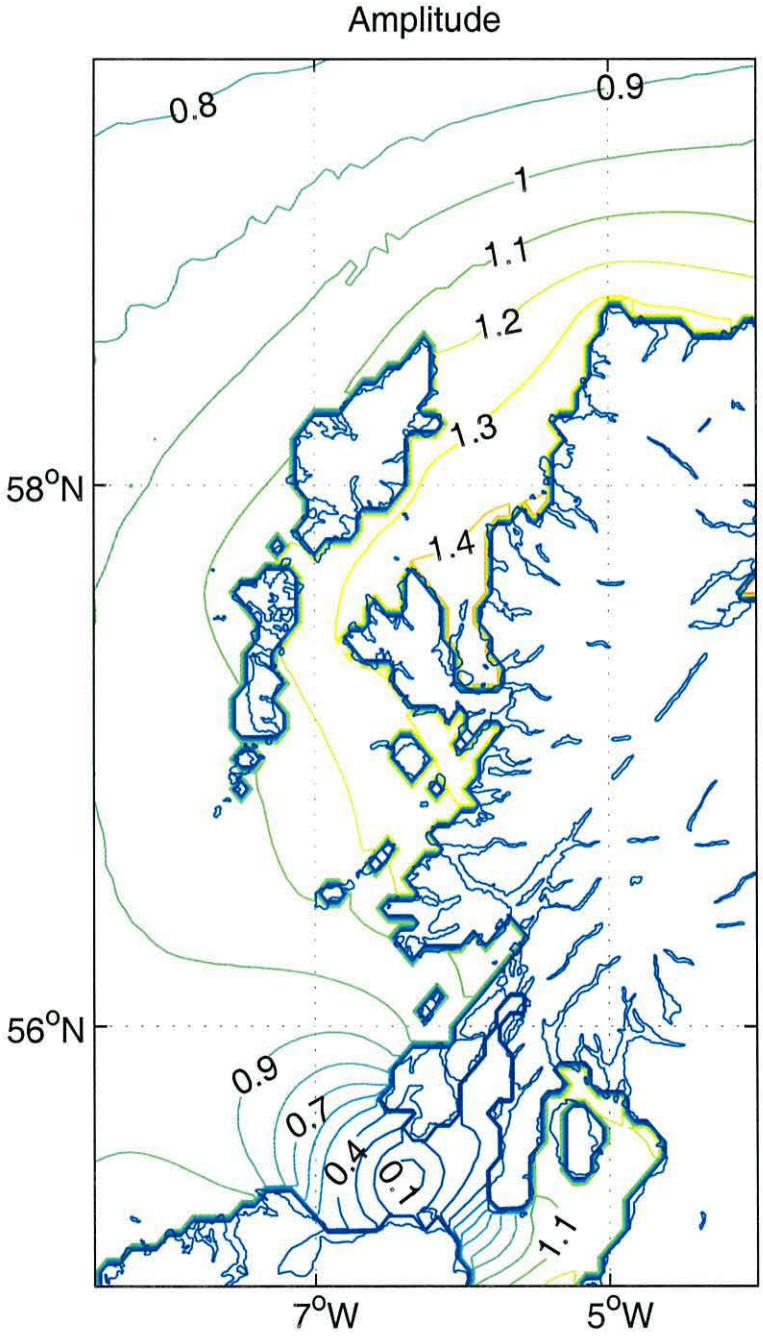

Figure 4.1: Calculated M_2 elevation chart, amplitude in metres. Contours are plotted at 0.1 m intervals.

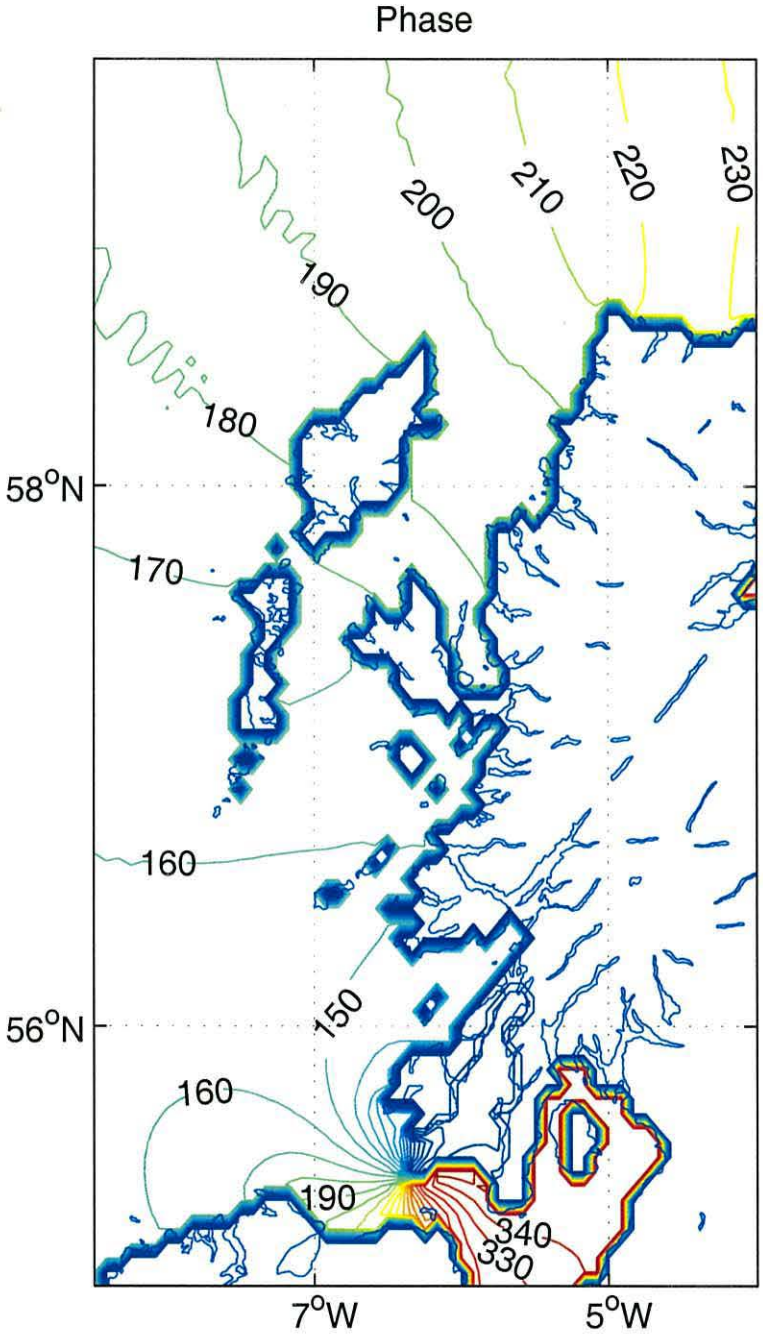

Figure 4.2: Calculated M_2 co-tidal chart, phase in degrees. Contours are plotted at 10° intervals.

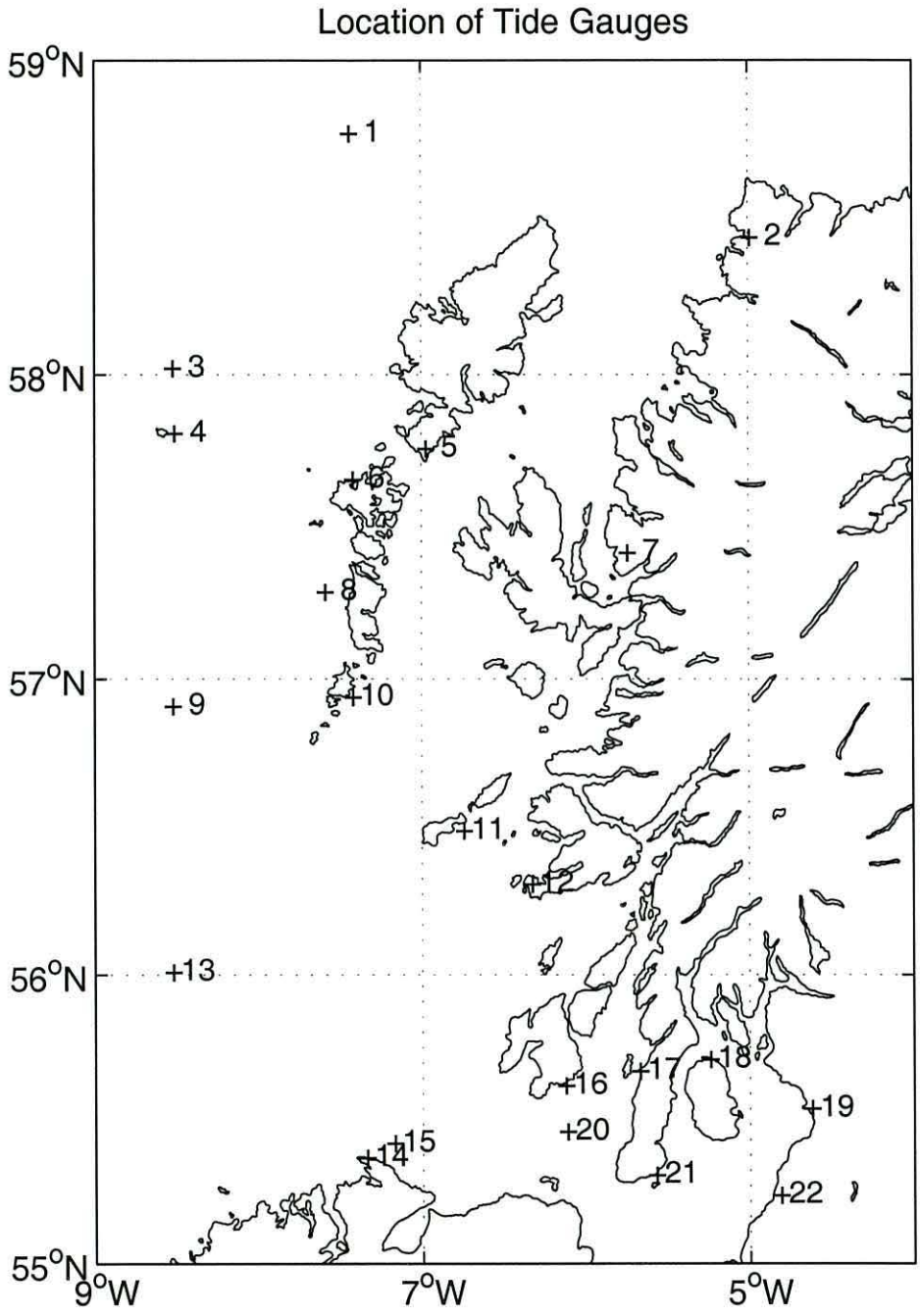

Figure 4.3: Location of the tidal gauges used in the comparison of the tidal constituent M_2.

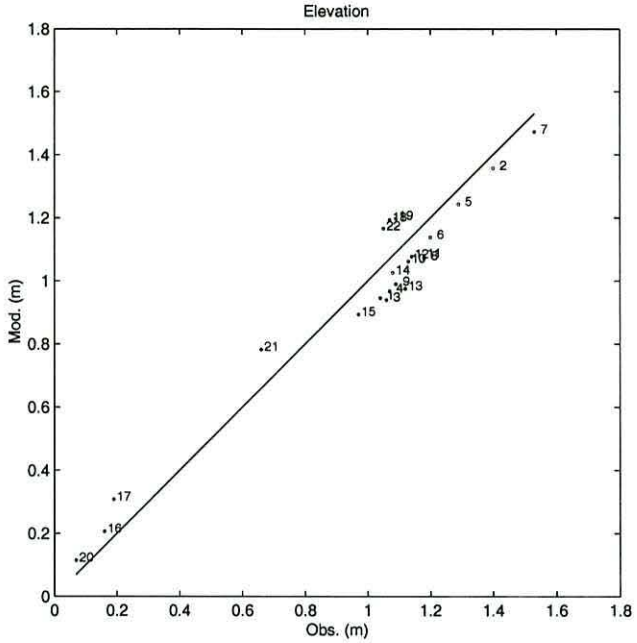

(a)

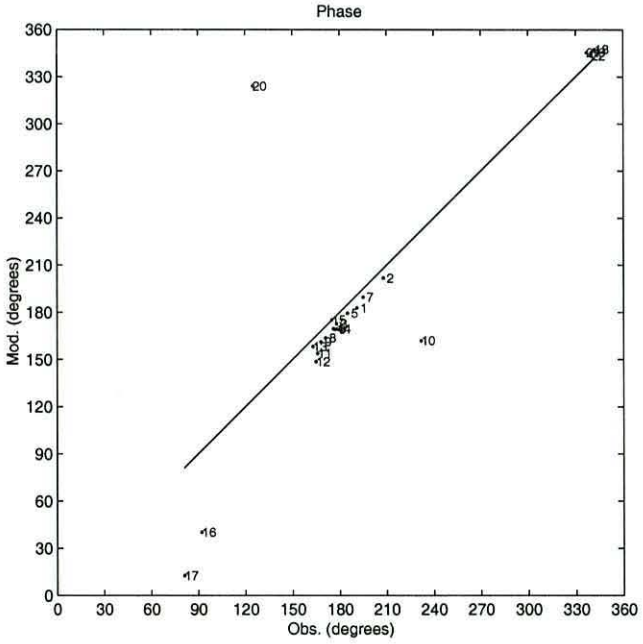

(b)

Figure 4.4: Comparison between observations and computed results for a) elevation (m) and b) phase (degrees)for M_2. Numbers refer to locations shown in Fig. 4.3.

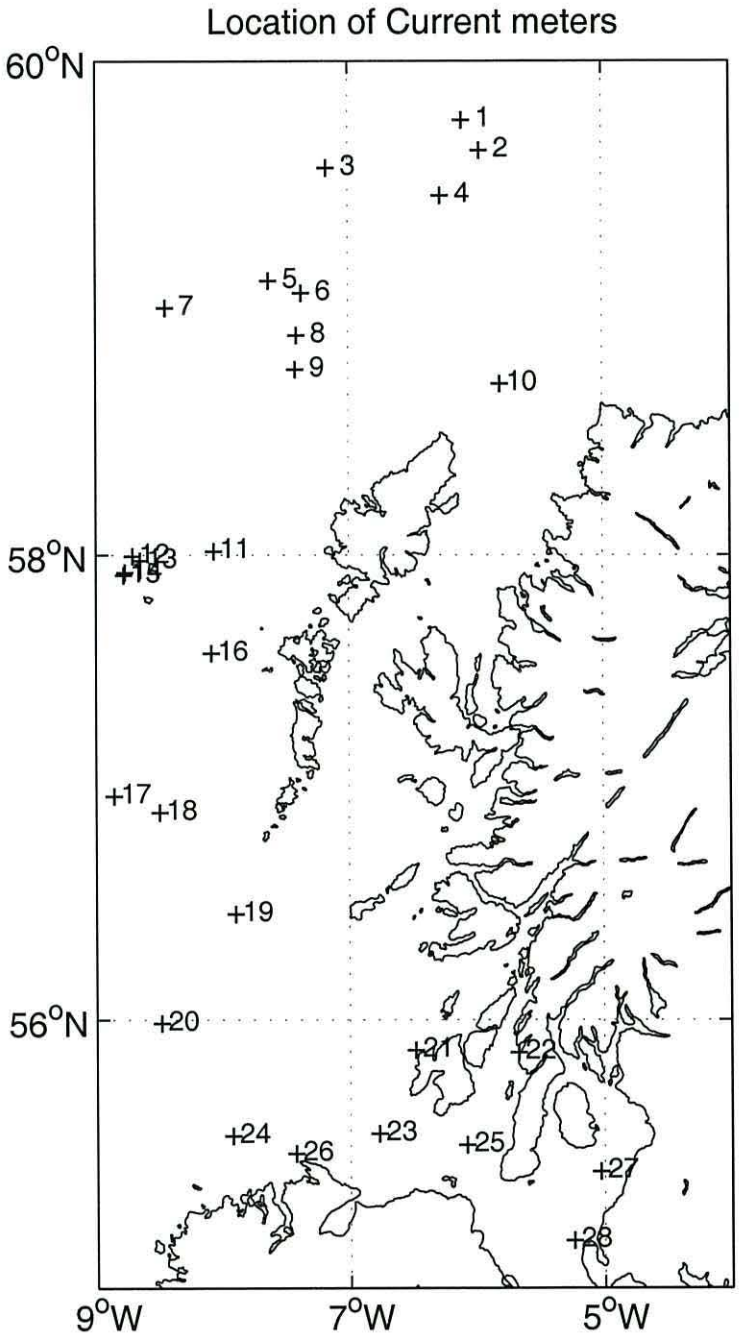

Figure 4.5: Location of the current meters used in the comparison.

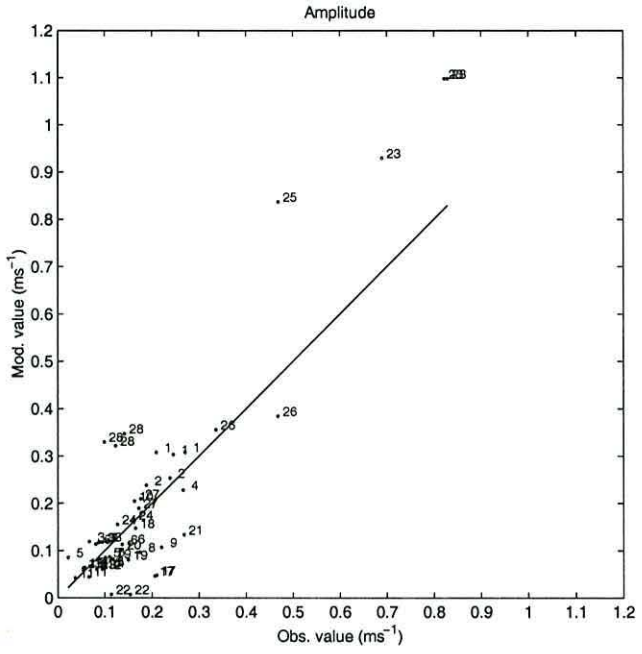

(a)

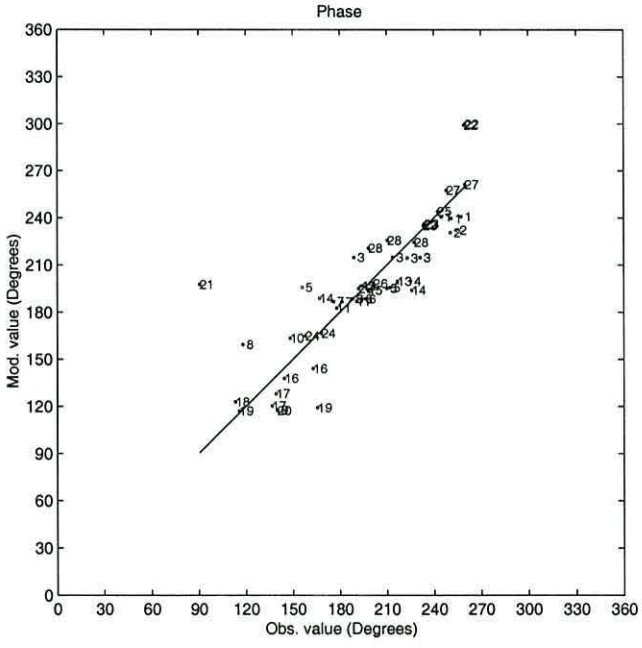

(b)

Figure 4.6: Comparison between observations and computed results for a) amplitude (m s^{-1}) and b) phase (degrees) for the M_2 u component. Numbers refer to locations shown in Fig. 4.5.

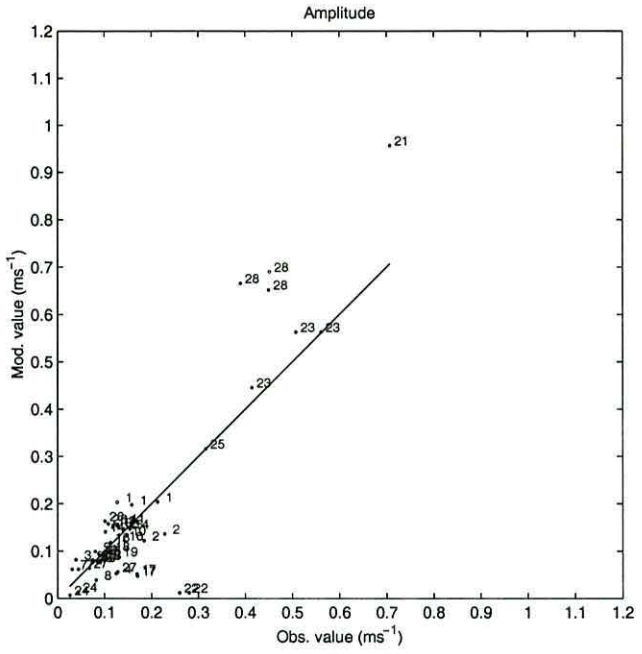

(a)

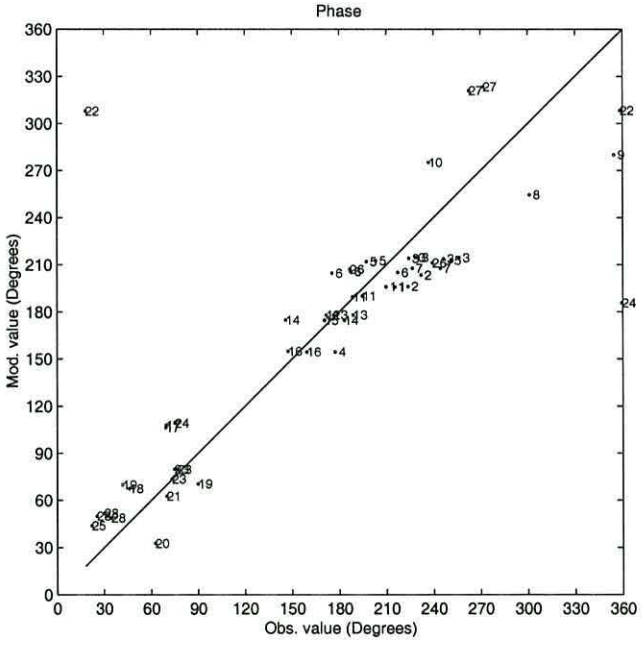

(b)

Figure 4.7: Comparison between observations and computed results for a) amplitude (m s^{-1}) and b) phase (degrees) for the M_2 v component. Numbers refer to locations shown in Fig. 4.5.

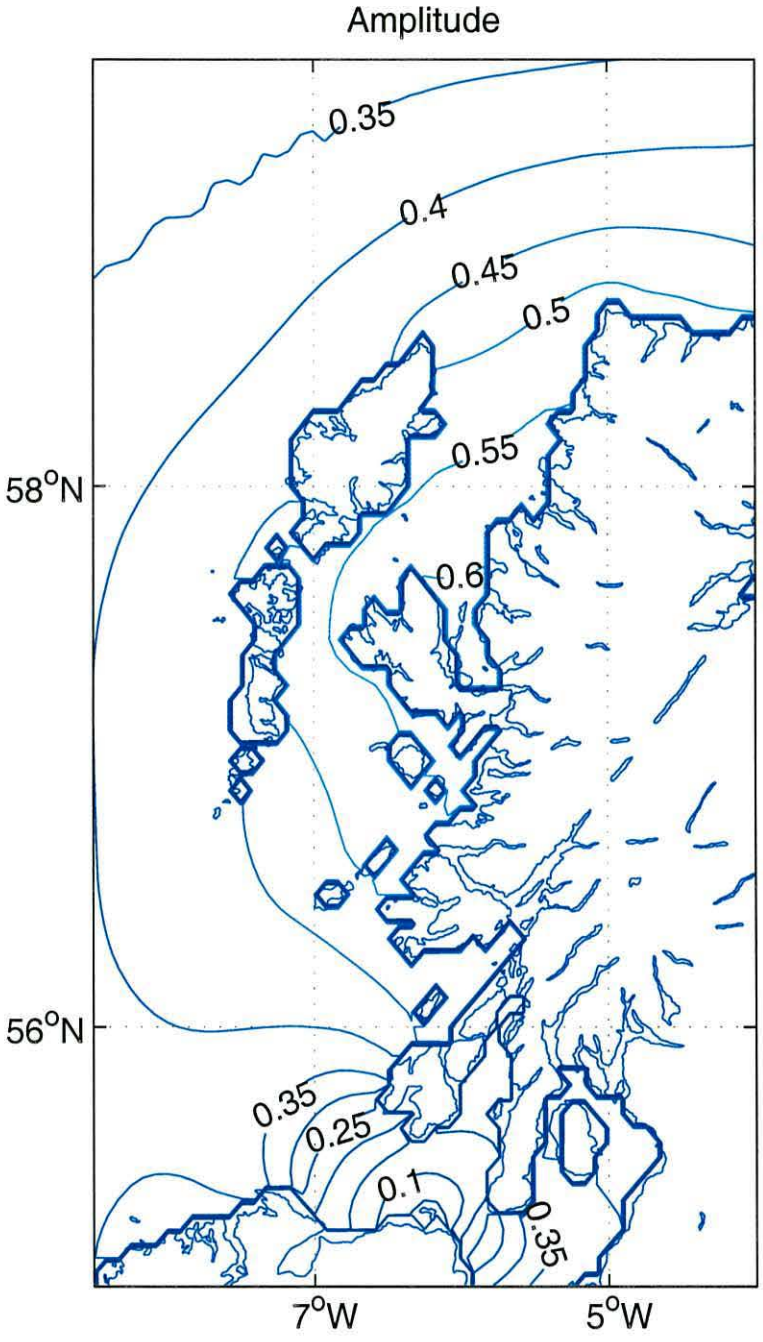

Figure 4.8: Calculated S_2 elevation chart, amplitude in metres. Contours are plotted at 0.05 m intervals.

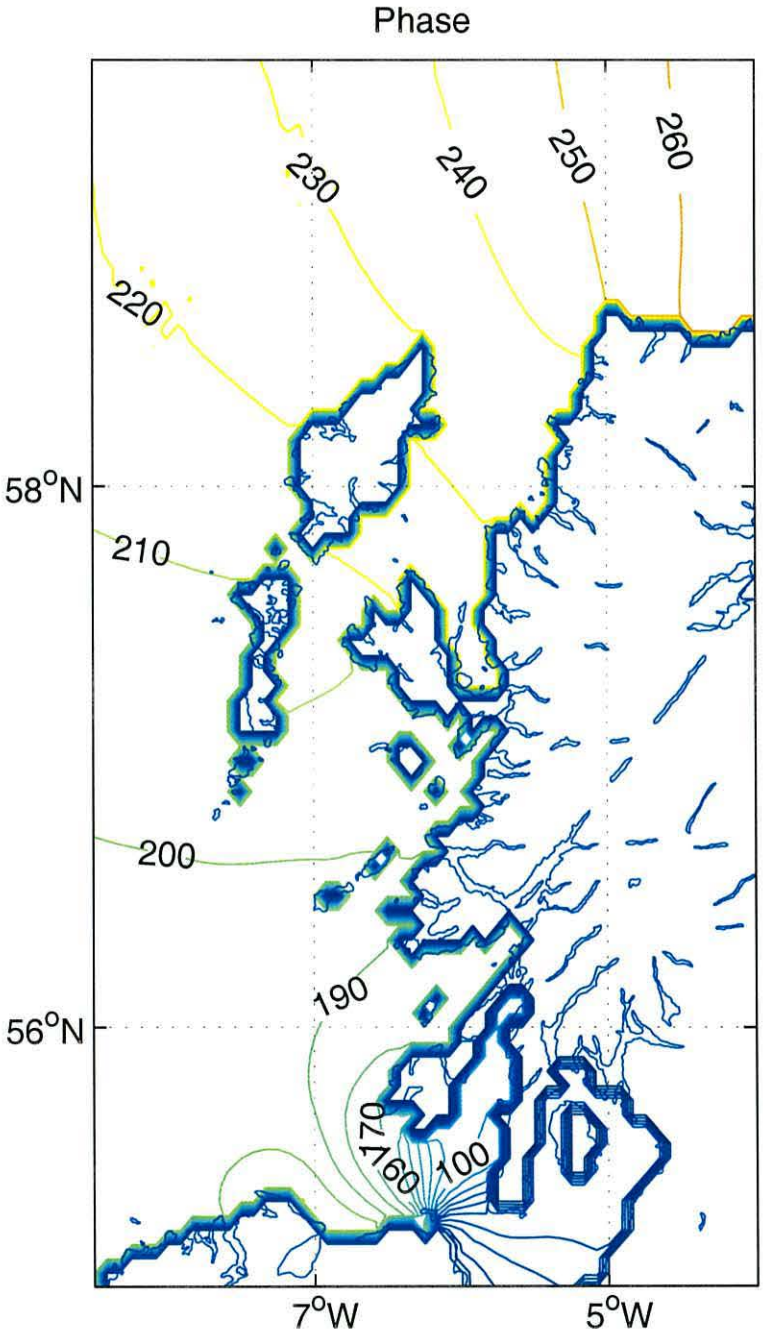

Figure 4.9: Calculated S_2 co-tidal chart, phase in degrees. Contours are plotted at 10° intervals.

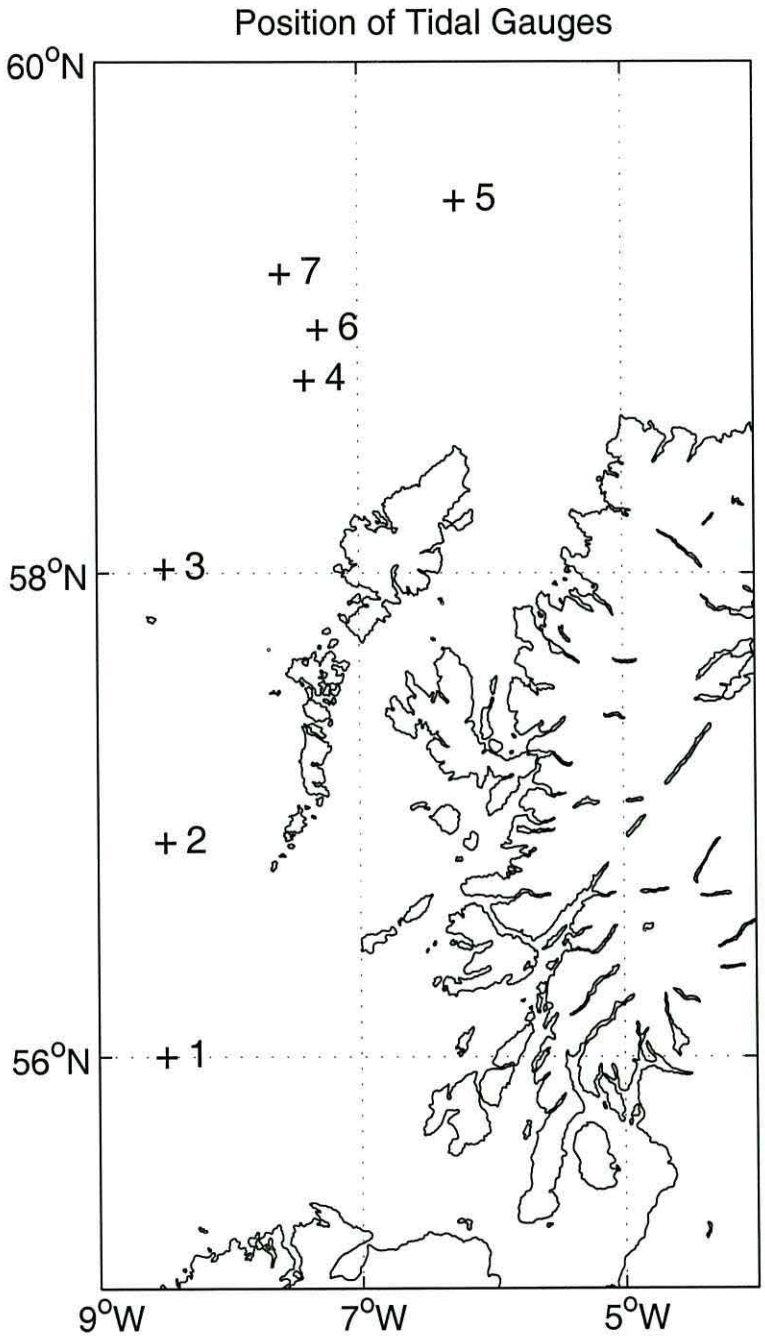

Figure 4.10: Location of the tidal gauges used in the comparison of the tidal constituent S_2.

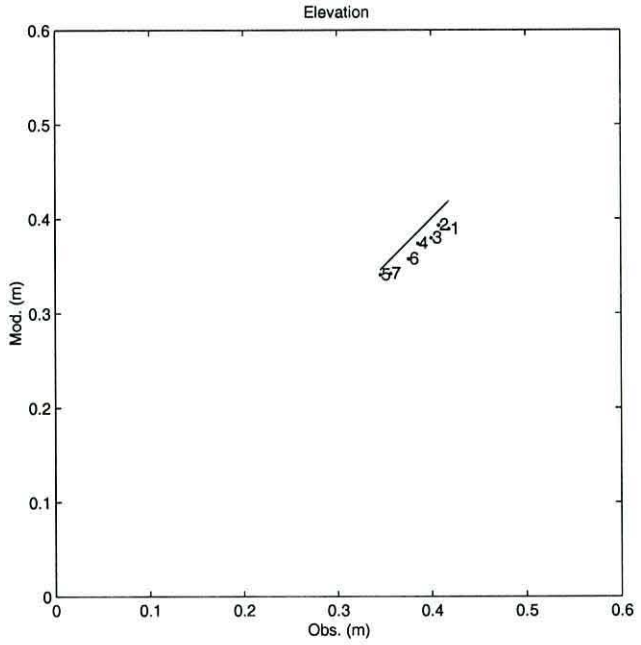

(a)

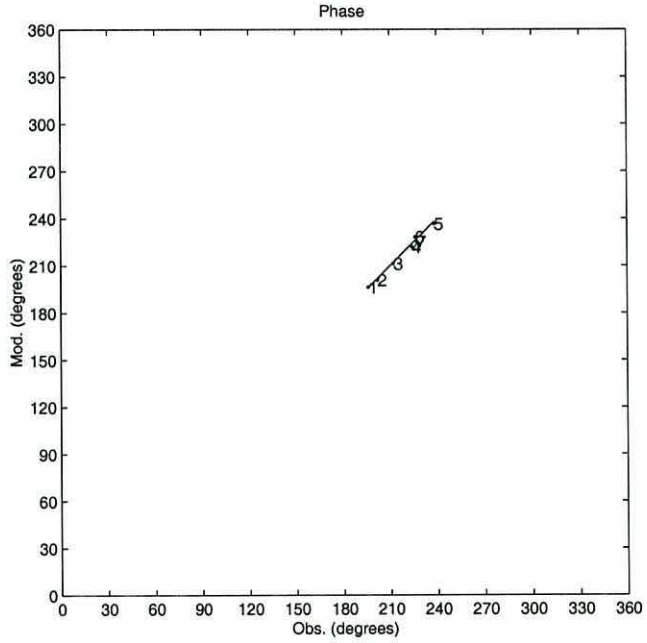

(b)

Figure 4.11: Comparison between observations and computed results for a) elevation (m) and b) phase (degrees). Numbers refer to locations shown in Fig. 4.10.

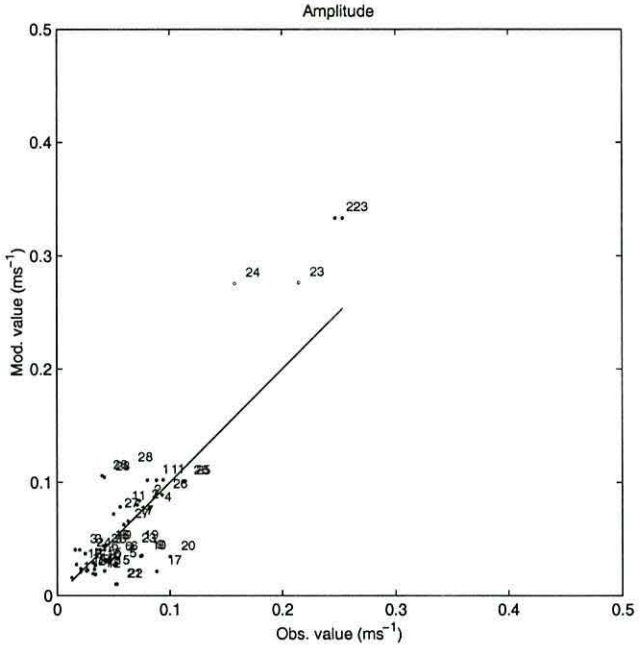

(a)

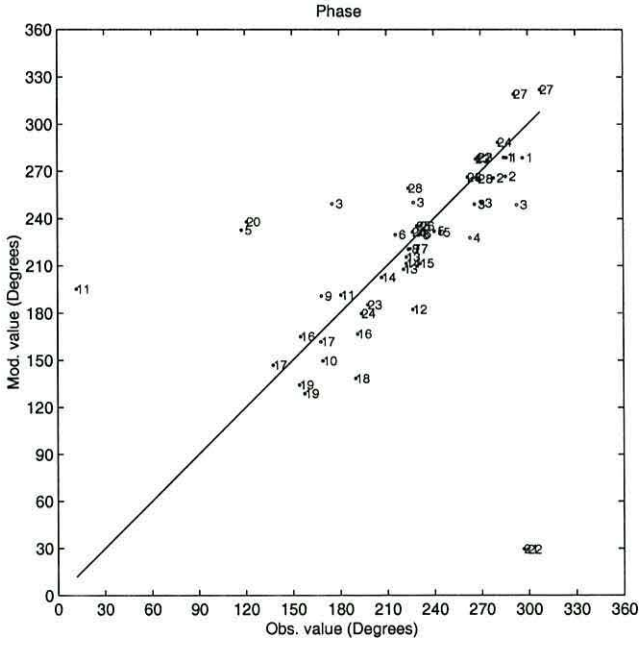

(b)

Figure 4.12: Comparison between observations and computed results for a) amplitude (m s^{-1}) and b) phase (degrees) for the S_2 u component. Numbers refer to locations shown in Fig. 4.10.

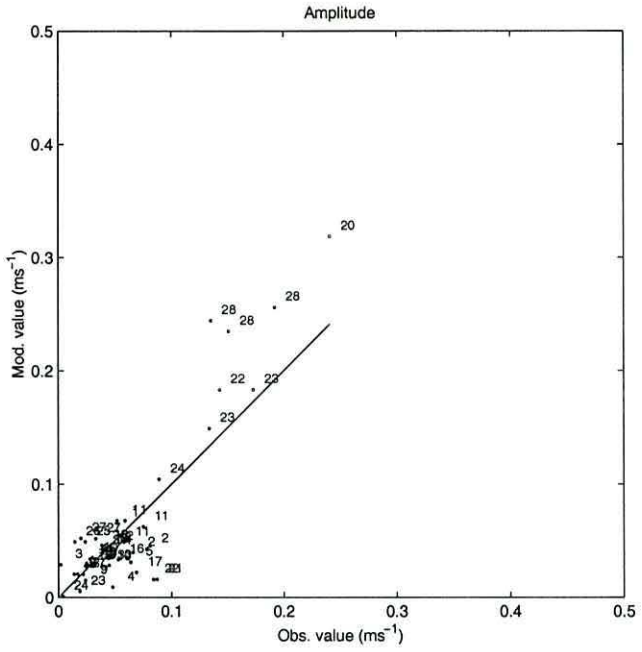

(a)

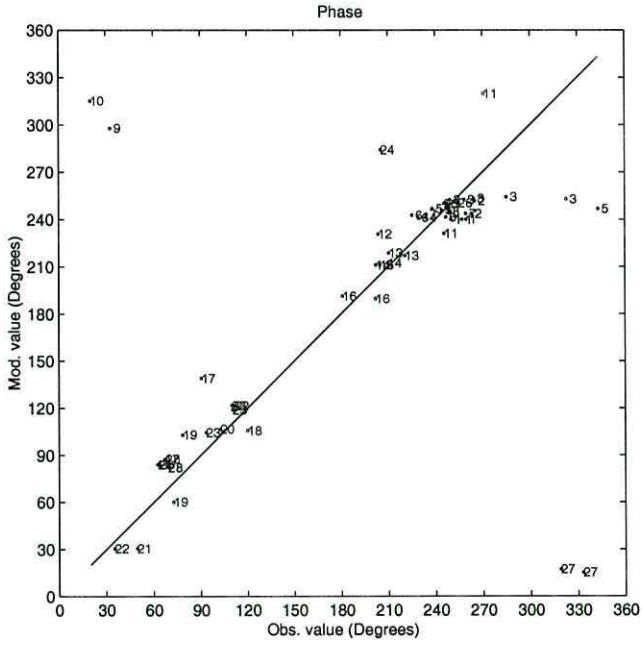

(b)

Figure 4.13: Comparison between observations and computed results for a) amplitude (m s^{-1}) and b) phase (degrees) for the S_2 v component. Numbers refer to locations shown in Fig. 4.10.

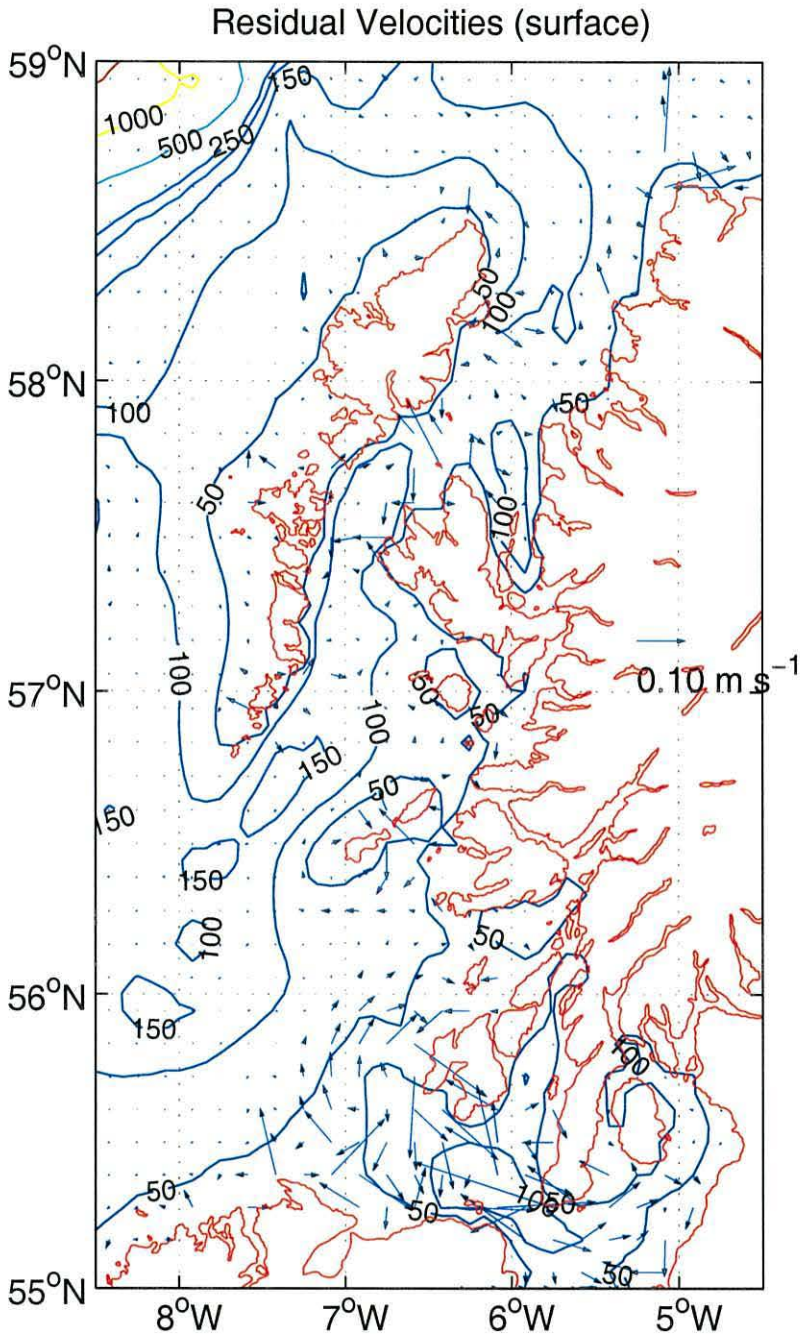

Figure 4.14: Predicted surface tidal residual velocities (every 2 grid points).

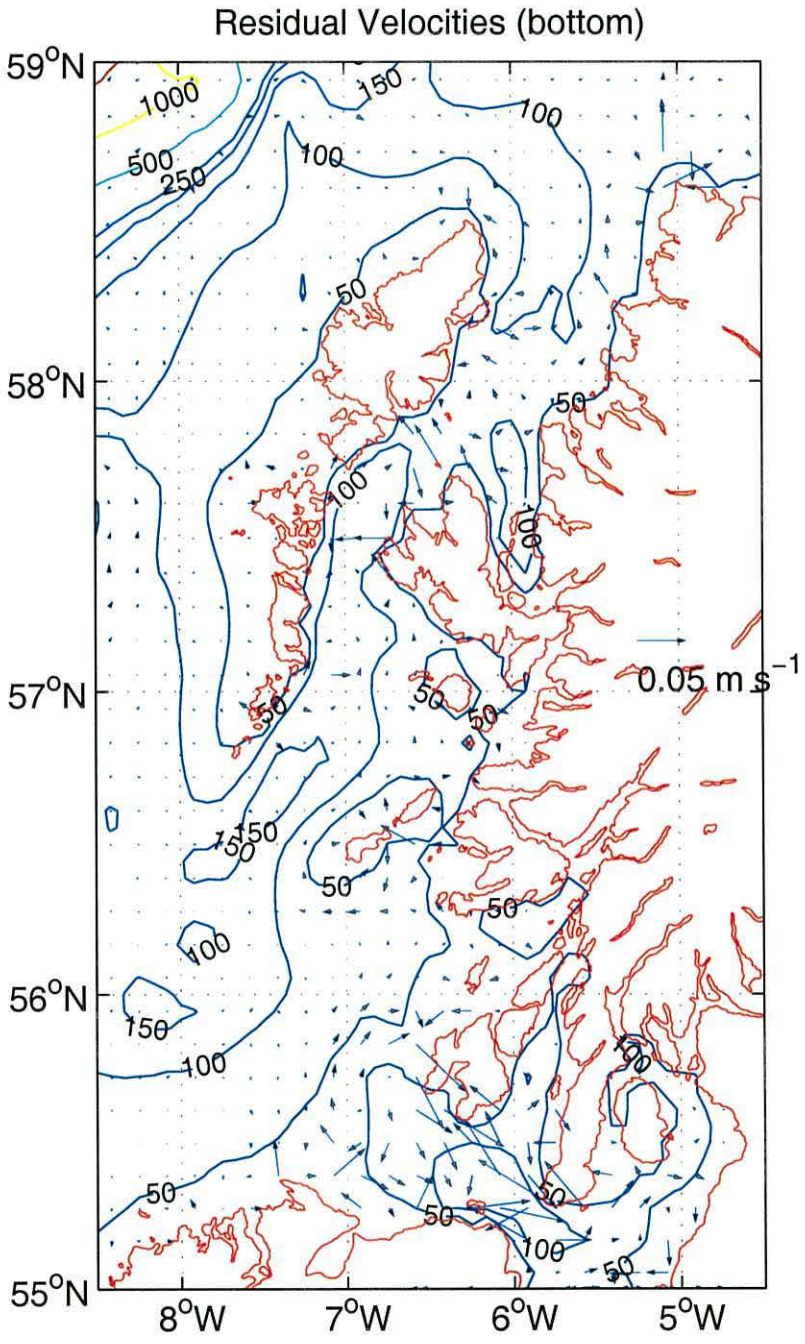

Figure 4.15: Predicted bottom tidal residual velocities (every 2 grid points).

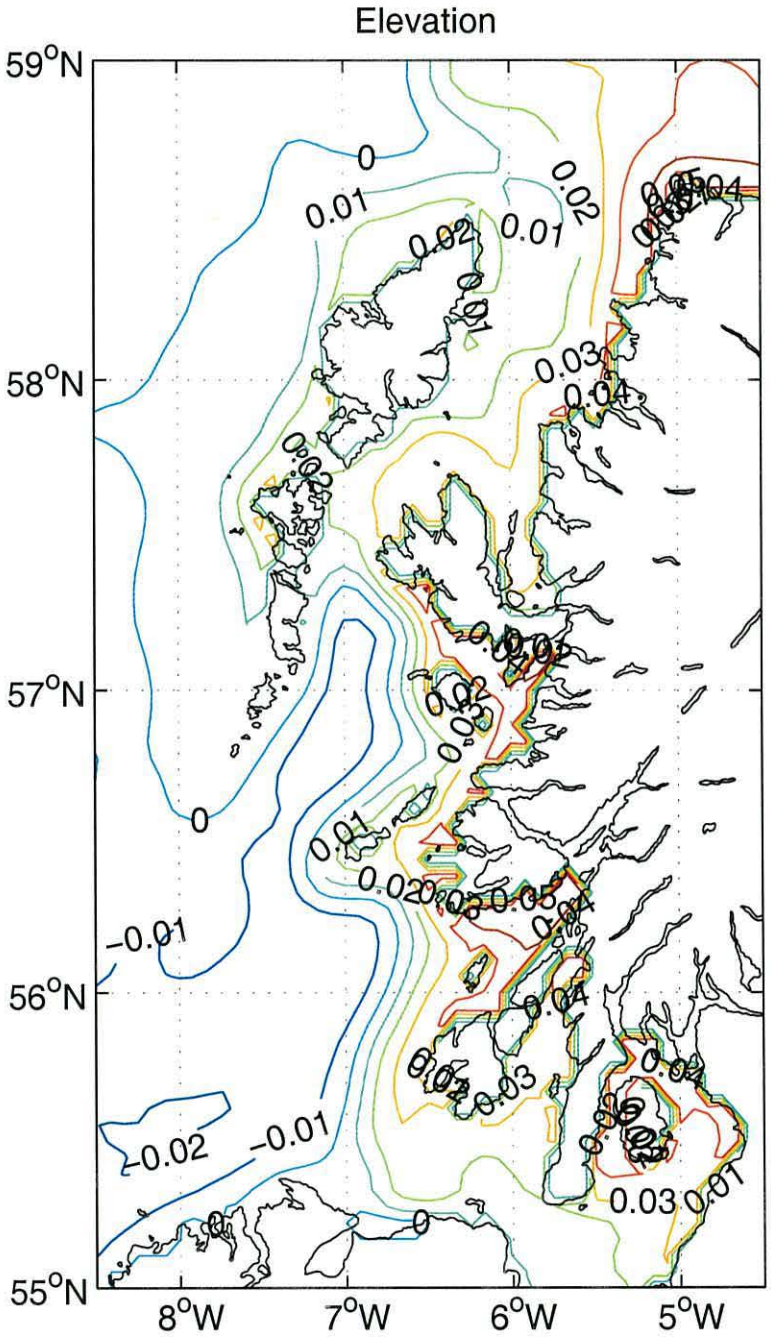

Figure 4.16: Predicted daily averaged elevation for southerly wind forcing of 10 m s^{-1}. Contours are plotted at 1 cm intervals.

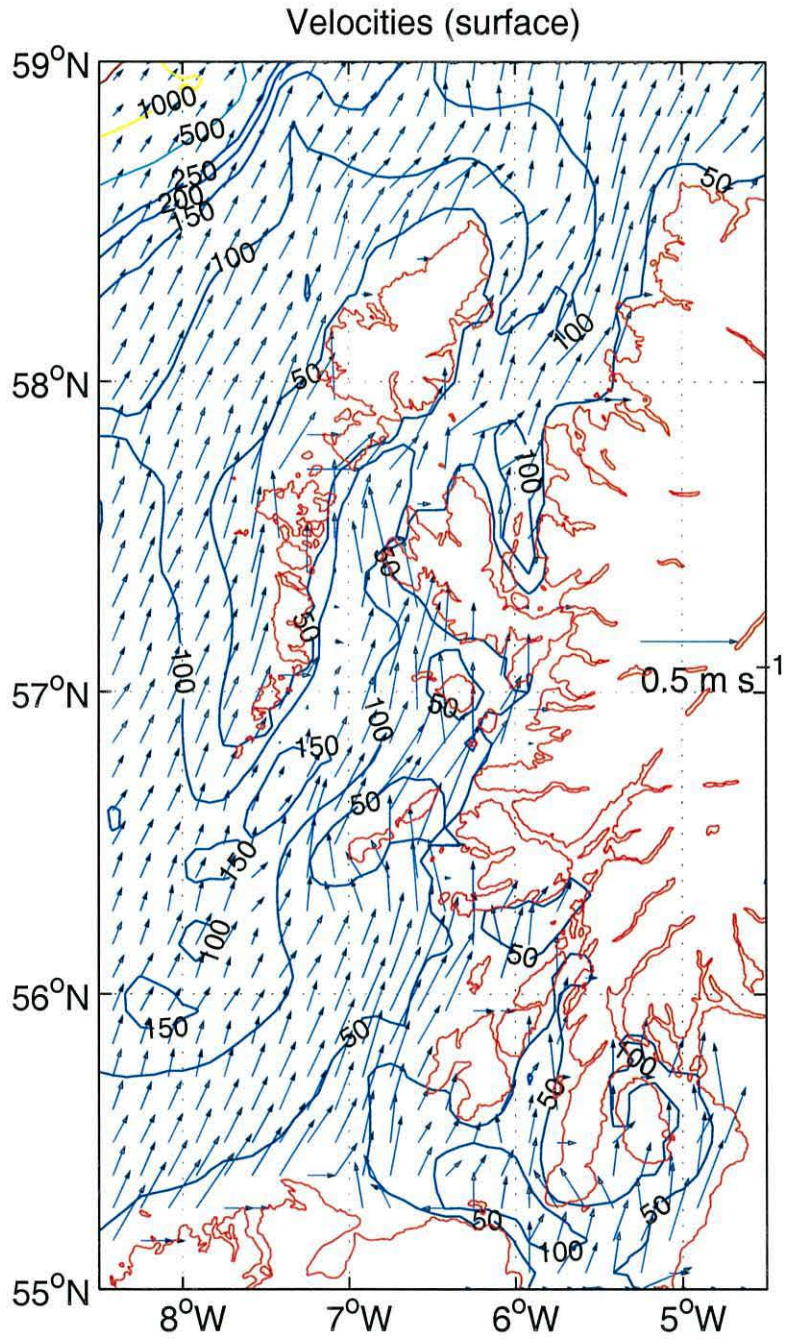

Figure 4.17: Predicted circulation at the surface (every 2 grid points) for southerly wind forcing of 10 m s^{-1}.

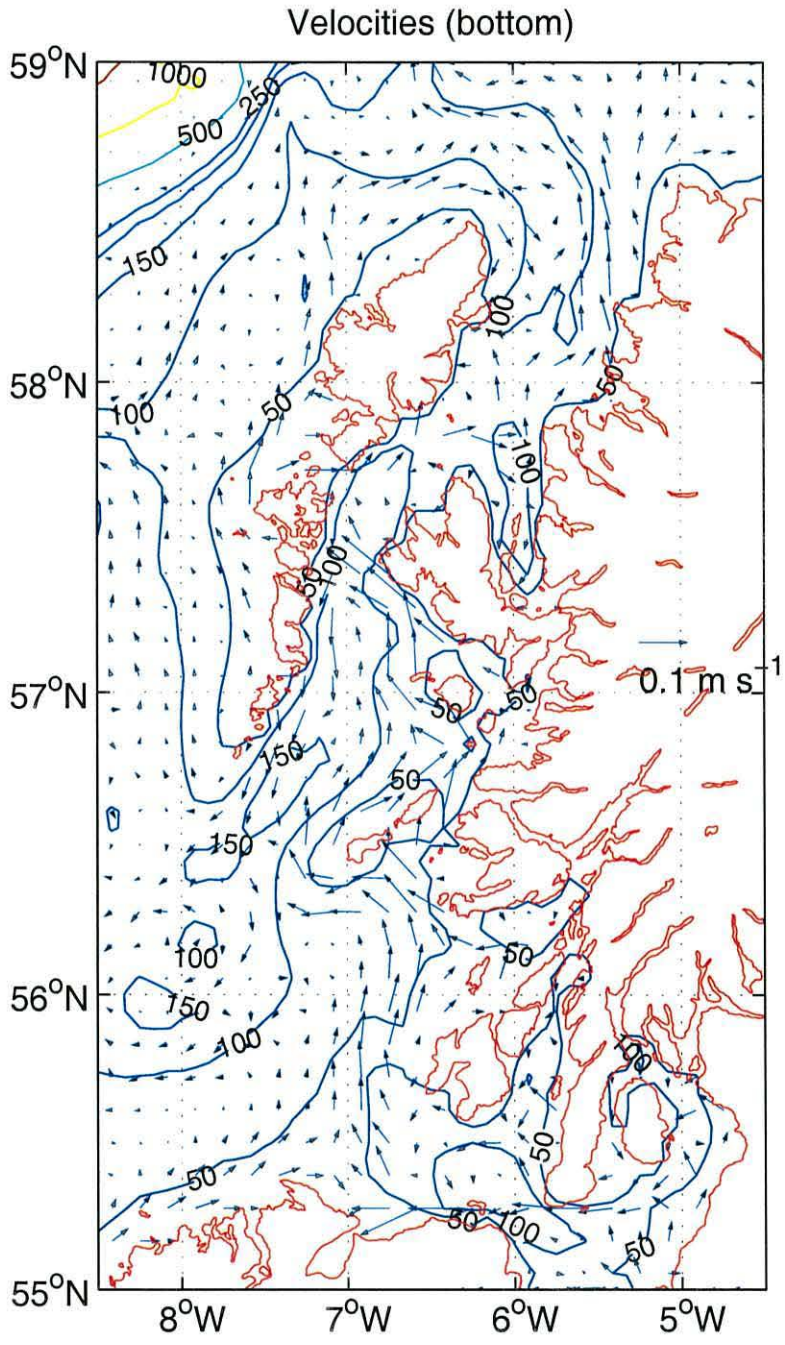

Figure 4.18: Predicted circulation at the bottom (every 2 grid points) for southerly wind forcing of 10 m s^{-1}.

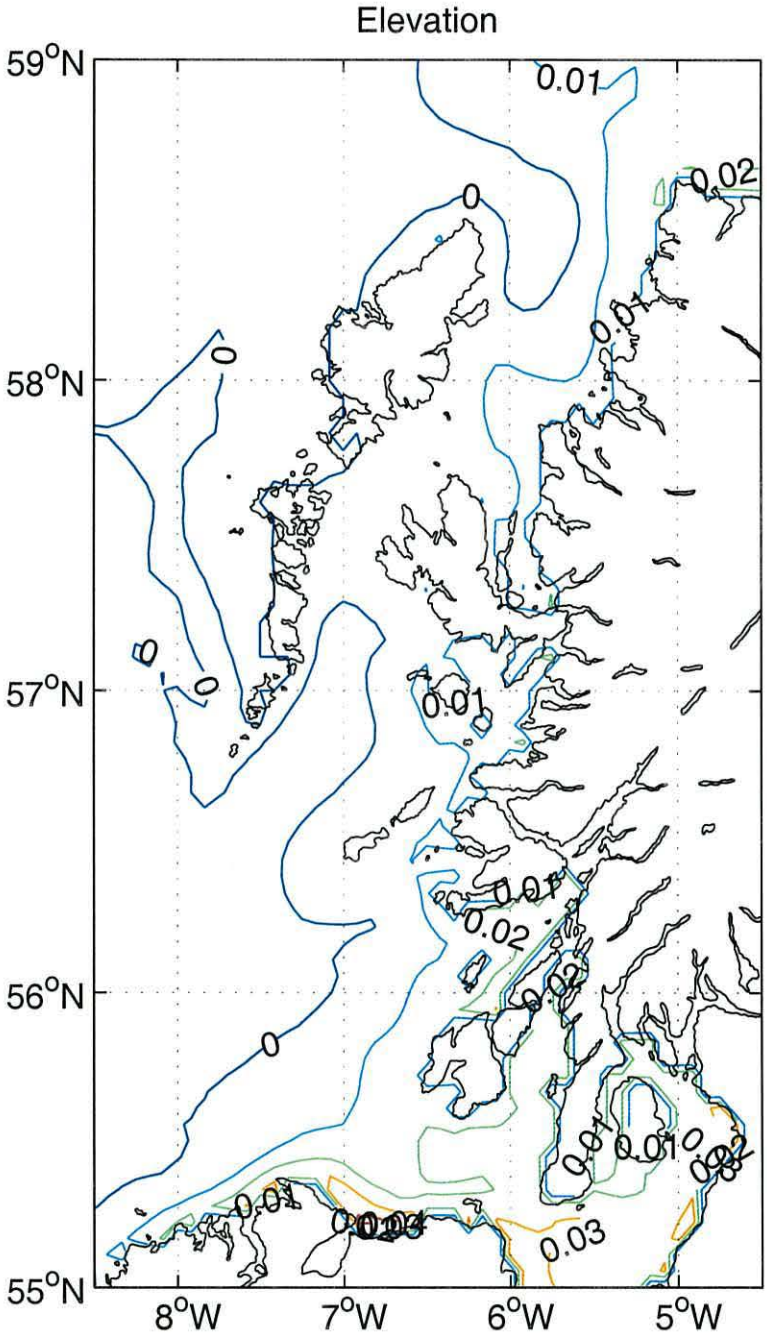

Figure 4.19: Predicted daily averaged elevation for westerly wind forcing of 10 m s^{-1}. Contours are plotted at 1 cm intervals.

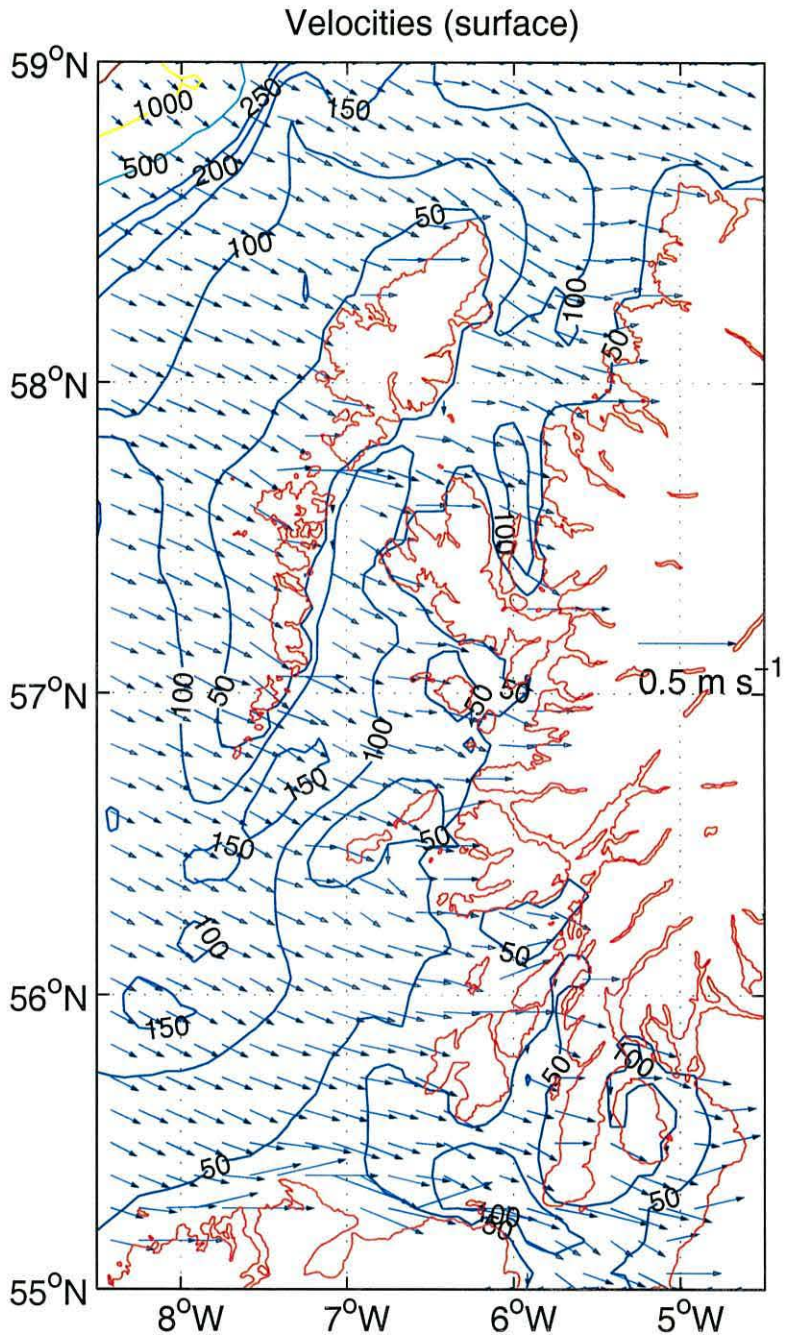

Figure 4.20: Predicted circulation at the surface (every 2 grid points) for westerly wind forcing of 10 m s^{-1}.

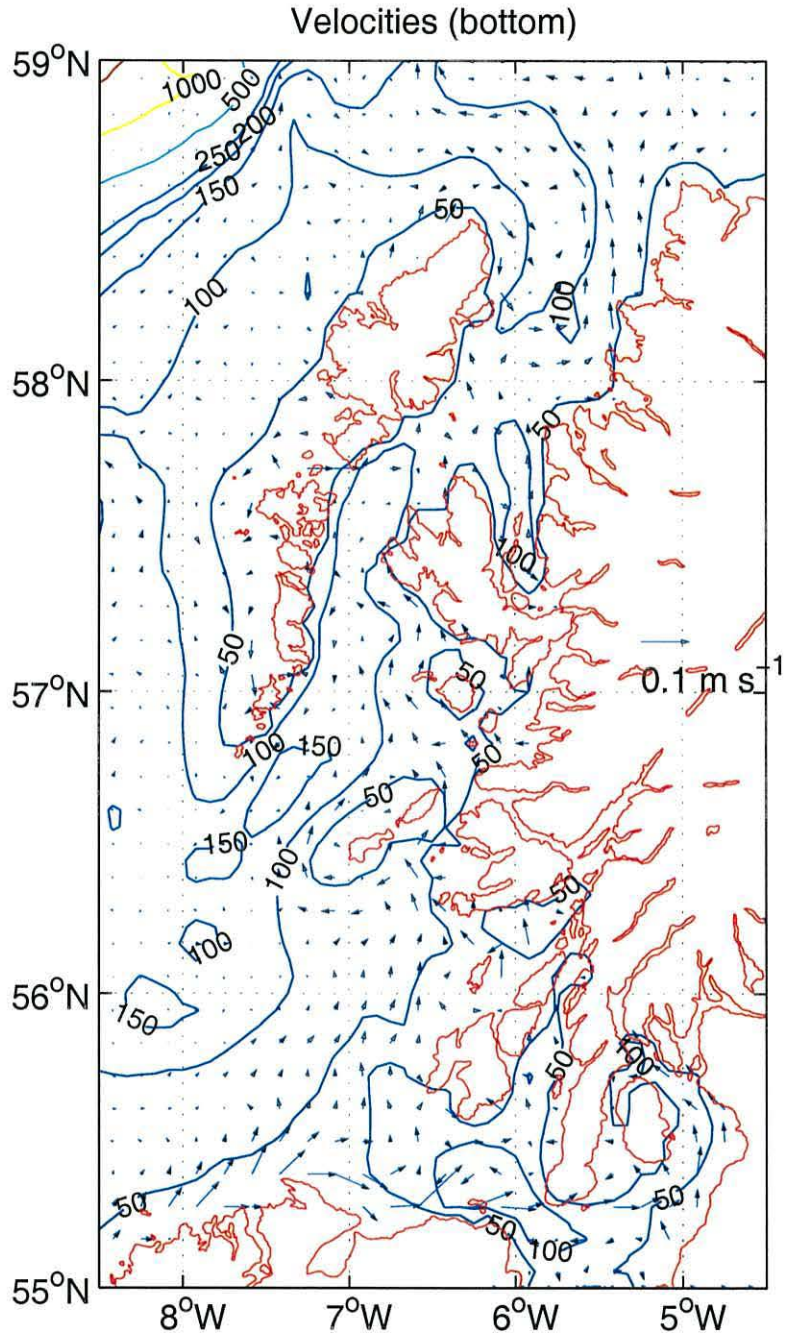

Figure 4.21: Predicted circulation at the bottom (every 2 grid points) for westerly wind forcing of 10 m s^{-1}.

Chapter 5

Seasonal Evolution

5.1 Introduction

The previous chapter demonstrated that residual circulation caused by tides is negligible on the Scottish Shelf (see Figs. 4.14 and 4.15); wind can contribute to the circulation but, to describe the pattern observed in reality, baroclinic effects must be included in the simulations. This chapter will deal with these effects. Results with baroclinic forcing will be presented and, where possible, comparisons with observation will be made to assess the capabilities of the model when climatological forcing and "close to reality" boundary conditions are employed. Predictions from the model will be interpreted with particular attention to seasonal cycles of temperature and salinity. Baroclinic features such as the recirculation at the entrance of the Minch and the tidal front on the Malin shelf region will be investigated in detail in the next chapter.

5.2 Climatological Forcing

For realistic seasonal simulations the model must be forced with conditions which have been derived from observations. For these simulations meteorological forcing was derived from data obtained from the British Atmospheric Data Centre (BADC) and the Scottish Environment Protection Agency (SEPA). The model was set up with data from 1997 so comparison with observations collected by the Marine laboratory was possible.

5.2.1 Wind forcing

The model was forced with hourly wind data (direction and speed) coming from the archive of the BADC for the weather station located at Tiree (see Fig. 5.1) which were taken to be representative of the real wind blowing on the whole domain of simulation. These velocities were transformed to surface stresses using the formula already discussed previously (see (4.1)) with the coefficient C_d a function of the wind speed U following

$$C_d = \begin{cases} 1.4 \times 10^{-3} & 0 \leq U < 10 \text{ m s}^{-1} \\ (0.49 + 0.065U) \times 10^{-3} & 10 \leq U < 26 \text{ m s}^{-1} \end{cases} \tag{5.1}$$

Since this is a station located on land (see Fig. 5.1) the wind was multiplied by a factor of 1.3 to take into account the reduced friction due to the sea surface (Galperin and Mellor, 1990a). Fig. 5.2 shows the wind vectors averaged every 24 hours; Figs. 5.3a,b illustrate the distributions of direction and speed for the wind at this weather station. The wind did not have a preferential direction throughout all the year, most of the time it blew from the 2 southern quadrants with exceptions in May (where there was no precise direction) and in June where there was a strong tendency for northerlies. Speed followed a seasonal pattern with strong winds in winter (February) and a decrease in intensity in summer, to increase again during Autumn. The area is generally windy with up to 50 days of gales per year with a mean of 10-15 knots (5-7 m s^{-1}) (Green and Harding, 1983)

5.2.2 Solar heating

Hourly solar heating flux from Stornoway Airport weather station (see Fig. 5.1) supplied the heat forcing for the model. These data were implemented in the model following the previous discussion (§ 3.3.2), the input Q_s was measured directly at the weather station (see Fig. 5.4) whilst the other quantity Q_{wc} was derived from equations (3.73)-(3.76). As in the case of wind, this solar flux was thought to be representative for all the domain of simulation (in doing so variations of solar heating with latitude were ignored). Tiree weather station also supplied the air temperature (see Fig. 5.5) needed in the calculation of latent and sensible heat

fluxes. In this set of calculations the short wave radiation was applied at the sea surface and exponential absorbtion was allowed in the first several metres of the water column with a coefficient of extinction of 0.042 m^{-1}, following the classification of Jerlov (1976). Other data required for these simulations were the cloud cover and the relative humidity; in both cases assumptions were made because of the lack of reliable observations. The cloud cover was set to a constant 50% whilst the relative humidity was set to 80%, close to the annual mean value of 86% measured at Tiree (Green and Harding, 1983).

5.2.3 Fresh water input

Fresh water runoff is very important in the dynamics of this area. It supplies buoyancy to the Scottish coastal current system and its value has been already shown to be correlated to the strength of the current (Simpson and Hill, 1986). Fig. 5.6 shows the annual runoff for the 3 sources of fresh water considered in this simulation - the river Clyde, the river Lochy and the river Carron (observations obtained from SEPA gauges). The first source is located in the Firth of Clyde (see Fig. 5.7) and, to take into account all the other sources in the area, its discharge has been multiplied for 2.17 since it contributes for the 46% of the total discharge into the Clyde Sea (Poodle, 1986). The other two are located along the Scottish coast. The river Lochy flows into Loch Linnhe and the river Carron flows into Loch Carron, close to the Isle of Skye (see Fig. 5.7). The distribution of the runoff was strongly seasonal with maxima in winter and negligible inflow during the summer months. These daily averaged observations were interpolated so that the inflow was modelled through the continuity equation (§ 3.3.2) at hourly intervals for consistency with other forcing.

5.3 Lateral boundary conditions

Boundary conditions for temperature and salinity were prescribed at 3 of the 4 open boundaries of the domain of simulation, leaving the fourth boundary to adjust. This solution was implemented for lack of observations along the open eastern boundary. The Levitus archive (Levitus, 1982) supplied the data for both salinity and temperature for the northern and western boundaries. These averaged observations were

available with a resolution of $1° \times 1°$ so that they had to be interpolated on the model's grid. Fig. 5.8 and Fig. 5.9 illustrate the annual development of salinity at the two boundaries. The western boundary shows the direct influence of the Atlantic ocean with the saltier water. The same pattern can be seen in the temperature field, Fig. 5.10 and Fig. 5.11 show the seasonal changes in temperature for the northern and western boundary respectively;. The Atlantic Ocean shows its effects on the warmer western side and the development of the seasonal thermocline can be followed, with peaks in the period between August and September. The southern boundary was treated in a different way. Boundary forcing for salinity and temperature for the St. George's Channel was obtained from another model (Horsburgh, 1999) and was consistent with observations in the area; the water was approximated as well mixed throughout the year with constant salinity (S=34) and temperature shown in Fig. 5.12 which follows the seasonal pattern, with a maximum in the same period (August-September).

On the western boundary the momentum contribution of the Scottish continental slope current was neglected because of lack of observations. This current has been studied and observed (see for example Booth and Ellett, 1983; Huthnance, 1986) but a complete seasonal picture is lacking; its major feature is persistent northward flow of the order 0.1 m s^{-1} along the continental slope, associated with a core of warm light water (Booth and Ellett, 1983). Dickson *et al.* (1986) hinted at a seasonal variation of this current with a peak reached in November, which coincided with its spilling onto the Shelf. Model studies (Xing and Davies, 2001) showed that the shelf edge flow can influence the dynamics of the shelf; Xing and Davies (2001) also demonstrated how Atlantic water can intrude into the Irish Sea as an effect of the presence of the slope current. Since data are sparse, and it was not possible to obtain a reliable source of forcing for the slope current, the overall phenomenon was not included and the continental slope was treated as a perfect insulator, inhibiting ocean-shelf exchanges.

5.4 Initial Conditions

A late winter condition was chosen as the initial condition. In this way it was possible to specify a homogenous vertical profile for salinity and temperature fields.

Observations of temperature in the Scottish area (see for example Craig, 1959; Ellett, 1979; Ellett and Edwards, 1983) and observations and model simulations on the whole European shelf (Elliott *et al.*, 1991; Elliott and Clarke, 1991) corroborates this assumption: the water column reaches an homogenous thermal state in February-March. On the other hand salinity is influenced by the Atlantic inflow on the Western side of the European continental shelf and northern side of the North sea and from fresher inflow in its Southern part (the river Rhine in the German Bight and the Norwegian Coastal Current in its eastern side) so that the vertical profile is not so robust an assumption.

Fig. 5.13 and Fig. 5.14 show the initial conditions for temperature and salinity used in these seasonal simulations. The initial time of simulation was chosen to be the 1st of February 1997. These two fields were built with observations coming from two sources; Ellett and Edwards (1983) supplied data for the Scottish shelf whilst data for the Irish Sea were gathered from Bowden (1980). Using the Matlab package they were interpolated and smoothed on the model's grid. Initial conditions were therefore consistent with observations, temperatures on the inner shelf were mostly of the order $6° - 7°$C with minima of $4°$ on the shallowest part of the eastern Irish Sea. The distribution followed the bathymetry with cold water associated with shallow topography as in the central Minch, close to the coast of the Outer Hebrides. The mitigating effect of the Atlantic water can be seen in the western part of the domain where temperature in winter reaches 9°C (see for example Ellett and Edwards, 1983). The Atlantic effect was also present in the distribution of salinity; in this case the difference is more marked and horizontal gradients are sharper. The coastal water was fresher, due to river inflows, with salinity ranging from 34 to 34.8 whilst Atlantic water shows salinity greater than 35. Figs. 5.14a,b clearly illustrate this with a sharp front running along $7°$ W.

The reason for choosing a winter initial condition was two-fold. Firstly to demonstrate that the model was capable of reproducing the seasonal development of the temperature field, because of its importance in the dynamics of the shelf (i.e. the model had to reproduce the heating due to the incoming solar radiation). Secondarily because these particular initial conditions were easy to implement in the model, especially when observational data were lacking as here. However, some inconsistencies were created with this arrangement; in the oceanic part of the domain close to the continental shelf break the bottom water was unrealistically warm and salty

(see the Levitus data in Figs. 5.8 and 5.11). The solution to this problem was left to the diffusivity present in the model. Since the model was forced with "realistic" boundary conditions it was assumed the the numerical and prescribed diffusion would restore these initial condition to conditions that are internally consistent. Fig. 5.15 shows that this assumption was correct; it shows the bottom temperature and salinity after 5 and 30 days of simulation and it is possible to see the the deep water is going toward the correct values for these quantities. After 5 days both salinity and temperature decreased toward the forcing values. Furthermore the model was still in its dynamical adjustment being in the phase of "spinning up", and the area in which this effect took place was far from the area of interest. The continental slope acts as an insulator for any signals travelling inshore (see previous discussion and Hill, 1995). All these factors contributed in accepting the homogenous conditions since adjustment is rapid and has no effect on the area of interest.

5.5 Evolution of scalar fields

The next two sections will present the seasonal evolution of the thermal and haline fields with the boundary and initials conditions previously discussed. In the second chapter regional observations were described with particular attention to the data collected by the Marine Laboratory, Aberdeen; this set of data will be used for comparison since it is one of the more complete. The data collected in spring 1997 (*Spring*, cruise CU199706, see Table 2.1) allows a direct comparison with the output of the model. The other observations (*Summer*, *Autumn* and *Winter*) will be used for a qualitative comparison allowing for interannual variability. In addition to regional fields of salinity and temperature (daily averages will be shown to smooth diurnal changes in these quantities), some points were chosen where these scalar values have been extracted every hour for the entire length of the simulation (together with velocity which will be analysed in the next chapter). Figs. 5.16a,b and Table 5.1 show the position of these points on the Scottish shelf.

There are three subsets of points: the first set have been situated to follow in detail the development of the Islay front (points A and B) and the recirculation in the Sea of the Hebrides (point C to F). The other subset (points Y, HS1 and M2) have been located in the same position as the current meters used in the work of Hill

and Simpson (1988). Finally the third set (Fig. 5.16b) represents the location of 10 current meters deployed by the Marine Laboratory, Aberdeen in Spring-Summer 1997 which will supply observations of currents for the next chapter. In these positions temperature and salinity (only for some locations) were collected during the deployment and these data will be compared with the model results at the closest grid point to such locations.

N.	Position	Lat.	Lon.	Period deployment	Depth (m)
1	A	55° 59.9′ N	7° 10.0′ W	01/2/1997 - 01/2/1998	79.0
2	B	55° 43.2′ N	6° 50.0′ W	01/2/1997 - 01/2/1998	46.8
3	C	57° 13.2′ N	7° 35.0′ W	01/2/1997 - 01/2/1998	44.3
4	D	57° 13.2′ N	7° 0.0′ W	01/2/1997 - 01/2/1998	128.0
5	E	56° 49.9′ N	7° 25.0′ W	01/2/1997 - 01/2/1998	123.7
6	F	57° 49.9′ N	6° 20.0′ W	01/2/1997 - 01/2/1998	64.8
7	G	58° 29.9′ N	5° 45.0′ W	01/2/1997 - 01/2/1998	106.4
8	M2	56° 9.9′ N	6° 55.0′ W	01/2/1997 - 01/2/1998	69.7
9	HS1	57° 26.5′ N	7° 0.0′ W	01/2/1997 - 01/2/1998	102.0
10	Y	56° 39.9′ N	6° 20.0′ W	01/2/1997 - 01/2/1998	50.0
11	5571	56° 40.36′ N	6° 40.13′ W	16/4/1997 - 7/6/1997	76 (28)
12	5581	56° 49.41′ N	7° 4.98′ W	16/4/1997 - 2/6/1997	143 (35)
13	5582	56° 49.41′ N	7° 4.98′ W	16/4/1997 - 9/6/1997	143 (130)
14	5602	57° 27.63′ N	7° 3.10′ W	18/4/1997 - 16/7/1997	108 (96)
15	5611	58° 26.34′ N	6° 3.05′ W	19/4/1997 - 23/6/1997	89 (34)
16	5612	58° 26.34′ N	6° 3.05′ W	19/4/1997 - 1/5/1997	89 (77)
17	5621	58° 27.09′ N	5° 39.27′ W	19/4/1997 - 15/7/1997	118 (44)
18	5622	58° 27.09′ N	5° 39.27′ W	19/4/1997 - 15/6/1997	118 (116)
19	5631	58° 27.41′ N	5° 15.18′ W	20/4/1997 - 7/6/1997	81 (34)
20	5632	58° 27.41′ N	5° 15.18′ W	20/4/1997 - 15/7/1997	81 (69)

Table 5.1: Coordinates of points shown in Fig. 5.16a,b. The two last columns indicate the period of deployment and the water depth in metres with the depth of the current meter in brackets.

5.5.1 Temperature

The time for the start of the seasonal simulation was set to the 1st February at 00.00 with homogeneous vertical conditions; only horizontal gradients were present,

especially in the area of the Malin shelf. The seasonal evolution can be seen in Figs. 5.17a-j, which illustrate the development of the thermal field (hourly temperature) for the locations in Table 5.1. Surface temperature followed almost the same pattern at all locations: from minima of about 8°C in February, it slowly increased with the incoming solar radiation reaching maxima of $14° - 15°C$ with extreme peaks of $16° - 18°C$ in late August - early September depending on the location, as expected in this part of the European shelf (Elliott *et al.*, 1991). The development of temperature in the Minch can be seen by looking at the behaviour of points E, D, F ,G and HS1. All locations were relatively deep (see Table 5.1) and tidal currents are not strong enough to keep the water completely mixed throughout the year, so the water column becomes stratified in summer. This is clearly visible in Figs. 5.17e-g and Fig. 5.17i; Point E (the deepest) is the best example whilst at point F (the shallowest) the stratification was not so marked as in the other cases. Model results agreed with observations; temperatures in July are around 12°-13°C (for example Ellett, 1979; McKay *et al.*, 1986), reaching their maxima in August until the breakdown of stratification in Autumn (September-October) as observed by Craig (1959). The surface temperature did not have a constant trend with a steady increase from February to August, but reflected the behaviour of the air temperature and incoming solar radiation. A sudden increase is noticeable with a peak in June, detectable in every location but location B.

The increase of bottom temperatures in all location was similar to the surface but was more gradual. The direct effect of solar heating was not as strongly marked and the rise was smoother. The model was also able to reproduce the correct stratification at locations A and B. These were chosen so that one was situated in relatively deep water and outside the estimated position of the tidal mixing front (station A) whilst the other was inside the front, where the water is always thermally homogeneous due to strong tidal currents (station B). Figs. 5.17a and 5.17b illustrate this fact. Temperatures on both sides of the fronts agreed well with observations (Simpson *et al.*, 1978). The development of the thermal front, together with its haline structure, will be investigated in the next chapter.

For a quantitative assessment modelled temperatures were compared against the observations discussed in the second chapter. Table 5.2 shows the time when temperature and salinity were extracted from the model to be compared with these data. For simplicity, a single 24h mean set of values was extracted from the sim-

ulation in the middle of each cruise period. The model was run for 1997 in order to concentrate on comparison with CU199706. Comparison with the other seasonal observations therefore assume an interannual consistency.

Cruise	Denom.	Duration	Model time
CU199706	*Spring*	6/4/97 - 20/4/97	11/4/97 (70)
CU199610	*Summer*	6/7/96 - 12/7/96	10/7/97 (160)
CU199815	*Autumn*	5/9/98 - 19/9/98	13/9/97 (225)
CU199689	*Winter*	19/11/96 - 15/12/96	7/12/97 (310)

Table 5.2: Duration of cruises and day of simulation used for the comparison with observations. In the last column the number in brackets indicates the number of day elapsed from the start of simulation (1/2/97).

Comparing Fig. 5.18a with Fig. 2.15a and Fig. 5.20a with Fig. 2.16a one sees that in April the model tends to be around 0.5°C cooler than observation and tends to show less spatial variability. Observations show that the North Minch was colder than the Sea of the Hebrides by 2°C at the surface and 1°C at the bottom due to the effects of the Atlantic water. This can be seen in Fig. 5.19a which compares observations and model results; at the surface the model has almost a constant temperature, with values in the interval $8° - 9°$C. On the other hand, observations stretch from $7.5° - 9.5°$C. Bottom temperature follows an identical pattern with the same ranges for both observations and results. A statistical analysis gives a correlation coefficient r^2 of 0.46 for the surface and 0.47 for the bed. The model showed a weak stratification in temperature (0.1°C between surface and bottom), weaker than in observations where the difference in temperature was around 0.4°C in the Sea of the Hebrides.

The *Summer* condition illustrates the opposite situation, the observed surface temperature did not show a large north-south variation and the bottom temperature was characterised by the intrusion of Atlantic water. The model tended to overestimate temperature at both surface and bottom, Figs. 5.18b and 5.20b demonstrate this fact; the intrusion of cold Atlantic water was reproduced but the bottom temperatures in the other parts of the Minch are larger than the observed ones. Fig. 5.19b and Fig. 5.21b showed that modelled surface temperatures showed greater spatial variability and were larger than observations, the effect was not so marked at the bottom. Errors visible in Fig. 5.18b are due to the turbulence sub-closure scheme

and will be discussed in major detail in the next chapter. When the wind is weak as in this period (see Fig. 5.3) the scheme is not capable of correctly distributing the incoming thermal energy downward so that a very shallow thermocline is generated with high surface temperature as in this particular case, this fact was already noted by Martin (1985) during his work on the simulation of mixed layers.

In the *Autumn* conditions temperature was approaching or just passed through the maximum, depending on the locations (see Figs. 5.17a,j); the model correctly reproduced the strength of the bottom horizontal gradient in the Sea of the Hebrides (compare Fig. 2.16c and Fig. 5.20c). Also in this case the model was overestimating temperature by 1°-2°C with larger discrepancies on the surface and in the shallow parts of the domain. Surface inflow of warmer water in the North Minch and in the Sea of the Hebrides were not as well reproduced as at depth where these inflows (which are colder than the Minch coastal water) were clearly present. Figs. 5.19c and 5.21c show some differences, at the surface the spatial variation is well reproduced whilst for the bottom temperature observations exhibit a large scatter. Finally the *Winter* condition illustrates the return to an homogenous vertical state, due to the breakdown of stratification. Modelled and observed surface temperatures are shown in Fig. 5.18d and Fig. 2.15d respectively and Fig. 5.20a and Fig. 2.16a. Also in this case observations had a larger variability, the model reproduced the Atlantic intrusion in the Sea of the Hebrides but not with a strong horizontal gradient, as observed in reality. In the model bottom and surface temperature were identical since, at this time, there is vertical homogeneity (see Figs. 5.17a-j). The model overestimated temperature and underestimated spatial variability (Figs. 5.19c and 5.21c). Another assessment of the model came from Figs. 5.22a-5.22k which compare temperature by the Marine Laboratory, Aberdeen (see Table 5.1) and the temperature generated by the model at the same time and locations. In all cases the trend was correctly reproduced, temperature increased with time and for most of the locations difference between data and model results are smaller than 2°C, an exception being the current meter CM5622 (Fig. 5.22h).

5.5.2 Salinity

The previous analysis was also carried out for salinity using the same locations described above in Table 5.1. Unfortunately salinity was not sampled in every location

where a current meter was deployed so that fewer data are available. Salinity on the Scottish shelf can be influenced mainly by 3 sources - Atlantic water, Irish Water and fresh water inflow from the coast (Craig, 1959; McKay *et al.*, 1986). The oceanic contribution was modelled through the boundary conditions which supplied the seasonal variation for the western contribution; observations from the Marine Laboratory, Aberdeen showed that the intrusion of Atlantic water in the Sea of the Hebrides should reach its peak during spring and relax to smaller values as the year progresses. Points D and E (see Fig. 5.16a) showed an increase in bottom salinity with a subsequent decrease (Fig. 5.23d and Fig. 5.23e) but this event took place during July, and in the case of point E coincides with a decrease in the surface salinity, which was not observed in reality when the saline dome strengthened. These locations showed a decrease in salinity going from summer to winter. The fresh water runoff has a more marked seasonal cycle, showing a sudden increase in winter followed by a summer period with negligible contribution. This change in salinity (surface and bottom) is visible in locations A, B, M2 and Y (Figs. 5.23a,b,h,j) situated in proximity of the sources of fresher water. The eventual freshening effect of the Irish Sea was neglected since its salinity was kept constant during all simulations. There are other variations in salinity that can be observed during the annual simulation; points A, G and M2 experienced a pulse of high salinity in July-August. This feature can be associated with the intrusion of the Atlantic water, a view which is backed by the temperature data in these locations which show a sudden decrease although this explanation may not be conclusive because the change in temperature could be linked to changes in solar heat flux since this feature is detectable in almost all locations.

In the model surface and bottom salinity (Figs. 5.24a and 5.26a) the intrusion of Atlantic water was not as developed as in reality (Figs. 2.13a and 2.14a). The model failed also to capture the vertical variation of salinity; in reality a weak vertical stratification was observable whereas the model showed homogeneous water. Correlation coefficients were calculated as r^2=0.19 at the surface and r^2=0.25 at the bottom. As for temperature, the model exhibited a lesser spatial variation than the data, with salinity almost constant inside the Minch (Fig. 5.25a and Fig. 5.27a). During the *Summer* period, bottom salinity was reasonably reproduced, with the intrusion reaching the narrowest part of the Central Minch, west of Skye (compare Fig. 5.26b with Fig. 2.14b). Surface salinity was dominated by the intrusion inside all the Minch and not only in the Sea of the Hebrides, as from observations (compare

Fig. 5.24b with Fig. 2.13b). This resulted in an overestimate of salinity which can be seen in Fig. 5.25b. Also in this case the horizontal variation was not captured by the model. Bottom salinity showed the same behaviour with overestimated values and a reduced spread of data (Fig. 5.25b and Fig. 5.27b).

In Autumn the bottom intrusion was still in place and spread northward, entering the North Minch (Fig. 5.26c). This feature was not observed in reality (Fig. 2.14c) and surface salinity showed a similar behaviour (compare Fig. 5.24b and 2.13b). The comparison pictured in Fig. 5.25c and Fig. 5.27c exhibited a common pattern to that observed previously. A retreat of the intrusion took place in the modelled *Winter* conditions (Figs. 5.24d and 5.26d). At the bottom the intrusion was located in the western part of the Sea of the Hebrides, and the surface followed the same pattern. The effect of the freshening due to increased river runoff was correctly simulated and similar to the conditions observed in reality (Fig. 2.13d and Fig. 2.14d). The model did not reproduce with great accuracy the measured vertical gradients, showing an almost homogeneous picture of the salinity inside the Minch but it was able to capture the horizontal variations recorded in the area, as seen in Fig. 5.25d and Fig. 5.27d.

For a further comparison of the temporal evolution of salinity, data collected by some of the current meters were compared with the model output in Figs. 5.28a-f. The first thing to notice is that model showed less local variability; calculated salinity was always smoother with a definite upward trend whilst the trend in observations depended on location. The observational data shows small scale variability which the model cannot emulate, since it is forced with large scale salinity variations at its boundaries.

5.6 Summary

The model was forced with real meteorological and lateral boundary forcing for the year 1997. Three major sources of fresh water were also considered and observations were supplied by SEPA. Data were spatially interpolated onto the model's grid and temporally interpolated so to have values for every internal step of simulation. Simulations started from an homogenous state of the water column for salinity and temperature to mimic winter conditions, usually reached on the Scottish shelf in

February (Craig, 1959). Only horizontal gradients were present, where Atlantic water meets the coastal water and a haline front develops on the Malin shelf. This arrangement was also adopted for its easy implementation on the vertical grid.

The development of the thermal field was tested throughout the seasonal simulations using some observations distributed on the Scottish shelf and inside the Minch. The heating-cooling process is reproduced with the onset of stratification in April-May where tidal currents are not strong enough to maintain vertical mixing. Only one direct analysis was possible with the data, the other three sets were used for a qualitative comparison having been collected in different years to 1997. The *Spring* condition shows similarity with observations, temperatures in places differ from observations by $1° - 2°C$ but exhibit less horizontal and vertical variability than in reality. This can be also seen in all the locations and during the *Summer*, *Autumn* and *Winter* conditions. The model has an overall tendency to overestimate temperature, especially the surface value; this effect could be caused by the Mellor-Yamada turbulence closure sub-model (Mellor and Yamada, 1982) in the presence of weak wind. Martin (1985) observed the same effect in his simulations of the temperature conditions at the Ocean Weather Stations November and Papa. That particular scheme underestimated the depth of the mixed layer giving rise to an increase of surface temperature. The surface temperature was also sensitive to the type of absorbtion used (see Mellor, 1998). This model correctly simulated the breakdown of thermal stratification in late September but the final temperature remains higher than observed. This fact will be discussed further in the next chapter which deals with the seasonal development of the tidal mixing front on the Malin shelf.

Salinity is also overestimated by the model. Simulations showed a weak seasonal cycle where salinity increases in summer to decrease in winter following the cycle of river runoff. In addition, the model simulated the salinity change at the bottom due to the intrusion of saltier Atlantic water in the Sea of the Hebrides. The timing did not coincide with observations, which showed the intrusion to be stronger in spring whilst the model showed these changes to happen in July. An episode of Atlantic intrusion is also simulated by the model confirming early observations by Craig (1959). The difference in the simulation of temperature and salinity can be probably explained by their different physical nature and in the factors which control them. The temperature cycle in shelf seas is mostly local (Bowers and Simpson, 1990) and advection can be disregarded in its simulation (Simpson and Bowers, 1981) so

that simple heating stirring models can reproduce correctly the seasonal cycle (see for example James, 1977). The balance is almost purely local, between the vertical tidal mixing and the heat input from the sun. Salinity presents the opposite feature; its balance is controlled by non-local effects such as the boundaries, the locations of the source of fresh water and in general by its advection so that it is critical to reproduce correctly the entire regional circulation to obtain a realistic simulation of salinity. Only three major sources were present in this work and the net runoff was not distributed along all the Scottish coast as in reality; precipitations was not modelled so that its contribution was not taken into account but in reality on the Scottish shelf precipitation can have a comparable effect to the other sources of fresh water. Assuming a rate of 20 cm per month on a surface of 1000 km^2 the net inflow is of the order 50 m^3 s^{-1} which is of the same order of some of the sources. Evaporation and salinity fluxes can be implemented in POM but in this study the fluxes were set to zero because of lack of reliable observations of the whole of the domain.

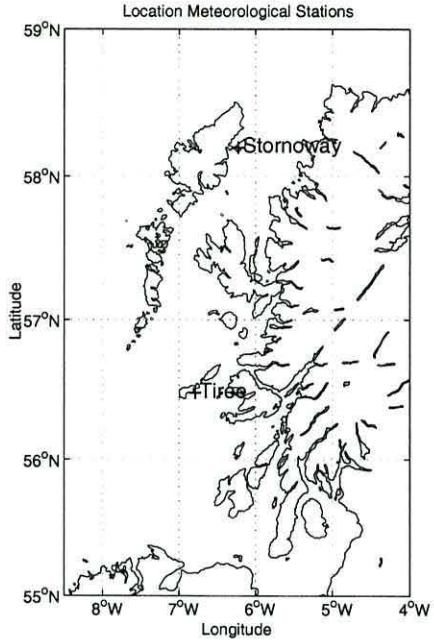

Figure 5.1: Locations of the Meteorological Stations that supplied the climatological forcing for wind (Tiree) and solar heat flux (Stornoway)

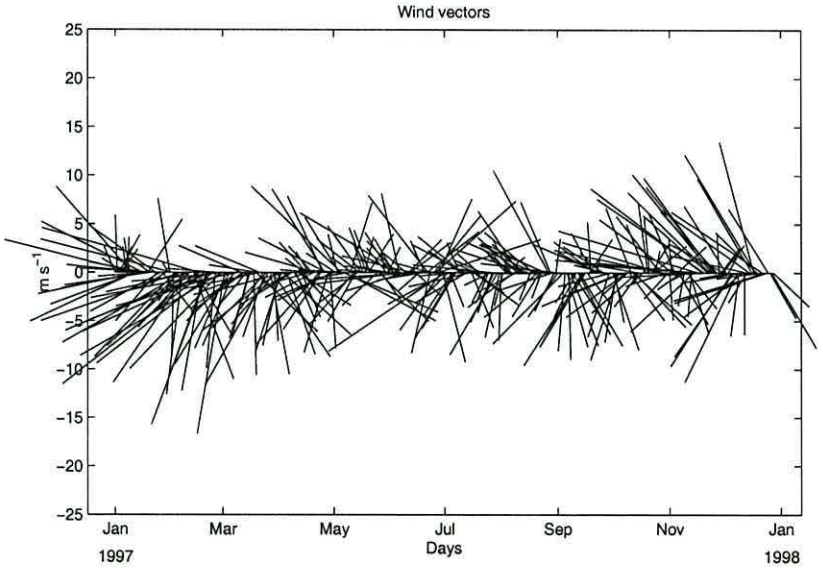

Figure 5.2: Wind vectors (24 hours average) for the station of Tiree (year 1997).

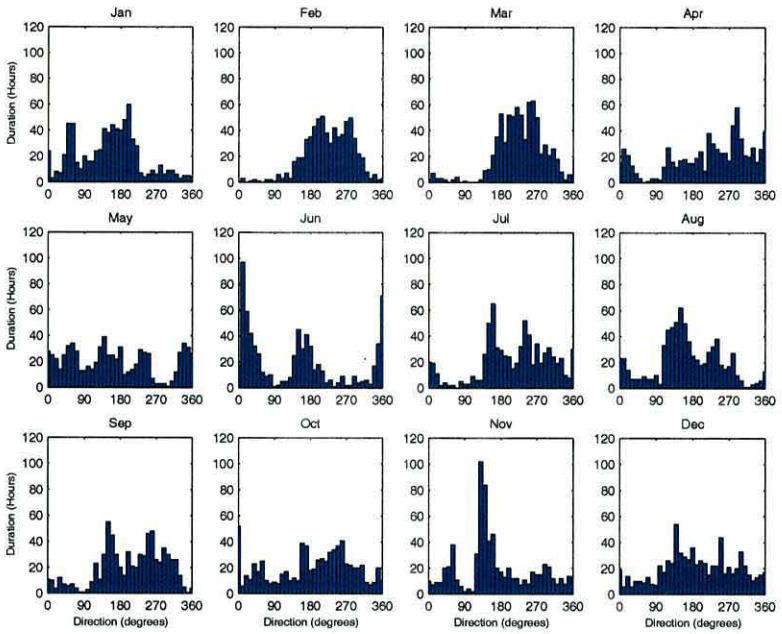

(a)

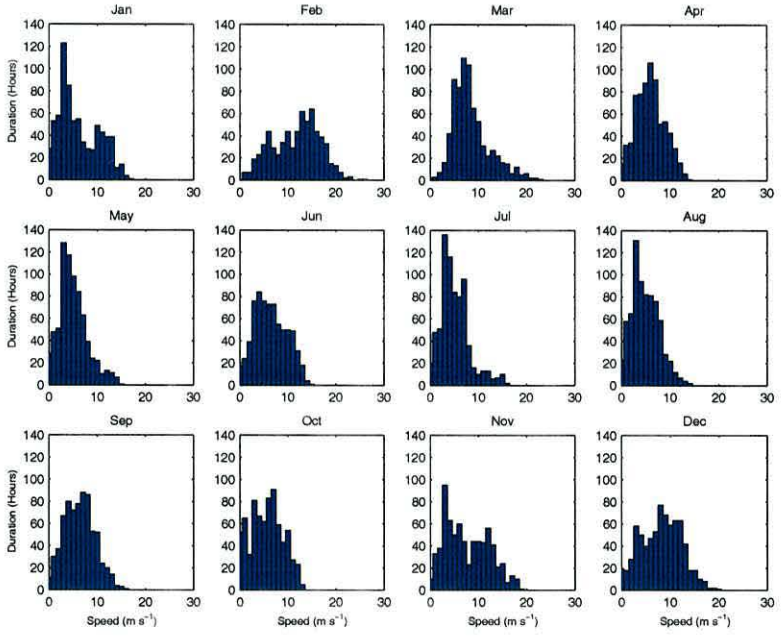

(b)

Figure 5.3: Monthly distribution of a) wind direction (degrees) and b) speed (m s^{-1}) for the station of Tiree (year 1997)

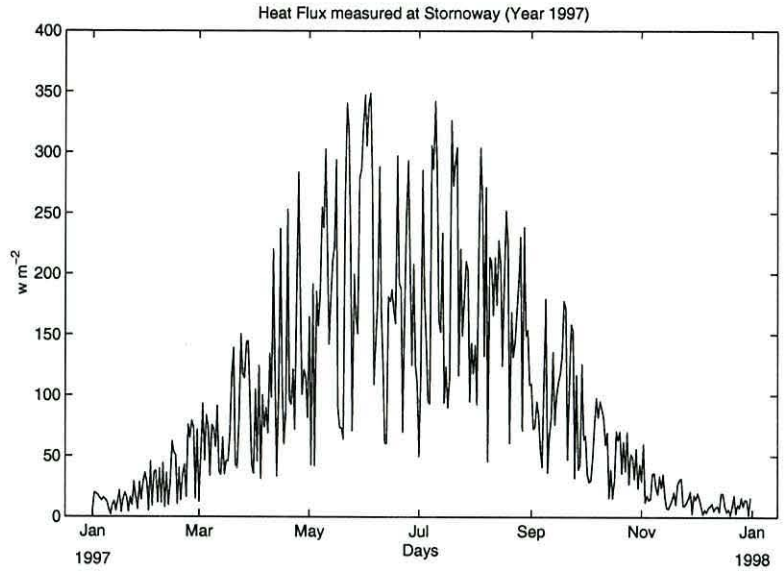

Figure 5.4: Daily averaged solar insolation (W m^{-2}) measured at the station of Stornoway airport (year 1997).

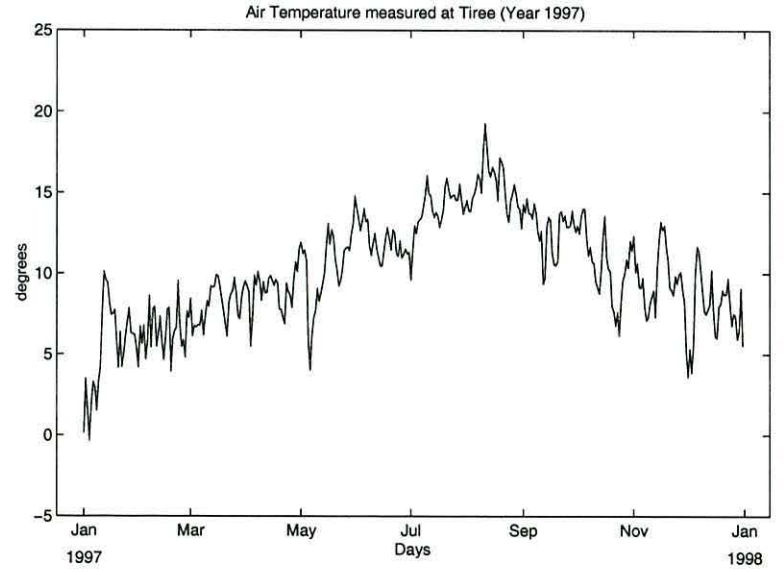

Figure 5.5: Daily averaged air temperature (degrees) measured at the station of Tiree (year 1997).

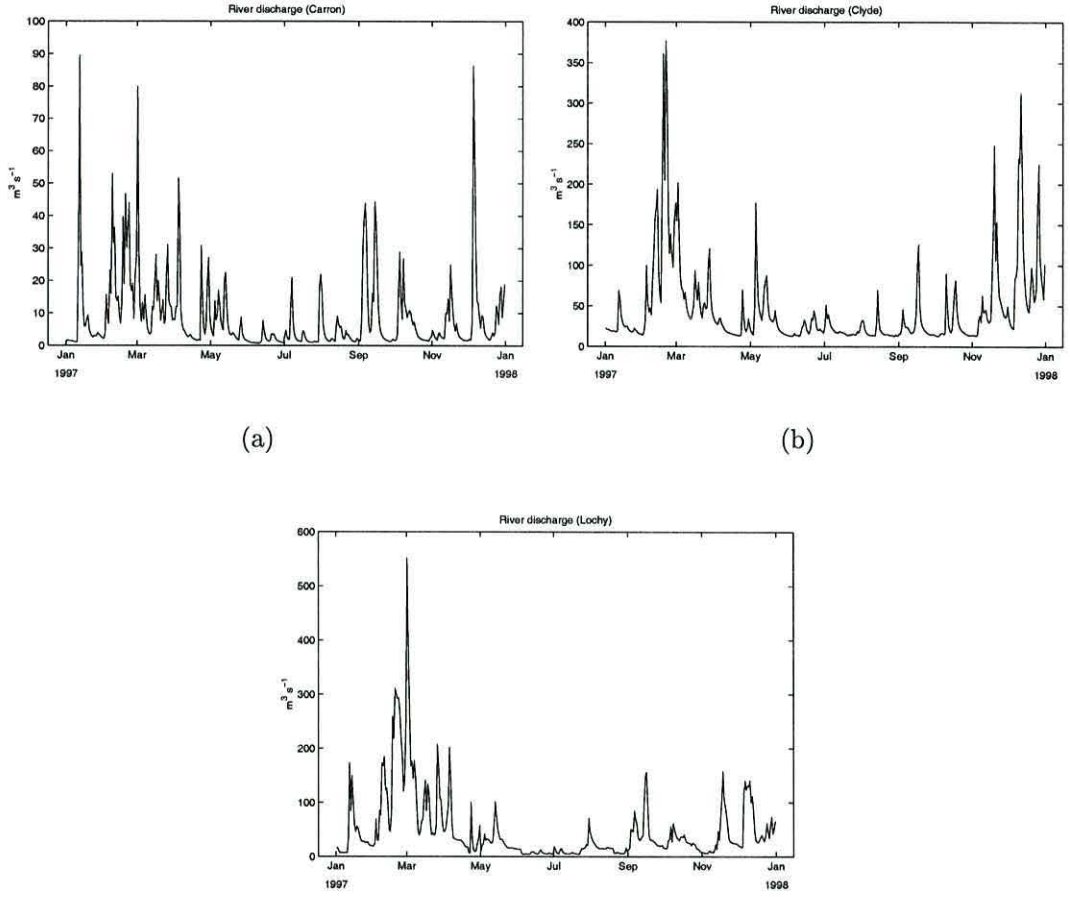

Figure 5.6: Daily discharge ($m^3\ s^{-1}$) for the rivers a) Carron b) Clyde and c) Lochy for year 1997. Observations supplied by SEPA.

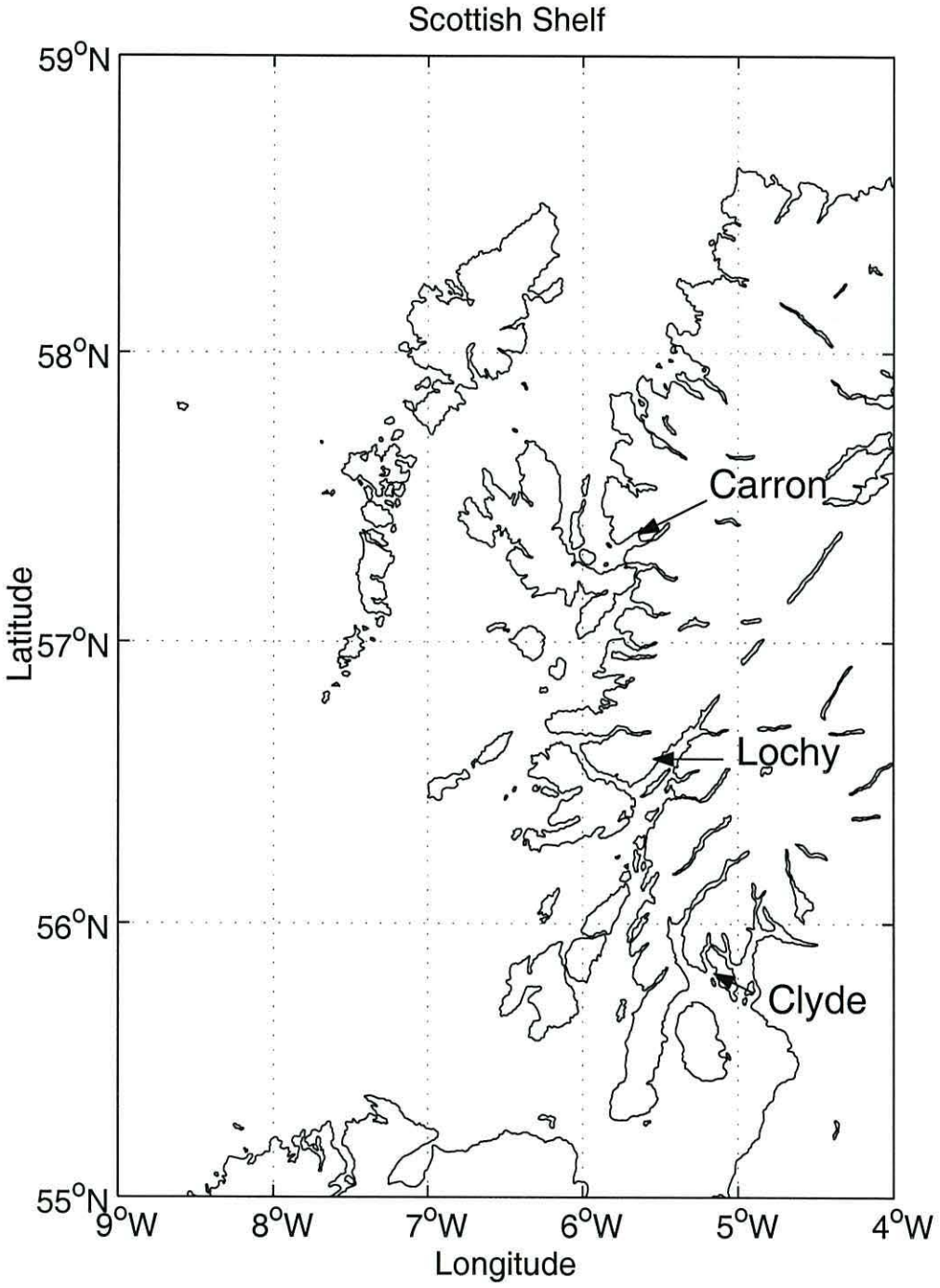

Figure 5.7: Locations of the 3 sources of fresh water considered in these simulations.

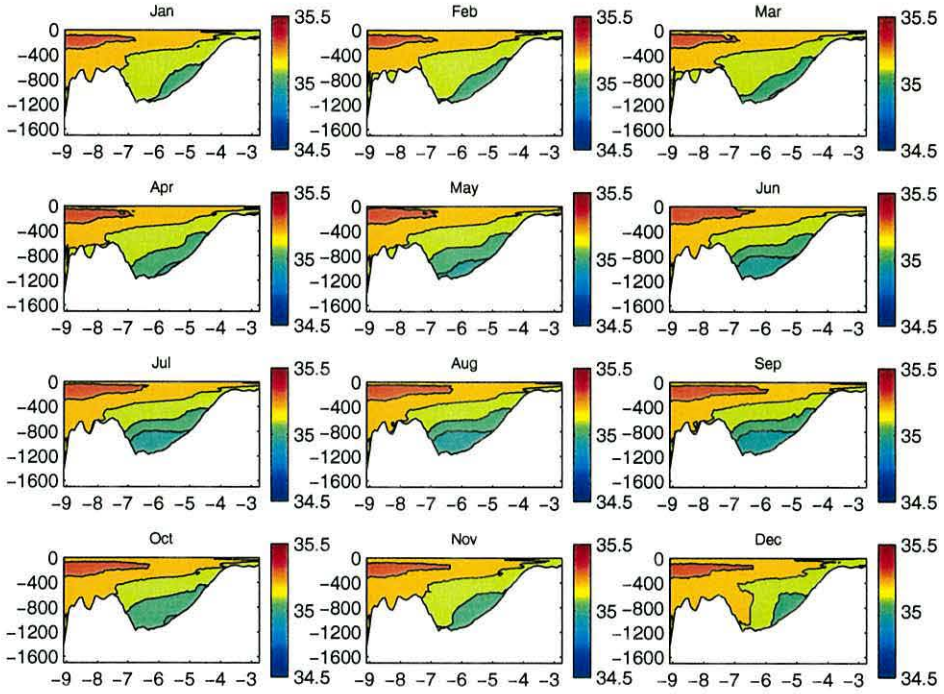

Figure 5.8: Monthly salinity at the northern boundary (60° N) used as boundary condition, contours drawn at every 0.1 unit.

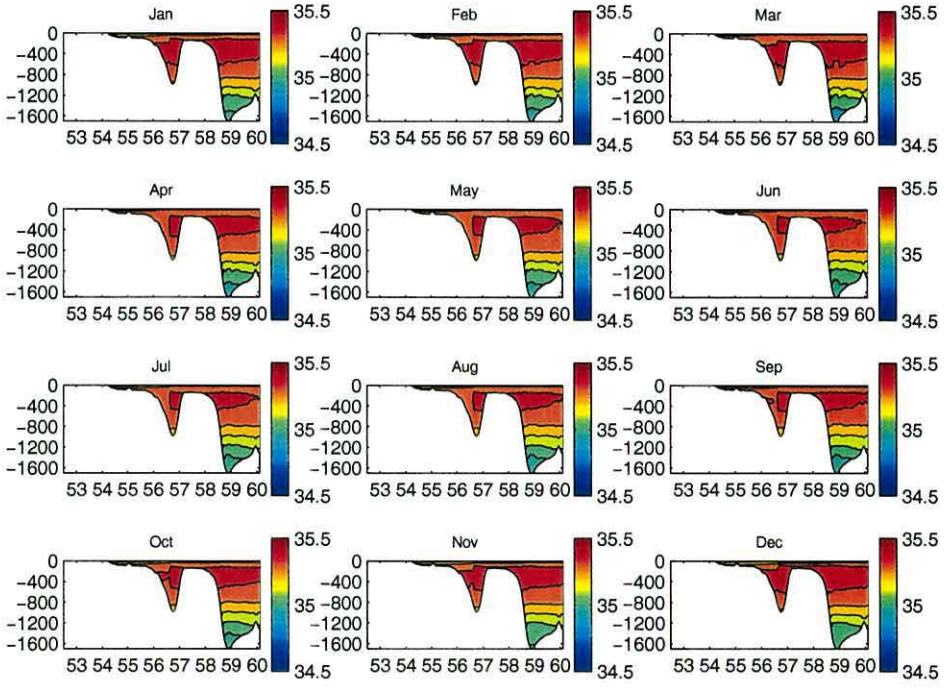

Figure 5.9: Monthly salinity at the western boundary (9° W) used as boundary condition, contours drawn at every 0.1 unit.

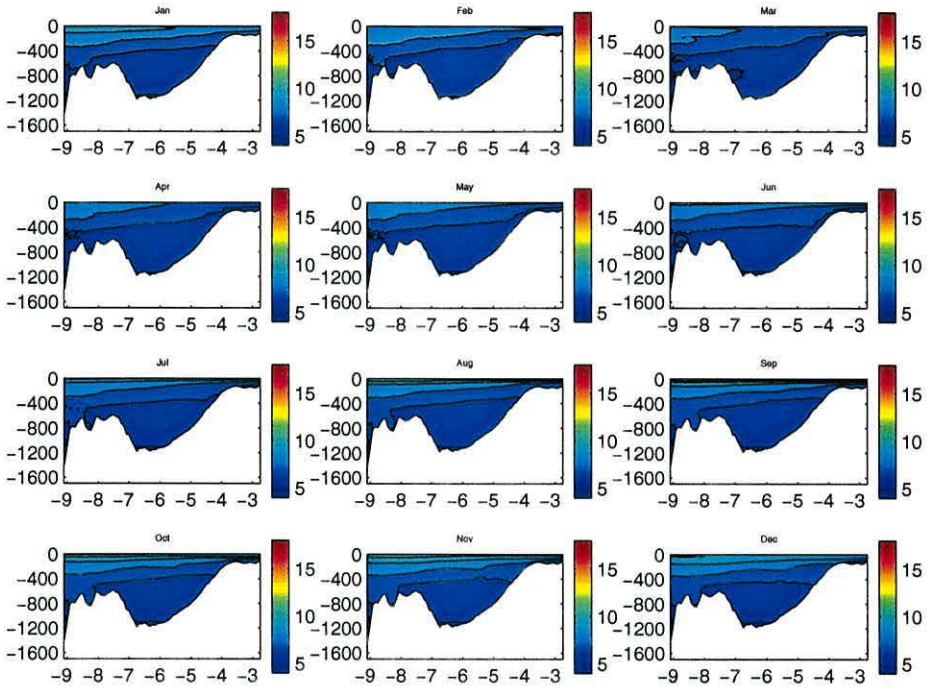

Figure 5.10: Monthly temperature at the northern boundary (60° N) used as boundary condition, contours drawn at every degree.

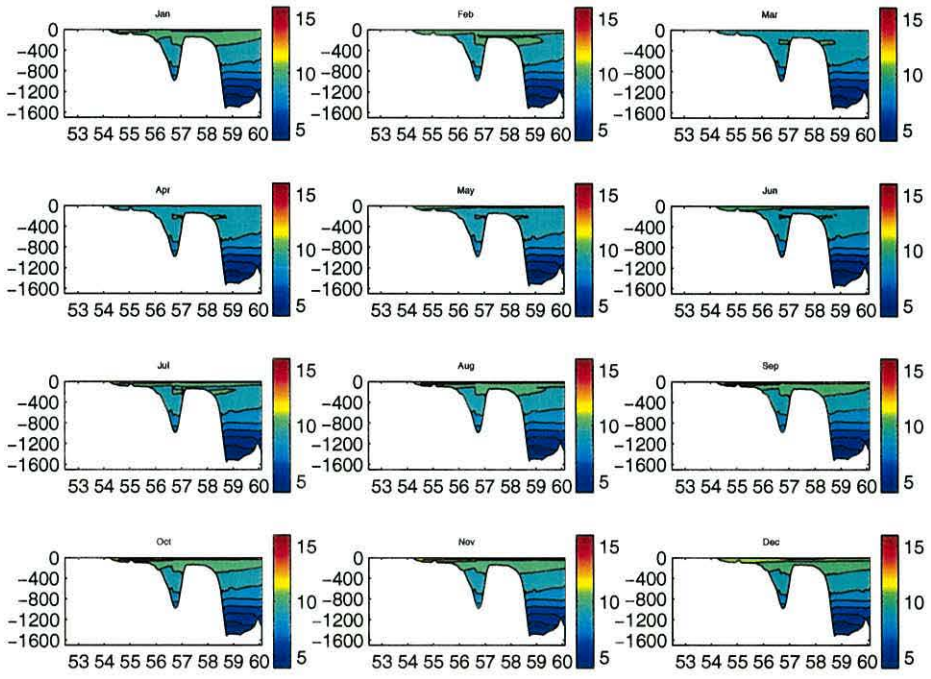

Figure 5.11: Monthly temperature at the western boundary (9° W) used as boundary condition, contours drawn at every degree.

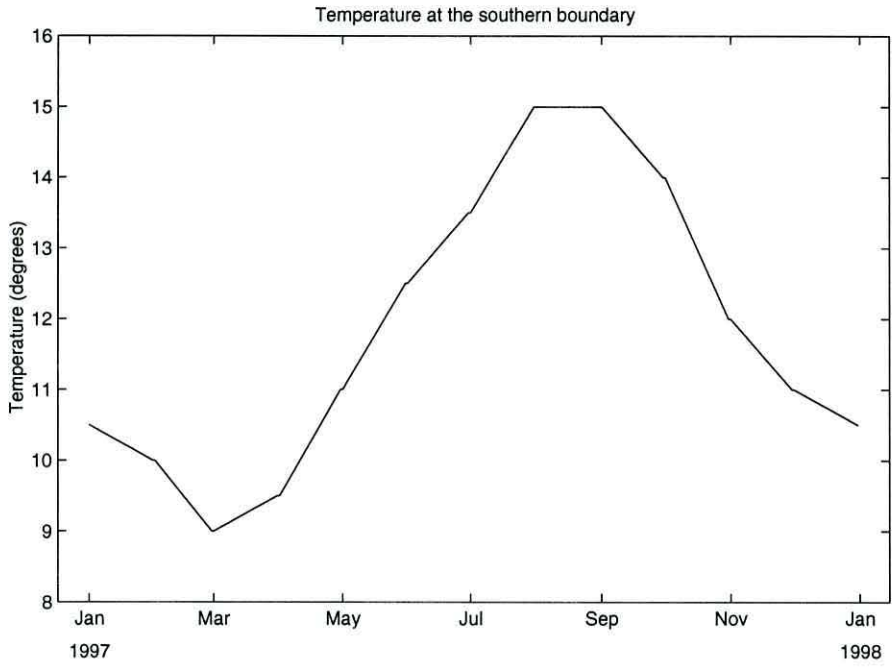

Figure 5.12: Monthly temperature at the southern boundary (Long. 52.1° W) used as open boundary condition.

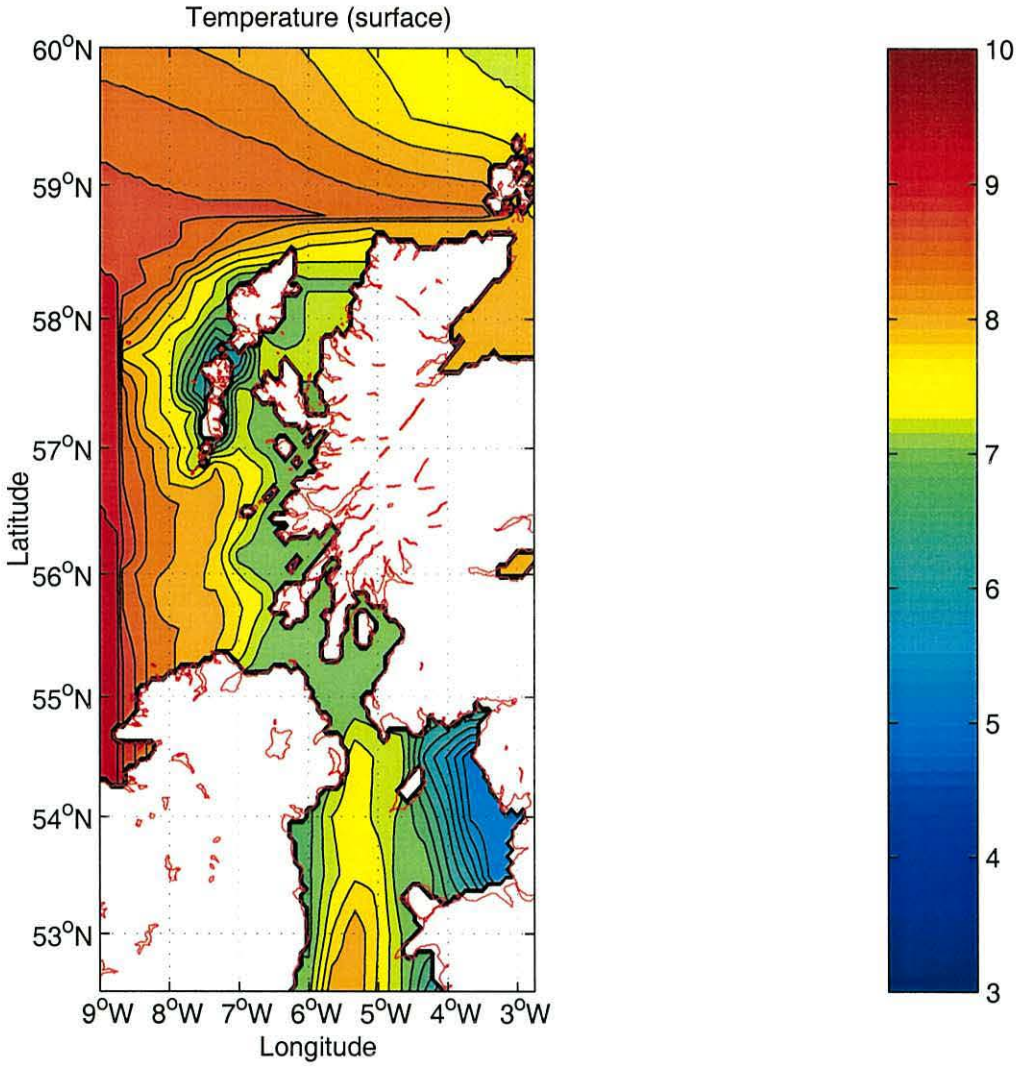

Figure 5.13: Initial conditions for temperature.

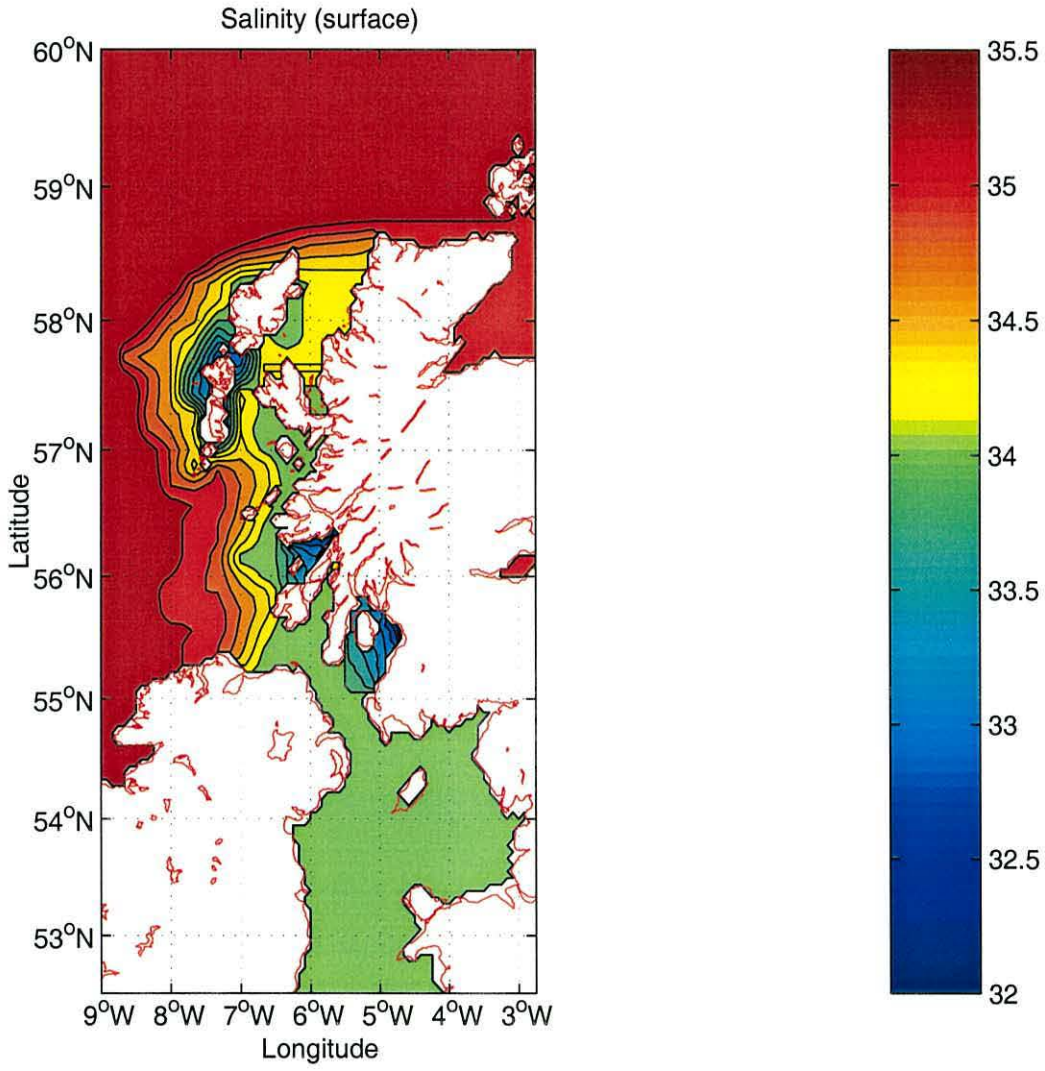

Figure 5.14: Initial conditions for salinity.

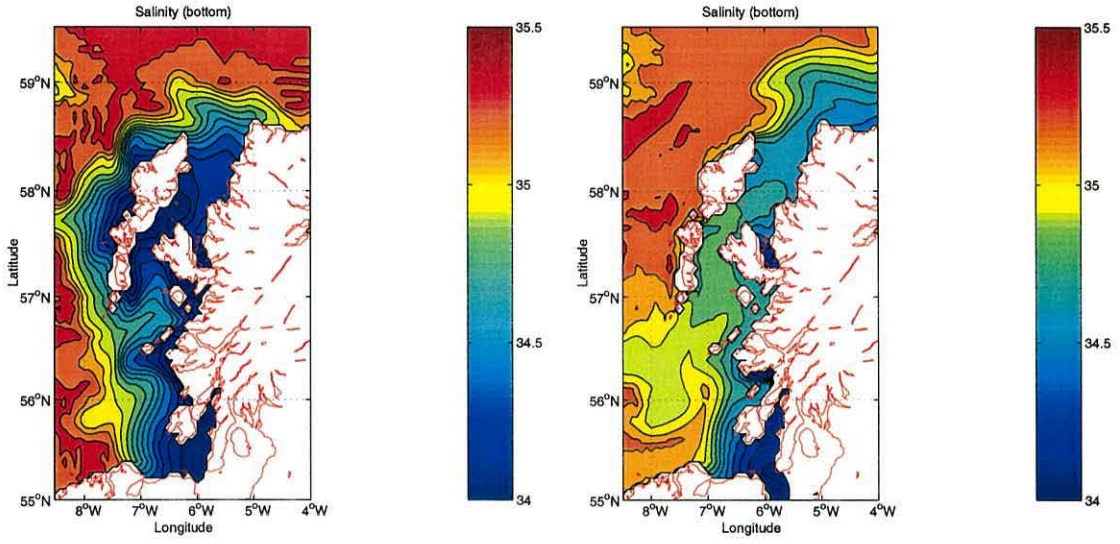

(a) (b)

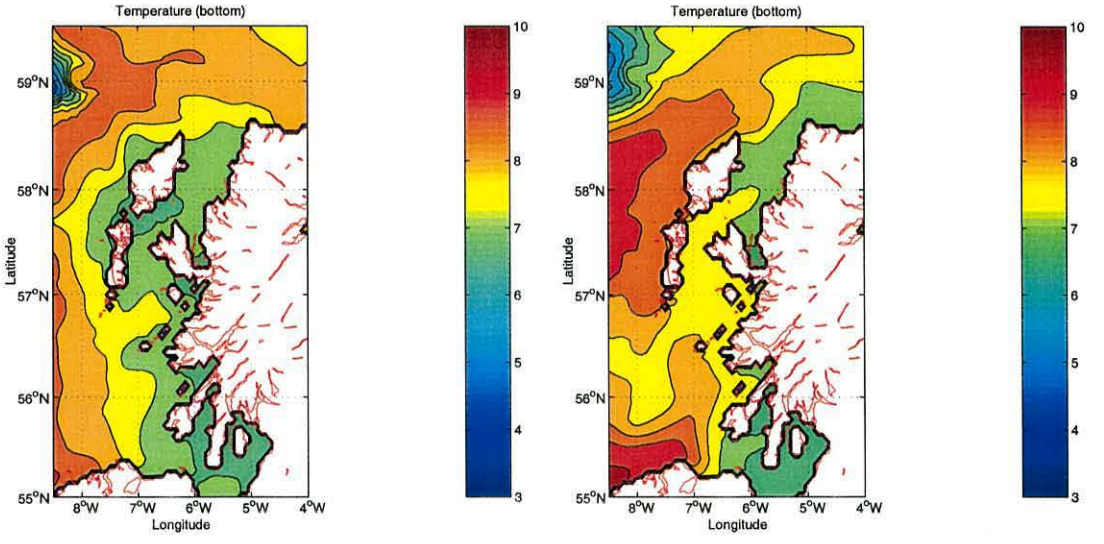

(c) (d)

Figure 5.15: Bottom salinity and temperature after 5 days (a and c) and after 30 days (b and d).

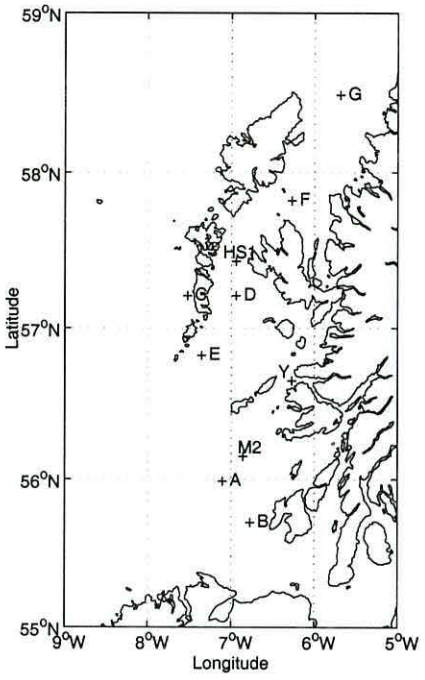

(a)

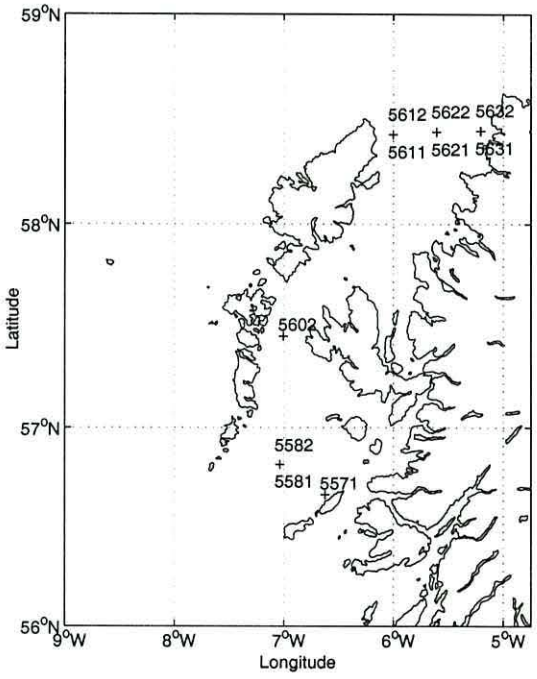

(b)

Figure 5.16: Location of points used in the comparison: a) chosen for this simulation and from Hill and Simpson (1988) and b) from deployment of current meters by the Marine Laboratory, Aberdeen.

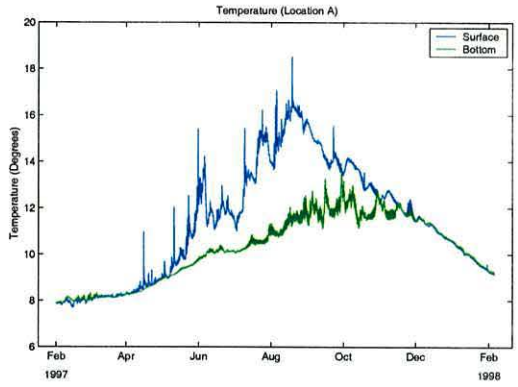
Temperature (Location A)
Surface
Bottom
Temperature (Degrees)
20
18
16
14
12
10
8
6
Feb
1997
Apr
Jun
Aug
Oct
Dec
Feb
1998

(a)

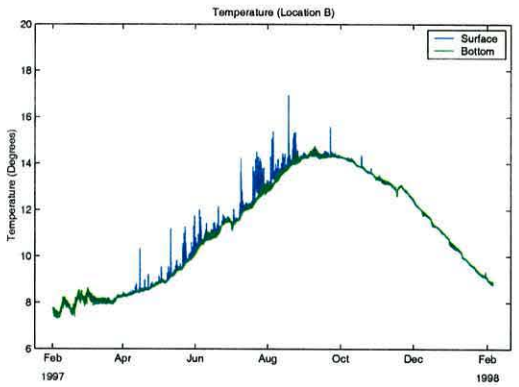
Temperature (Location B)
Surface
Bottom
Temperature (Degrees)
20
18
16
14
12
10
8
6
Feb
1997
Apr
Jun
Aug
Oct
Dec
Feb
1998

(b)

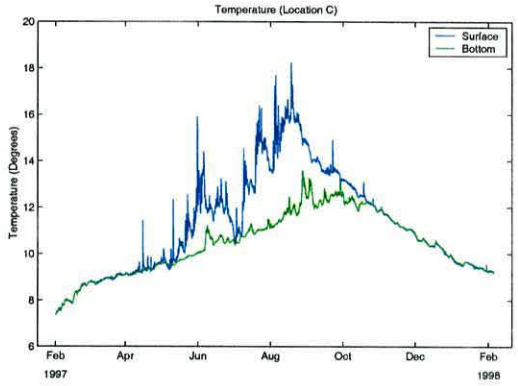
Temperature (Location C)
Surface
Bottom
Temperature (Degrees)
20
18
16
14
12
10
8
6
Feb
1997
Apr
Jun
Aug
Oct
Dec
Feb
1998

(c)

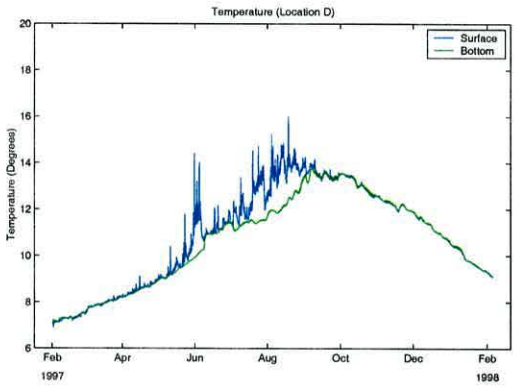
Temperature (Location D)
Surface
Bottom
Temperature (Degrees)
20
18
16
14
12
10
8
6
Feb
1997
Apr
Jun
Aug
Oct
Dec
Feb
1998

(d)

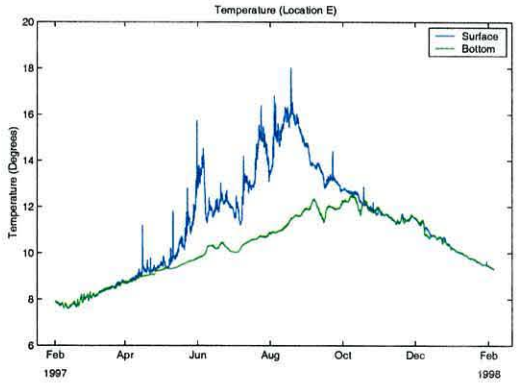
Temperature (Location E)
Surface
Bottom
Temperature (Degrees)
20
18
16
14
12
10
8
6
Feb
1997
Apr
Jun
Aug
Oct
Dec
Feb
1998

(e)

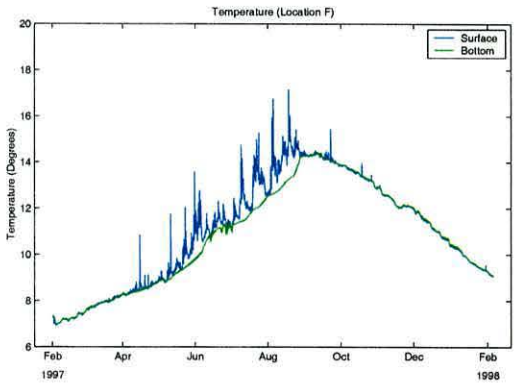
Temperature (Location F)
Surface
Bottom
Temperature (Degrees)
20
18
16
14
12
10
8
6
Feb
1997
Apr
Jun
Aug
Oct
Dec
Feb
1998

(f)

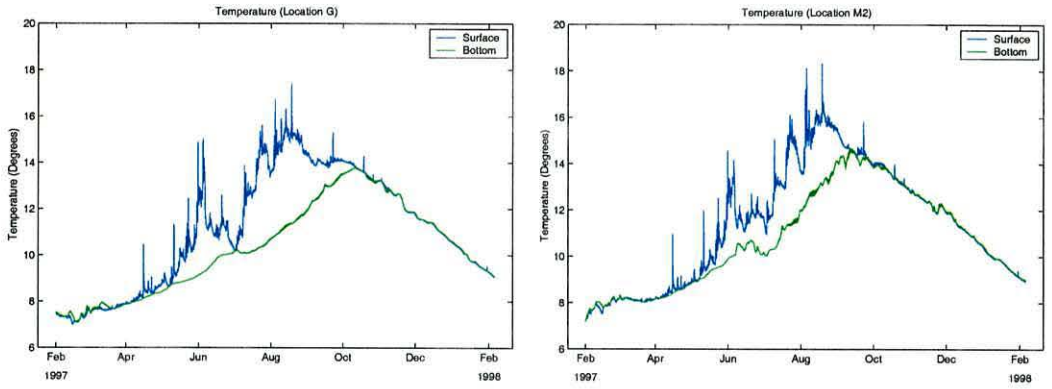

(g)

(h)

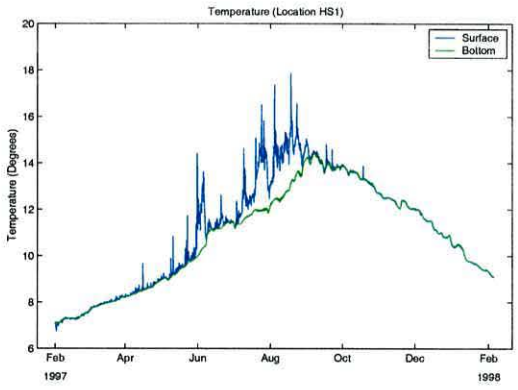

(i)

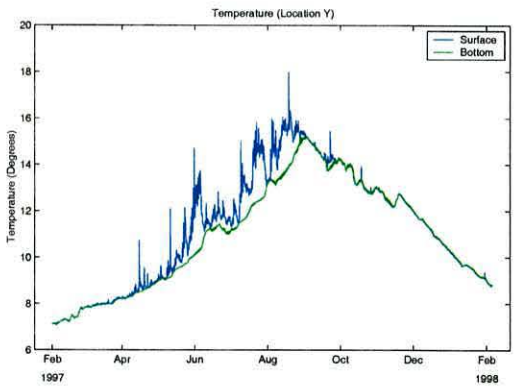

(j)

Figure 5.17: Seasonal evolution (from February 1997 to February 1998) of predicted hourly surface temperature (blue line) and bottom temperature (green line) for location shown in Table 5.1. Pictures from a) to g) refers to position A to G whilst h), i) and j) refer to positions M2, HS1 and Y respectively.

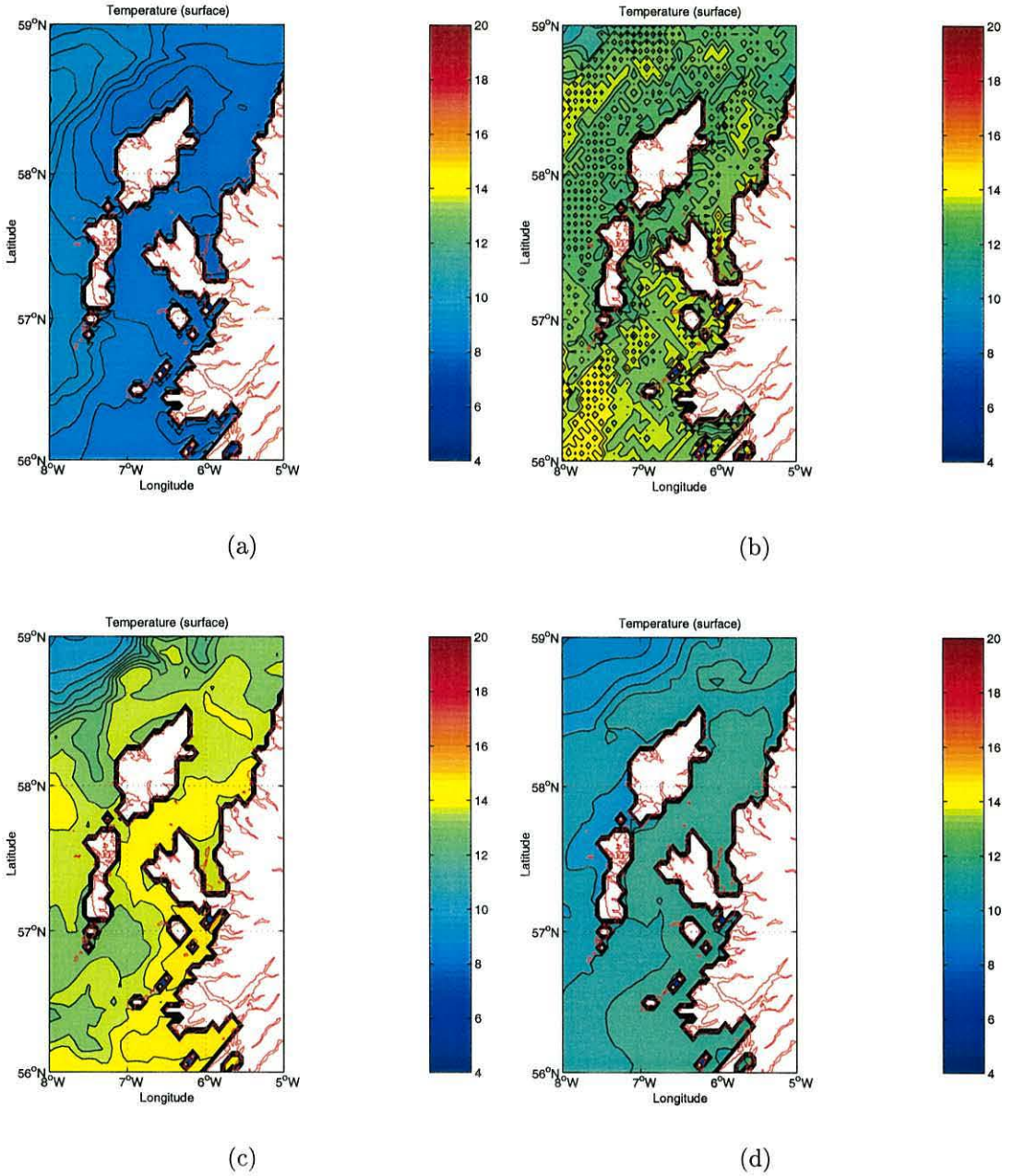

Figure 5.18: Modelled surface temperature used as comparison with the data collected by the Marine laboratory, Aberdeen (see Table 2.1) for a) *Spring*, b) *Summer*, c) *Autumn* and d) *Winter*.

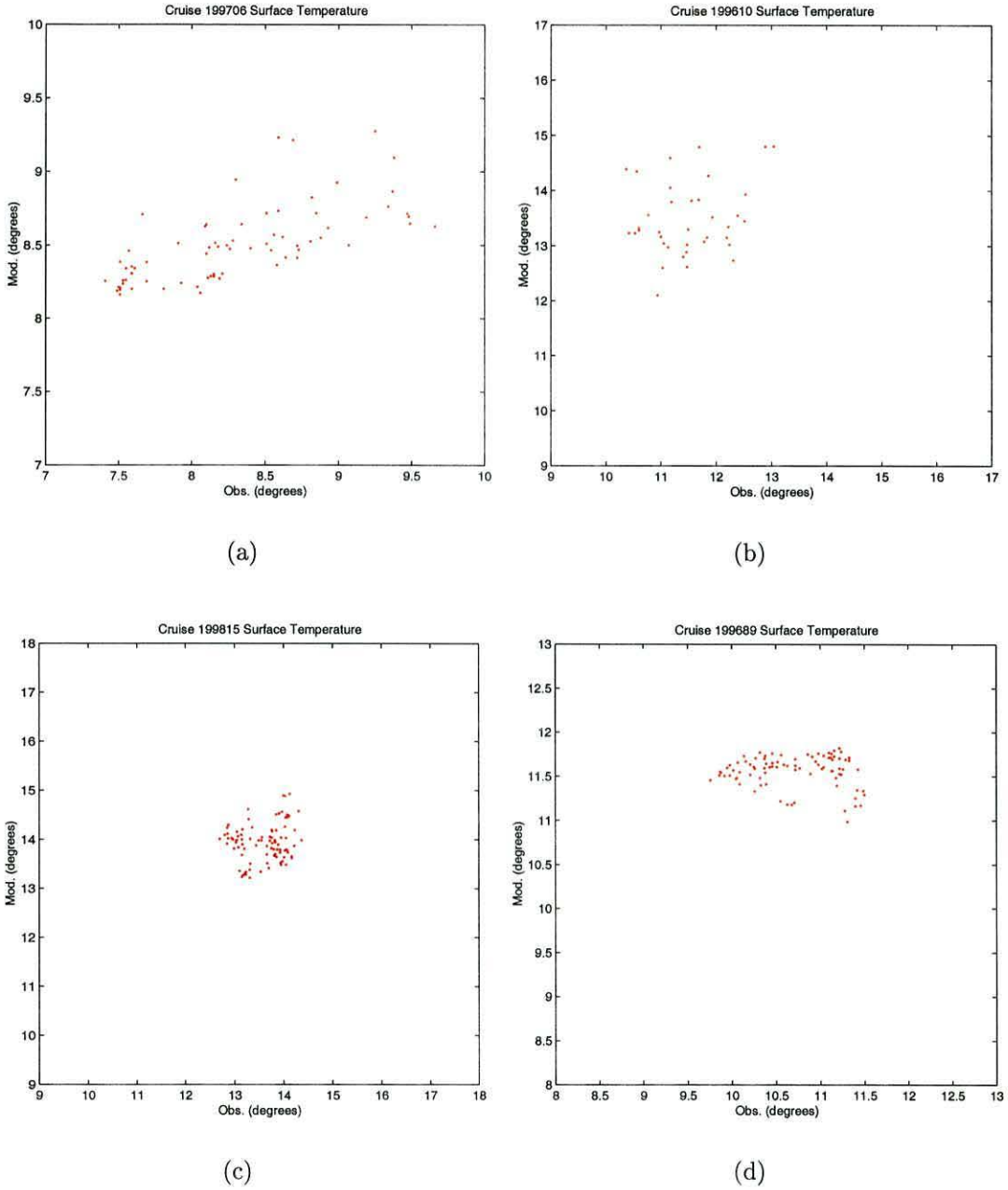

Figure 5.19: Comparison between surface temperature observed by the Marine laboratory, Aberdeen and the model results for a) *Spring*, b) *Summer*, c) *Autumn* and d) *Winter*.

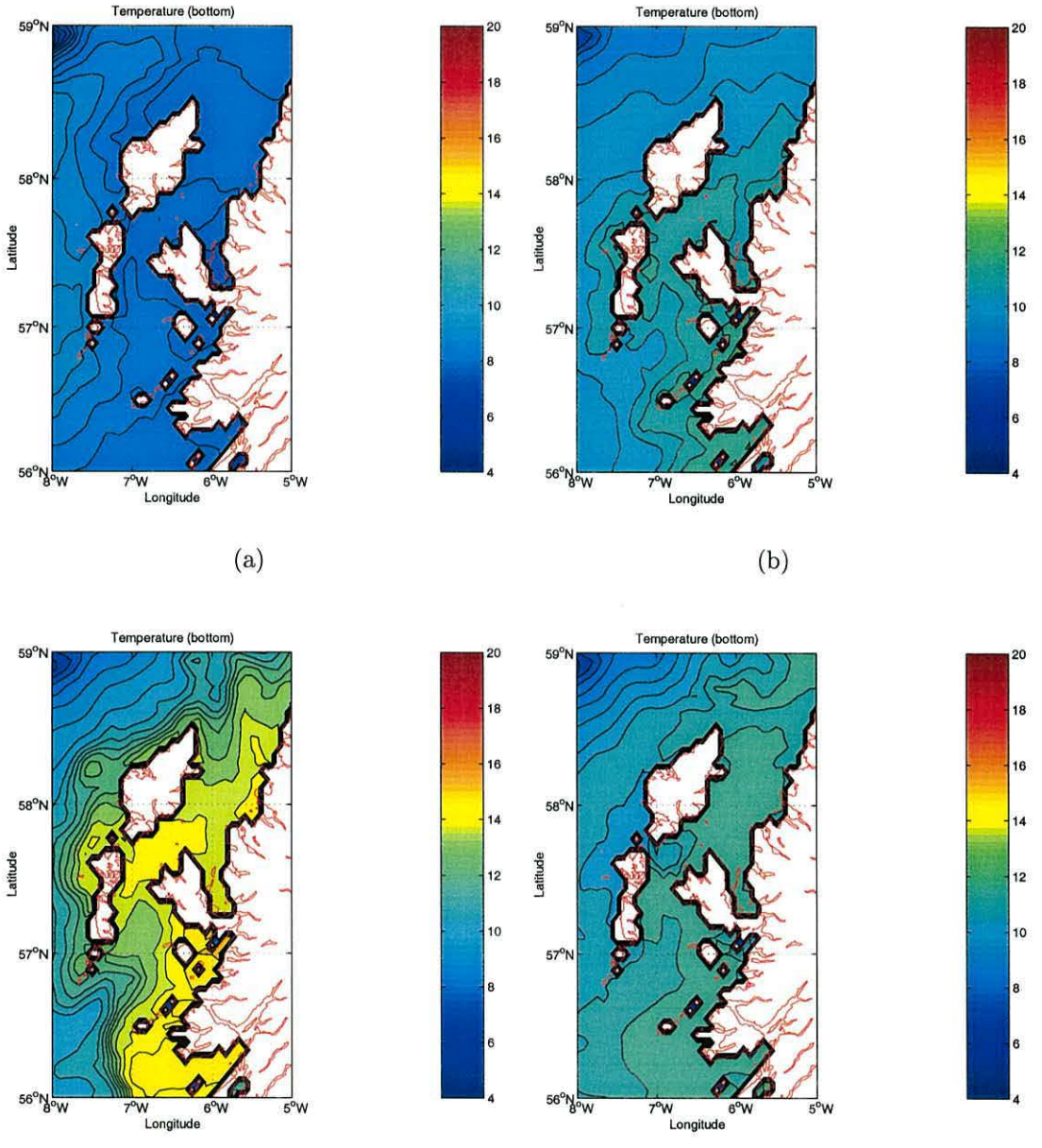

Figure 5.20: Modelled bottom temperature used as comparison with the data collected by the Marine laboratory, Aberdeen (see Table 2.1) for a) *Spring*, b) Summer, c) *Autumn* and d) *Winter*.

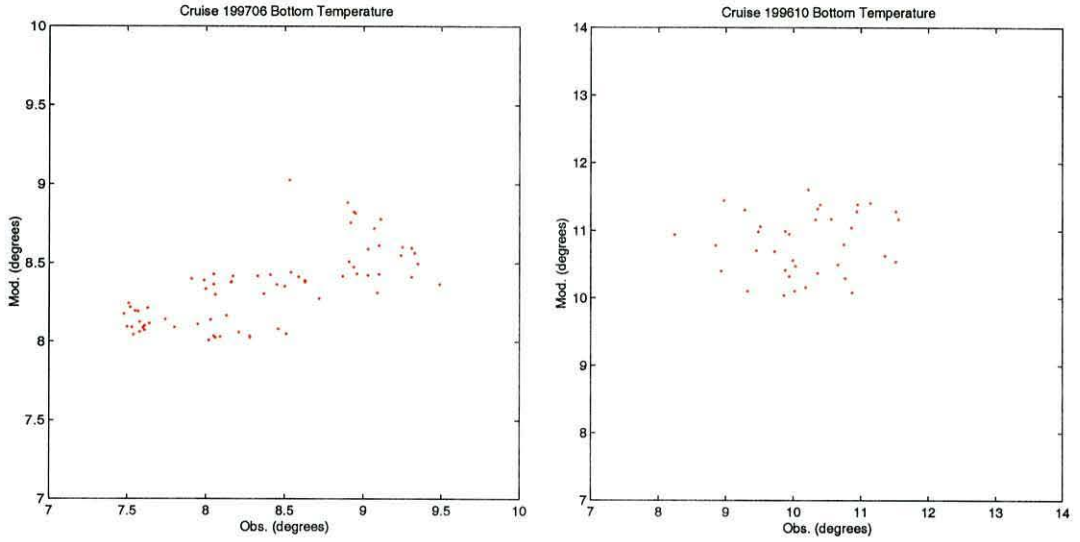

(a) (b)

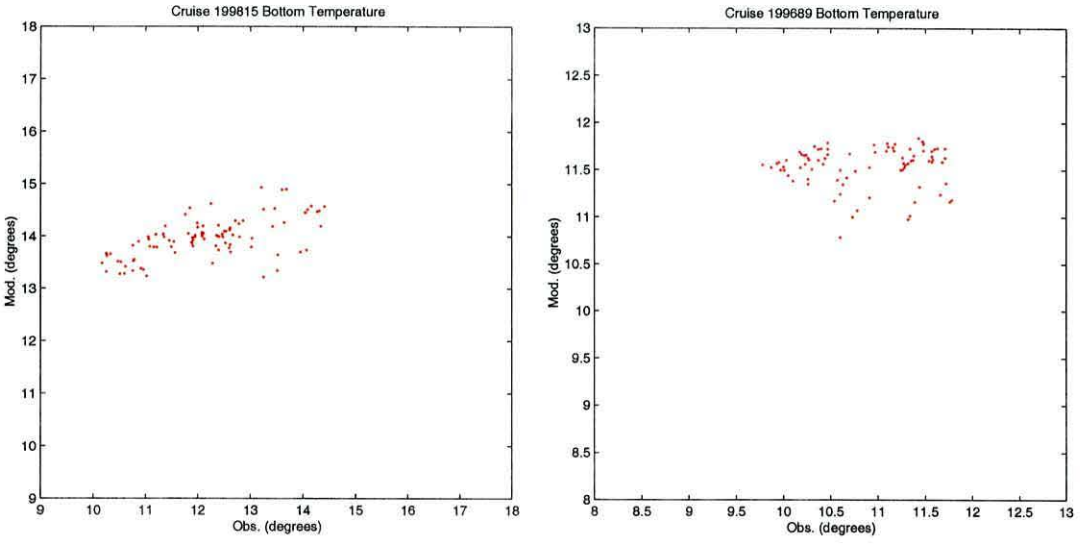

(c) (d)

Figure 5.21: Comparison between bottom temperature observed by the Marine laboratory, Aberdeen and the model results for a) *Spring*, b) *Summer*, c) *Autumn* and d) *Winter*.

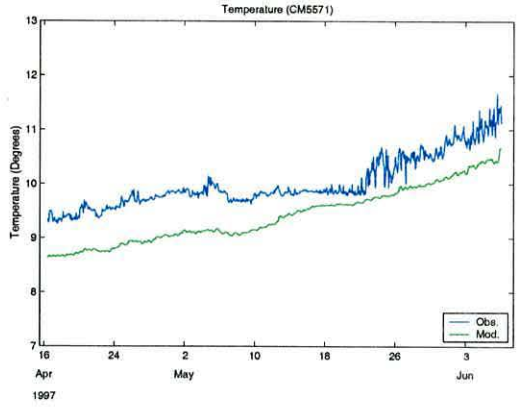

(a) CM 5571

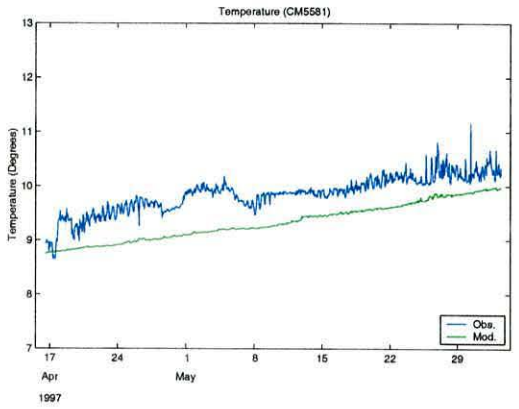

(b) CM 5581

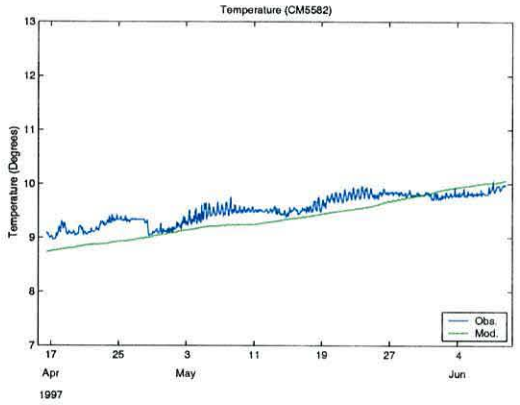

(c) CM 5582

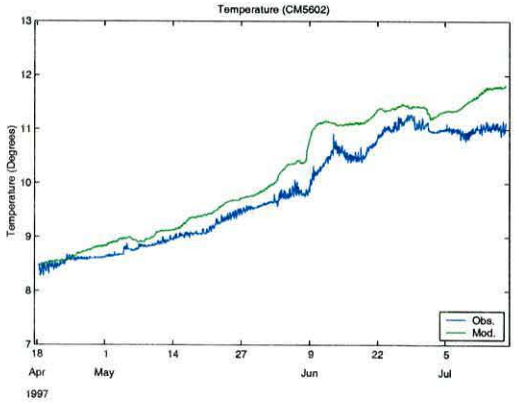

(d) CM 5602

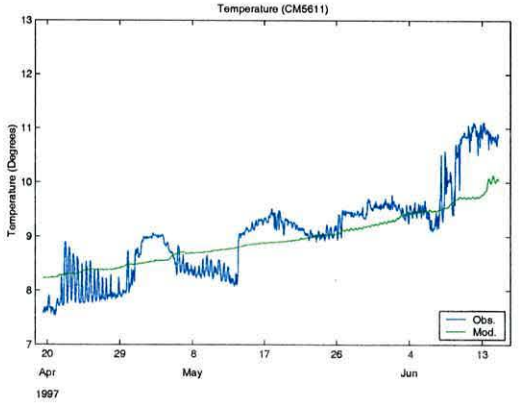

(e) CM 5611

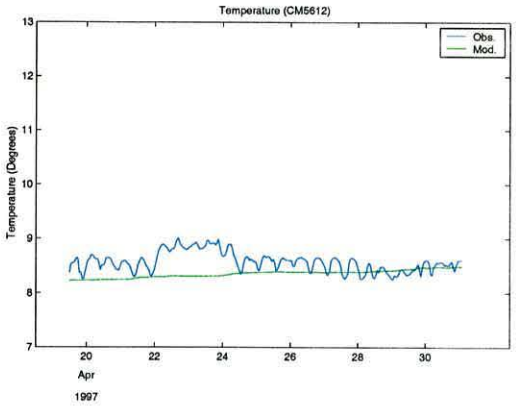

(f) CM 5612

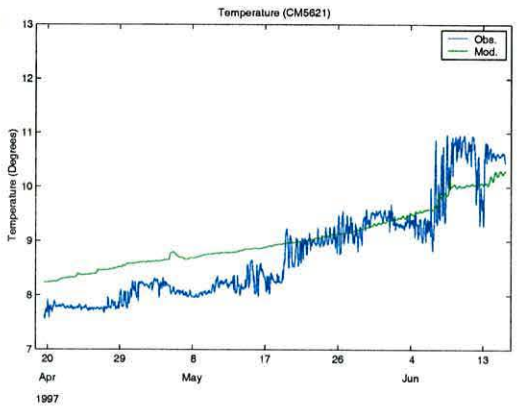

(g) CM 5621

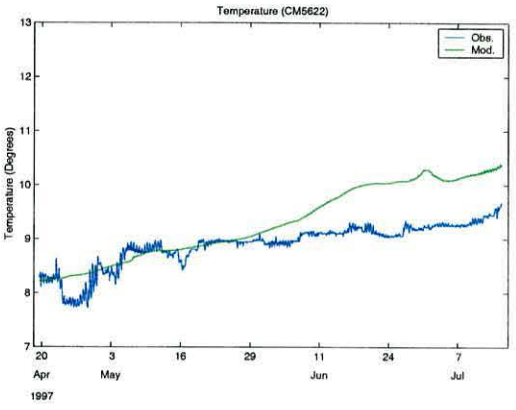

(h) CM 5622

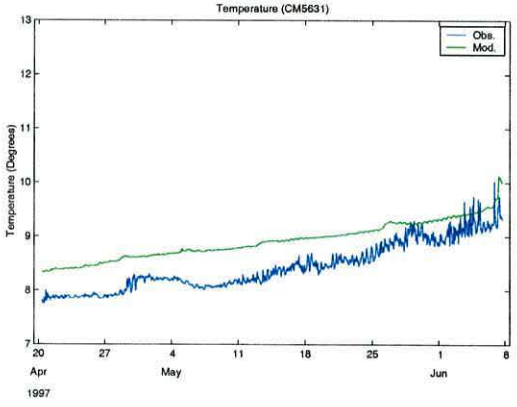

(i) CM 5631

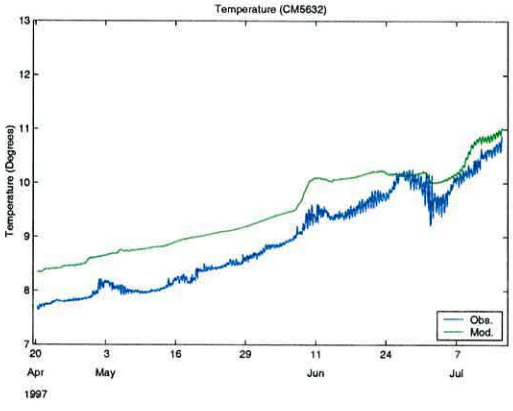

(j) CM 5632

Figure 5.22: Comparison between temperature measured by current meters deployed in locations described in Table 5.1 the model results for the same locations.

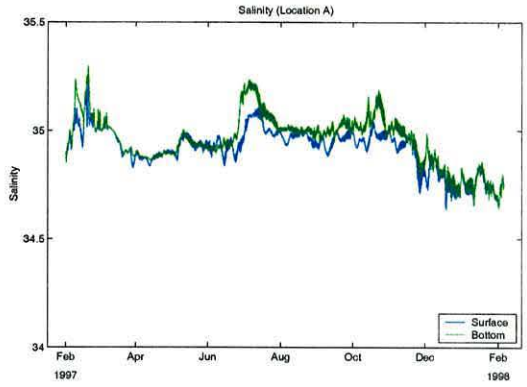
Salinity (Location A)
Salinity
35.5
35
34.5
34
Feb
1997
Apr
Jun
Aug
Oct
Dec
Feb
1998
Surface
Bottom

(a)

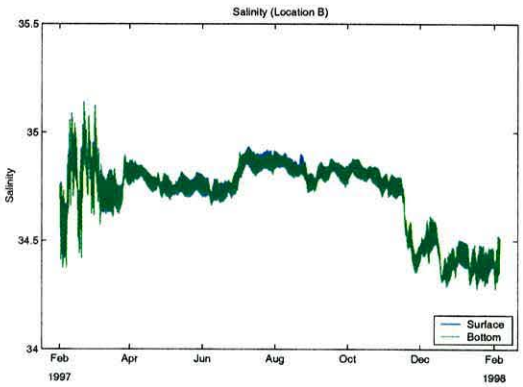
Salinity (Location B)
Salinity
35.5
35
34.5
34
Feb
1997
Apr
Jun
Aug
Oct
Dec
Feb
1998
Surface
Bottom

(b)

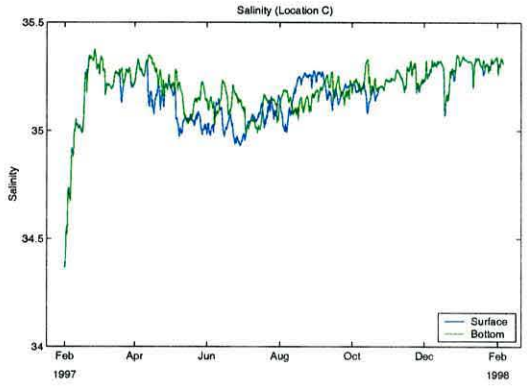
Salinity (Location C)
Salinity
35.5
35
34.5
34
Feb
1997
Apr
Jun
Aug
Oct
Dec
Feb
1998
Surface
Bottom

(c)

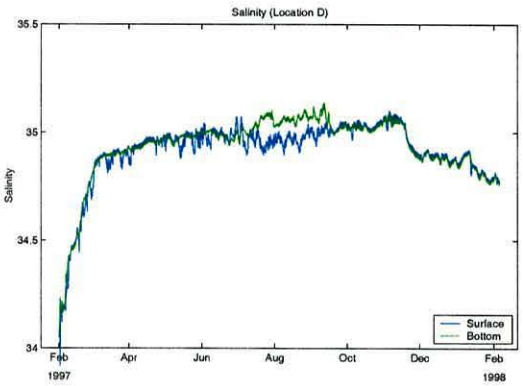
Salinity (Location D)
Salinity
35.5
35
34.5
34
Feb
1997
Apr
Jun
Aug
Oct
Dec
Feb
1998
Surface
Bottom

(d)

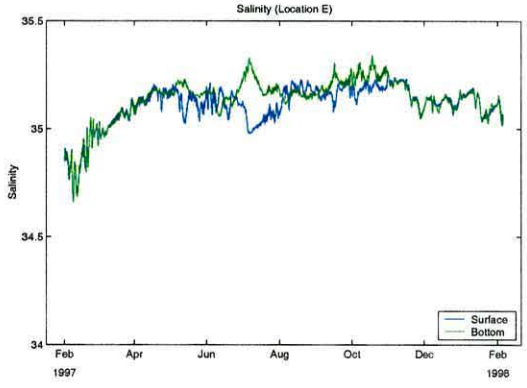
Salinity (Location E)
Salinity
35.5
35
34.5
34
Feb
1997
Apr
Jun
Aug
Oct
Dec
Feb
1998
Surface
Bottom

(e)

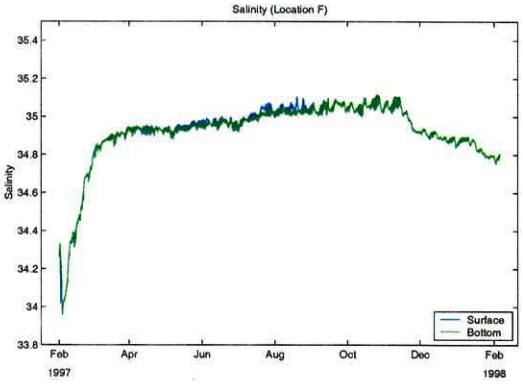
Salinity (Location F)
Salinity
35.4
35.2
35
34.8
34.6
34.4
34.2
34
33.8
Feb
1997
Apr
Jun
Aug
Oct
Dec
Feb
1998
Surface
Bottom

(f)

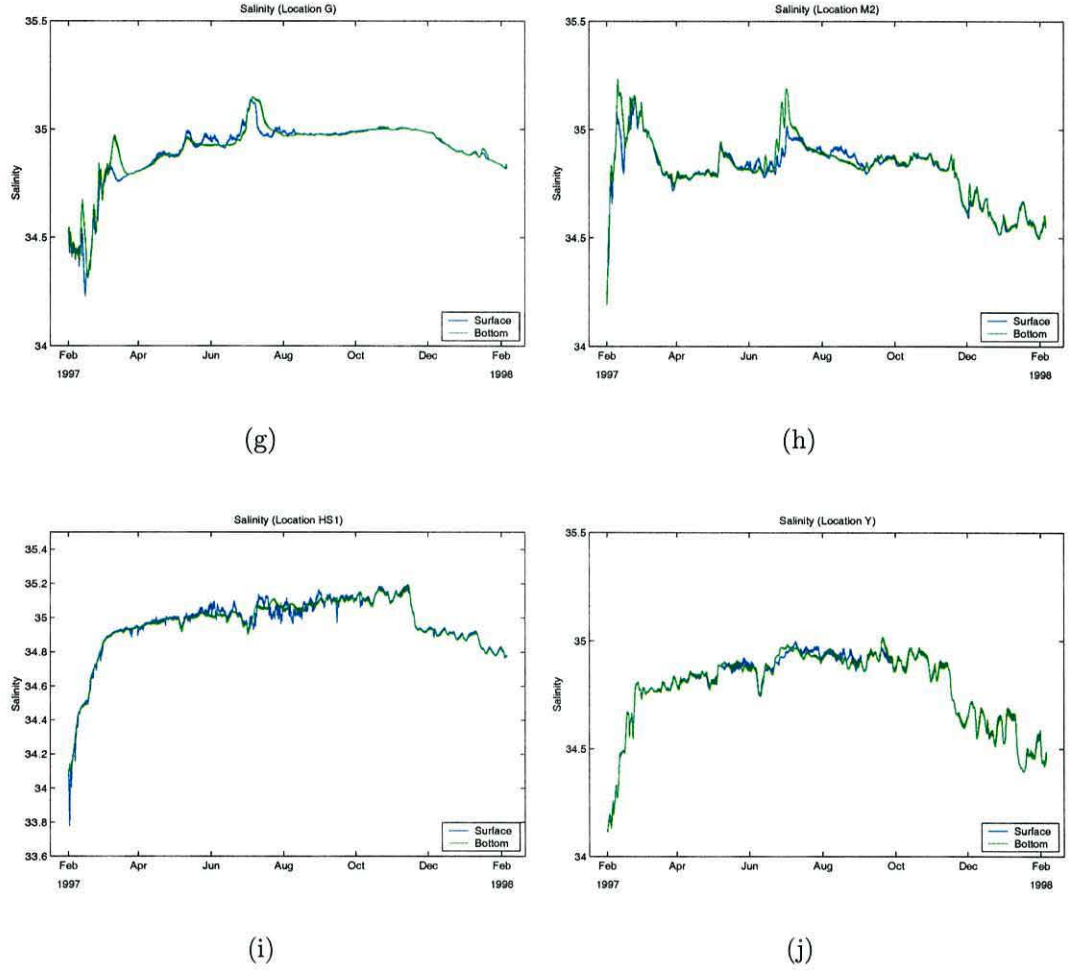

Figure 5.23: Seasonal evolution (from February 1997 to February 1998) of predicted hourly surface salinity (blue line) and bottom salinity (green line) for location shown in Table 5.1. Pictures from a) to g) refers to position A to G whilst h), i) and j) refer to positions M2, HS1 and Y respectively. Notice the different scale for salinity in fig. f) and i).

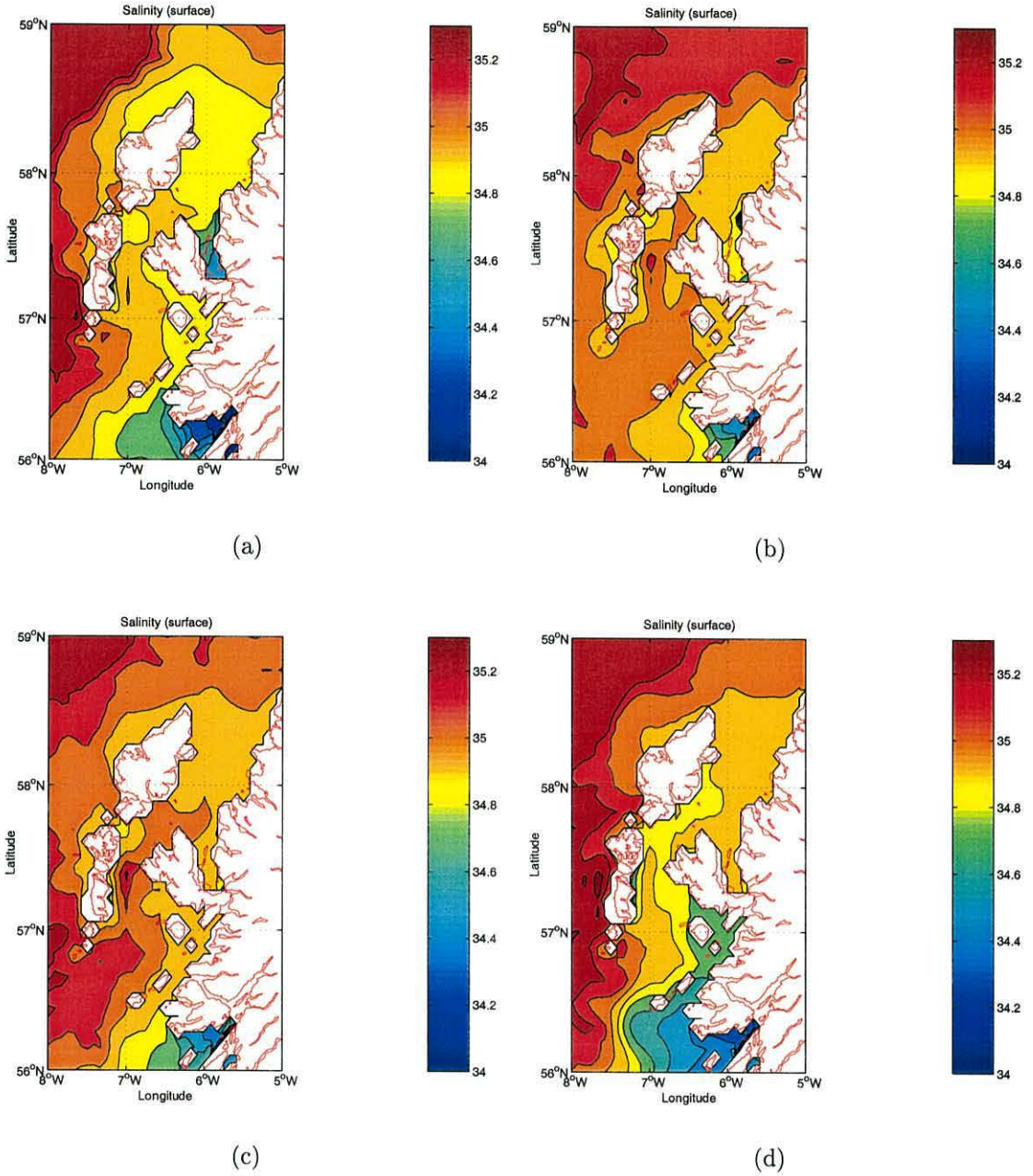

Figure 5.24: Modelled surface salinity used as comparison with the data collected by the Marine laboratory, Aberdeen (see Table 2.1) for a) *Spring*, b) *Summer*, c) *Autumn* and d) *Winter*.

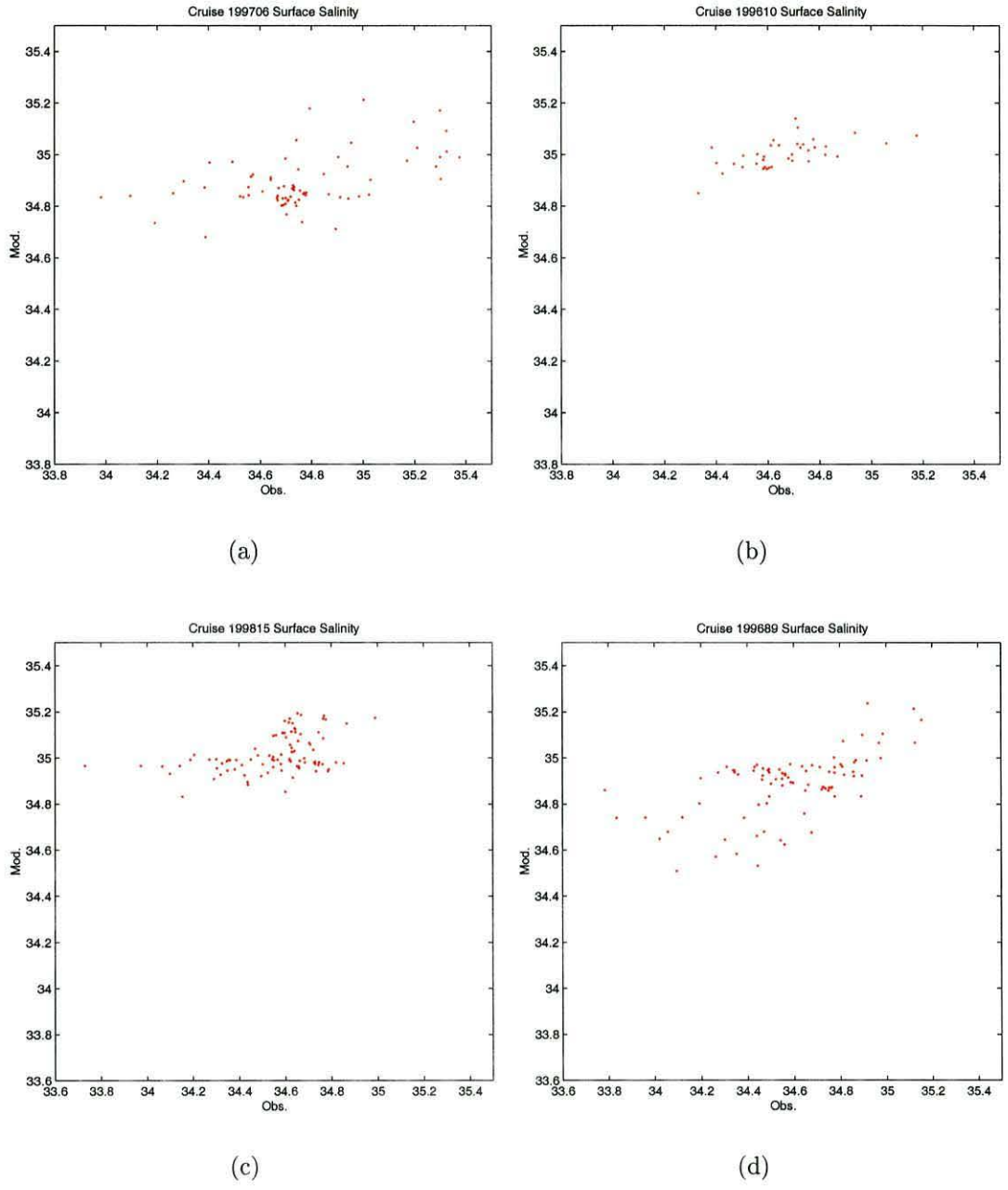

Figure 5.25: Comparison between surface salinity observed by the Marine laboratory, Aberdeen and the model results for a) *Spring*, b) *Summer*, c) *Autumn* and d) *Winter*.

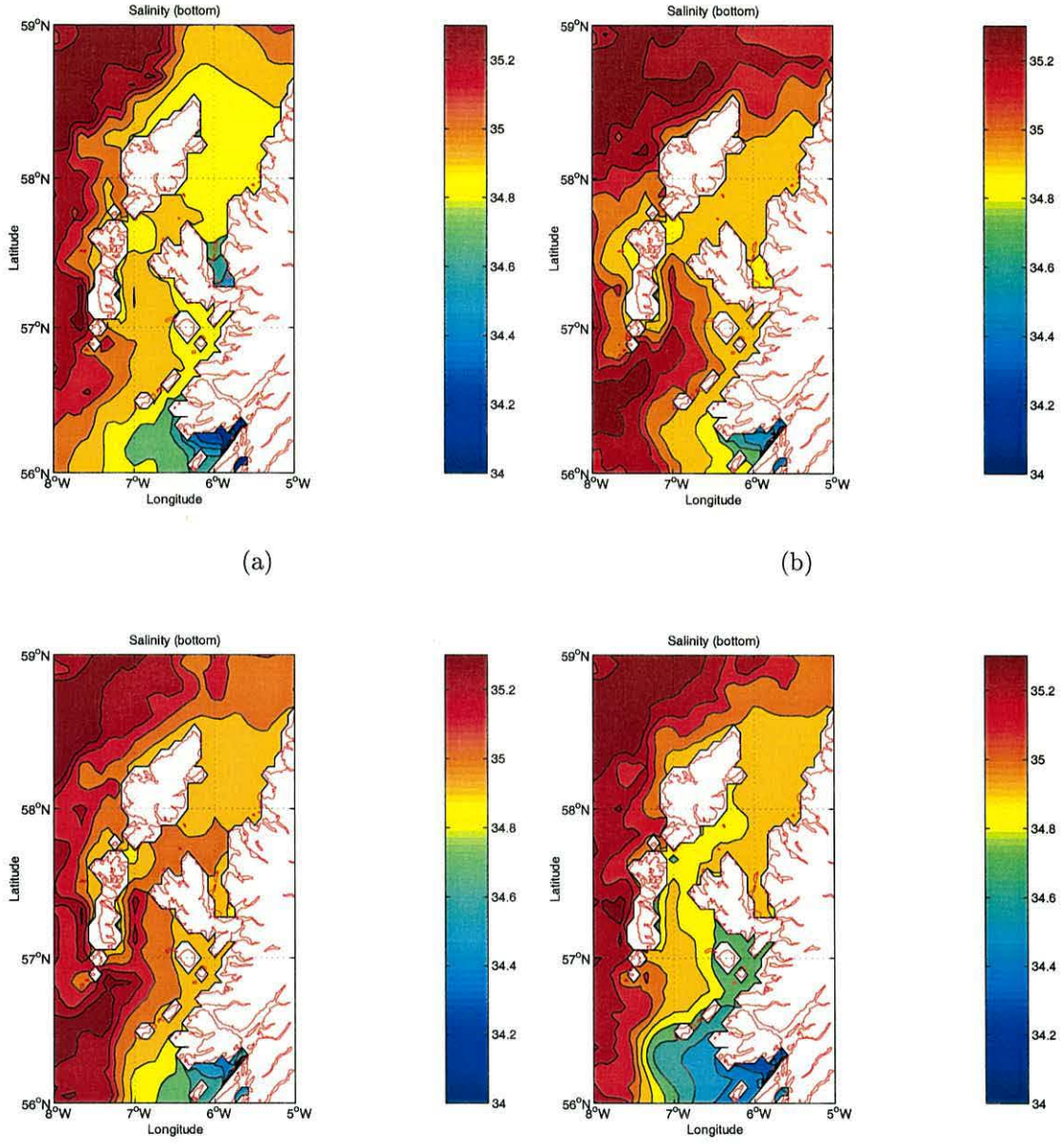

Figure 5.26: Modelled bottom salinity used as comparison with the data collected by the Marine laboratory, Aberdeen (see Table 2.1) for a) *Spring*, b) *Summer*, c) *Autumn* and d) *Winter*.

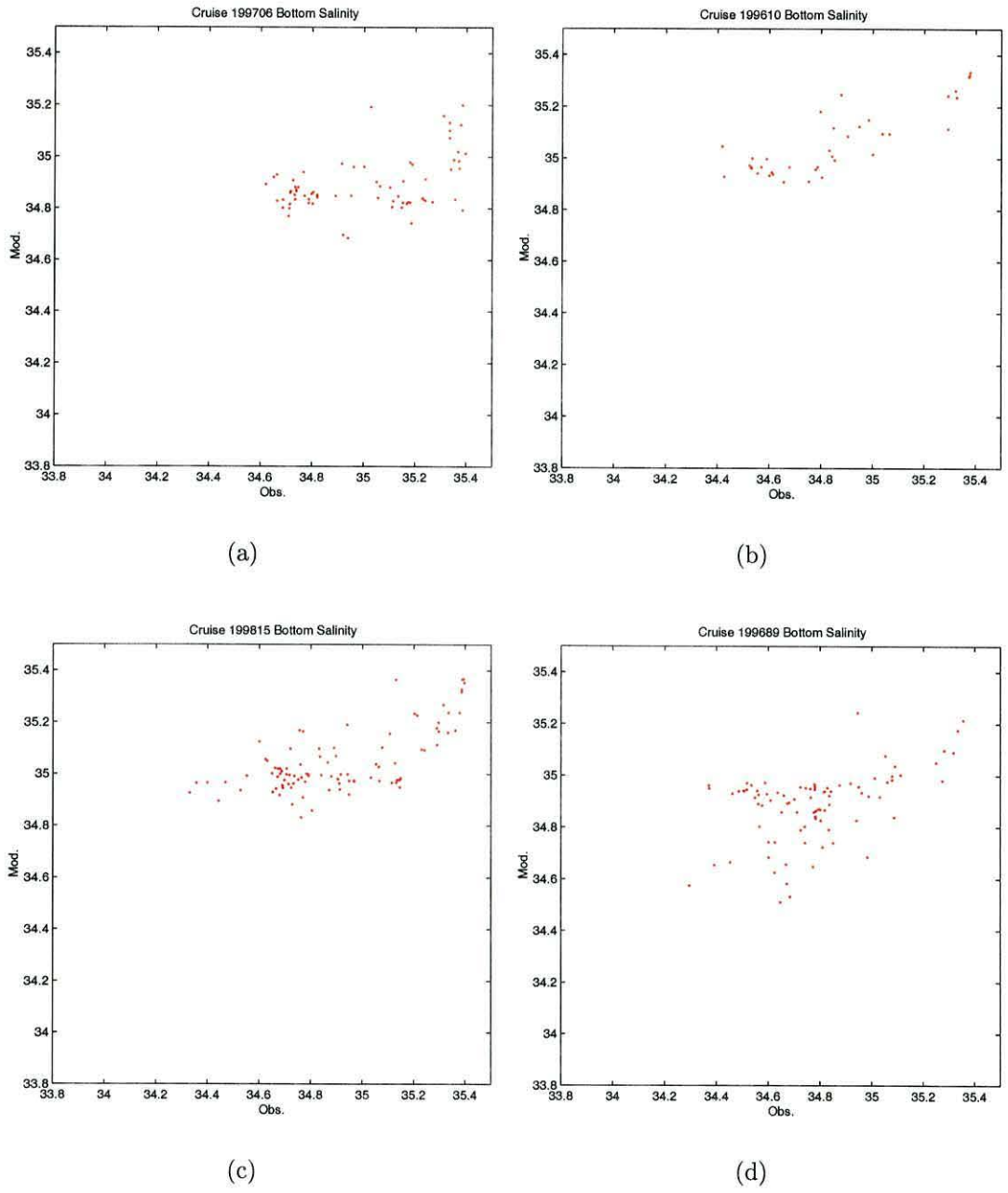

Figure 5.27: Comparison between bottom salinity observed by the Marine laboratory, Aberdeen and the model results for a) *Spring*, b) *Summer*, c) *Autumn* and d) *Winter*.

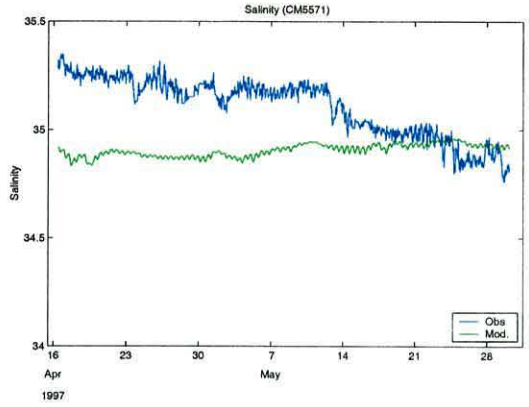

(a) CM 5571

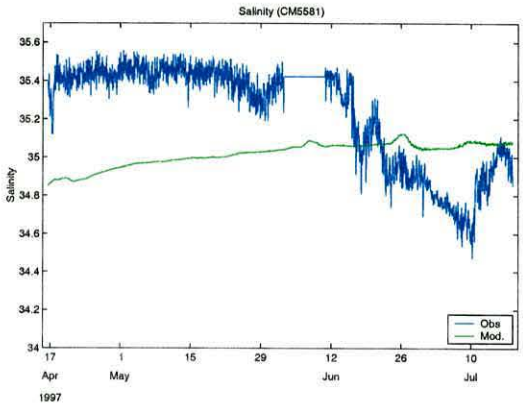

(b) CM 5581

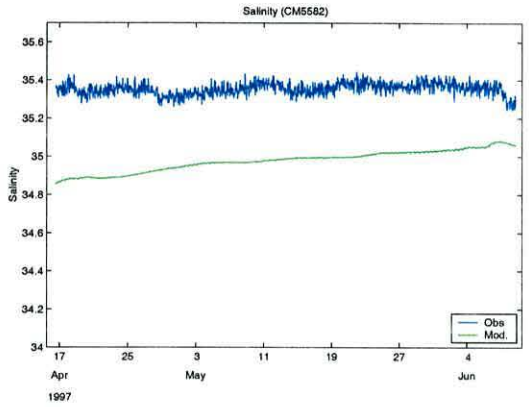

(c) CM 5582

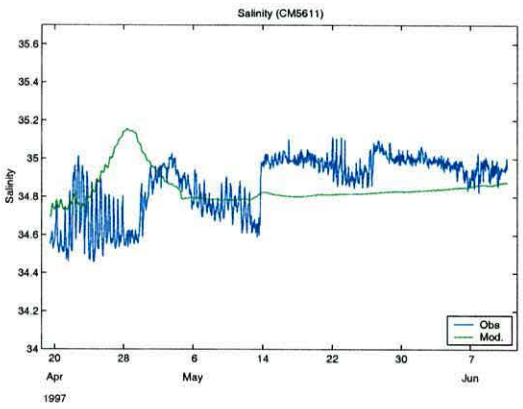

(d) CM 5611

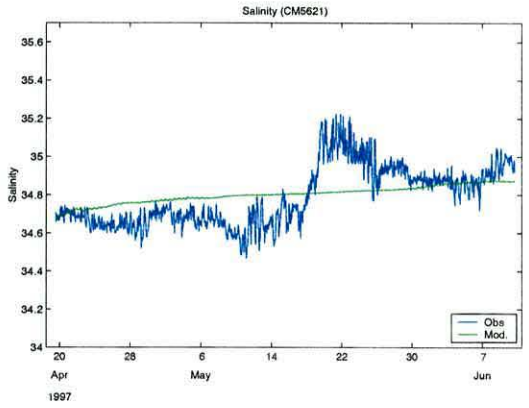

(e) CM 5621

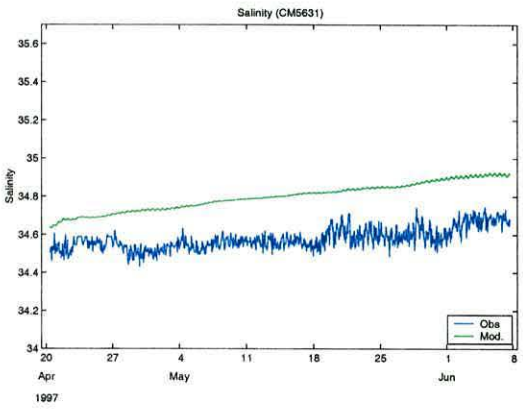

(f) CM 5631

Figure 5.28: Comparison between salinity measured by current meters deployed in locations described in Table 5.1 (blue line) the model results for the same locations (green line) .

Chapter 6

Baroclinic features on the Scottish shelf

6.1 Introduction

Results in the previous chapter demonstrate that the Princeton Ocean Model applied on the Scottish shelf is capable of reproducing the seasonal cycles of temperature and to a lesser degree salinity. Temperature was modelled in reasonable agreement with available observations. Simulated salinity showed lesser agreement with observations, the model was 'saltier' and there was not as much horizontal and vertical variability as measured in reality. In this chapter, two major features are investigated in detail, the tidal mixing front on the Malin shelf - also known as the Islay front in literature (see for example Simpson *et al.*, 1979; Hill and Simpson, 1989) - and the circulation on the Scottish shelf in the Sea of the Hebrides and the Minches, with particular interest in the associated transport. For both phenomena the model settings were unchanged.

6.2 The Islay front

In the first chapter the dynamics of tidal mixing fronts was reviewed whilst observations of this particular front were discussed in the second chapter. Some of the capabilities of the model to reproduce the front in the observed location are visible

in Figs. 5.18b,c and 5.20b,c which show the modelled temperature used for comparison with observations. The bottom front is clearly visible in the former set of pictures. During the summer and autumn the water column is almost vertically homogenous in the shallow part of the shelf, adjacent to the coast meanwhile strong stratification is present in the oceanic side of the region. Another indicator is the difference between surface and bottom temperature measured in locations A and B (see Table 5.1 and Fig. 5.16b) showing that the model can correctly reproduce the differential mixing. To further investigate the frontal position calculated by the model, the stratification parameter χ, introduced in (1.3), was calculated using tidal velocities of the M_2 constituent. Fig. 6.1 shows the results of this calculation; the critical value of 2.7 for $\log \chi$ is located in the expected position (between Malin head and the isle of Mull) and is in agreement with observation of the position of the Islay front (Simpson *et al.*, 1979). This parameter has been already used in other studies on frontal position with remarkable success when compared with satellite imagery (Pingree and Griffiths, 1978). In any case this parameter only gives information on the location of the front when it is fully developed and can be used to follow the spring-neap modulation and the consequent frontal movement (Simpson and Bowers, 1981). As shown by Hill and Simpson (1989) and as previously discussed, the Islay front also has a haline component which must be taken into consideration since there may be interaction between these two aspects. In both cases calculated salinity and temperature were compared with observations already discussed in the second chapter (Hill and Simpson, 1989) since there is no seasonal coverage for the year 1997 in this region of the shelf. Vertical sections were extracted from the model at latitude 56°13′ N, almost at the same location of observations (Hill and Simpson, 1989), to make the comparison as accurate as possible.

6.2.1 Evolution of temperature

The model started from a state of vertical homogeneity as discussed in the previous chapter. Fig. 6.2 shows that only horizontal gradients existed at the beginning of the simulation. At the end of February the situation is not changed, Fig. 6.3 and Figs. 6.4a,b showed a situation where only the horizontal front was present and the water was vertically well mixed. The shape of the front at this point was probably due to strong winds (velocities around 20 m s^{-1}) which were used to force the model. The same pattern was detected in the surface salinity and was the first indication

of the sensitivity of the model to the wind field (see later discussion). Temperatures were slightly warmer than observations by around 1°C and the surface to bottom front was not so sharp (see Fig. 2.10). A strong horizontal gradient is detectable close to the North Channel separating, as expected, the cold coastal water from the warmer oceanic water. In April (see Figs. 6.5 and 6.6a,b) surface temperature showed the effect of the increase of incoming solar radiation; in the deep western part a seasonal thermocline started to appear with a weak stratification (ΔT surface-bottom of the order of 0.5°C) whilst the water adjacent to the coast still remained mixed. Comparison with observations demonstrated that the model was reproducing reasonably temperature in this section with the weak thermocline was also present in April 1984 (Hill and Simpson, 1989). Another comparison with a satellite picture, already shown in Fig. 2.11, demonstrated that the model was not simulating the front with the correct intensity. In reality the front was already established with a horizontal gradient of 2°C whilst Fig. 6.6a,b showed no frontal signature in surface and bottom temperature.

A very different picture was found between simulated and observed temperature for the month of May, similar to the situation depicted in the satellite imagery. The simulation showed a frontal structure (Fig. 6.7 and Figs. 6.8a,b) with a well defined thermocline at a depth of 20 m and the characteristic isotherm outcropping at the surface (Simpson *et al.*, 1978), delimiting the thermally stratified area from the vertically homogenous one. The temperature field is slowly building toward summer values; Figs. 6.9 and 6.10a,b demonstrated that, at the beginning of June, the frontal structure was well developed. The thermocline was strong, separating bottom water with temperature around 9°C from surface water with temperature of almost 15°C. In this case it was possible to make a direct comparison with a satellite picture (shown in Fig. 6.11) taken during the same period of time (02/06/1997); comparing it with Fig. 6.10a the front appeared to be located in the same position and the horizontal temperature gradient was reproduced correctly with a difference of 4°C in both cases between the region delimited by the front. In both case, May and June, surface temperature showed the presence of ripples which contaminated the picture. To prove that these were generated by the turbulence closure scheme and not by the advection scheme the model was run again with the same settings but after day 70 the wind speed was doubled to increase the wind stress acting on the surface. Results for the temperature are shown in Figs. 6.12 and 6.13a,b and refer to the same time (125 days after the start of the simulation). The pattern of

surface and bottom temperature is completely changed; surface ripples are absent and the thermocline is not shallow any longer but has reached a depth of almost 40 m. Another factor concurring in creating the observed phenomenon may have been the fact that this part of the shelf presents a thermocline which intersects the coastline and could sustain internal waves, these waves could transfer energy in the high frequency thus creating unphysical grid scale noise (Mellor, 2003). The frontal structure is still present although with a weaker gradient with respect to the previous simulation (compare with Figs. 6.10a,b). Temperatures on the inner part of the front are unchanged (around $10° - 11°C$ in both cases) with differences up to 2°C on the Atlantic side of the front. Increased wind stress brought about a decrease of the surface temperature due to a better vertical mixing, bottom temperature showed also an increase with this new simulation, strengthening the case for a better penetration of the incoming solar heating downward into the water column. Where the mixing were already efficient (i.e. the coastal side of the front) differences were minimum. The agreement with the satellite picture of surface temperature is not as accurate as before, showing the difficulty of correctly reproducing the mechanisms of vertical mixing. Wind was not increased for the whole simulation because this action would have strongly contaminated the wind-driven dynamics.

The simulated picture for the end of July (Fig. 6.14 and Figs. 6.15a,b) agreed with the observations for July 1983; the front is still well developed and temperature were correctly reproduced with the outcropping of the thermocline at the surface as observed by Hill and Simpson (1988) (see Fig. 3d). The heat started to penetrate the water column; the thermocline deepened in the oceanic region and temperature increase also in the mixed region of the front, close to the coast. In the western oceanic region the heating is slower, the thermocline acting as an insulator barrier to further increases in temperature of the bottom cold pool. At the end of August (Fig. 6.16 and Figs. 6.17a,b) this phenomenon was more marked, the west-east section illustrated that temperature increased in the shallowest part and the cold water was pushed westward in the deep part of the domain strengthening the bottom front. This trend continued during the month of September where the outcropping of the isotherms at the surface was almost negligible (Fig. 6.18) and the front was concentrated at the bottom, with a neat separation between the oceanic and coastal water (Fig. 6.19b) whilst there was almost no thermal signature at the surface (Fig. 6.19a). In this case the mixed side was slightly warmer than the stratified, probably due to differential tidal mixing so that heat was propagating

downward more efficiently in this area. The front was approaching the breakdown so that isotherms were almost vertical, the situation in October (Fig. 6.20 and Figs. 6.21a,b) reflected better this fact; the shallow coastal area was vertically well mixed with temperatures around 13°C and the bottom front lost its sharp gradient. At the surface there was no front in this case. The complete breakdown of the frontal structure was reached at the end of November (Fig. 6.22 and Figs. 6.23a,b). Qualitative comparisons with temperature observations from November 1983 showed that the model was reproducing this field, with a weak horizontal gradient separating the ocean from the coastal waters. Unfortunately a more direct comparison could not be carried out since measurements and computed results referred to different years and interannual variations could not be taken into account but were supposed to be small. A similar situation was present in December (Fig. 6.24 and Figs. 6.25a,b) with lower temperatures due to winter cooling.

6.2.2 Evolution of salinity

In the case of the salinity field it was more difficult to observe a seasonal cycle, as mentioned in the previous chapter, and the changes are mainly due to fresh water discharge. The model started from a homogeneous condition (Fig. 6.26) and there was a sharp front separating the saltier oceanic water from the coastal fresher water. At the end of February (Fig. 6.27 and Figs. 6.28a,b) the front became more spread but it was still oriented along 7° W. A comparison with observations showed that the model was overestimating salinity by around 0.2 in the coastal area whilst underestimating it in the western part of the domain. A weaker front is still present in April (Fig. 6.29 and Figs. 6.30a,b) whilst Hill and Simpson (1989) showed that a very sharp front was present in April 1984 (Fig. 2.9c). Another feature missing in the model results was the wedge of very fresh water in the eastern part of the region due to the river runoff from the river Lochy. In the simulation the water was vertically homogenous; some errors could have been due to the fact that data in Fig. 6.29 were sampled along a parallel whilst the observations followed a curved path (see Fig. 1(b), Hill and Simpson, 1989). Another reason could be interannual variability, but no direct measurement was available for a comparison. In any case the most likely reason is that the model was not capable of reproducing correctly the salinity field (see previous discussion). The salinity field showed almost no changes at the end of May (Fig. 6.31 and Figs. 6.32a,b). There were no vertical gradients,

the only difference with the previous picture was an advance of the Atlantic water (see 34.8 isohaline) toward the coast. Observations (May 1986) were still picturing a sharp front, opposite to the simulations. This eastward movement of the front was still visible at the end of July (Fig. 6.33 and Figs. 6.34a,b). In this case the lateral intrusion of the saltier water was clearly visible at the western edge of the domain where salinity reached Atlantic values in relatively shallow waters ($\sim$ 35.1 in 120 m). Salinity from the end of August (Fig. 6.35 and Figs. 6.36a,b) to the end of October (Fig. 6.39 and Figs. 6.40a,b) was stationary in the section considered in this description and no isohaline movements were detected apart from a slight adjustment in the deepest part of the domain. In the horizontal plan some freshening was observed in the area adjacent to the North Channel due to the increase of the river runoff at the end of autumn. This was observed in the section at the end of November, when this pulse of fresh water reached this area with Fig. 6.41 and Figs. 6.42a,b depicting the fact. The front along 7° W strengthened recreating a salinity field similar to the one found in February. Comparison with observations in November 1983 showed that the position of the front was displaced westward (clearly visible in 6.42a,b) so that coastal water invaded a bigger portion of the coastal shelf. This was enhanced in December (Fig. 6.43 and Figs. 6.44a,b) where the coastal plume was present at the eastern part of the section but not in a form of a wedge as expected (Hill and Simpson, 1989) so that the model was slowly returning to the winter situation.

The picture of the seasonal evolution of the Islay front presented by these simulations agrees reasonably with direct observations in the region (Simpson *et al.*, 1979; Hill and Simpson, 1989) and with satellite imagery. In this particular case it is important to take into consideration that the dynamics of the front is controlled by two distinct contribution; the thermal generated by the seasonal interplay between tides and solar radiation and the haline controlled by the different masses of water converging in the region.

The thermal aspect of the tidal mixing front is well reproduced, at least until the breakdown in autumn. The model was capable of reproducing the frontogenesis, qualitatively and quantitatively in good agreement with the observations available. Starting from vertical homogeneity in late winter (February in this simulation) the incoming solar radiation slowly raised the temperature of the water column, reaching a maximum in late August - beginning of September with little spatial variation.

This was due to the fact that the heating flux supplied to the model was the same on the whole domain (the value measured at Tiree weather station). A comparison with a satellite picture showed that the model had a lag since the thermal front was already established when model results showed the contrary but this delay was minimal. The time of the frontal maximum gradient was not the same for surface and bottom. The surface front reached its maximum with an horizontal gradient of around 3°C early in the summer, the gradient peaked in May-July whilst the bottom gradient reached its maximum, again around 3°C, at the end of summer (August-September). As the heating continues throughout the year the heat penetrates the water column but the penetration does not happen at the same rate everywhere since in the strongly stratified areas the thermocline acts as an insulator. So the bottom water remains cool whilst the adjacent well mixed water slowly increases its temperature, strengthening the bottom front. As more time elapses, both regions cool reaching an isothermal situation in late winter due to strong wind and decreased heat input.

Simulations showed the frontal surface moving eastward in the first period, during the development, in agreement with Hill and Simpson (1989). After reaching the maximum the front moved back westward, as the water cooled down. This dynamical adjustment was less clearly visible at depth. The bottom front was more stable, its position did not change and there was only the sharpening described above. Local topography had a stabilising effect; the bottom front followed closely the bathymetry, being confined between the 60 m and 80 m isobaths. The importance of this topographic effect on shelf seas fronts was discussed by James (1990). In his work on the Flamborough front he showed, with the help of numerical simulations, that bathymetry and friction played an important role in stabilising the density front and the associated baroclinic flow. The surface front followed the isopleths of $\log(\chi)$ as expected (Simpson and Hunter, 1974) so that the surface position of the front was mainly controlled by the vertical mixing. The topographic effect was more marked with the salinity field, both bottom and surface fronts were orientated along isobaths but in this case numerical reasons could have enhanced this particular feature.

The interplay between the haline and thermal component is more difficult to interpret because of the poor quality reproduction of the salinity field. Also in this case it was possible to see an adjustment in the position of the front. Starting from the

situation in February, as time evolves so the saltier part of the front moves toward the coast but without evident changes in the coastal values. This corresponds with the diminished value of the fresh water discharge from the coast. As autumn is approached the front tends to move back and the coastal water becomes fresher again, to reach a peak in winter. The interaction envisaged by Hill and Simpson (1989) is not distinguishable in this set of simulations. The Rossby adjustment caused by the reduction of vertical mixing due to the presence of a strong thermocline can not be clearly seen in the section of salinity. Hill and Simpson (1989) expected the S shaped configuration of the top to bottom front to be stronger in summer when the thermal stratification is almost at its maximum. Model simulations show that isohalines are bent in the region of the thermocline (see Fig. 6.15 and Fig. 6.33) but the shape is not the one expected. In autumn the S shape in the isohaline is still present but can not be related with certainty to the collapsed of stratified fluid in a rotating frame.

Major errors for temperature in this set of simulations are caused by inability of the surface heat to penetrate the water column downward, as shown with the simulation with increased wind stress. Errors are mainly present in the surface layer, especially in the summer months, as can be seen in the temperature fields for June and July. Errors are bigger when stratification starts to develop, the thermocline is very shallow (Figs. 6.8a and 6.10a) and ripples can be observed. When the heat finally is transmitted downward the thermocline deepens and the surface ripples disappear. Bottom temperatures are not contaminated as much as in the surface front but the increase in wind stress determinates an increase in their values, weakening the vertical gradient. Salinity is overestimated, especially in the coastal region; Jones and Howarth (1995) encountered the same problem in their simulation of the southern North Sea. Supplying realist river runoffs and taking into consideration the balance between precipitation and evaporation they still found salinity to be overestimated in the regions close to the coast. Resolution was investigated but with unclear results (Jones and Howarth, 1995). A good agreement with observations was reached by artificially increasing the value of precipitation showing that their model was sensitive to this factor. In this study there was no mechanism for precipitation and evaporation so it is difficult to quantify their importance in the simulation but in the previous chapter it was shown that the buoyancy input from rain may be comparable with some of the other sources. Jones and Howarth (1995) also found that the model was also sensitive to boundary inputs making a point for the different

mechanisms which control salinity and temperature. Whereas temperature seems to have a strong local behaviour, mainly due to vertical processes of heat exchange, advection and surface and lateral boundary values play a more important role in the dynamics and simulation of salinity.

6.3 Recirculation cells

The regional long term circulation has been already discussed in a previous section (§2.4) and the main feature is a weak northward flow along the Scottish coast with a recirculation cell observed in the Sea of the Hebrides (Hill *et al.*, 1997b). The pattern is consistent with a density driven current which interacts with the topography and with the meteorological forcing (Simpson and Hill, 1986; Hill and Simpson, 1988). Available observations were also discussed together with estimates for the transport from radioactive isotopes measured in the area (McKay *et al.*, 1986; McKinley *et al.*, 1981). In this section the results from a fully seasonal simulation are presented and compared with the above data.

When dealing with long term circulation it is important to separate its various components. On the Scottish shelf the major components are the wind-driven and the density-driven circulation; it has been already shown in this work (see chapter 4) and others (Proctor and Davies, 1996; Xing and Davies, 1996c) that residual circulation caused by the interaction of tides with topography is almost negligible. The barotropic circulation caused by wind was also previously discussed; both southerly and westerly wind triggered a northward flow and in both cases the recirculation was present, with a larger strength associated with winds blowing from the south. Hill *et al.* (1997b) showed that the recirculation in the Sea of the Hebrides can be correlated with the density structure in the area; satellite tracked drifters released in 1995 followed trajectories closely related to the spatial distribution of the observed dome.

To separate the baroclinic component from the wind and from tidal residual, the approach utilised by Horsburgh (1999) was followed during these runs. Monthly prognostic fields were stored separately (at the last day of the month, from February 1997 to December 1997) and with these data a new series of runs were initialised. In these simulations the model was forced only with the tidal constituent M_2, with

no wind stress, active boundary conditions for temperature and salinity and with no heat flux. The model was run for 3 tidal cycles so that wind-driven currents were able to relax, maintaining the majority of the tidal energy Horsburgh (1999). In this way it was possible to obtain the residual circulation caused by the starting density structure, after having subtracted the tidal residual previously computed. Monthly surface and bottom circulation for the area are presented in Figs. 6.45a,b to 6.55a,b describing the seasonal evolution of the long term circulation. Figs. 6.56a,k and 6.57a,k show bottom σ_t and a vertical section of σ_t respectively, to correlate the evolution of density with this circulation; the vertical section was at the cell grids closest to the location of the sections used in (Hill *et al.*, 1997b).

The circulation at the end of February (Figs.6.45a,b) was marked by a strong northward flow of the order of 5 cm s^{-1} on the shelf and by a strong recirculation in the Sea of the Hebrides; velocities at the surface were around 10 cm s^{-1} whilst at the bottom they reached 5 cm s^{-1}. This pattern stretched from the entrance until the Little Minch, westward of Skye. The flow was both inside the Minch and outflanking the western side of the Outer Hebrides, as described by Craig (1959). In the North Minch the intrusion of the Atlantic water was clearly visible with a strength comparable to the southern cell. In both cases the topographic steering played a big role with the flow closely following the bathymetry. The contrast in density is not very marked (Figs. 6.56a) and there was no dense dome (Figs. 6.57a). At the end of March (Figs. 6.46a,b) the pattern of the flow remained very similar to the previous case, the strength diminished both in the southern and northern cells. After a month (Figs. 6.47a,b) the circulation still possessed the same strength as March with surface velocity around 5 cm s^{-1} and bottom currents around 2 cm s^{-1}. The bottom intrusion is also receding in the Sea of the Hebrides (Figs. 6.57c) and the effect of the solar heating started to be detectable in the density (lighter water flanking the Scottish coast close to the isle of Mull). At the end of May the overall picture for the surface and bottom circulation (Figs. 6.48a,b) became chaotic in the northern part of the region. On the Malin shelf the coastal current was still flowing northward with unaltered strength but the presence of the dense dome well outside the Sea of the Hebrides disrupted the pattern, bringing the recirculation cell to coincide with its position. Inside the Sea of the Hebrides there was still a faint recirculation together with a counter flow. This counter flow was more marked in the bottom currents with velocities of the order of $2 - 3$ cm s^{-1}. Densities (Figs.6.56d and Figs.6.57d) were assuming summer characteristics, with a pycnocline at the surface

and with an increase of contrast between deep waters and coastal waters. In June the circulation retained the above pattern, both in surface and at depth, but with an increase in strength (Figs.6.49a,b). The counterflow reached almost 10 cm s^{-1} at the surface and up to 5 cm s^{-1} at the bottom but the weak cyclonic recirculation was still present. The dome of denser water was clearly defined (Fig.6.56e and Fig.6.57e), with a pycnocline at depth of around 40 m. The recirculation returned in place after a month, in July (Figs.6.50a,b). The gradient of horizontal density was strong (Fig.6.56e) and this was reflected in the increase of surface and bottom velocities. The circulation closely followed the topographic constraint, showing also in this case a strong bathymetric control on density fronts. This was seen also in the northern cell; in July the northward intrusion reappeared, with the establishment of a strong density gradient and consequent associated flow. August showed a readjustment of the flow (Figs.6.51a,b) with a return to the conditions seen in first months of summer. The denser intrusion retreated again (Fig.6.56g), preserving its dome structure (Fig.6.57g) and the pattern of the flow followed this adjustment so that the residual flow was deviated westward, outside the chain of the Hebrides before entering them. In the Sea of the Hebrides the flow remained ill-defined. September displayed a similar condition (Figs.6.52a,b) with the dense structure in almost the same position (Fig.6.56h and Fig.6.57h) with a slight weakening of the density gradient inside the entrance of the Minch. Again October showed a readjustment of the flow structure (Fig.6.53a,b). The bottom density structure moved further south and the gradients weakened (Fig.6.56i and Fig.6.57i). Recirculation of the flow was detected at both end of the Minches with a strength of the order of 5 cm s^{-1}; the coastal current had the same strength in surface with velocities around 1 cm s^{-1} at the bottom. November displayed a 'summer-like' flow pattern (Figs.6.54a,b) again although the density structure was almost unchanged with respect to the previous month (Fig.6.56j and Fig.6.57j). Finally in December the recirculation was active again in both southern and northern areas (Figs.6.55a,b).

The picture emerging from these simulations is that the density-driven flow is not steady throughout the year, the main features are preserved with small-scale temporal and spatial variability. As observed by Simpson and Hill (1986) and Hill and Simpson (1988) the Malin shelf is characterised by a weak northward circulation, flanking the coast of Scotland. Simulations confirmed this picture although in their work the long term circulation was caused by the combined effects of wind, density, tidal and topographic effect. The coastal current was detected all year round with

a steady direction from the North Channel toward the isle of Tiree. Bathymetry is a key factor, the flow closely followed isobaths especially in the area of Tiree. From salinity and temperature sections and from the width of the coastal current itself it is possible to infer that the Scottish coastal current has a large Ekman number and a small Burger number. In this case the flow is non-linear and moderately stratified (Münchow and Garvine, 1993) and bottom friction plays an important role in defining the dynamics of the flow; there is disruption of the thermal-wind balance in the alongshore direction with a secondary circulation - offshore at the surface on onshore at the bottom (Hill, 1998).

The recirculation in the Sea of the Hebrides and in the North Minch displayed a less steady behaviour. In winter and spring time the cyclonic cell is active in both locations and follows the density structure but the flow becomes less defined when the dome moves from its original position, as observed during these simulations. It has been shown that the dome is not a static structure but exhibits variability according to the salt inflow from the ocean, the buoyancy from the coast and the solar heating. During these simulations the strength of the dome was not constant but was modulated by these three effects. It is difficult to separate their contributions but it is possible to say that in summer, close to the coast, the density was mainly controlled by temperature since the fresh water inflow was negligible but at the same time in the Sea of the Hebrides, there was a haline contribution due to the salty intrusion. Therefore it is not correct to assume that the flow is generated only by a process similar to the one discussed by Hill (1996) because this presupposes the dome to be static and these simulations showed that this assumption is not correct.

6.3.1 Estimates of Transport

Estimates of transport on the Scottish shelf have been made mainly with the use of tracers; salinity in the early stages (Craig, 1959) and the radioactive ^{137}Cs more recently (McKinley *et al.*, 1981; McKay *et al.*, 1986). These two works showed an average total transport of 11.5 $\times 10^4$ m^3 s^{-1} and 11.0 $\times 10^4$ m^3 s^{-1} respectively. This was the total transport along the shelf; the partition of the flow flowing inside the Minch and outside it was less clear. One of the aims of this particular project was to assess new transport rates and compare these with previous estimates. Transports were calculated using a method similar to the one employed by Young *et al.* (2001) for

their calculations of the fluxes through the North Channel. Instantaneous transport $Tr(t)$ for every east-west section of interest was calculated as

$$Tr(t) = \sum_n v_n(t)(H + \eta(t))\triangle x_n \tag{6.1}$$

where n was the number of elements on the section, v_n the instantaneous northern component of the depth-integrated velocity, H and $\eta(t)$ the depth and elevation of the element and $\triangle x_n$ its width. This value was calculated every hour for the length of the simulation and the result was harmonically analysed to extract the residual transport. This procedure was applied to all the sections of the grid contained in the Minch, delimited by the Scottish coast and the coast of the outer Hebrides. In this work no attempt was made to try to estimate the transport outside the chain of the Hebrides because of the lack of a boundary. Results for this seasonal analysis is shown in Fig. 6.58; histograms represent the average monthly transport, expressed in 10^4 m^3 s^{-1}, through four sections in the region of interest. These sections were chosen so that two were lying in the Sea of the Hebrides (latitude 57.22° N and latitude 57.66° N) whilst the remaining two were situated in the North Minch (latitude 58.00° N and latitude 58.55° N). This particular arrangement sampled the transport at both ends and followed its seasonal development. Results showed the largest transport in February with a minimum in June. This picture was evident at both ends although there was a difference in the magnitude of the transport in the northern region. To try to understand the causes of this pattern the transport was compared with the wind; the monthly average of the northward component of the wind used in the simulation was correlated with the monthly transport and correlation coefficients r^2 were between 0.89 and 0.90 showing a strong link between wind-forced circulation and transport.

To evaluate the contribution of the density driven circulation to the overall transport a barotropic seasonal simulation was set up. In this case the model was forced for one year with the same wind stress as before but with no solar heating or exchange of temperature and salinity at the boundaries. This method allowed separation of the wind contribution. The transport through the Minch was calculated as above and results are shown in Fig. 6.59; Fig. 6.60 illustrates the difference in transport between these two runs to emphasize the density contribution. Differences in total baroclinic and barotropic transports (Fig. 6.60) showed there was a significant density contribution but with differences between the southern and northern region.

Density contribution for the transport in the North Minch reached its minimum in February as expected because of the homogeneity of the water in winter. The magnitude of the contribution increased as time elapsed, showing the growth in importance of the baroclinic component during the summer. There was another peak in December which was thought to be linked to the increase of buoyancy due to the fresh water inflow (probably still not visible in February). The cell in the Sea of the Hebrides displayed the same trend but relative differences between months were larger suggesting the fact that northern recirculation presented a more stable character throughout the year and southern transport depends on the variability of the intrusion.

For a further estimate of the influence of the wind on rates of transport, monthly calculations of cross-correlation between the northward wind and residual current component were executed using hourly values. Fig. 6.61a,k show the results graphically; wind and transport were significantly correlated as expected, the lag corresponding to the maximum of the cross-correlation varied between 4-6 hours depending on the month and the section considered. The lag increased with time being shorter in February and the peak was more marked. As the spring and summer developed peaks became more spread to become sharper again in winter. These results strengthen the view that modelled transport was mainly wind-driven with weaker density-driven components contributing especially in summer, when baroclinic effects reached their maximum. In any case the fact that the wind is also weaker in this period must be taken into consideration so that baroclinic effect on the overall circulation is enhanced.

Comparisons with previous estimates showed that this model predicted an annual averaged transport through the Minches at times a factor of two larger than previous estimates made with passive tracers and current meters. For the fully baroclinic runs the annual average spanned from 15.8 and 15.9×10^4 m^3 s^{-1} in the southern sections to 19.2 and 19.1×10^4 m^3 s^{-1} in the two northern sections. A direct annual comparison with the observations listed in McKay *et al.* (1986) is not possible since these were obtained in a shorter periods of time, mainly in summer and in different years. In any case the estimate for the transport in July 1997 varies from 8.8 to 11.6×10^4 m^3 s^{-1} in good agreement with the transport of 9×10^4 m^3 s^{-1} calculated in 1981 by McKay *et al.* (1986) and close to the estimate give by Craig (1959). It should be noted that those were values for the entire transport (inside and outside

the Minch) whilst in this study only the inner transport was considered.

Data from corresponding model cells were analysed and compared with current meters observations collected by the Marine Laboratory, Aberdeen in the same locations (see chapter 5). Only the current meter CM5612 was not used because of the very short period of time when velocities were recorded. To evaluate the steadiness of the flow the Neumann factor, b defined in Ramster *et al.* (1978) as

$$b = \frac{|<\mathbf{v}>|}{<|\mathbf{v}|>} \times 100\% \tag{6.2}$$

was calculated for the observed and the computed series of the residuals. This approach was already used by Hill and Simpson (1988) in their work on the variability of the Scottish Coastal Current. Their evaluation showed that the parameter b was smaller than 70% in all locations and during all deployments. This threshold value defines when the flow can be considered steady but care must be taken in interpreting a lower value when only a short period of observation is available (Ramster *et al.*, 1978).

Current meter	b_m	b_m	b_o	cc (u)	cc (v)	cc (u)	cc (v)
CM5571	12.4%	48.2%	90.4%	0.07	0.63	0.26	0.68
CM5581	96.5%	69.6%	54.9%	-0.31	-0.21	-0.27	-0.16
CM5582	92.6%	61.6%	60.5%	0.04	-0.31	-0.17	-0.30
CM5602	89.3%	77.9%	91.9%	-0.51	-0.01	-0.55	-0.01
CM5611	68.4%	31.6%	65.1%	-0.01	0.38	-0.10	0.32
CM5621	71.7%	77.9%	84.2%	-0.11	0.26	-0.06	0.43
CM5622	59.9%	77.1%	41.1%	-0.06	0.44	-0.09	0.36
CM5631	69.3%	6.7%	90.5%	-0.46	0.48	-0.18	0.60
CM5632	27.2%	47.3%	8.1%	-0.34	0.63	-0.33	0.51

Table 6.1: Values of the steadiness parameter for computed series of velocities (b_m) - first column refers to the period of deployment and the second column for the whole length of simulations - and observations (b_o) and correlation coefficients between eastward (cc (u)) and Northward component of wind and computed residual velocity - first column refers to the period of deployment and the second column for the whole length of simulations.

A quantitative description of these data is given in Table 6.1 which contains the values of the parameter b for the period of simulations for both observation and computed residual plus the value of this parameter for the whole of the simulation and correlation coefficients for the simulated components for the two set of data. The computed flow was relatively stable during the period of deployment for both series of predicted and observed velocities. For the majority of the points the steadiness parameter was bigger than 60% with peaks of 90% denoting a very stable flow. Differences between observations and predictions are more marked for the first three current meters; CM5581 and CM5582 recorded a flow less stable than simulations whereas data from current meter CM5571 showed the opposite with no steady computed flow. In this case observations and simulations seem to describe a different picture; in reality the flow in the Sea of the Hebrides is steady close to Tiree and less steady at the entrance of the Minch to exhibit stable direction again in the Little Minch, close to Skye. At the northern end there is better agreement, showing the flow being steady. An alternative picture of the nature of the current is described in Table 6.2 which shows the comparison between the mean of the observed and predicted components of the residuals for the period of deployment.

Current meter	u_{ro} (cm s^{-1})	v_{ro} (cm s^{-1})	u_{rm} (cm s^{-1})	v_{rm} (cm s^{-1})
CM5571	7.0 (4.8)	1.3 (1.6)	0.2	0.76
CM5581	-2.0 (3.6)	1.5 (2.7)	-3.2	-4.8
CM5582	-2.5 (2.9)	0.7 (2.7)	-5.1	-3.3
CM5602	4.2 (2.0)	-6.2 (4.7)	0.1	-2.4
CM5611	-1.2 (2.9)	-3.6 (3.1))	0.1	-1.9
CM5621	2.6 (4.0)	5.8 (3.9)	-2.9	2.3
CM5622	1.8 (3.0)	0.1 (3.6)	0.3	1.1
CM5631	1.1 (2.0)	4.2 (2.6)	-0.1	-2.6
CM5632	-0.1 (2.0)	0.1 (1.5)	1.1	0.1

Table 6.2: Comparison between observed residual components (first two columns, values of standard deviation are in brackets) and computed residual components (last two columns) of the residual flow averaged on the period of deployment of the current meters. Velocities are in cm s^{-1}.

Current meters in the southern part recorded a net northward flow which is not

reproduced correctly by the model. This could be related to the inability of the model to reproduce the density driven flow as demonstrated early. In this case data contain also tidal and wind contributions both for observations and simulations showing that the density driven flow has a net effect on the total flow. In the middle of the Minch both observations and simulations present a southward flow which is also found at the western side of the northern end of the North Minch, showing a net intrusion of Atlantic water. Again there is disagreement between observations and model results on the eastern side of the North Minch but on the whole the model predicts the right order of magnitude for the residual flow. Finally correlation coefficients in Table 6.1 show that there was correlation between the northward component of the wind and the simulated northward residual as expected since the wind represents the major forcing.

6.4 Conclusions

Evolution of temperature, salinity and water transport in three locations of the Scottish shelf were investigated in detail, namely the tidal mixing front in the Malin region and the two recirculation cells at both extremities of the Minch. All displayed a strong seasonal signature, in particular the frontal system. Simulations confirmed the dual nature of the Islay front (Hill and Simpson, 1989), a tidal mixing front with a seasonal development driven by the solar heating and tidal mixing and a haline component.

Seasonal development of the temperature field was qualitatively and quantitatively well reproduced. The model simulated correctly the frontogenesis. Starting from a condition of vertical homogeneity a fully stratified condition was reached in July-August with only a small delay when compared with observations from satellite imagery. The model was able to recreate the structure of a shelf sea coastal front. Surface temperatures were overpredicted in places by $2° - 3°$C due to a combination of the bulk heating parameterisation and the turbulence sub-closure scheme responsible for the mixing coefficient of diffusivity and viscosity (Mellor and Yamada, 1982). The breakdown of stratification was not reproduced perfectly. Water showed a tendency to retain the heat acquired during summer. Again the likely candidate was the heating flux routine probably because of a feed back mechanism. The well

mixed condition was again reached in winter, showing that the model reasonably reproduced the seasonal cycle of temperature on this region of the European shelf.

The haline component was not simulated with the same accuracy. In this case the seasonal signal was weaker and comparisons with observations (Hill and Simpson, 1989) showed that modelled gradients were smoother than reality. The model overestimated the computed salinity field and the plume of fresher coastal water, seen in observations (Ellett, 1979; McKinley *et al.*, 1981; Ellett and Edwards, 1983; McKay *et al.*, 1986), was poorly reproduced so that the wedge of fresher water flowing along the coast was almost absent. Because of this inability of the model, the interplay between the two components of the front envisaged by Hill and Simpson (1989) was not investigated and this needs to be addressed in further simulations. Topography and its interactions with the field of density was again shown to be important as a stabilising factor for the position of the front. Both thermal and haline components of the Islay front were lying along isobaths with almost no change throughout the length of the simulation.

The density-driven component of the circulation was studied on a monthly basis, as a first step to try to understand the contribution of various components of the circulation to the total transport. Results confirmed the existence of recirculation cells at both ends of the Minch. While having a steady character in winter months, the southern cell showed episodes of flow reversal in the summer which are difficult to explain using a simple theory of a static dense dome triggering a cyclonic circulation. During the simulation the dome was not static but displayed a dynamic nature, intruding and retracting in the Sea of the Hebrides. Contributions from the Atlantic could have played a role in creating these episodes. The density driven circulation on other parts of the shelf was in agreement with the idea of a weak baroclinic circulation due to horizontal density differences. Computed values were of the order of $2 - 3$ cm s^{-1} on the majority of the shelf and are compatible with the fact that the tidal front is not disrupted by the long term circulation (Simpson, 1981).

The total transport was calculated, using the vertically averaged northward component, in various sections of the Minch. Residual transport showed a marked seasonal behaviour and this was correlated to the fact that it was thought to be mainly wind-driven. Fluxes were at their peak in winter, when winds were strong. In summer (with weaker winds) transport decreased but the baroclinic component showed an increase in strength; transport increased again in winter with an increase

in the density-driven component due to increased fresh water runoff. Computed results were in reasonable agreement with previous observations with the flux passing between the Outer Hebrides and the Scottish mainland. Stability analysis of the observed and predicted flow showed the flow was relatively stable during the period of deployment of the current meters with some difference between the southern and northern part of the region which were also visible in the mean values of residuals.

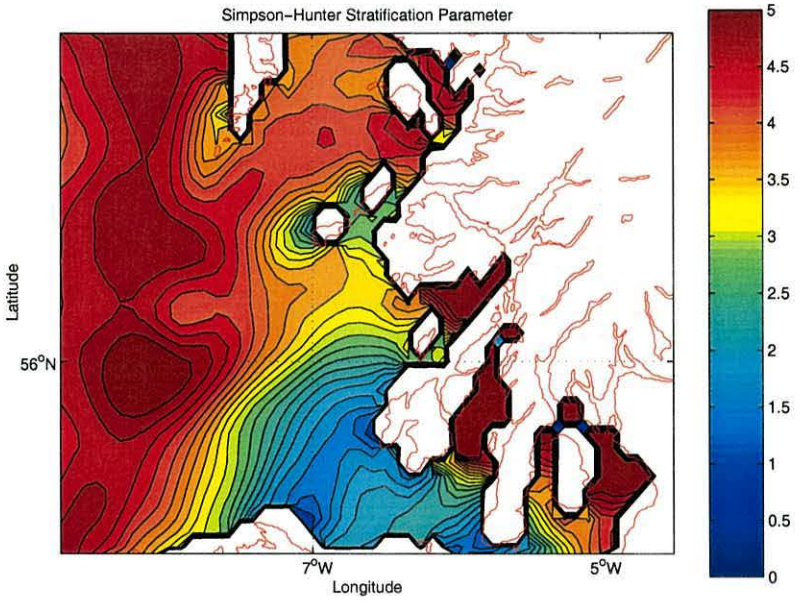

Figure 6.1: Calculated Stratification parameter defined in (1.3). Contours every 0.1 units.

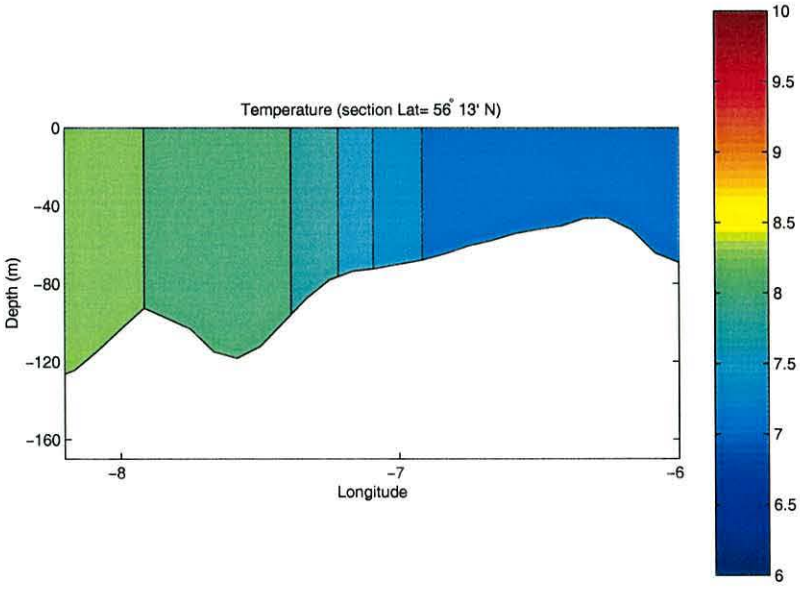

Figure 6.2: East-west section at Lat. 56°13′ N of initial temperature (corresponding to the 01/02/97). Contours at 0.1°C intervals.

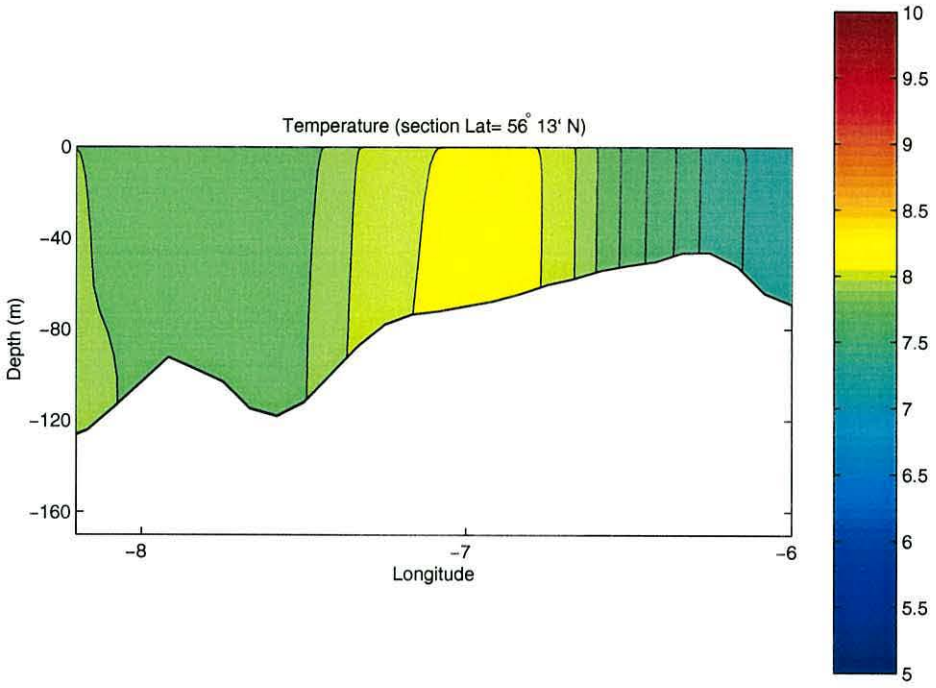

Figure 6.3: East-west section at Lat. 56°13′ N of modelled temperature after 28 days of simulation (corresponding to the 28/02/97). Contours at 0.1°C intervals.

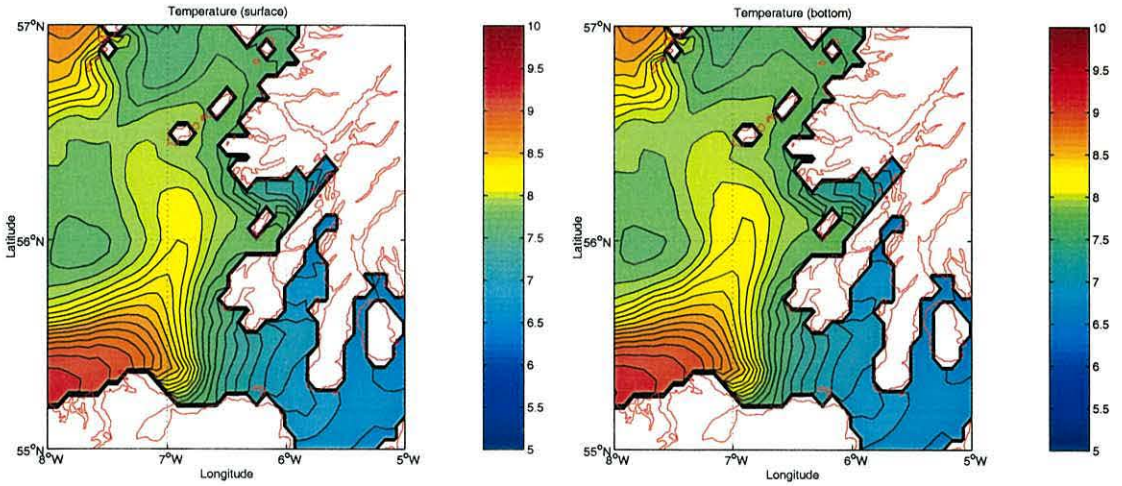

(a) (b)

Figure 6.4: Computed temperature: a) surface b) bottom after 28 days of simulation (corresponding to the 28/02/97). Contours at 0.1°C intervals.

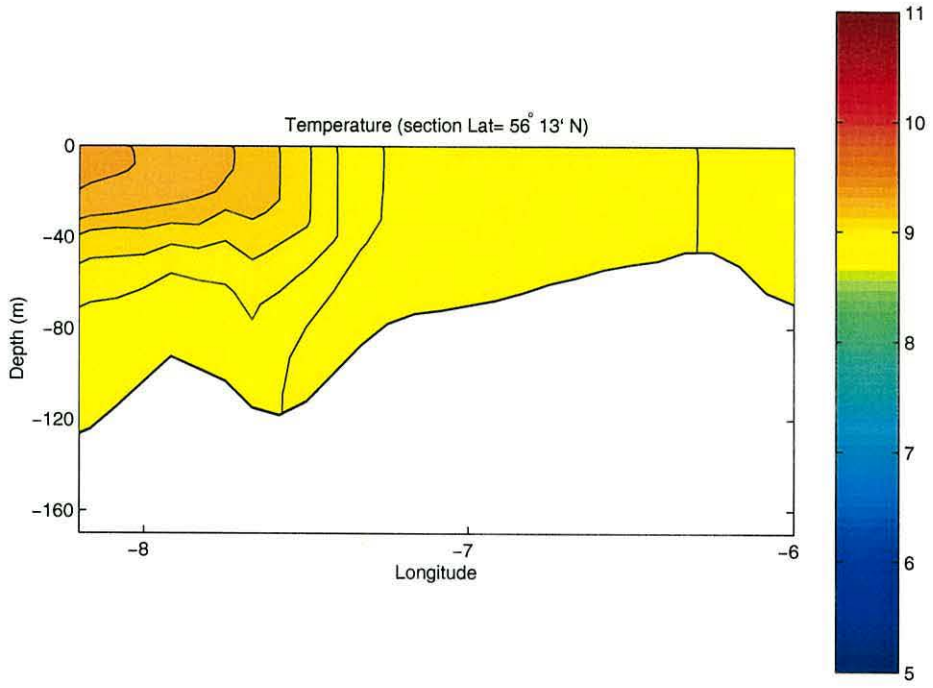

Figure 6.5: East-west section at Lat. 56°13′ N of modelled temperature after 89 days of simulation (corresponding to the 30/04/97). Contours at 0.1°C intervals.

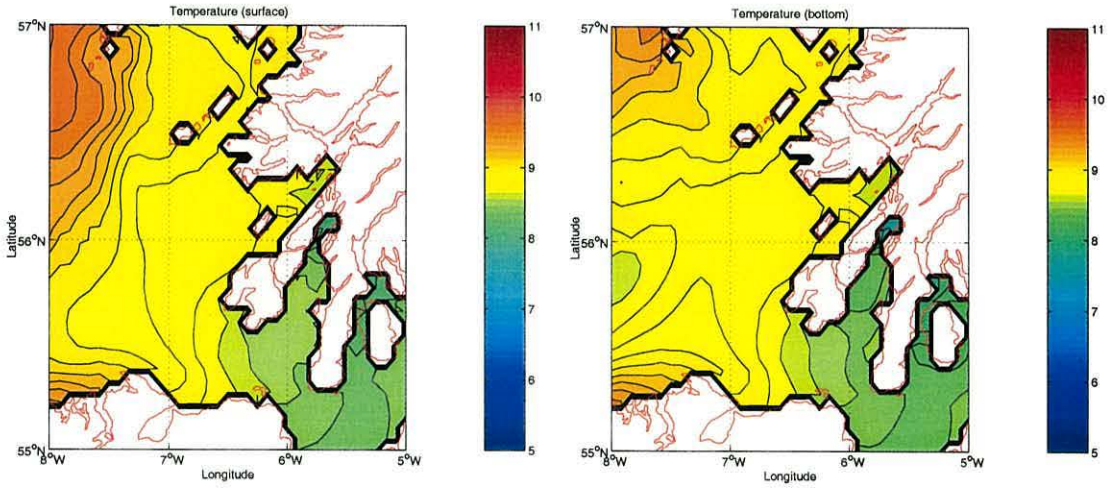

(a) (b)

Figure 6.6: Computed temperature: a) surface b) bottom after 89 days of simulation (corresponding to the 30/04/97). Contours at 0.1°C intervals.

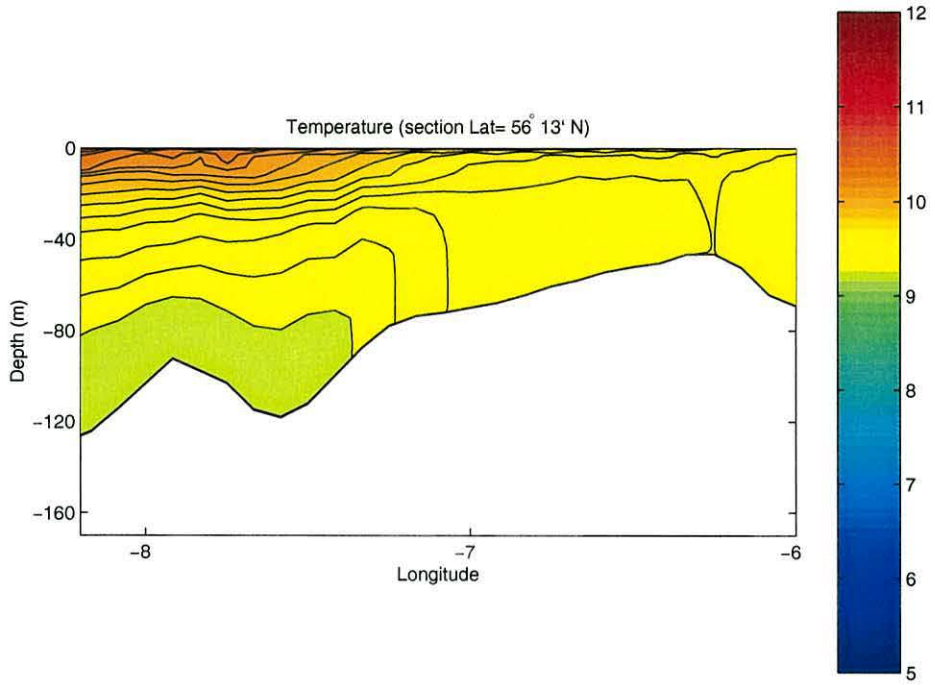

Figure 6.7: East-west section at Lat. 56°13′ N of modelled temperature after 110 days of simulation (corresponding to the 21/05/97). Contours at 0.1°C intervals.

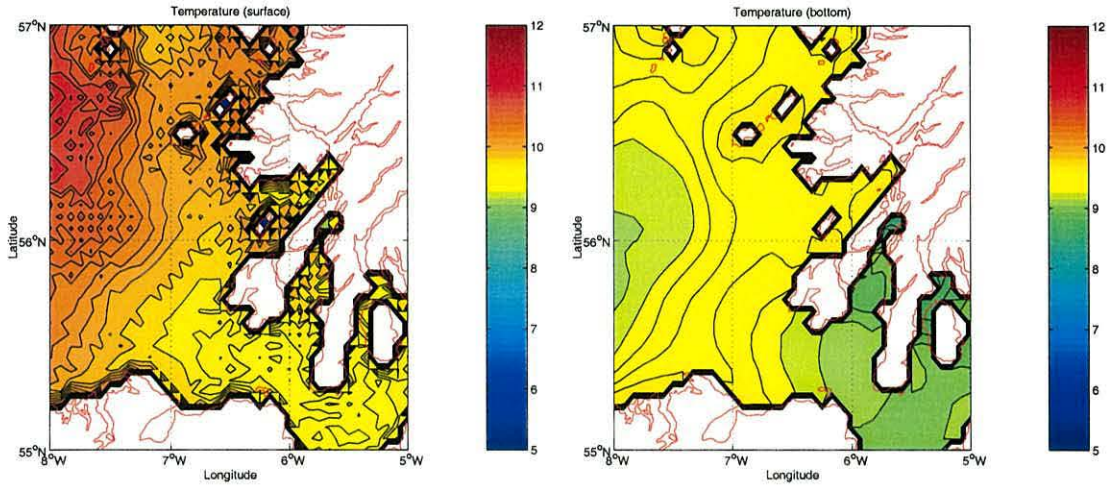

(a) (b)

Figure 6.8: Computed temperature: a) surface b) bottom after 110 days of simulation (corresponding to the 21/05/97). Contours at 0.1°C intervals.

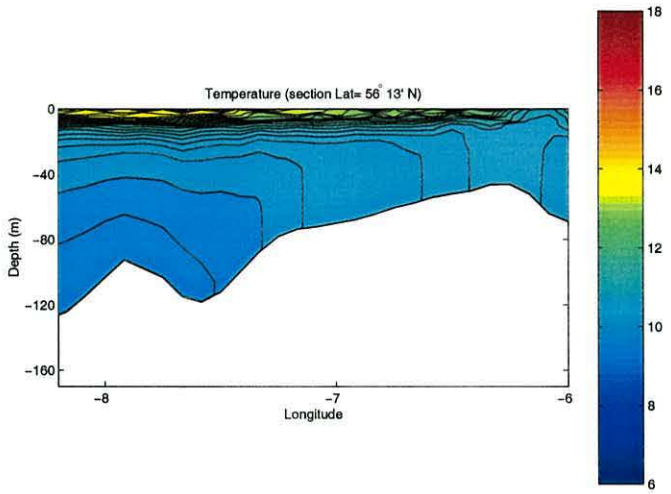

Figure 6.9: East-west section at Lat. 56°13′ N of modelled temperature after 125 days of simulation (corresponding to the 04/06/97). Contours at 0.25°C intervals.

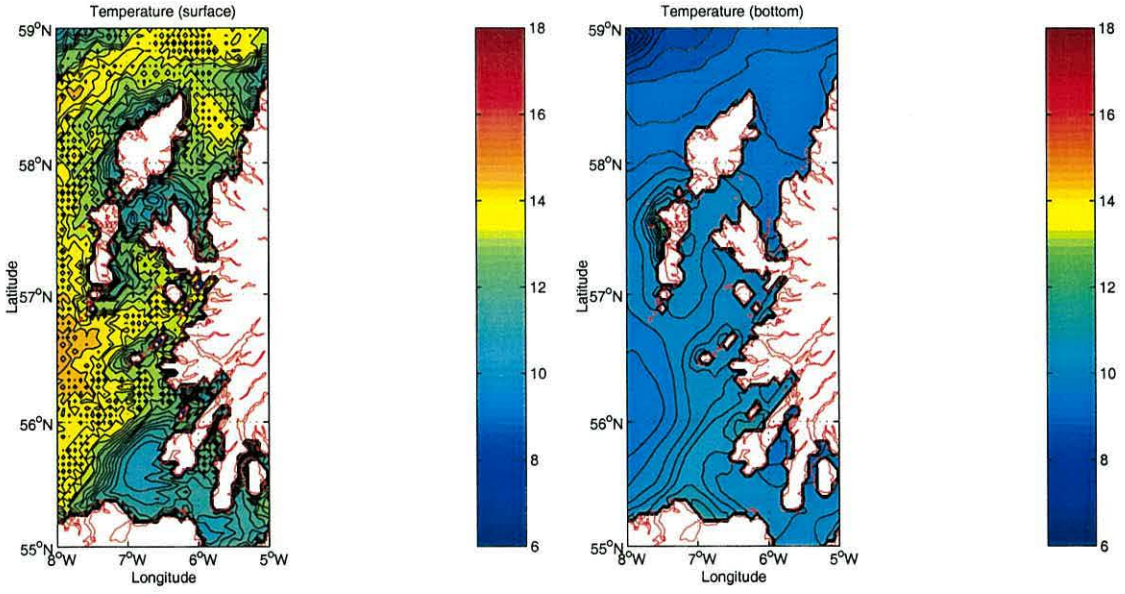

(a) (b)

Figure 6.10: Computed temperature: a) surface b) bottom after 125 days of simulation (corresponding to the 04/06/97). Contours at 0.25°C intervals.

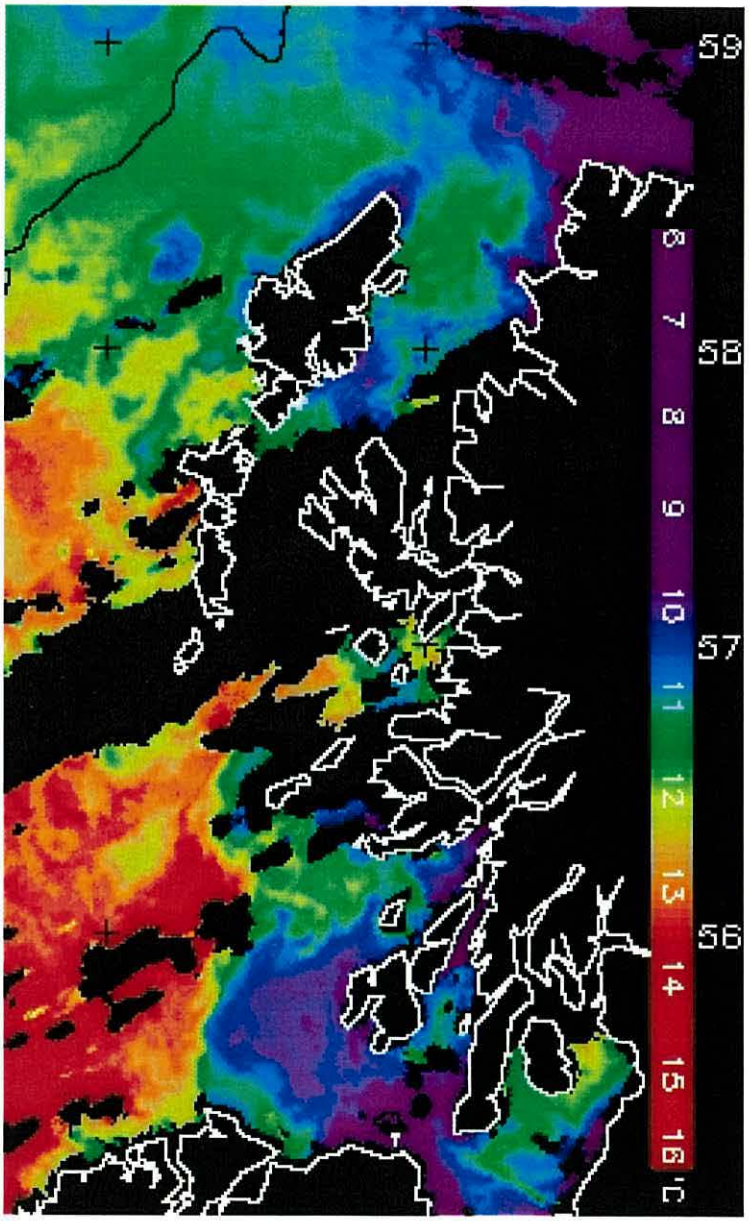

Figure 6.11: Satellite picture showing sea surface temperature for the 02/06/97.

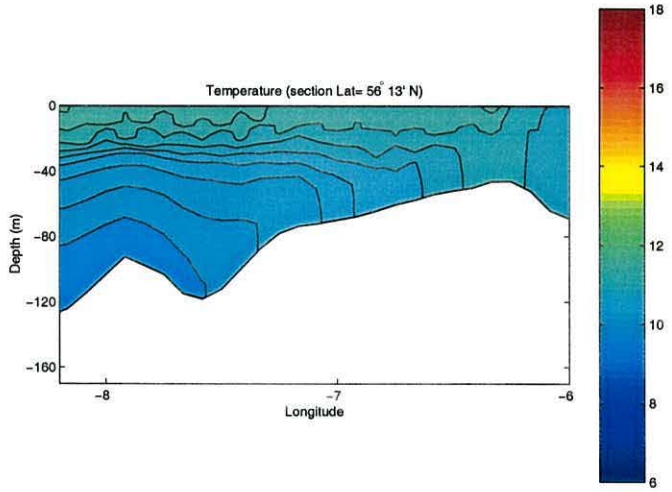

Figure 6.12: East-west section at Lat. 56°13′ N of modelled temperature after 125 days of simulation (corresponding to the 04/06/97) with increased wind stress. Contours at 0.25°C intervals.

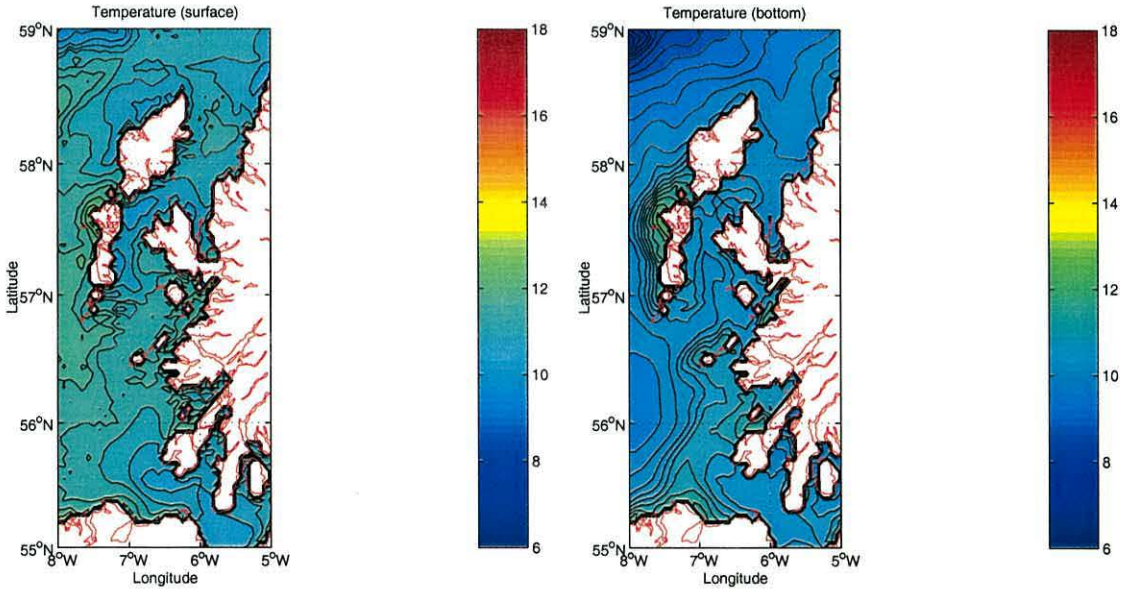

(a) (b)

Figure 6.13: Computed temperature: a) surface b) bottom after 125 days of simulation (corresponding to the 04/06/97) with increased wind stress. Contours at 0.25°C intervals.

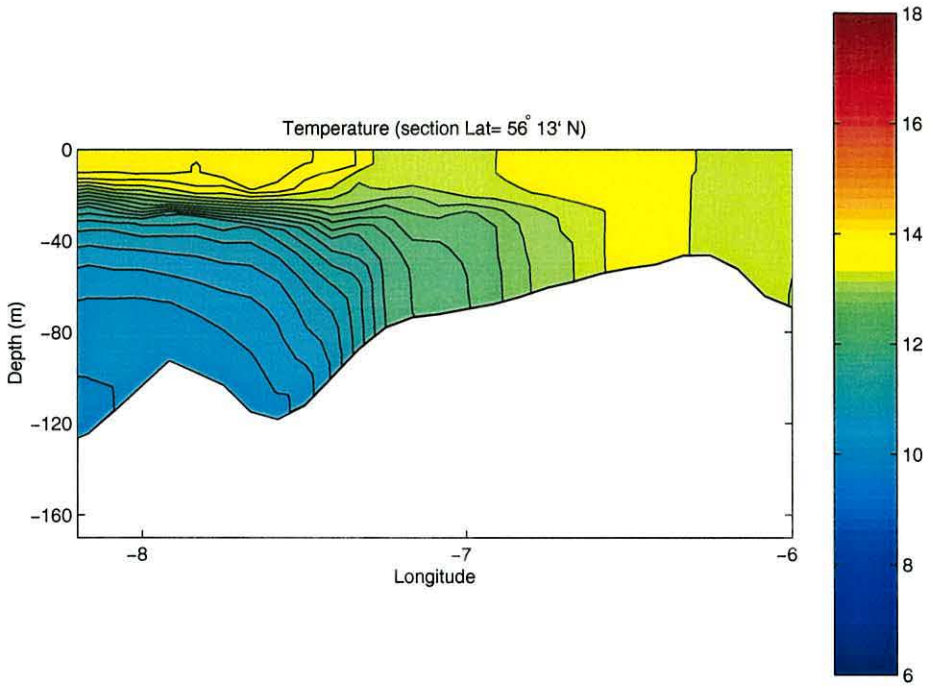

Figure 6.14: East-west section at Lat. 56°13′ N of modelled temperature after 181 days of simulation (corresponding to the 31/07/97). Contours at 0.25°C intervals.

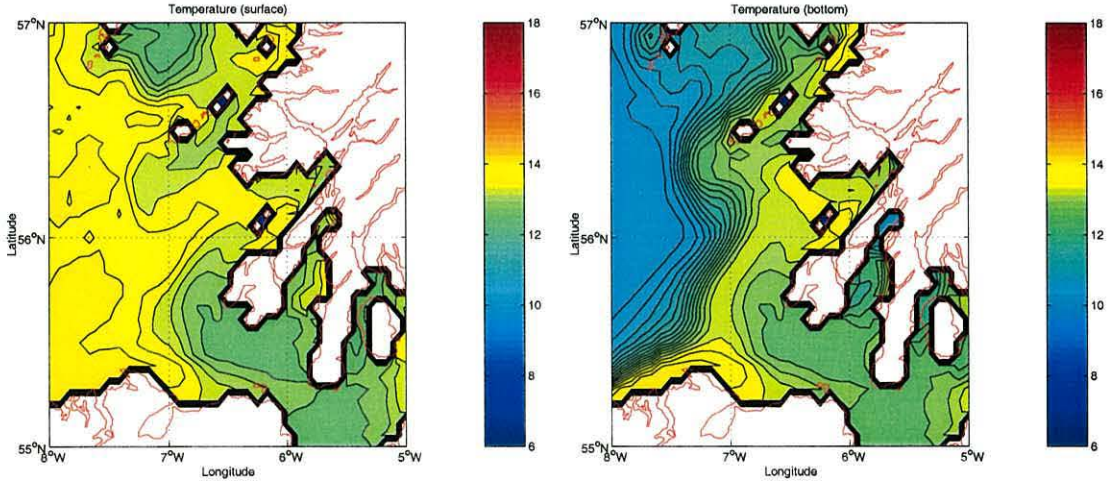

(a) (b)

Figure 6.15: Computed temperature: a) surface b) bottom after 181 days of simulation (corresponding to the 31/07/97). Contours at 0.25°C intervals.

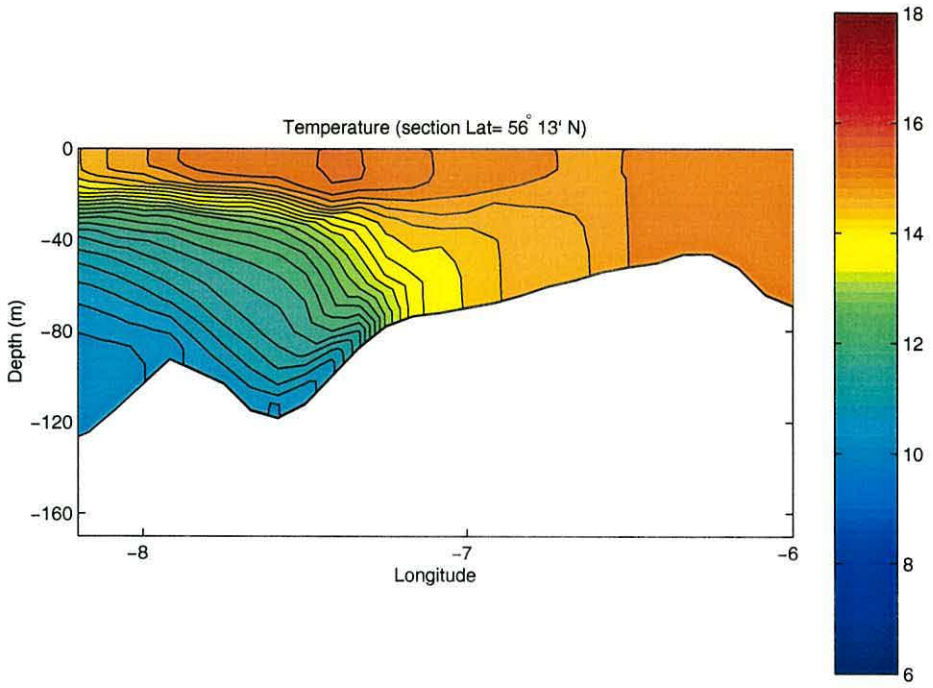

Figure 6.16: East-west section at Lat. 56°13′ N of modelled temperature after 212 days of simulation (corresponding to the 31/08/97). Contours at 0.25°C intervals.

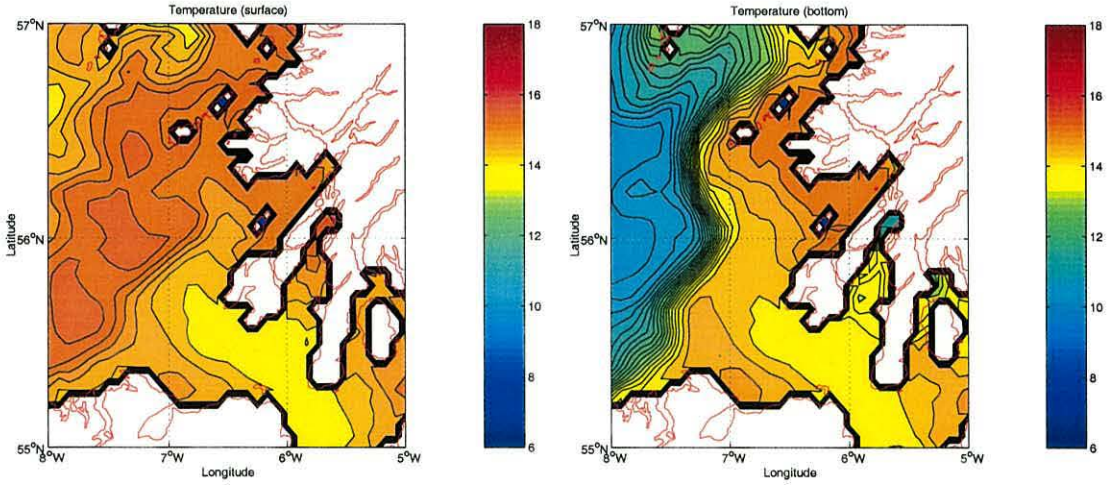

(a) (b)

Figure 6.17: Computed temperature: a) surface b) bottom after 212 days of simulation (corresponding to the 31/08/97). Contours at 0.25°C intervals.

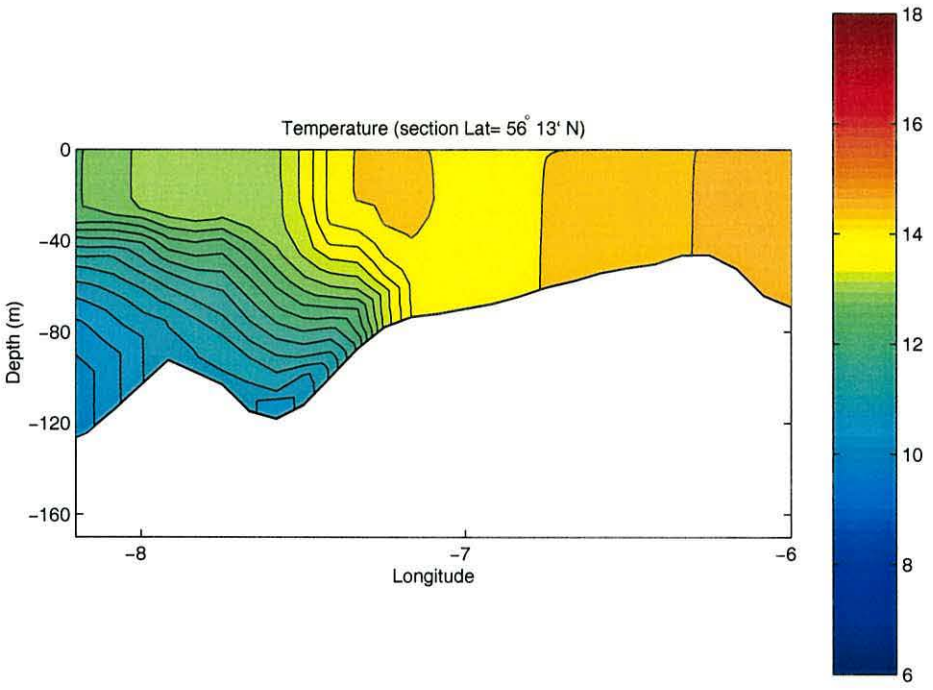

Figure 6.18: East-west section at Lat. 56°13′ N of modelled temperature after 242 days of simulation (corresponding to the 31/09/97). Contours at 0.25°C intervals.

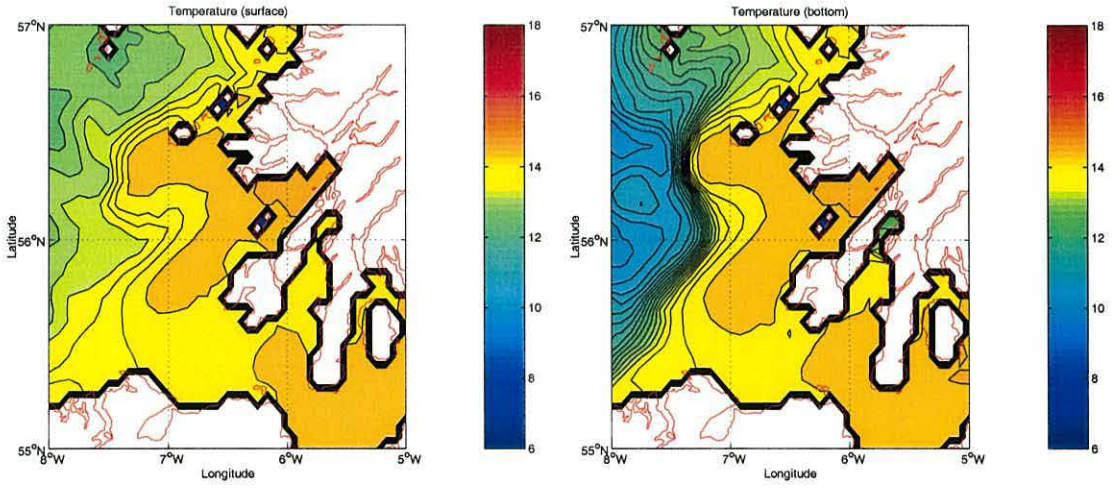

(a) (b)

Figure 6.19: Computed temperature: a) surface b) bottom after 242 days of simulation (corresponding to the 31/09/97). Contours at 0.25°C intervals.

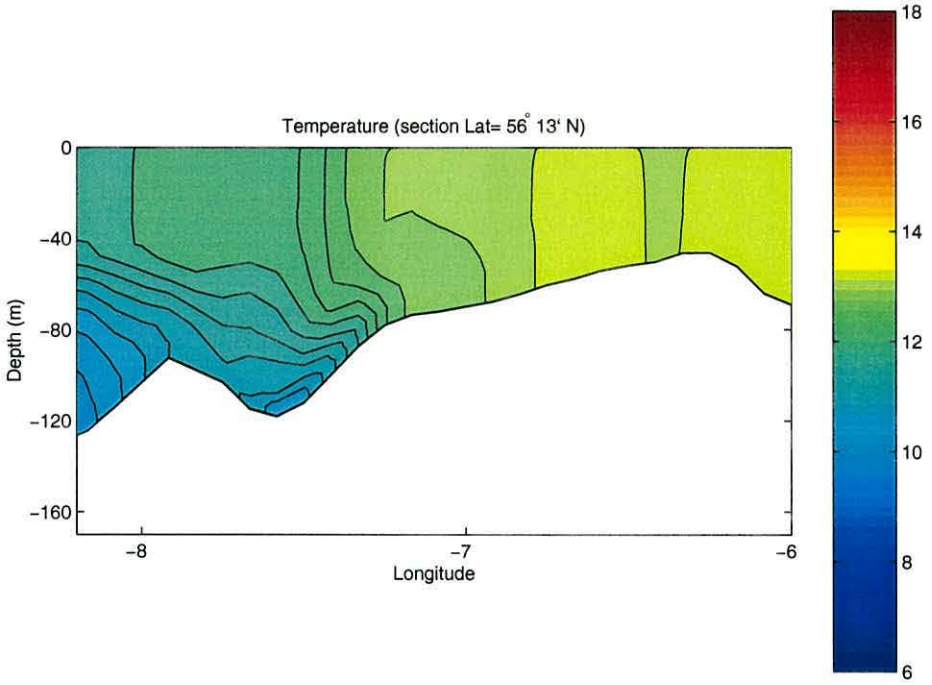

Figure 6.20: East-west section at Lat. 56°13′ N of modelled temperature after 273 days of simulation (corresponding to the 31/10/97). Contours at 0.25°C intervals.

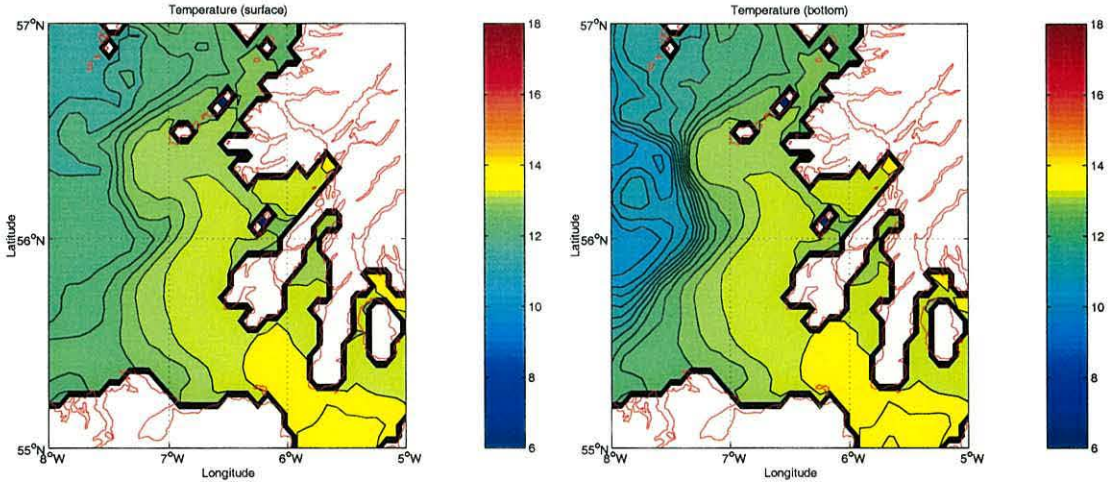

(a) (b)

Figure 6.21: Computed temperature: a) surface b) bottom after 273 days of simulation (corresponding to the 31/10/97). Contours at 0.25°C intervals.

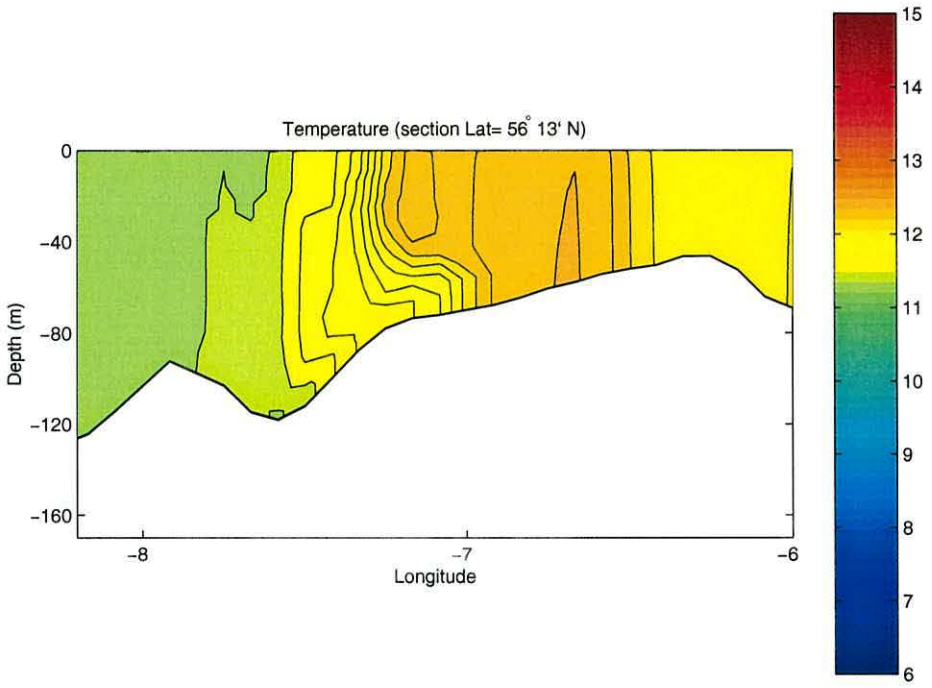

Figure 6.22: East-west section at Lat. 56°13′ N of modelled temperature after 303 days of simulation (corresponding to the 30/11/97). Contours at 0.1°C intervals.

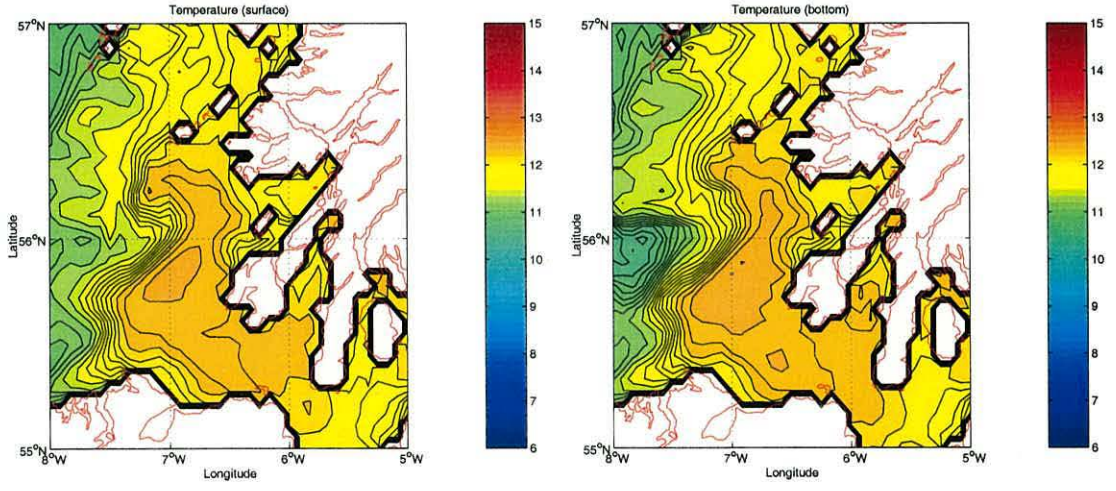

(a) (b)

Figure 6.23: Computed temperature: a) surface b) bottom after 303 days of simulation (corresponding to the 30/11/97). Contours at 0.1°C intervals.

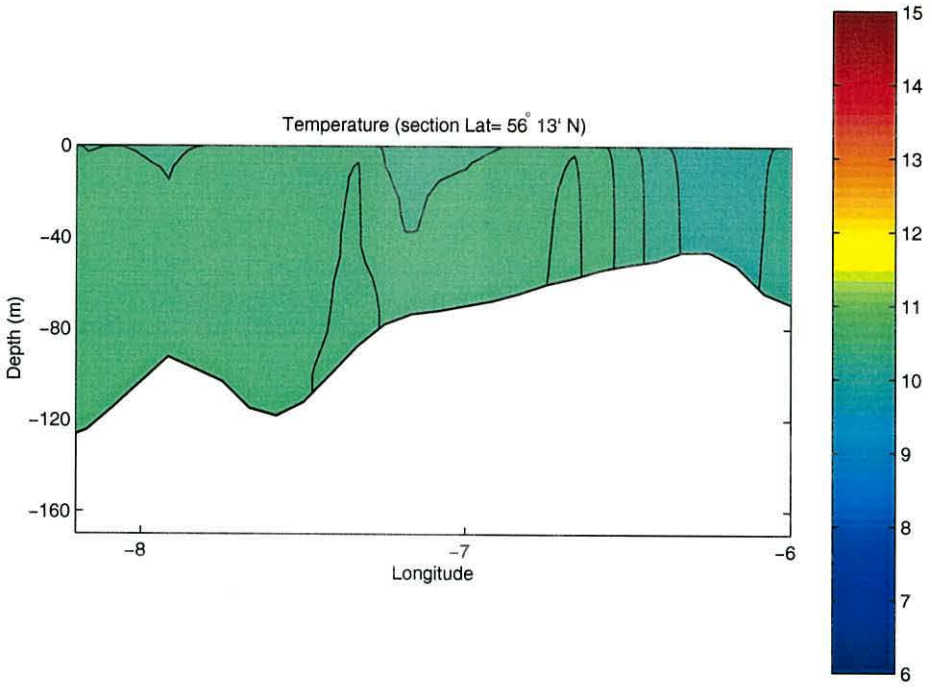

Figure 6.24: East-west section at Lat. 56°13′ N of modelled temperature after 334 days of simulation (corresponding to the 31/12/97). Contours at 0.1°C intervals.

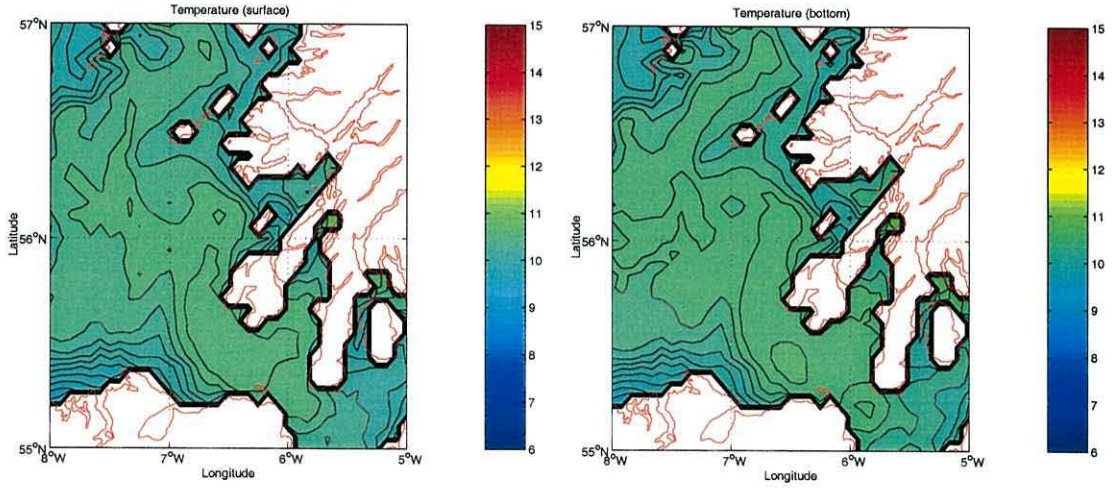

(a) (b)

Figure 6.25: Computed temperature: a) surface b) bottom after 334 days of simulation (corresponding to the 31/12/97). Contours at 0.1°C intervals.

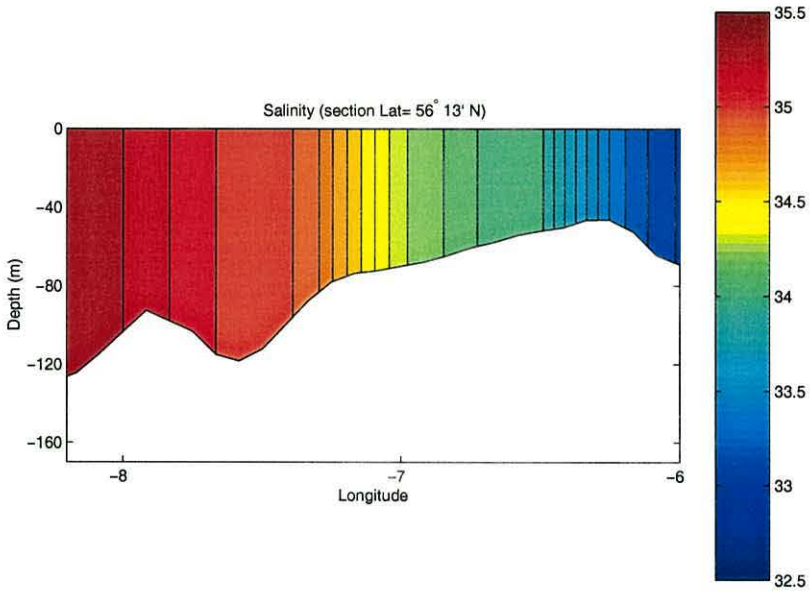

Figure 6.26: East-west section at Lat. 56°13′ N of initial salinity (corresponding to the 01/02/97). Contours at 0.1 intervals.

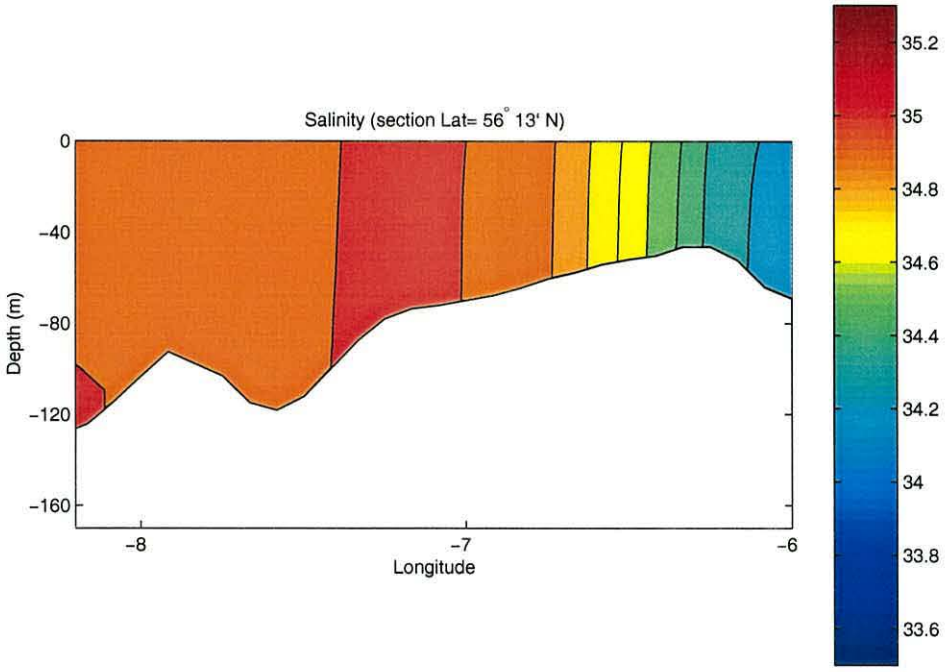

Figure 6.27: East-west section at Lat. 56°13′ N of modelled salinity after 28 days of simulation (corresponding to the 28/02/97). Contours at 0.1 intervals.

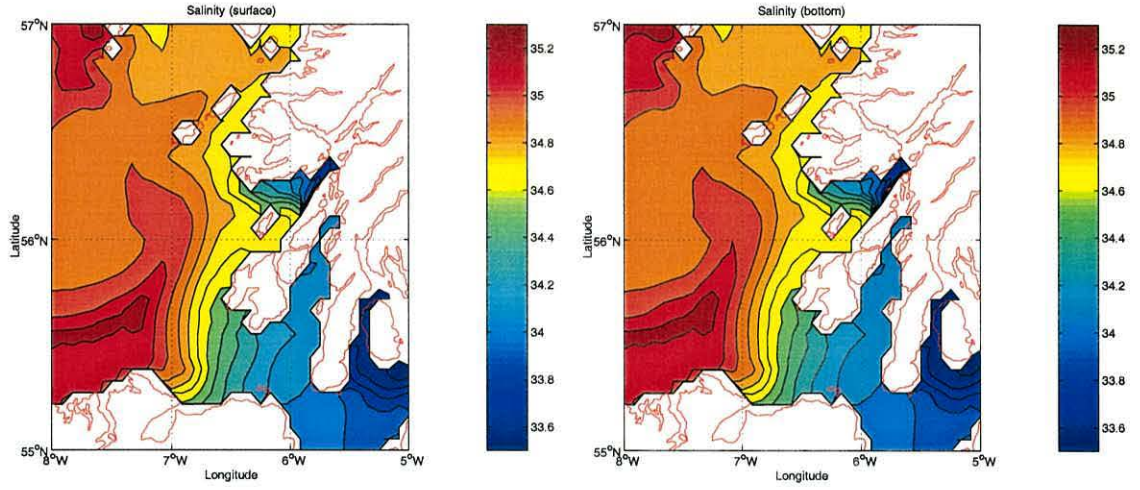

(a) (b)

Figure 6.28: Computed salinity: a) surface b) bottom after 28 days of simulation (corresponding to the 28/02/97). Contours at 0.1 intervals.

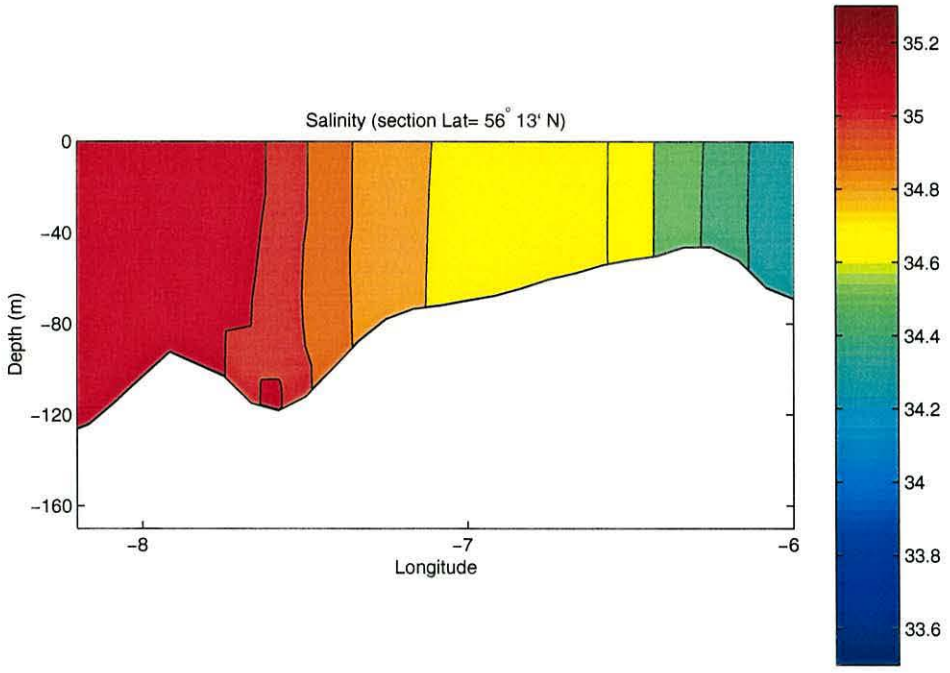

Figure 6.29: East-west section at Lat. 56°13′ N of modelled salinity after 89 days of simulation (corresponding to the 30/04/97). Contours at 0.1 intervals.

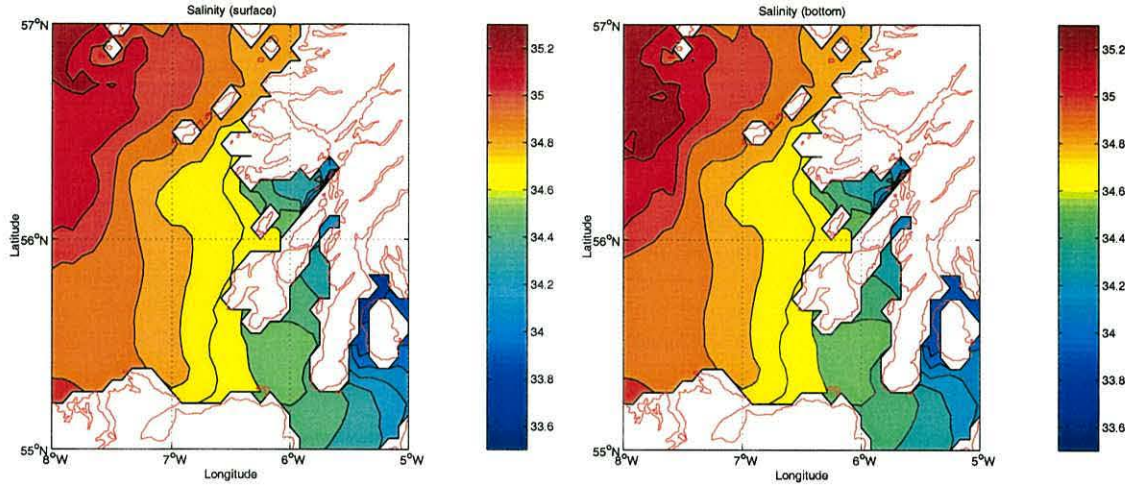

(a) (b)

Figure 6.30: Computed salinity: a) surface b) bottom after 89 days of simulation (corresponding to the 30/04/97). Contours at 0.1 intervals.

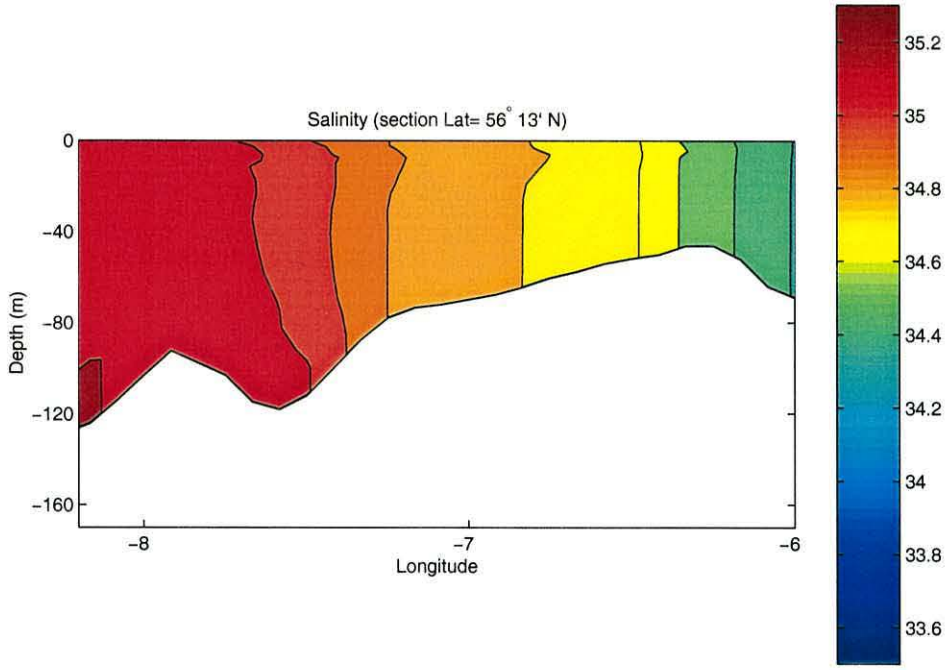

Figure 6.31: East-west section at Lat. 56°13′ N of modelled salinity after 120 days of simulation (corresponding to the 31/05/97). Contours at 0.1 intervals.

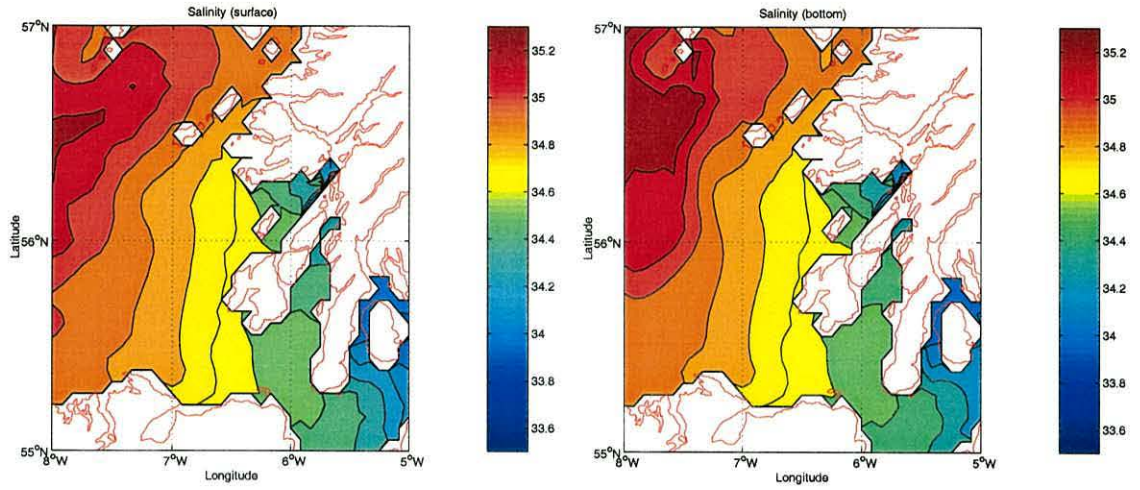

(a) (b)

Figure 6.32: Computed salinity: a) surface b) bottom after 120 days of simulation (corresponding to the 31/05/97). Contours at 0.1 intervals.

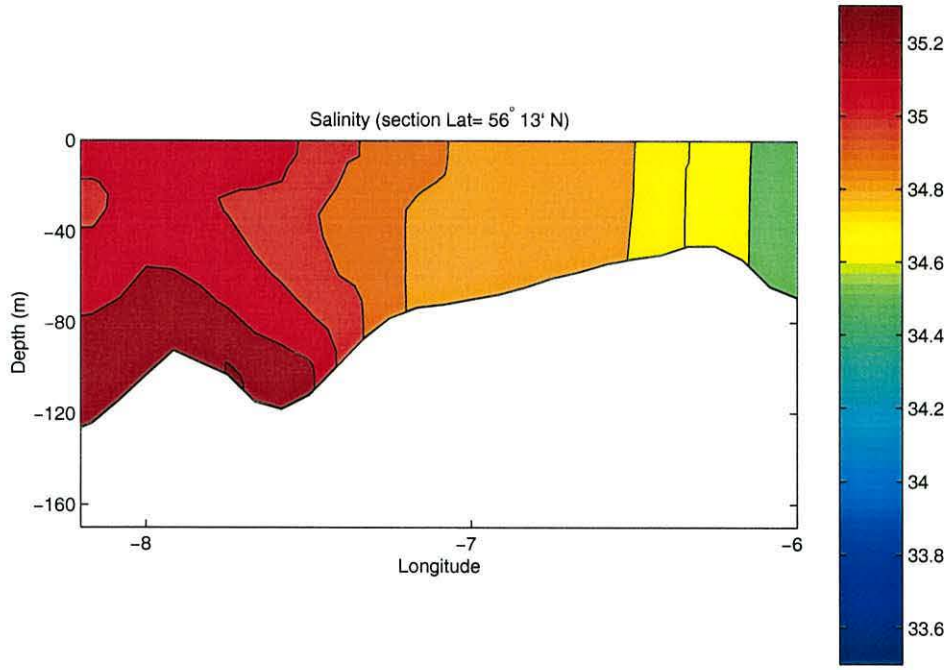

Figure 6.33: East-west section at Lat. 56°13′ N of modelled salinity after 181 days of simulation (corresponding to the 31/07/97). Contours at 0.1 intervals.

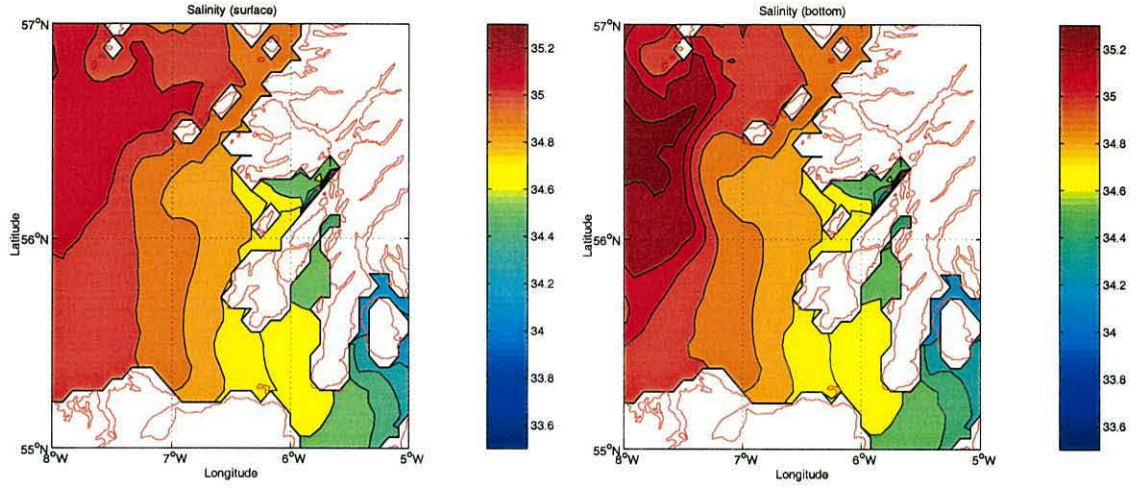

(a) (b)

Figure 6.34: Computed salinity: a) surface b) bottom after 181 days of simulation (corresponding to the 31/07/97). Contours at 0.1 intervals.

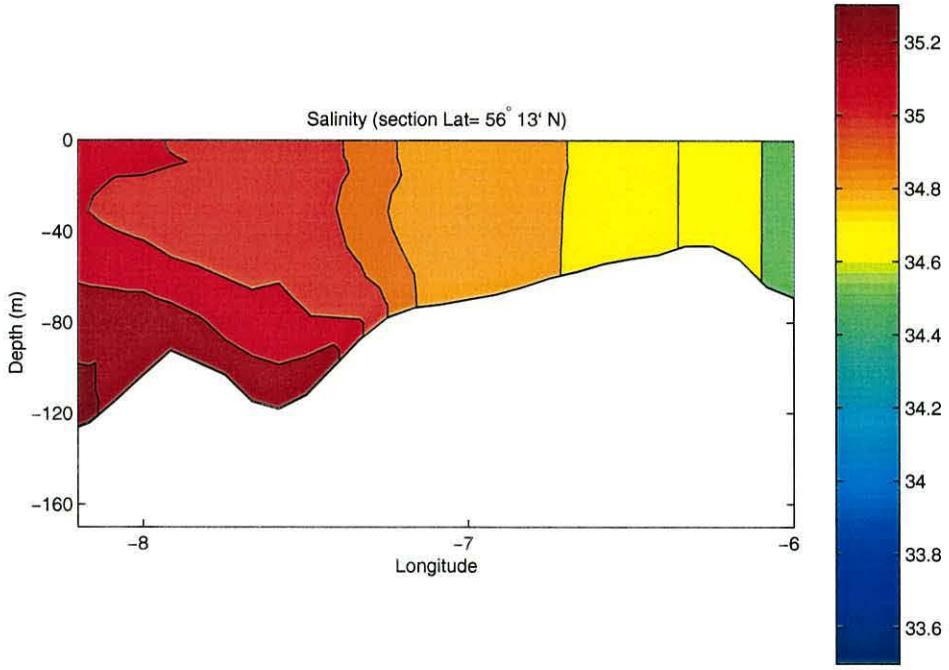

Figure 6.35: East-west section at Lat. 56°13′ N of modelled salinity after 212 days of simulation (corresponding to the 31/08/97). Contours at 0.1 intervals.

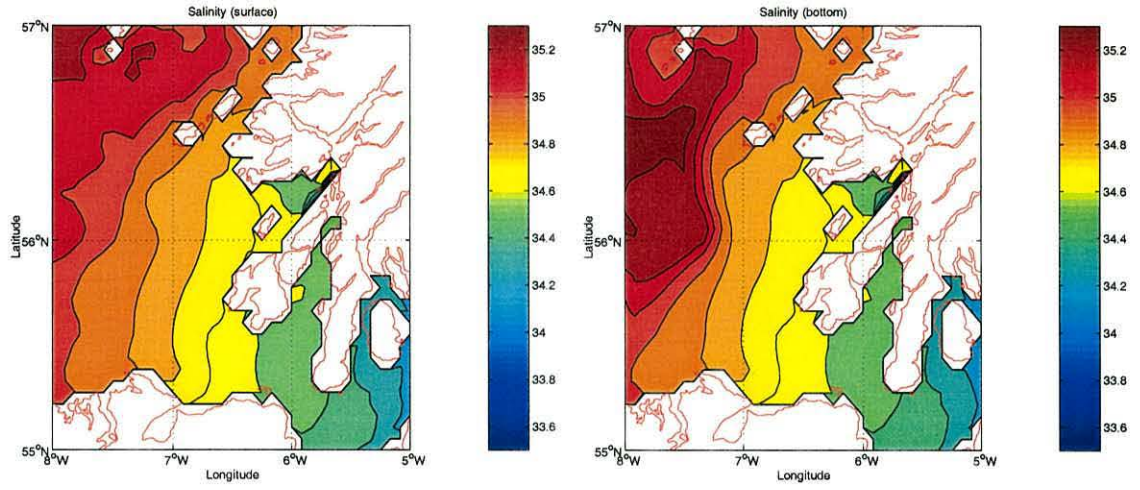

(a) (b)

Figure 6.36: Computed salinity: a) surface b) bottom after 212 days of simulation (corresponding to the 31/08/97). Contours at 0.1 intervals.

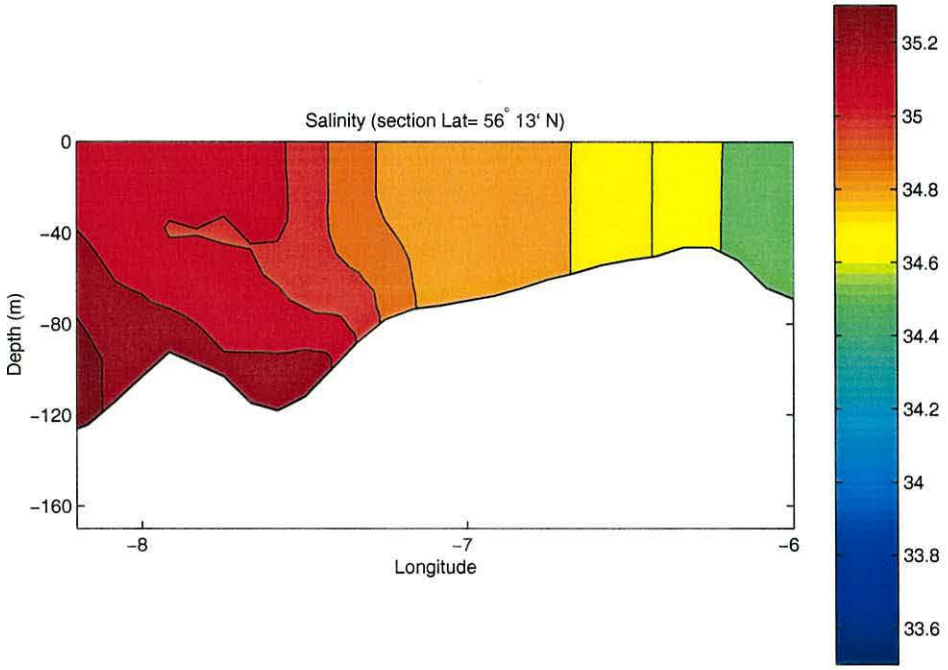

Figure 6.37: East-west section at Lat. 56°13′ N of modelled salinity after 242 days of simulation (corresponding to the 30/09/97). Contours at 0.1 intervals.

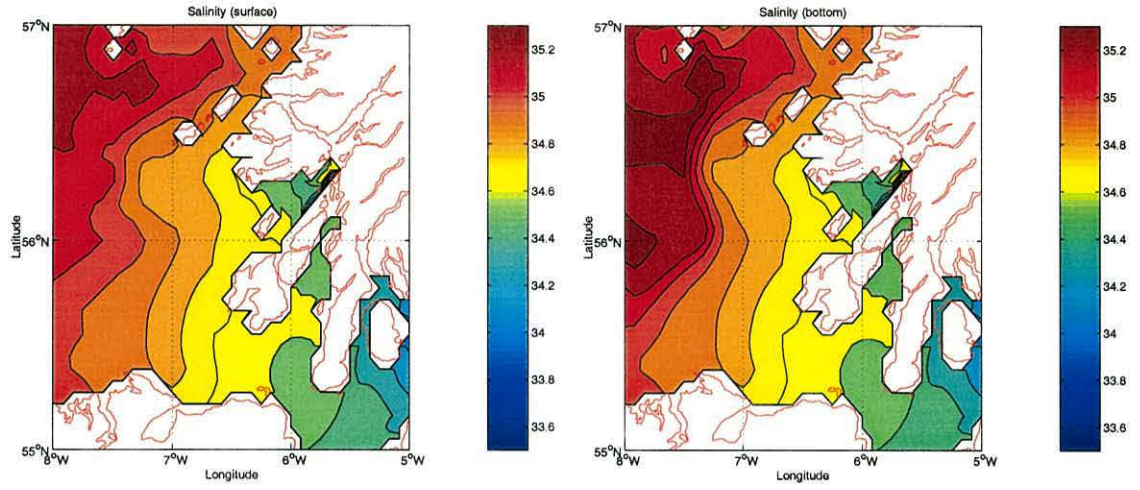

(a) (b)

Figure 6.38: Computed salinity: a) surface b) bottom after 242 days of simulation (corresponding to the 30/09/97). Contours at 0.1 intervals.

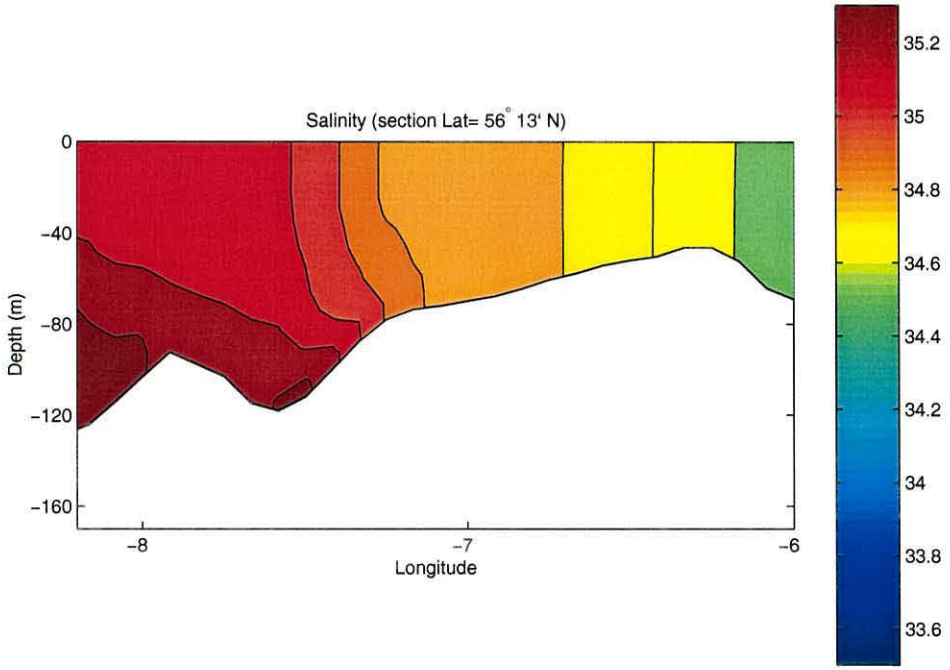

Figure 6.39: East-west section at Lat. 56°13′ N of modelled salinity after 273 days of simulation (corresponding to the 31/10/97). Contours at 0.1 intervals.

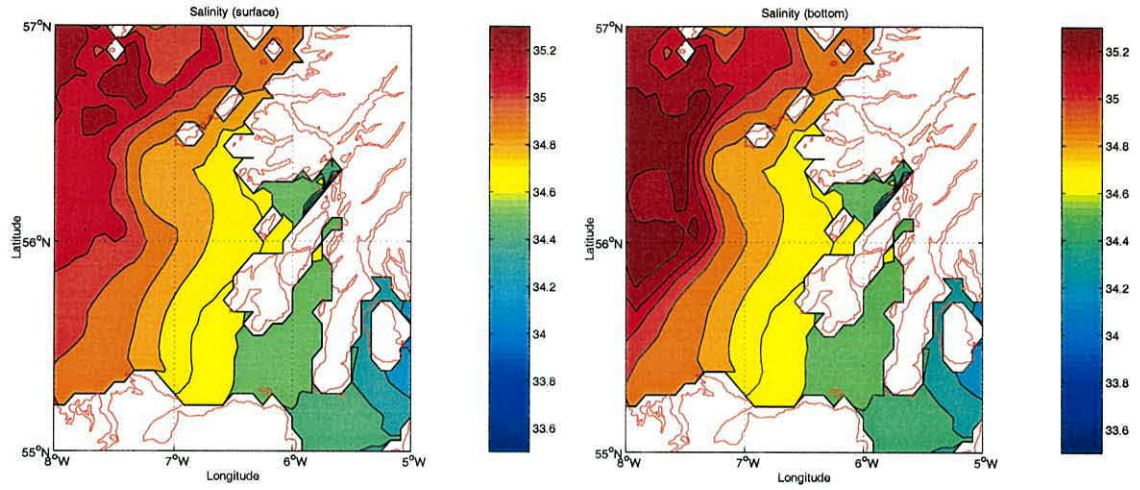

(a) (b)

Figure 6.40: Computed salinity: a) surface b) bottom after 273 days of simulation (corresponding to the 31/10/97). Contours at 0.1 intervals.

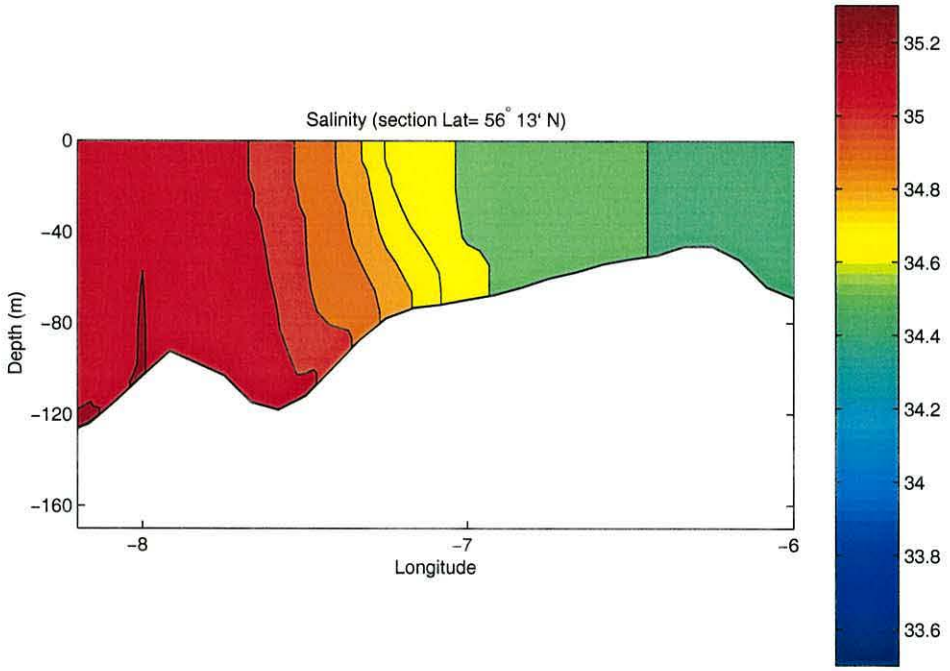

Figure 6.41: East-west section at Lat. 56°13′ N of modelled salinity after 303 days of simulation (corresponding to the 30/11/97). Contours at 0.1 intervals.

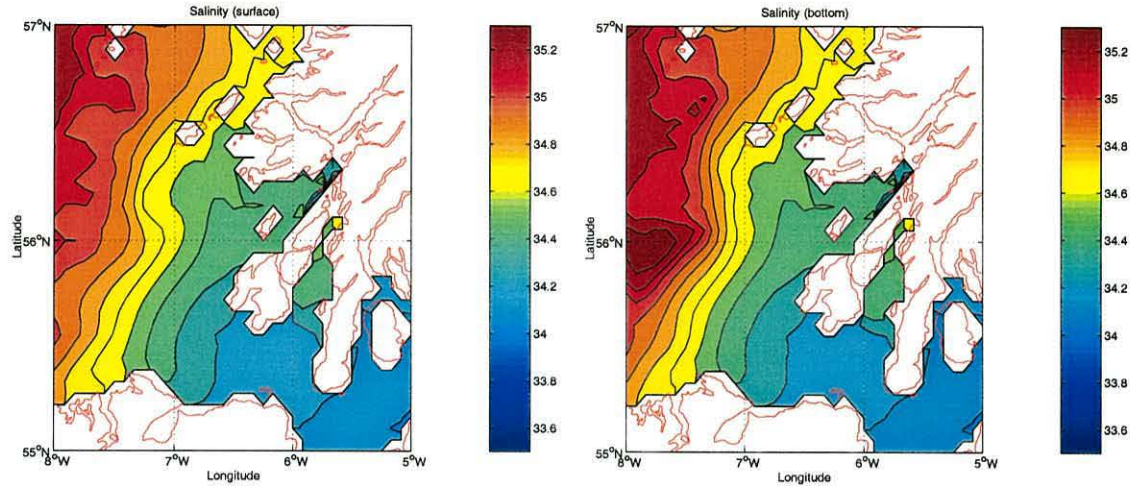

(a) (b)

Figure 6.42: Computed salinity: a) surface b) bottom after 303 days of simulation (corresponding to the 30/11/97). Contours at 0.1 intervals.

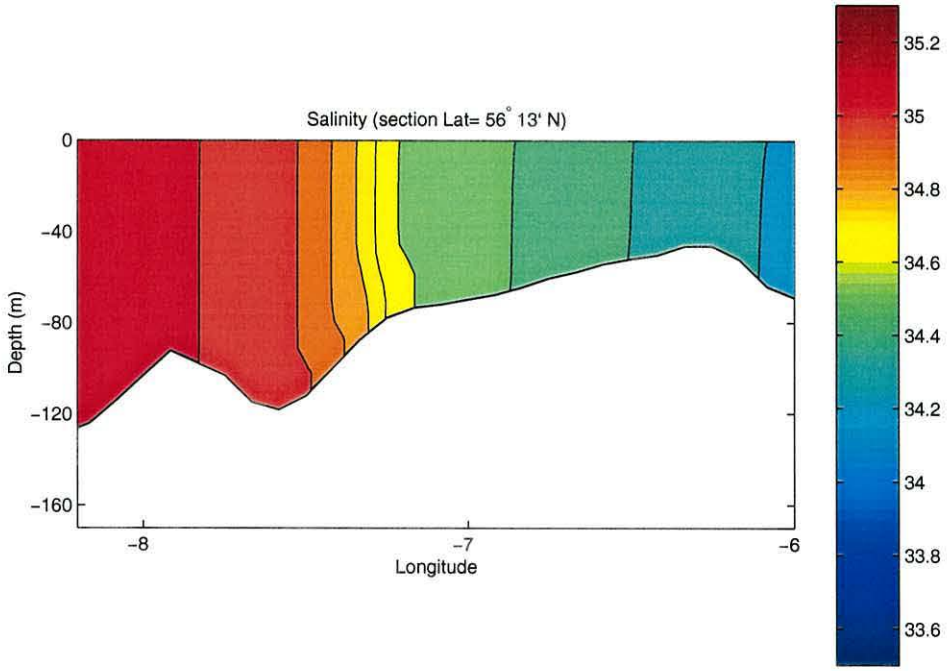

Figure 6.43: East-west section at Lat. 56°13′ N of modelled salinity after 334 days of simulation (corresponding to the 31/12/97). Contours at 0.1 intervals.

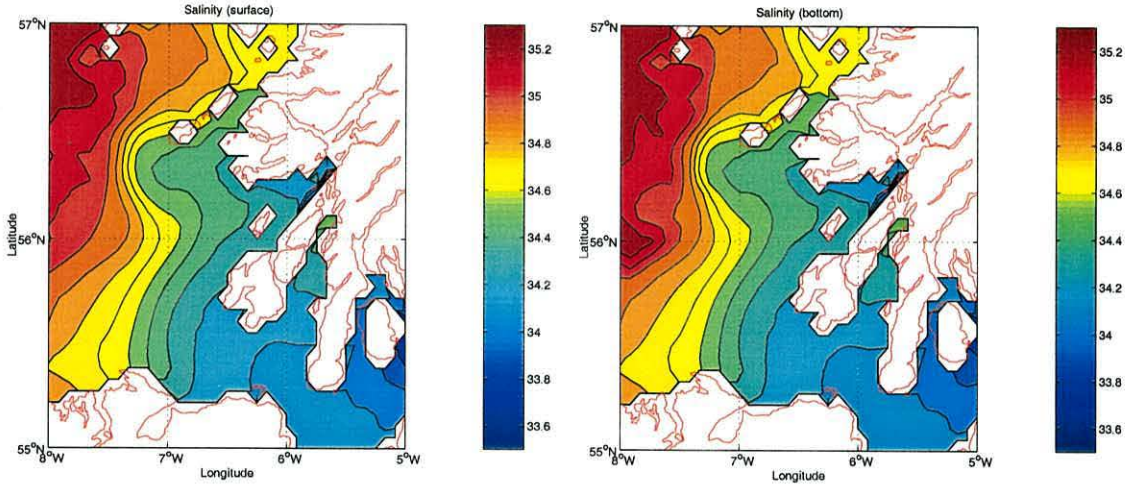

(a) (b)

Figure 6.44: Computed salinity: a) surface b) bottom after 334 days of simulation (corresponding to the 31/12/97). Contours at 0.1 intervals.

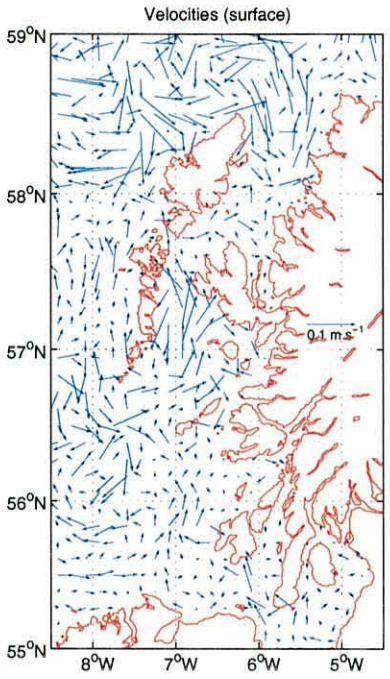

(a)

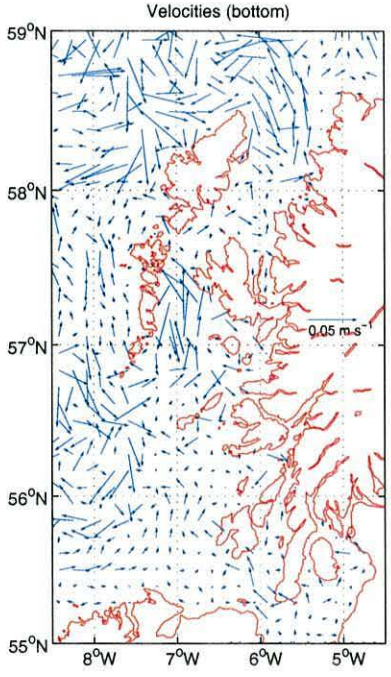

(b)

Figure 6.45: Computed residual circulation for the end of February 1997 (28/02/97): a) surface and b) bottom.

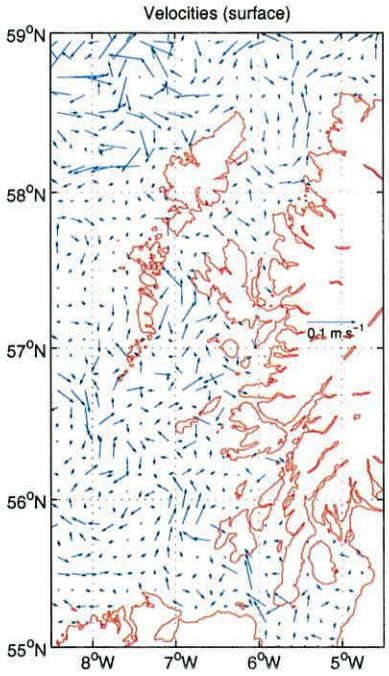

(a)

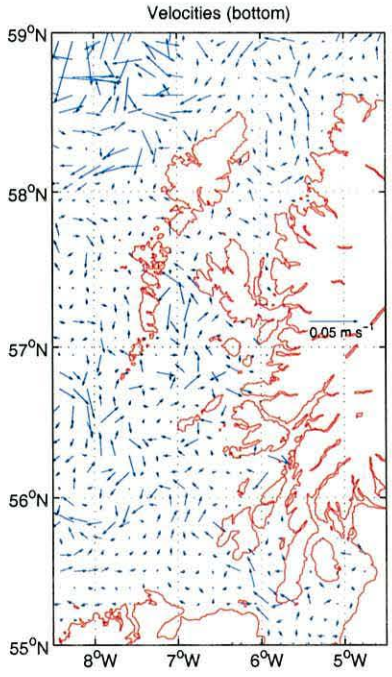

(b)

Figure 6.46: Computed residual circulation for the end of March 1997 (31/03/97): a) surface and b) bottom

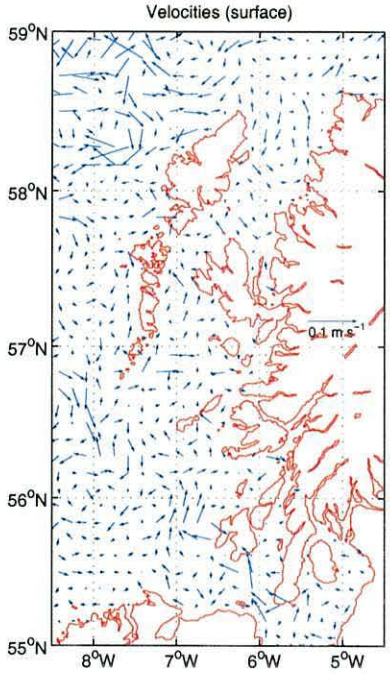

(a)

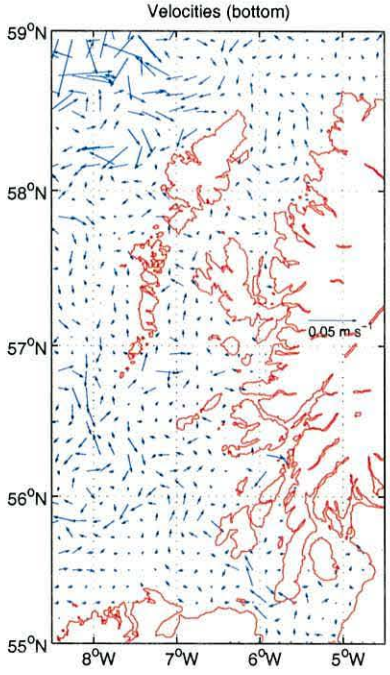

(b)

Figure 6.47: Computed residual circulation for the end of April 1997 (30/04/97): a) surface and b) bottom.

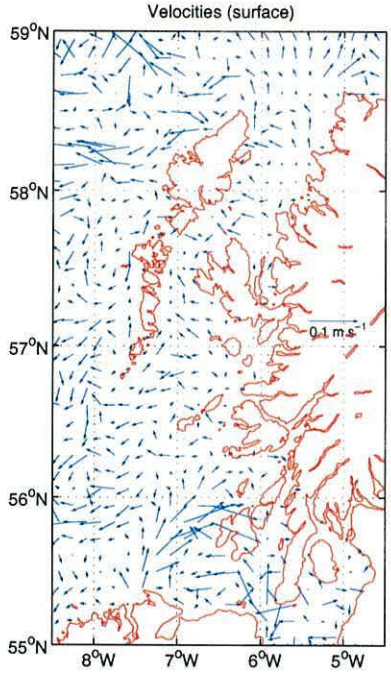

(a)

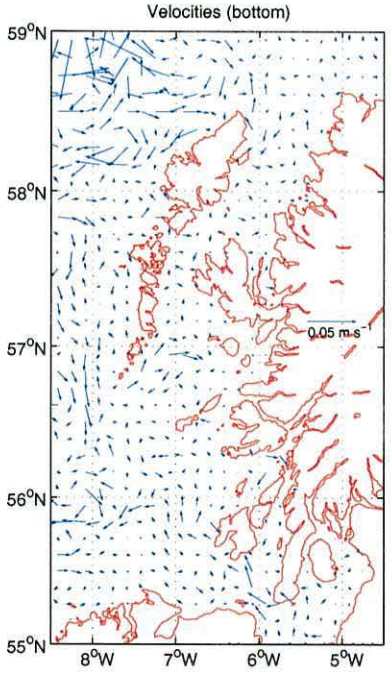

(b)

Figure 6.48: Computed residual circulation for the end of May 1997 (31/05/97): a) surface and b) bottom.

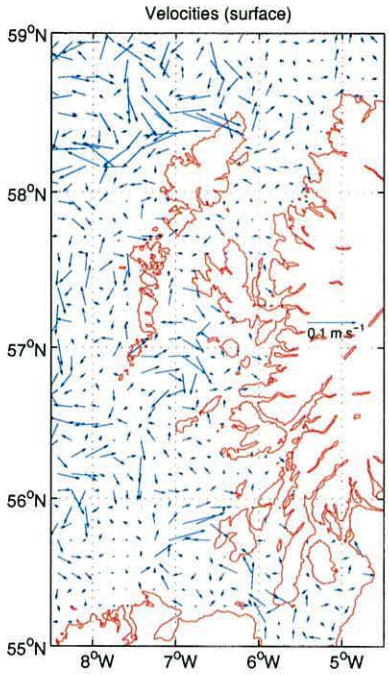

(a)

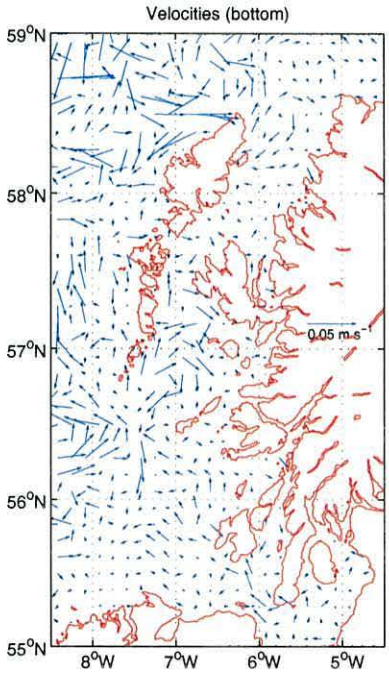

(b)

Figure 6.49: Computed residual circulation for the end of June 1997 (30/06/97): a) surface and b) bottom.

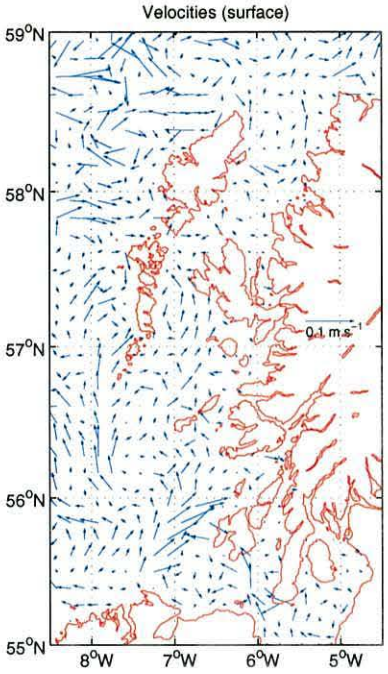

(a)

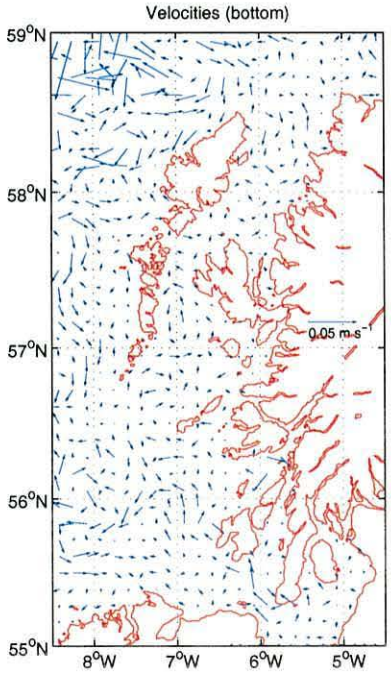

(b)

Figure 6.50: Computed residual circulation for the end of July 1997 (31/07/97): a) surface b) bottom.

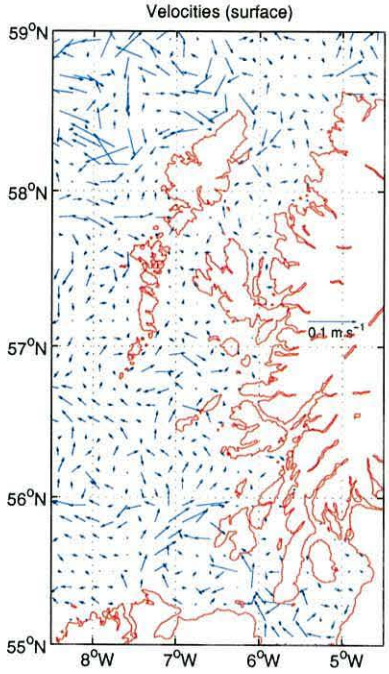

(a)

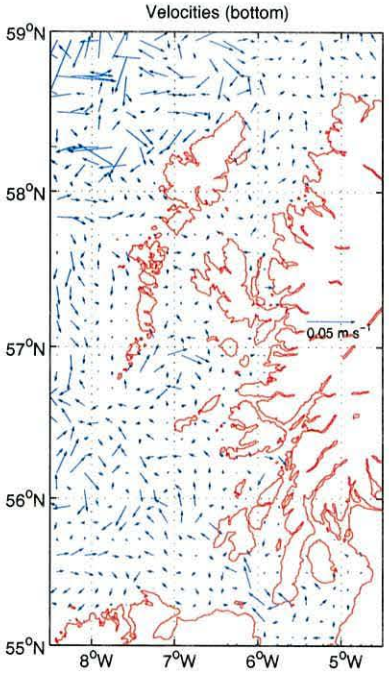

(b)

Figure 6.51: Computed residual circulation for the end of August 1997 (31/08/97): a) surface and b) bottom.

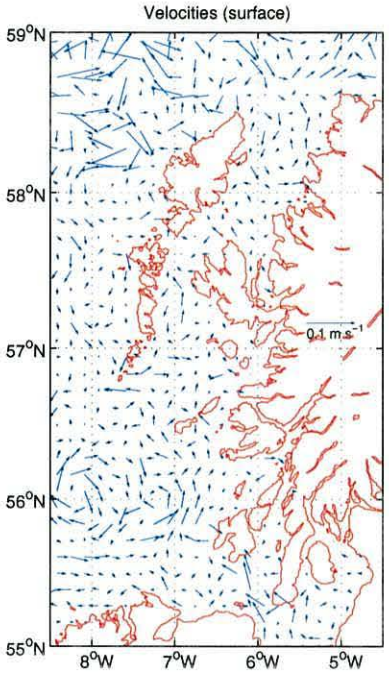

(a)

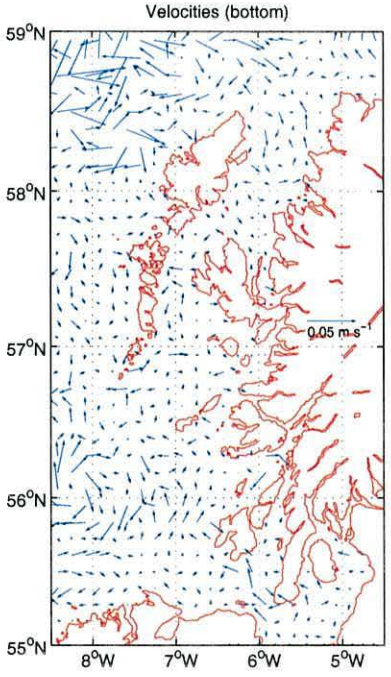

(b)

Figure 6.52: Computed residual circulation for the end of September 1997 (30/09/97): a) surface and b) bottom.

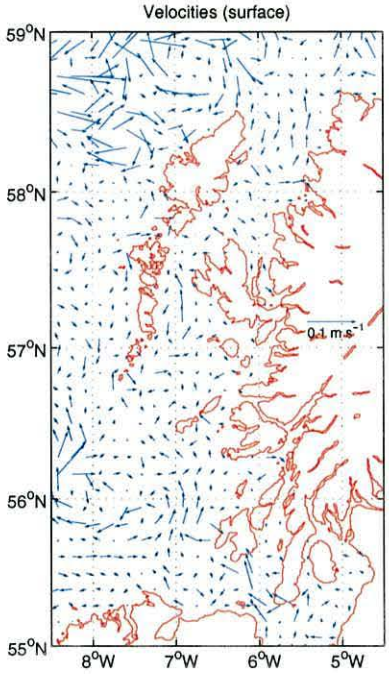

(a)

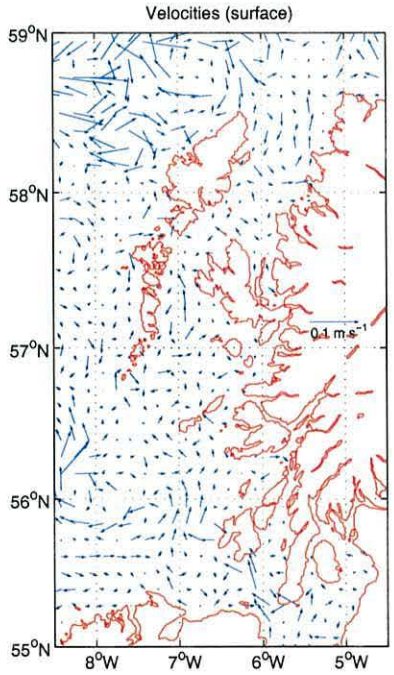

(b)

Figure 6.53: Computed residual circulation for the end of October 1997 (31/10/97): a) surface and b) bottom.

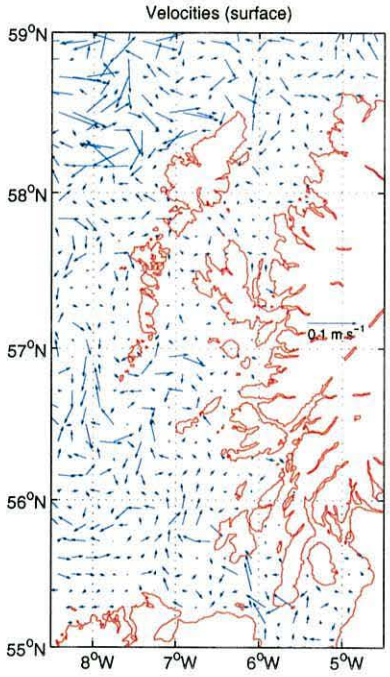

(a)

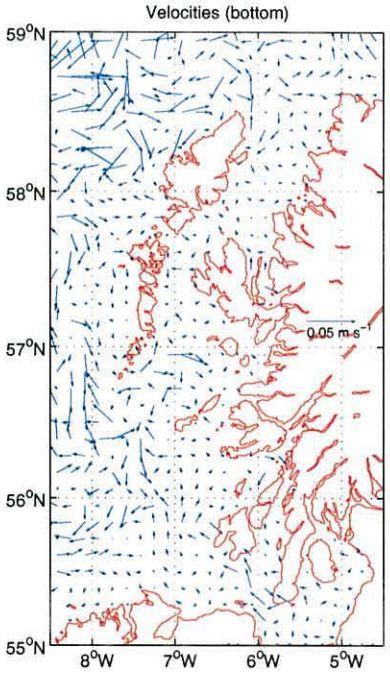

(b)

Figure 6.54: Computed residual circulation for the end of November 1997 (30/11/97): a) surface and b) bottom.

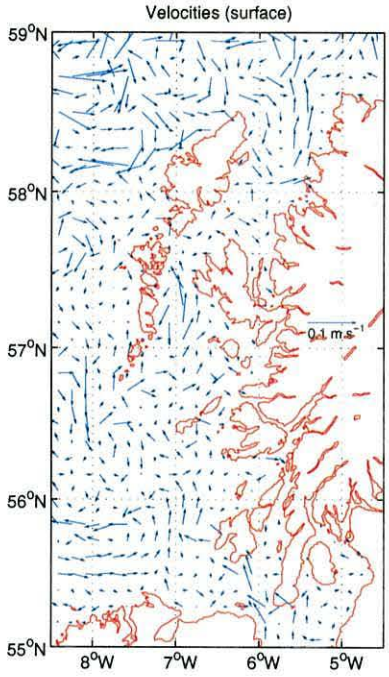

(a)

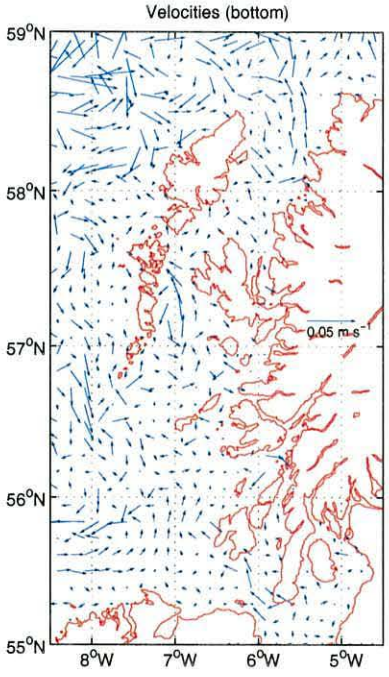

(b)

Figure 6.55: Computed residual circulation for the end of December 1997 (31/12/97): a) surface and b) bottom.

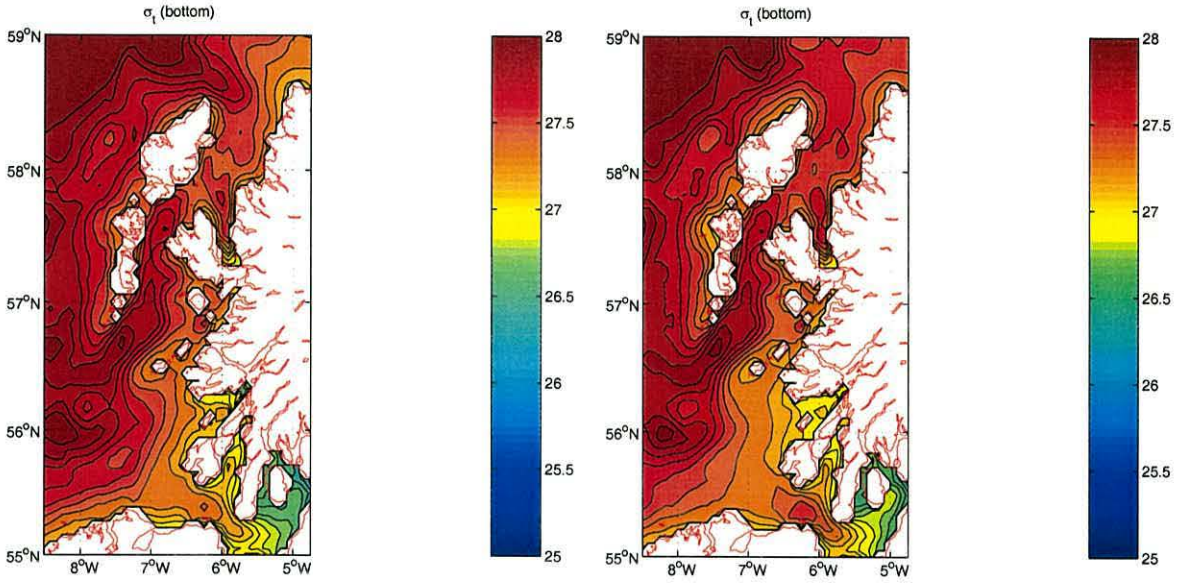
σt (bottom)
59°N
58°N
57°N
56°N
55°N
8°W
7°W
6°W
5°W
28
27.5
27
26.5
26
25.5
25

(a)

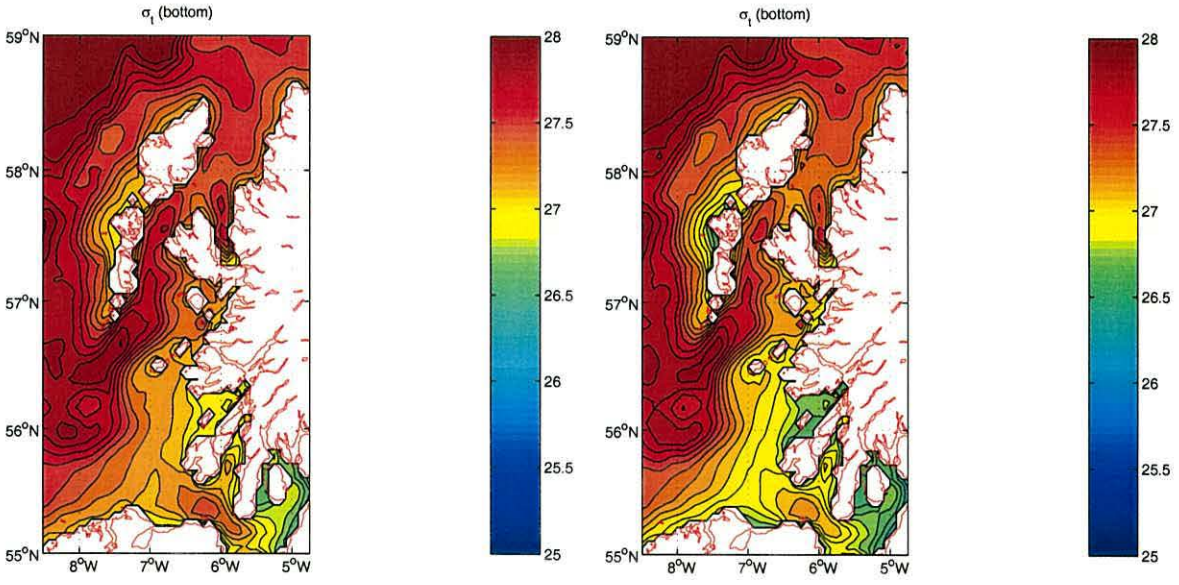
σt (bottom)
59°N
58°N
57°N
56°N
55°N
8°W
7°W
6°W
5°W
28
27.5
27
26.5
26
25.5
25

(b)

σt (bottom)
59°N
58°N
57°N
56°N
55°N
8°W
7°W
6°W
5°W
28
27.5
27
26.5
26
25.5
25

(c)

σt (bottom)
59°N
58°N
57°N
56°N
55°N
8°W
7°W
6°W
5°W
28
27.5
27
26.5
26
25.5
25

(d)

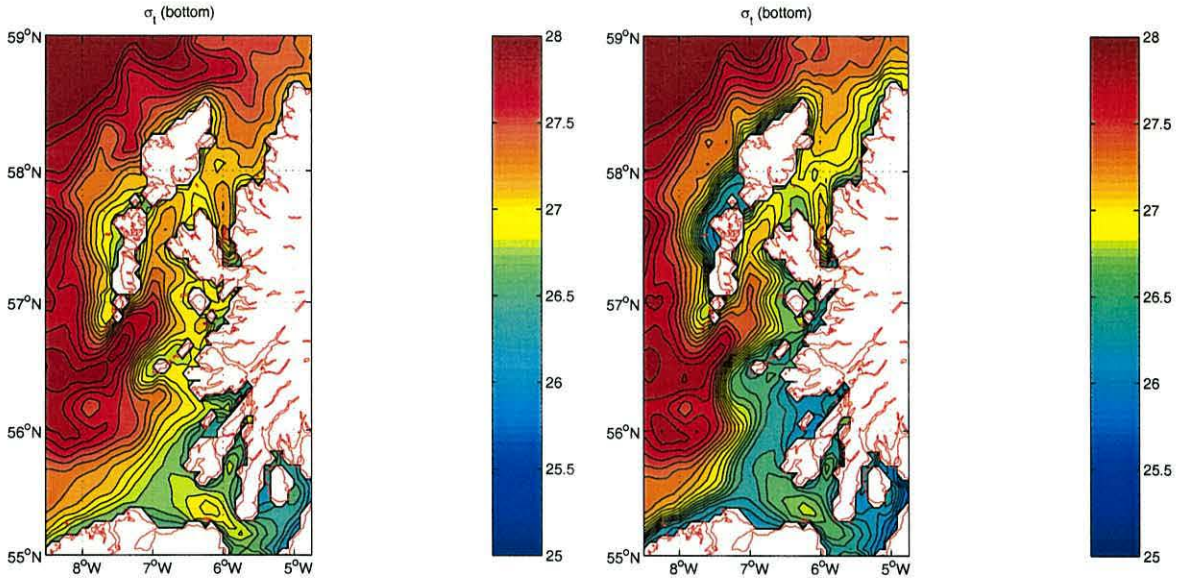
σt (bottom)
59°N
58°N
57°N
56°N
55°N
8°W
7°W
6°W
5°W
28
27.5
27
26.5
26
25.5
25

(e)

(f)

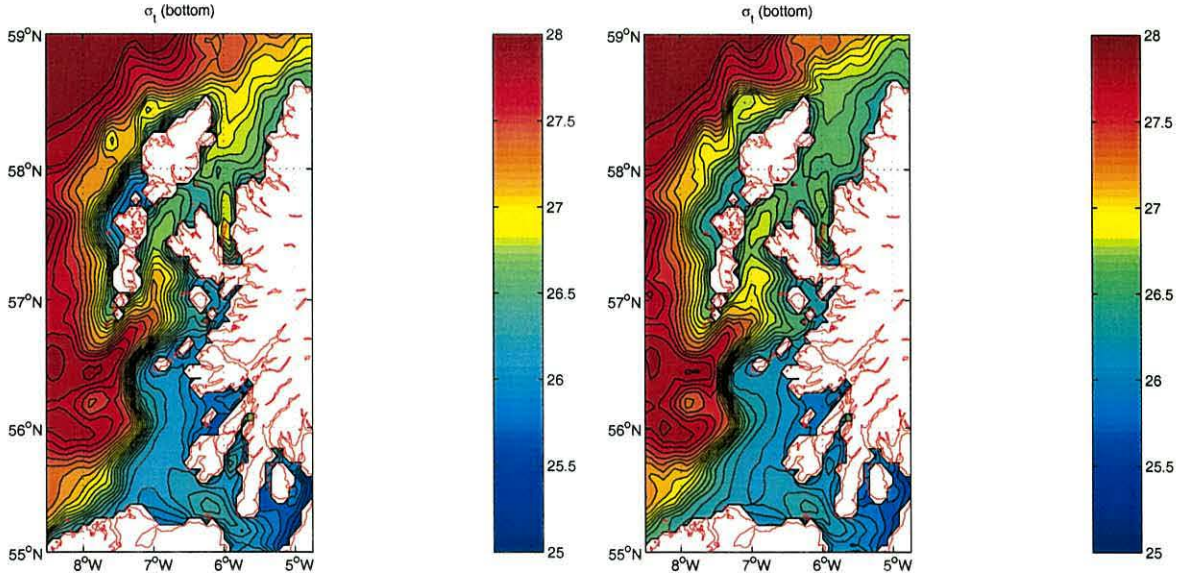
σt (bottom)
59°N
58°N
57°N
56°N
55°N
8°W
7°W
6°W
5°W
28
27.5
27
26.5
26
25.5
25

(g)

(h)

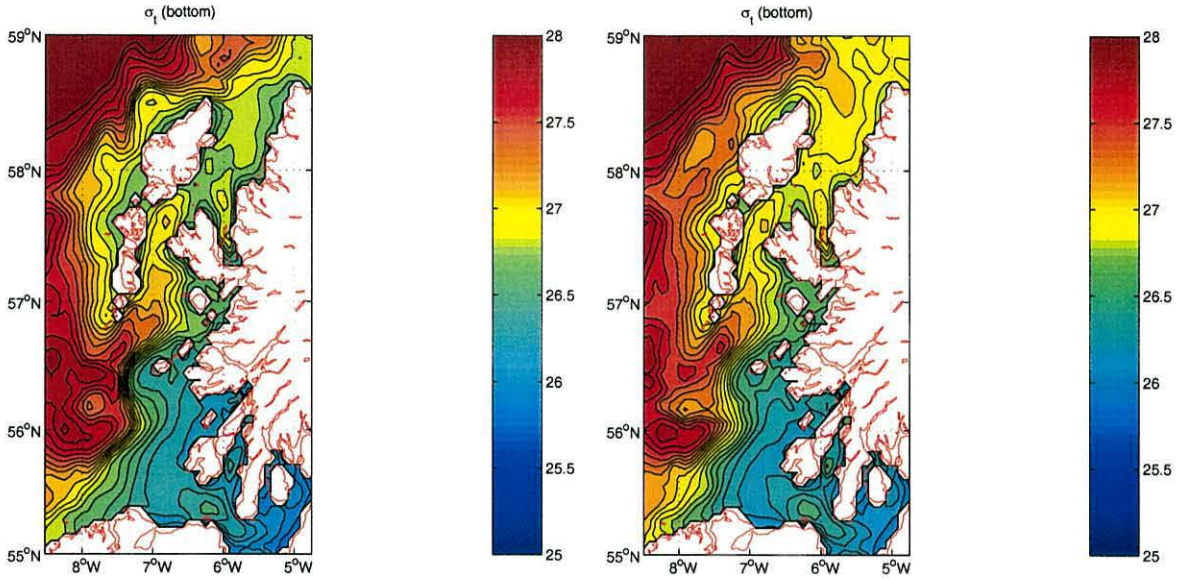

(i) (j)

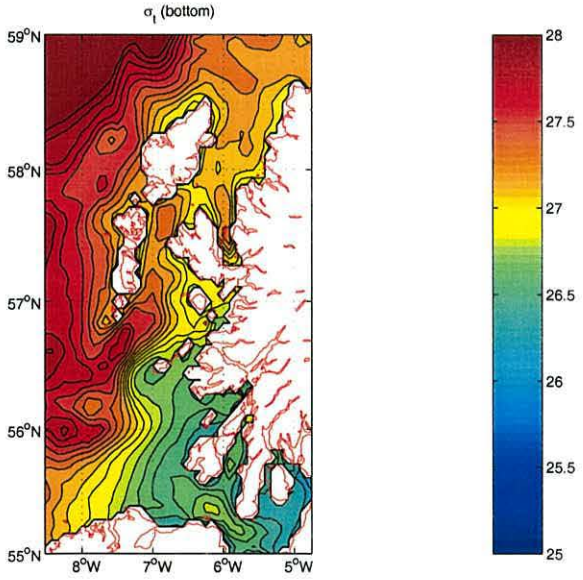

(k)

Figure 6.56: Monthly distribution of computed bottom σ_t for the same period of residual circulation (contours at 0.1 intervals).

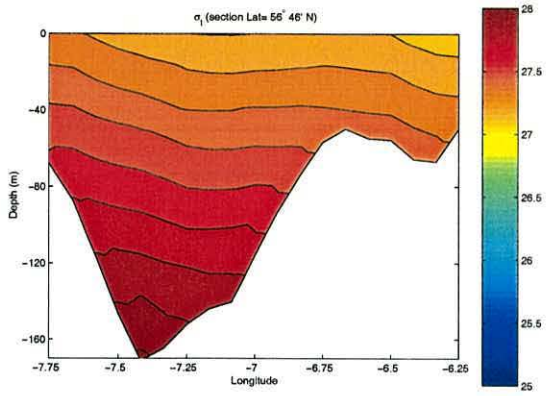
σt (section Lat= 56° 46' N)
Depth (m)
Longitude
0
-40
-80
-120
-160
-7.75
-7.5
-7.25
-7
-6.75
-6.5
-6.25
28
27.5
27
26.5
26
25.5
25

(a)

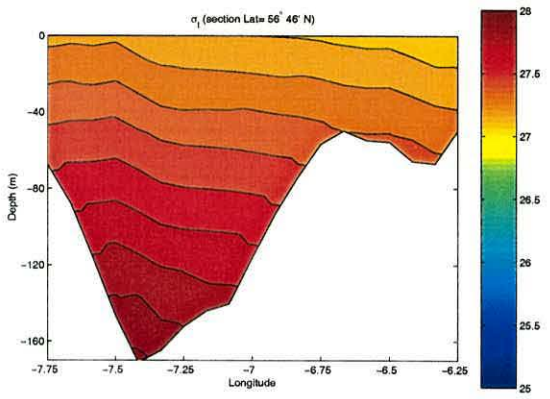
σt (section Lat= 56° 46' N)
Depth (m)
Longitude
0
-40
-80
-120
-160
-7.75
-7.5
-7.25
-7
-6.75
-6.5
-6.25
28
27.5
27
26.5
26
25.5
25

(b)

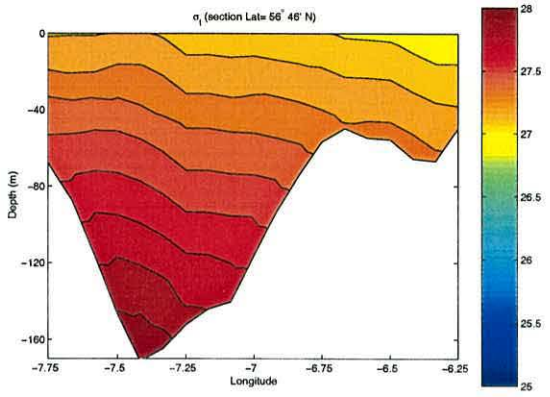
σt (section Lat= 56° 46' N)
Depth (m)
Longitude
0
-40
-80
-120
-160
-7.75
-7.5
-7.25
-7
-6.75
-6.5
-6.25
28
27.5
27
26.5
26
25.5
25

(c)

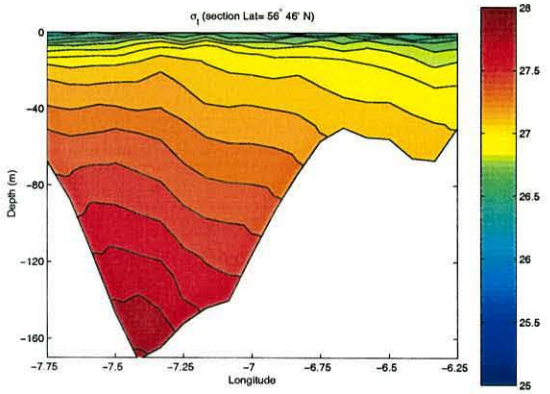
σt (section Lat= 56° 46' N)
Depth (m)
Longitude
0
-40
-80
-120
-160
-7.75
-7.5
-7.25
-7
-6.75
-6.5
-6.25
28
27.5
27
26.5
26
25.5
25

(d)

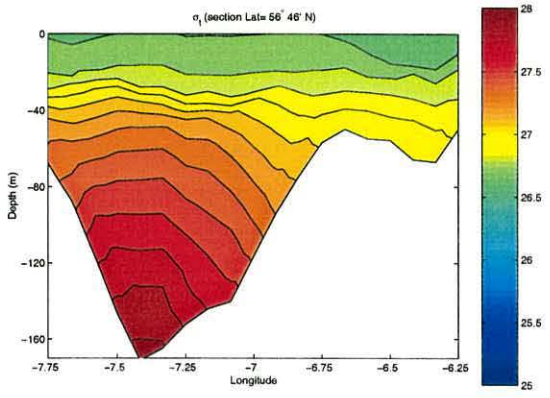
σt (section Lat= 56° 46' N)
Depth (m)
Longitude
0
-40
-80
-120
-160
-7.75
-7.5
-7.25
-7
-6.75
-6.5
-6.25
28
27.5
27
26.5
26
25.5
25

(e)

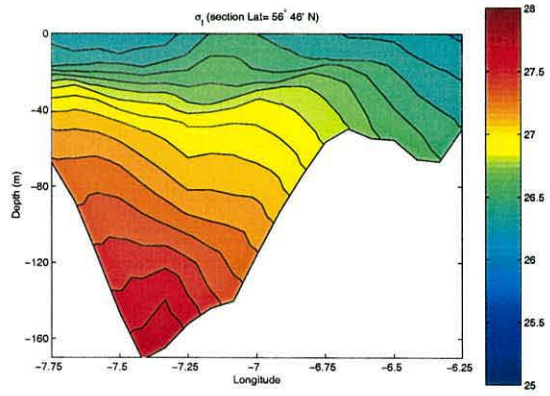
σt (section Lat= 56° 46' N)
Depth (m)
Longitude
0
-40
-80
-120
-160
-7.75
-7.5
-7.25
-7
-6.75
-6.5
-6.25
28
27.5
27
26.5
26
25.5
25

(f)

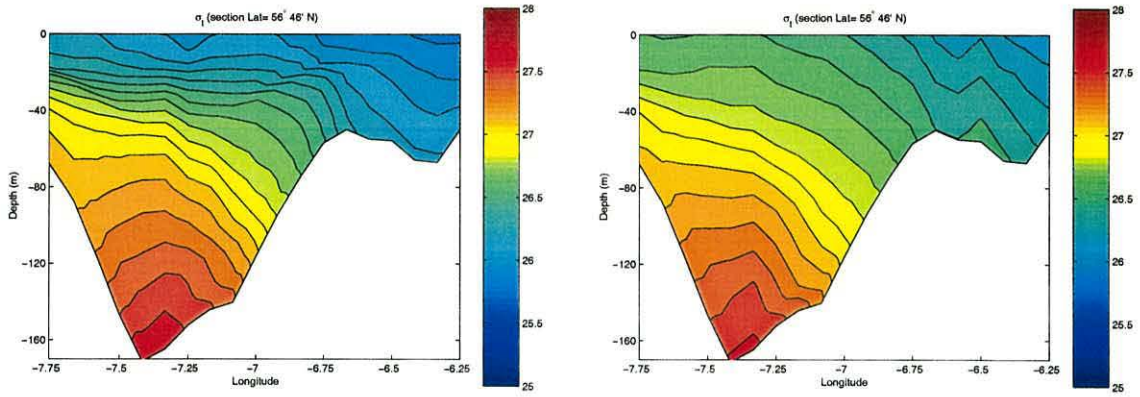

(g) (h)

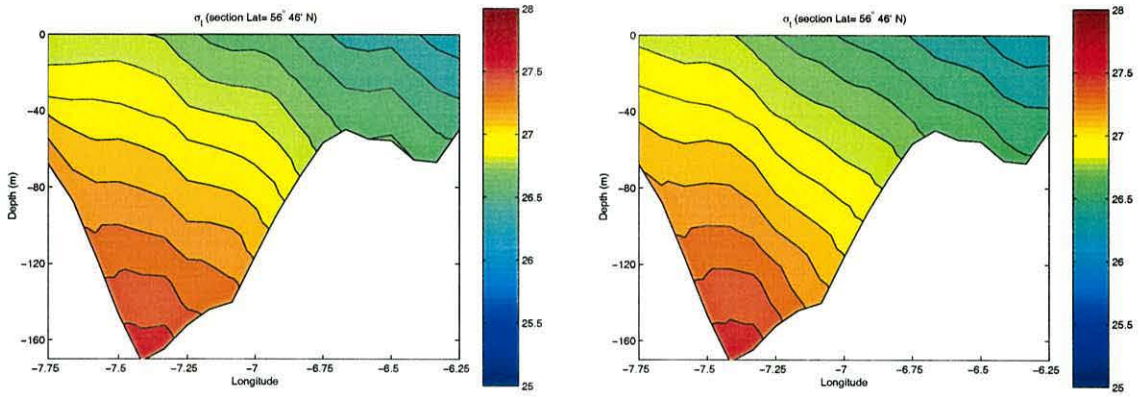

(i) (j)

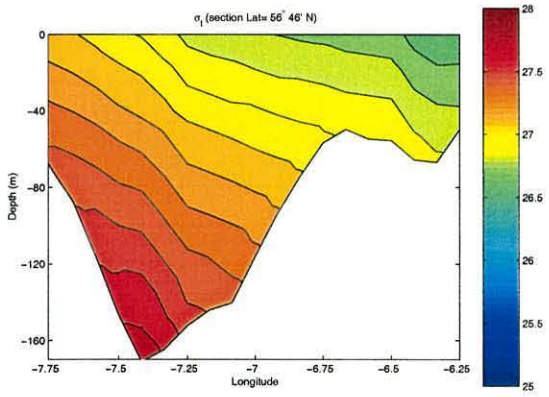

(k)

Figure 6.57: Monthly distribution of computed σ_t (section at Lat. 56°46′ N) for the same period of residual circulation (contours at 0.1 intervals).

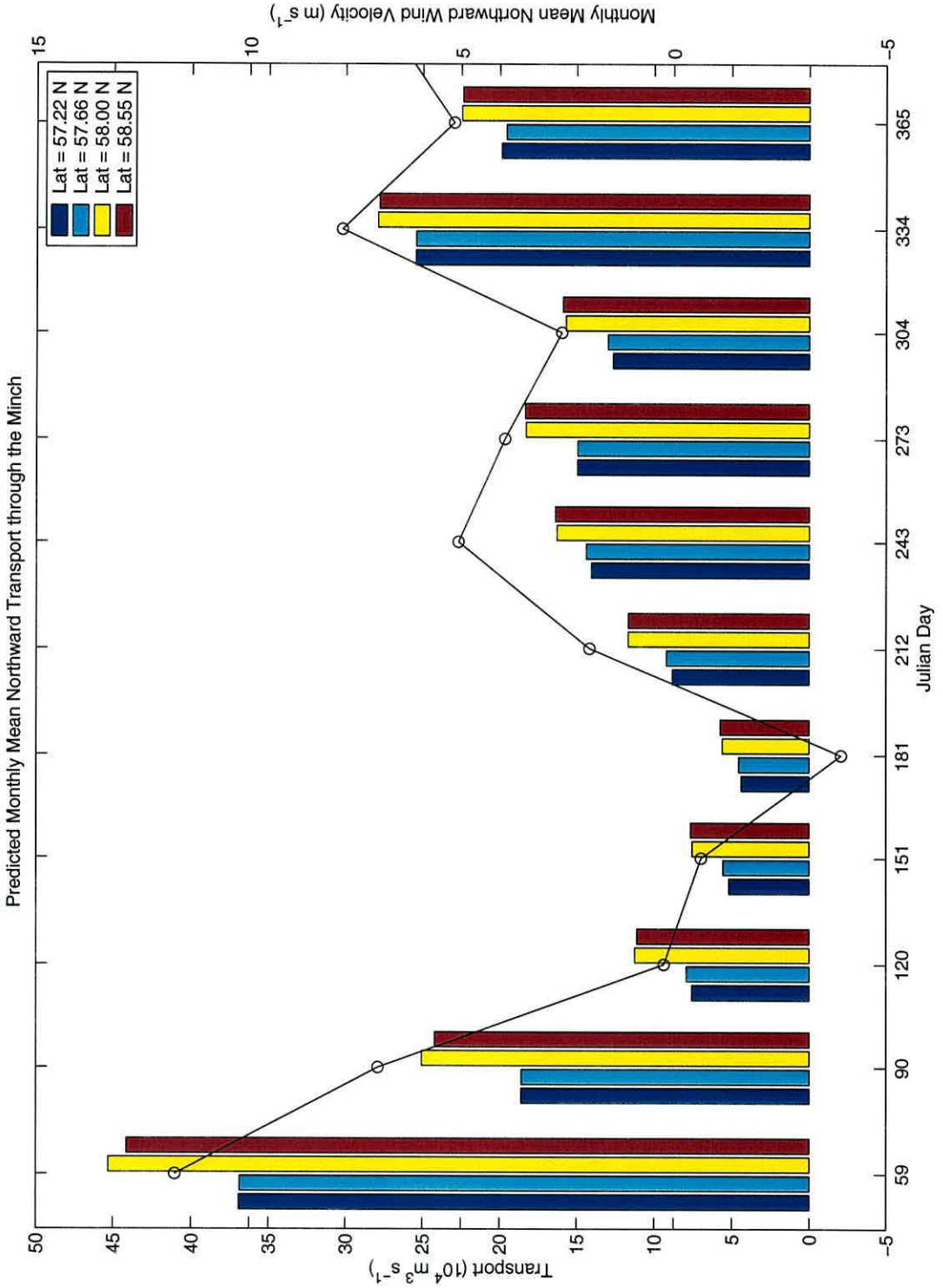

Figure 6.58: Histogram representing the computed total monthly averaged northward transport, including baroclinic effects, in (10^4 m^3 s^{-1}) through 4 section of the Minch for the year 1997. The solid line represents the monthly mean northward wind Velocity (m s^{-1}).

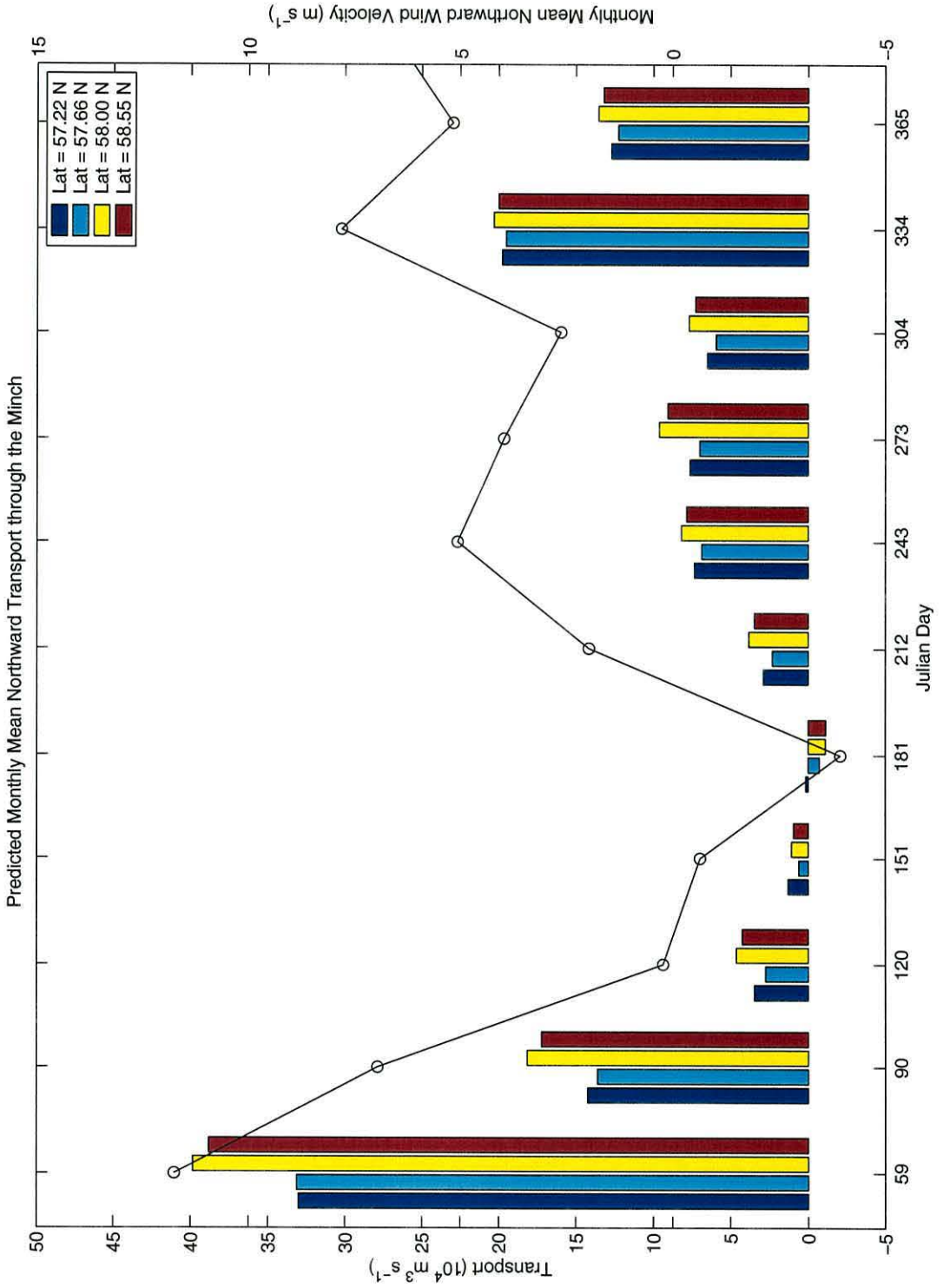

Figure 6.59: Histogram representing the computed total barotropic monthly averaged northward transport in (10^4 m^3 s^{-1}) through 4 section of the Minch for the year 1997. The solid line represents the monthly mean Northward Wind Velocity (m s^{-1}).

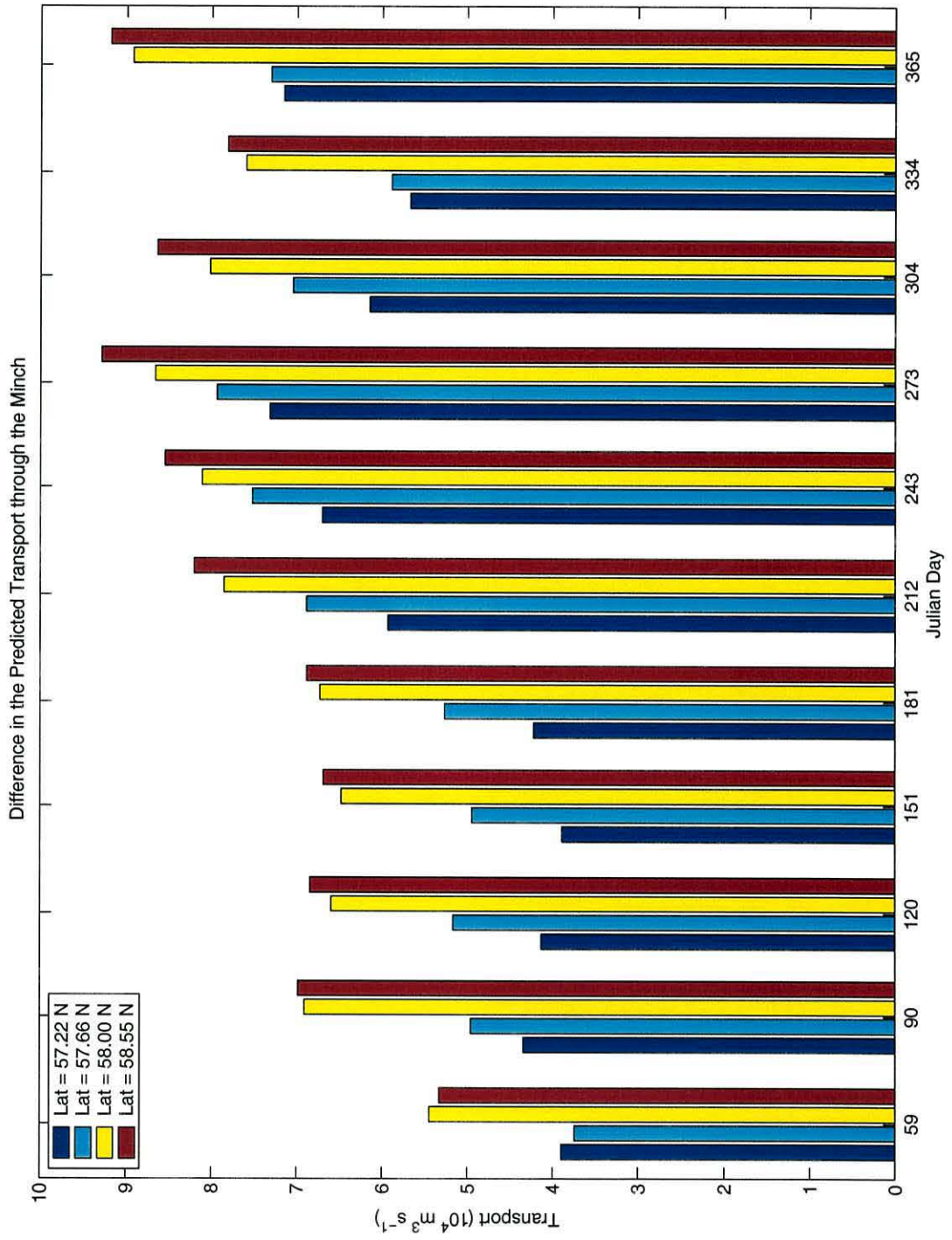

Figure 6.60: Histogram representing the difference between total baroclinic and barotropic Northward Transport in (10^4 m^3 s^{-1}) through 4 section of the Minch for the year 1997.

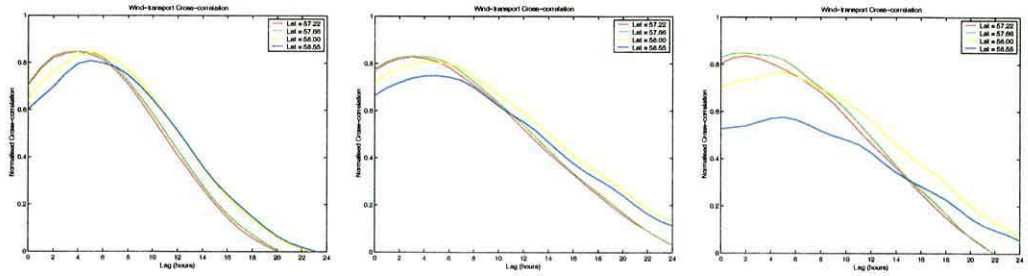

(a) February (b) March (c) April

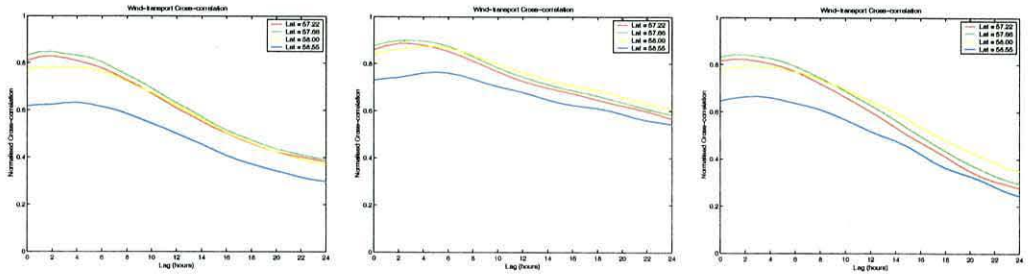

(d) May (e) June (f) July

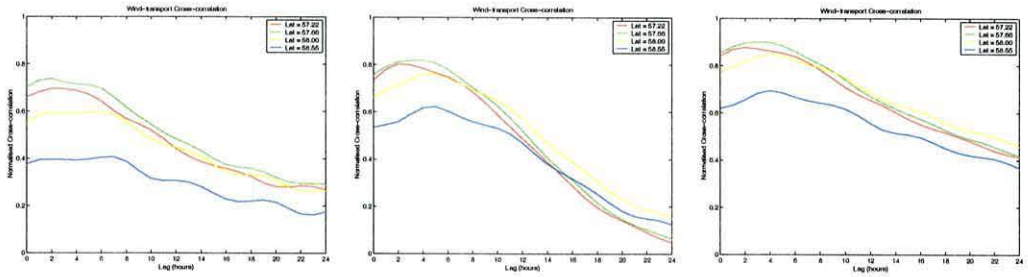

(g) August (h) September (i) October

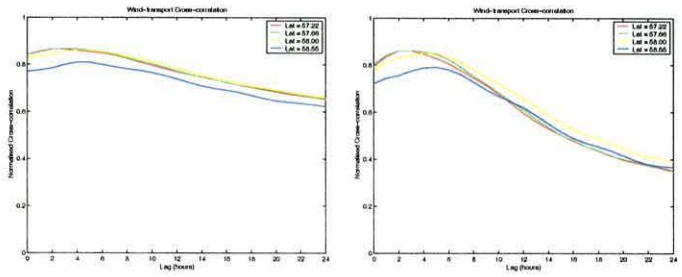

(j) November (k) December

Figure 6.61: Monthly computed cross-correlation between hourly northward component and northward hourly residual transport. Labels refer to sections in Fig.6.58.

Chapter 7

Discussion and conclusions

The aim of this project was to study the seasonal cycles of salinity and temperature and the seasonal circulation of the Scottish shelf with the help of a numerical model (the Princeton Ocean Model). Particular emphasis was given to the study of the density-driven component of the currents since changes in buoyancy play an important role in determining variations in the flow. For these reasons the model utilised was a fully non-linear three-dimensional model which was forced with climatological data for the year 1997 at the surface and at the lateral boundaries. This was the first time that such a model was used for this kind of study of this region and results are qualitatively and, generally, quantitatively comparable with observations available for the same period.

The first assessment of the predictive capabilities of The Princeton Ocean Model was done to see if it would reproduce the tidal characteristics of the region which play an important role in the dynamics of the area. The model was forced with only two tidal semidiurnal constituents (M_2 and S_2) which are the major contributors of tidal energy on this shelf. Results were similar to other tidal simulations of the area (Proctor and Davies, 1996; Xing and Davies, 1996c; Young *et al.*, 2001). Elevations and phases for both components were reproduced in acceptable way, showing the behaviour of a Kelvin wave travelling northward along the Scottish coast. Errors were present close to the amphidromic point located on the Malin shelf at the northern end of the North Channel, due to the inability of the model to reproduce the structure of the tides close to the coast because of the coarse resolution of the model grid. Velocity components were also simulated within reasonable agreement with observations. An important result was that tidal residual currents in the region

were weak (of the order of 2 cm s^{-1}) and showing a cyclonic tendency (both at the surface and bottom) as shown in previous studies (Xing and Davies, 1996c). Finally the response of the model to wind stress was also tested and results were again similar to previous studies (Xing and Davies, 1996c; Young *et al.*, 2001) showing that a recirculation can be triggered by southern winds. This is unlikely to happen in reality because of the variable nature of the wind field. All these results showed that tides and winds alone are not responsible for the observed pattern of the long-term circulation and baroclinic effects must be included in the simulations for a complete picture.

The next step was to arrange a fully seasonal simulation taking into account all the factors which can influence the dynamics of the Scottish shelf. The region under scrutiny is located between the coast of Scotland, Ireland and two open boundaries with the Atlantic Ocean. In this case the lateral boundaries are artificially delimitated by the meridian located at 7° of longitude west and by the parallel of 60° of latitude north. Seasonal variations in the circulation are controlled by buoyancy effects generated by changes in salinity and temperature fields, which affect the distribution of density, and by the interaction with the wind fields. The temperature cycle is mainly controlled by the solar energy flux and follows its seasonal pattern. The model was forced with hourly observations from weather stations located on Tiree and Stornoway which provided other forcing data such as solar heating flux, the air temperature and wind direction and speed. Changes in buoyancy due to salinity were implemented through fresh water inflow. Three major sources were distributed along the eastern coast of the domain to simulate the three real major sources of buoyancy.

The model seemed to reproduce correctly the seasonal cycle of temperature. Figs. 5.17a,j clearly show that the cycle of seasonal heating and cooling of the water column is simulated. Starting from a vertical condition of homogeneity (reproducing a winter condition) the surface temperature increased throughout the year to reach a maximum in late August - beginning of September. The model also reproduced horizontal variations in this cycle (see Fig. 5.17a and Fig. 5.17b) which, although displaying the same pattern at the surface, differed in the behaviour of the bottom temperature. These two particular points are located in the oceanic and the coastal area of the Islay front respectively. Due to different regimes of tidal mixing the oceanic side of the front remains stratified in summer. In contrast, near the coast,

strong tides maintain thermal homogeneity during the whole year. The development of the tidal front can be observed in the previous chapter which describes the monthly frontal structure. The model was initialised only with horizontal gradient (Fig. 6.2), the front started to develop between April and May. At the end of May the thermal structure was very similar to the structure observed by Hill and Simpson (1989) but a better qualitative agreement was reached at the end of July (Fig. 6.15). In this case there was also a topological agreement; the temperature field showed the structure normally associated with a tidal front. There were three distinct regions, a coastal region where the water is unstratified and two oceanic regions where a sharp thermocline divided a cold bottom pool from the warm surface. Stratification was maintained until late autumn with some variability according to the location on the shelf. By February an isothermal condition was reached again, showing that the model was able to reproduce the overall cycle of cooling and warming.

The behaviour of the bottom region is different. Also in this case a seasonal cycle was clearly detectable (see bottom temperatures in Figs. 5.17a,j) but the difference between minimum and maximum in temperatures was around $3° - 4°C$ depending on the position. Bottom temperatures were less sensitive to the forcing than the sea surface and they displayed less temporal variability. For this reason the bottom front was more clearly visible. Figs. 6.15 and 6.16 for the months of July and August respectively showed a strong front with an horizontal gradient of almost 4°C. An important result of this simulation was to further prove the stabilising effect of the bottom bathymetry; the above Figs. show that the bottom region of the tidal front closely followed the isobaths and its signal was detectable even with a weak surface gradient (see Fig. 6.21 for the month of October).

The situation was different for the simulation of the salinity. The agreement with observations was poorer; the computed results were constantly overestimating its value and showed less horizontal and vertical variability. Horizontal gradients were weaker than observations. The haline front, which represents a sharp boundary between salty oceanic and coastal fresher waters and which was shown to exist with direct observations and with the help of radioactive tracers, is almost missing in simulations. Whereas observations showed an horizontal difference of 1.0 between the two areas, simulations reached a maximum of 0.5 without the same sharpness. A seasonal cycle for salinity was not readily seen; a correlation was expected between the cycle of the sources of fresh water and the salinity on the shelf, with low salinity

in winter and higher salinity in summer, following the river runoff. This was not observed. A trend of this kind was predicted by the model (see Figs. 5.23a,j) but the differences between minimum and maximum do not show the large freshening expected for the end of the simulation, corresponding to the late Autumn. In any case the few observations available for the summer 1997 did not corroborate this theory. From April to July there was no increase in salinity (see Figs. 5.28) but the short period of deployment and the number of samples contributed to the uncertainty. The model was also capable of showing episodes of intrusion of salty water from the Atlantic inside the Minches.

The reason that may explain this poor agreement can be related to the mechanisms which control the spatial and temporal evolution of salinity on the shelf. Unlike temperature, salinity is mainly controlled by the advection of boundary values inside the region; the model was forced at the lateral boundaries with values from a climatological archive (Levitus, 1982) and with values from river runoff whilst temperature is mainly controlled by the downward vertical mixing of the incoming solar radiation. Poor knowledge of these boundary values reflects in the simulation of salinity. Another reason could be found in the reproduction of the mixing by the model. The thermal forcing is a strong signal which is propagated downward by vertical mixing and is very sensitive to all the phenomena which contribute to it such as tides and winds (as it was demonstrated with the increase of the wind stress in one of the simulations). On the other hand salinity has a much weaker signature and there were no surface fluxes which could have changed the local balance; rain was not included in this set of simulations and its contribution was shown to be comparable to the buoyancy contribution of the other sources.

There were thought to be two possible sources of numerical inaccuracies, the error due to the pressure gradient calculation and the error due to the advection scheme which could have contaminated the sharpness of the haline and thermal fronts. The Princeton Ocean Model is a model where the vertical motion is described by σ-coordinates and problems can arise when there are steep gradients in the bathymetry (Haney, 1991; Mellor *et al.*, 1994). In this work these kind of errors were negligible. The model could dynamically adjust in a short time so that errors were minimised as already shown by Mellor *et al.* (1994). Furthermore the steep region of the domain was located at its north western boundary, far from the area of interest so that eventual influences were minimal. The issue of the boundary conditions

was partially solved by choosing the position of the boundary of the domain of simulation as far as possible from the Scottish shelf with a compromise between size of the grid and computational time. Various solutions were tested and the more stable (a radiation condition suggested by Flather, 1976) was implemented for the velocity components. An upstream boundary condition was used for temperature and salinity but none of these were sources of appreciable errors.

Far more important was any possible error in the advection of scalars because this would have compromised the whole simulation and in particular the investigation of the evolution of the Islay front. The treatment of advection is one of the key issues in coastal modelling and various treatments have been devised to obtain acceptable solutions for the advection-diffusion equation in finite form. The model comes with a standard central difference scheme and after testing (not shown in this work) it was changed so that this version of POM utilised the MPDATA scheme (Smolarkiewicz, 1983, 1984) where an upstream scheme is corrected iteratively with an antidiffusive velocity. As discussed before the results did not show the presence of large errors. The thermal front was sharp particularly in its bottom region. The haline front did not display the same sharpness and was diffused but this was probably due to other reasons (see previous discussions).

The second aim of this project, to investigate circulation and the rate of transport through the Minch, was carried out using the same settings for the previous simulations. Observations show the presence of a coastal current flowing northward along the Scottish coasts (Simpson and Hill, 1986). When it reaches the Sea of the Hebrides it splits in two branches, one enters directly the Minch and the other turns south and proceeds flanking the outer coast of the chain of the Hebrides (Craig, 1959). Model results confirmed this picture; throughout the year the Scottish coastal current was always present and its strength, of the order of few cm s^{-1}, was in agreement with available data. Less agreement was reached for the recirculation in the sea of the Hebrides. It was expected to find a constant cyclonic circulation due to the presence of a dense dome (Hill *et al.*, 1997b) but results showed a variable structure of the currents. The model was used to compute the density-driven contribution which predicted a cyclonic circulation as well as episodes of reversal of the flow where sea water coming from the Atlantic intruded, both at surface and bottom, inside the Sea of the Hebrides. A constant recirculation is often assumed but observations in the area are sparse and these episodes could be real. Another explanation could lie in

the incorrect reproduction of the density field in the area. It was demonstrated that this feature has a strong baroclinic component, tidal residuals are weak and a long term flow is generated by the presence of horizontal density gradient. The bottom dome observed in the region hints to a flow in thermal wind balance but the model did not always reproduce a dome with the same shape and strength. Hill *et al.* (1997b) observed a strong dome in April whilst model results show a weak dome (see Fig. 6.57a,k) which strengthened with time as the contribution in buoyancy due to the solar heating became important. This weaker density gradient may be related to the lack of advection of fresher water to the Outer Hebrides. The model showed a cyclonic circulation during the early months of spring but the water on the Scottish side of the gyre was too saline so that there was not contrast in density and there was no feedback mechanism (where the horizontal density gradient creates a stronger flow which advects more fresh water). Another explanation could be found in intrusion of Atlantic water from the boundary which could lead to a counterflow. The importance of contributions from the oceanic boundary could be evaluated with the help of some sensitivity tests where Atlantic water is injected into the domain in different positions so to determine its effect on the positioning of the dome. Xing and Davies (2001) showed that coastal shelf and deep ocean are interlinked, as already discussed. This work also points to the fact the location of the haline structure in the Sea of the Hebrides is not controlled only locally in contrast with what happens, for example, in the western Irish Sea where the position of the dense dome is controlled locally by a heating-stirring balance mechanisms (Horsburgh, 1999). There is also a far-field effect where boundaries actively influences the interior of the region so that a accurate knowledge of the forcing at this locations is necessary for a correct simulation of the long term circulation.

The model showed the existence of two distinct recirculation cells, one at both ends of the Minch. The southern cell has been already observed whilst the second cell has not been directly observed yet. Craig (1959) hinted to its existence due to the interplay between the intrusion of salty Atlantic water and the bottom topography. Indirect evidence of its existence can be seen in Fig. 2.6 showing the position of the Nephrops grounds on the Scottish shelf. Such a ground is located in the North Minch and its presence can be explained with the existence of a retention mechanism; the recirculation cell may cause the larvae to be retained in this location. This has been already demonstrated by the work of Hill *et al.* (1996) where the summer gyre in the western Irish Sea acts in this fashion. The presence of a symmetrical ground in the

southern end, where the existence of the gyre is well established, strengthens this hypothesis. The spatial variability of this system was also confirmed were computed currents where compared with observations from current meters deployed by the Marine Laboratory, Aberdeen. Predicted and observed stability generally agree for the length of deployment of the instruments but long term residuals give a picture of a flow which is not always pointing northward but presents also southward flow. The period of deployment was too short for a complete picture but model results show a strong correlation between wind and current as expected.

For the first time rates of transport through the Minch were calculated and also in this case particular attention was given to the baroclinic component of the flow. The model was used to separate density-driven component from the total transport and it was possible to demonstrate that the former is significant. Predicted transport followed a seasonal pattern with higher rates in winter. On the other hand the baroclinic contribution followed the opposite trend with increased rates in summer and low rates in winter. This can be related with the fact that in summer there is stratification which enhances the baroclinic effects. In winter the water column is almost homogeneous and water fluxes tend to be correlated with the wind which may also explain the high rate since winds are stronger in this season. In summer the presence of stronger horizontal and vertical gradients may lead to stronger density-driven flow which do not exist in winter. To complete the picture one must consider also the changes in buoyancy due to fresh water inputs from rivers. Their cycles tend to mirror the seasonal pattern of the wind, high contribution in winter followed by low contribution in summer. This could also help to explain the picture observed in the Minch but since the model did not reproduce fresh water dynamics this point remain unclear. Total fluxes are in reasonable agreement with observations.

The model reproduced temperatures in good agreement with observation whilst salinities showed a lesser degree of accuracy. Seasonal cycles were captured, the warming and cooling of the water column was reproduced. The presence of the tidal front on the Malin shelf was confirmed and reproduced in agreement with previous observations. Salinity did not show any seasonal cycle and the presence of the haline front was not reproduced with the same accuracy but such a cycle is not present in observations either so that this question remains unanswered. This lack of accuracy in the salinity did not allow us to gain more insight in the interplay between the haline and thermal fields in the development of the Islay front.

Further work is needed to obtain a better agreement between observations and model results and to acquire a better knowledge of the region. Horizontal and vertical resolution do not seem to constitute a serious problem, the mesh of the grid is small enough to capture baroclinic effects but simulations can only benefit from its increase. It is necessary if studies of the velocity structure of the Islay front are to be undertaken. A smaller vertical resolution will decrease the error in the pressure gradient in the deeper part of the domain but the choice for this simulation is acceptable. Tidal forcing is also acceptable but more diurnal constituents can be included since on some parts of the Hebridean shelf they have the same order of magnitude of the semidiurnal components (Cartwright *et al.*, 1980b). The assumption of constant wind on the whole domain is a constraining requirement. In reality winds possess a highly spatial and temporal variability and this influences the wind-driven dynamics and consequently the whole pattern of the circulation. This variability needs to be incorporated in any future simulation to better simulate the circulation. For a realistic seasonal simulation the continental slope current must be also included in future. Its effects were briefly highlighted in section 5.3 together with some modelling works (Xing and Davies, 2001) which demonstrated that this current influences the shelf dynamics with episodes of "leakages" onto the Scottish shelf. Xing and Davies (2001) showed that these flows can drive water both into the North Channel and on the west coast of Scotland, with implications on the recirculation cell in the Sea of the Hebrides and the long term residual circulation. Their model did not take into account density flows created by the seasonal heating and different haline characteristics of the sea waters. These features and their effects could be further investigated with the help of the model used here. These simulations could show the eventual importance of the shelf current on the regional circulation and its seasonal development.

The major obstacle to overcome remains the poor agreement between observed and calculated salinity. Previous simulations of a fresh water river inflow (Kourafalou *et al.*, 1996a) demonstrated that the Princeton Ocean Model is capable of sustaining fresh water dynamics, with the development of a plume subjected to the influence of the rotation of the planet. These results were obtained with a river inflow larger than the outflow measured on the Scottish shelf (constant values of 3200 m^3 s^{-1} against values of 500 m^3 s^{-1} at maximum and for brief periods) and the only source of buoyancy was concentrated in few points. The present simulation was also forced only with a limited number of "point-like" sources of fresh water but the river runoff

is spread along all the Scottish coast so that this must be taken into consideration. Rain and evaporative fluxes need also to be considered because of their contribution to the overall budget. In this particular case resolution could have been an issue; probably it was not fine enough to capture the dynamics of such processes; its increase could lead to a better representation of buoyancy fluxes, especially close to the fresh water source. Further tests of the model with diffuse and variable outflow must be undertaken to improve its performance in dealing with this kind of forcing and to ascertain its capabilities where haline contributions are important for the physics of the circulation.

Finally, results obtained from these simulations highlight the importance of numerical models as invaluable tools for the investigation of the mechanisms which control the dynamics of the circulation and the thermohaline characteristic of shelf seas. These models need to be three-dimensional and baroclinic so to capture all the contributions to the long-term circulation which, as shown, is sensitive to changes of buoyancy. To obtain a complete picture of the region of interest this kind of study needs to be coupled with a campaign of observations which must be used to validate the model results.

Bibliography

Arakawa, A. and V. R. Lamb (1977) Computational design of the UCLA general circulation model. *Methods in Computational Physics*, **17**, 173 – 265.

Asselin, R. (1972) Frequency filters for time integrations. *Monthly Weather Review*, **100**, 487 – 490.

Backhaus, J. O. (1985) A three-dimensional model for the simulation of shelf sea dynamics. *Deutsche Hydrographische Zeirschrift*, **38**, 165 – 187.

Blackadar, A. K. (1962) The vertical distribution of wind and turbulent exchange in a neutral atmosphere. *Journal of Geophysical Research*, **67**, 3095 – 3120.

Bleck, R., C. Rooth, D. Hu and L. Smith (1992) Salinity-driven thermocline transients in a wind- and thermohaline-force isopycnic coordinate model of the North Atlantic. *Journal of Physical Oceanography*, **22**, 1486 – 1505.

Blumberg, A. F. and H. J. Herring (1987) Circulation modelling using orthogonal curvilinear coordinates. In N. Heaps, editor, *Three-Dimensional Models of Marine and Estuarine Dynamics*, p. 208. American Geophysical Union.

Blumberg, A. F. and G. L. Mellor (1983) Diagnostic and Prognostic Numerical Circulation Studies of the South Atlantic Bight. *Journal of Geophysical Research*, **88**, 4579 – 4592.

Blumberg, A. F. and G. L. Mellor (1987) A description of a three-dimensional coastal ocean circulation model. In N. Heaps, editor, *Three-dimensional Coastal Ocean Circulation Models*, number 4 in Coastal and Estuarine Sciences, p. 208. American Geophysical Union.

Blumberg, A. F. and D. W. Pritchard (1997) Estimate of the transport trough the East River, New York. *Journal of Geophysical Research*, **102**, 5685 – 5703.

Booth, D. A. and D. J. Ellett (1983) The Scottish slope current. *Continental Shelf Research*, **2**, 127 – 146.

Bowden, K. F. (1980) Physical and Dynamical Oceanography of the Irish Sea. In F. T. Banner, M. B. Collins and K. S. Massie, editors, *The North-West European Shelf Seas: The Sea Bed and the Sea in Motion II. Physical and Chemical*

Oceanography and Physical Resources, pp. 301 – 351. Elsevier Scientific Publishing.

Bowden, K. F., L. A. Fairbairn and P. Hughes (1959) The distribution of shearing stresses in a tidal current. *Geophysical Journal of the Royal Astronomical Society*, **2**, 288 – 305.

Bowers, D. G. and K. M. M. Lwiza (1994) The temperature minimum at tidal fronts. *Annales Geophysicae*, **12**, 683 – 687.

Bowers, D. G. and J. H. Simpson (1990) Seasonal variations in the seasonal heating cycle in the North-West European Shelf Seas. *Continental Shelf Research*, **11**(2), 185 – 196.

Brink, K. H. (1998) Deep Sea Forcing and Exchange Processes. In K. H. Brink and A. R. Robinson, editors, *The Sea*, volume 10, pp. 151 – 167. John Wiley and Sons, Inc.

Brown, J. and E. M. Gmitrowicz (1995) Observations of the Transverse Structure and Dynamics of the Low Frequency Flow Through the North Channel of the Irish Sea. *Continental Shelf Research*, **15**, 1133 – 1156.

Bryan, A. (1994) The Minch Review. Technical report, Scottish Natural Heritage.

Bryan, K. (1969) A numerical method for the study of the circulation of the world ocean. *Journal of Computational Physics*, **4**, 347 – 376.

Burchard, H. (2001) On the q^2l Equation by Mellor and Yamada (1982). *Journal of Physical Oceanography*, **31**, 1377 – 1387.

Burchard, H., O. Petersen and T. P. Rippeth (1998) Comparing the Performances of the Mellor-Yamada and the $k-\epsilon$ Two Equations Models. *Journal of Geophysical Research*, **103**, 10,543 – 10,554.

Cartwright, D. E., A. C. Edden, R. Spencer and J. M. Vassie (1980a) The tides on the north east Atlantic Ocean. *Philosophical Transaction of the Royal Society of London*, **298**, 87 – 139.

Cartwright, D. E., J. M. Huthnance, R. Spencer and J. M. Vassie (1980b) On the St. Kilda tidal regime. *Deep-Sea Research*, **27A**, 61 – 70.

Chapman, D. C. (1985) Numerical Treatment of Cross-Shelf Open Boundary in a Barotropic Coastal Ocean Model. *Journal of Physical Oceanography*, **15**, 1060 – 1075.

Clarke, A. J. and D. S. Battisti (1981) The Effect of Continental Shelves on Tides. *Deep Sea Research*, **28A**, 665 – 682.

Cox, M. D. (1984) A primitive equation three-dimensional model of the ocean. Technical report 1, GFDL Ocean Group, Princeton University, N.J.

Craig, R. E. (1959) Hydrography of Scottish Coastal Waters. *Marine Research*, **2**, 1 – 30.

Csanady, G. T. (1976) Mean Circulation in Shallow Seas. *Journal of Geophysical Research*, **81**, 5389 – 5399.

Csanady, G. T. (1978) Wind Effects on Surface to Bottom Fronts. *Journal of Geophysical Research*, **83**, 4633 – 4640.

Davies, A. M. (1987) Spectral models in continental shelf sea oceanography. In N. Heaps, editor, *Three-Dimensional Models of Marine and Estuarine Dynamics*, number 4 in Coastal and Estuarine Sciences, p. 208. American Geophysical Union.

Davies, A. M. (1997) A Three-Dimensional Model of the Diurnal and Semi - Diurnal Tides on the European Shelf. *Journal of Geophysical Research*, **102**, 8625 – 8656.

Davies, A. M. and J. N. Aldridge (1993) A numerical model study of parameters influencing tidal currents in the Irish Sea. *Journal of Geophysical Research*, **98**, 7049 – 7067.

Davies, A. M. and G. K. Furnes (1980) Observed and computed M_2 tidal currents in the North Sea. *Journal of Physical Oceanography*, **10**, 237 – 257.

Davies, A. M. and P. Hall (2000) The Response of the North Channel of the Irish Sea and Clyde Sea to Wind Forcing. *Continental Shelf Research*, **20**, 897 – 940.

Davies, A. M. and J. E. Jones (1992) A Three-Dimensional Wind Driven Circulation Model of the Celtic and Irish Seas. *Continental Shelf Research*, **12**, 159 – 188.

Davies, A. M., J. E. Jones and J. Xing (1997a) Review of Recent Developments in Tidal Hydrodynamic Modelling. I ; Spectral Models. *Journal of Hydraulic Engineering*, **123**, 278 – 292.

Davies, A. M. and S. C. Kwong (2000) Tidal Energy Fluxes and Dissipation on the European Continental Shelf. *Journal of Geophysical Research*, **105**, 21,969 – 21,898.

Davies, A. M., S. C. Kwong and R. A. Flather (1997b) A three-dimensional model of diurnal and semidiurnal tides on the European shelf. *Journal of Geophysical Research*, **102**, 8625 – 8656.

Dickson, R. R., W. J. Gould, C. Griffiths, K. J. Medler and E. M. Gmitrowicz (1986) Seasonality in Currents of the Rockall Channel. In *Proceedings of the Royal Society of Edinburgh*, volume 88B, pp. 103 – 125.

Dietrich, D. E., M. G. Marietta and P. J. Roache (1987) An ocean modelling system with turbulent boundary layers and topography: model description. *International Journal of Numerical Methods in Fluids*, **7**, 833 – 855.

Ellett, D. J. (1979) Some Oceanographic Features of Hebridean Waters. In *Proceedings of the Royal Society of Edinburgh*, volume 77B, pp. 61 – 74.

Ellett, D. J. and A. Edwards (1983) Oceanography and Inshore Hydrography of the Inner Hebrides. In *Proceedings of the Royal Society of Edinburgh*, volume 83B, pp. 143 – 160.

Ellett, D. J., A. Edwards and R. Bowers (1986) The Hydrography of the Rockall Channel - an Overview. In *Proceedings of the Royal Society of Edinburgh*, volume 88B, pp. 61 – 81.

Ellett, D. J. and J. H. A. Martin (1973) The Physical and Chemical Oceanography of the Rockall Channel. *Deep Sea Research*, **20**, 585 – 625.

Elliott, A. J. and T. Clarke (1991) Seasonal Stratification in the Northwest European Shelf Seas. *Continental Shelf Research*, **11**, 467 – 492.

Elliott, A. J., T. Clarke and Z. Li (1991) Monthly Distribution of Surface and Bottom Temperature in the Northwest European Shelf Seas. *Continental Shelf Research*, **11**, 453 – 466.

Ezer, T. and G. L. Mellor (1994) Diagnostic and prognostic calculations of the North Atlantic circulation and sea level using a sigma coordinate ocean model. *Journal of Geophysical Research*, **99**, 14,159 – 14,171.

Ezer, T. and G. L. Mellor (1997) Simulation of the Atlantic Ocean with a free surface sigma coordinate ocean model. *Journal of Geophysical Research*, **102**, 15,647 – 15,657.

Flather, R. A. (1976) A Tidal Model of the North-West European Continental Shelf. *Mémoires Société Royale des Sciences de Liège*, **X**, 141 – 161.

Galperin, B., L. H. Kantha, S. Assid and A. Rosati (1988) A Quasi-equilibrium Turbulent Energy Model for Geophysical Flows. *Journal of the Atmospheric Sciences*, **45**, 55 – 62.

Galperin, B. and G. L. Mellor (1990a) A time-dependent, Three-dimensional Model of the Delaware Bay and River System. Part 1: Description of the model and Tidal Analysis. *Estuarine, Coastal and Shelf Sciences*, **31**, 231 – 253.

Galperin, B. and G. L. Mellor (1990b) A time-dependent, Three-dimensional Model of the Delaware Bay and River System. Part 2: Three-dimensional Flow Fields and Residual Circulation. *Estuarine, Coastal and Shelf Sciences*, **31**, 255 – 281.

Garrett, C. J. R. and J. W. Loder (1981) Dynamical aspects of shallow sea fronts. *Philosophical Transactions of the Royal Society of London*, **302A**, 563 – 581.

Gary, J. M. (1973) Estimate of truncation error in transformed coordinate, primitive equation atmospheric models. *Journal of Atmospheric Sciences*, **30**, 223 – 233.

George, K. J. (1980) Anatomy of an Amphidrome. *The hydrographic Journal*, **18**, 5 – 12.

Gerdes, R. (1993) A Primitive Equation Ocean Circulation Model Using a General Vertical Coordinate Transformation 1. Description and Testing of the Model. *Journal of Geophysical Research*, **98**, 14,683 – 14,701.

Gill, A. (1982) *Atmosphere - Ocean Dynamics*. Academic Press, 662 pp.

Green, F. H. W. and R. J. Harding (1983) Climate of the Inner Hebrides. *Proceeding of the Royal Society of Edinburgh*, **83B**, 121 – 140.

Haidvogel, D. B. and A. Beckmann (1998) Numerical models of the coastal ocean. In K. H. Brink and A. R. Robinson, editors, *The Sea*, volume 10, pp. 3 – 20. John Wiley and Sons, Inc.

Haney, R. L. (1991) On the Pressure Gradient force over Steep Topography in Sigma Coordinate Ocean Models. *Journal of Physical Oceanography*, **14**, 610 – 619.

Heaps, N. S. (1969) A Two-Dimensional Model. *Philosophical transaction of the Royal Society*, **265A**, 93 – 137.

Hill, A. E. (1995) Leakage of Barotropic Slope Currents Onto the Continental Shelf. *Journal of Physical Oceanography*, **25**, 1617 – 1621.

Hill, A. E. (1996) Spin-Down and the Dynamics of Dense Pool Gyres in Shallow Seas. *Journal of Marine Research*, **54**, 471 – 486.

Hill, A. E. (1998) Buoyancy Effects in Coastal and Shelf Seas. In K. H. Brink and A. R. Robinson, editors, *The Sea*, volume 10, pp. 21 – 62. John Wiley and Sons, Inc.

Hill, A. E., J. Brown and L. Fernand (1996) The Western Irish Sea Gyre: A Retention System for Norway Lobsters (Nephros Norvegicus). *Oceanologica Acta*, **19**, 357 – 368.

Hill, A. E., J. Brown and L. Fernand (1997a) The Summer Gyre in the Western Irish Sea: Shelf Sea Paradigms And Management Implications. *Estuarine, Coastal and Shelf Sciences*, **44**, 83 – 95.

Hill, A. E., R. Durazo and A. D. Smeed (1994) Observation of a Cyclonic Gyre in the Western Irish Sea. *Continental Shelf Research*, **14**, 479 – 490.

Hill, A. E., K. J. Horsburgh, R. W. Garvine, P. A. Gillibrand, G. Slesser, W. R. Turrel and R. D. Adams (1997b) Observation of a Density-Driven Recirculation of the Scottish Coastal Current in The Minch. *Estuarine, Coastal and Shelf Sciences*, **45**, 473 – 484.

Hill, A. E., I. D. James, P. F. Linden, J. P. Matthews, D. Prandle, J. H. Simpson, E. M. Gmitrowicz, D. A. Smeed, K. M. M. Lwiza, R. Durazo, A. D. Fox and D. G. Bowers (1993) Dynamics of Tidal Mixing Fronts in The North Sea. *Philosophical Transaction of the Royal Society of London*, **343A**, 431 – 446.

Hill, A. E. and J. H. Simpson (1988) Low - Frequency Variability of The Scottish Coastal Current Induced by Along-Shore Pressure Gradients. *Estuarine and Coastal Sciences*, **27**, 163 – 180.

Hill, A. E. and J. H. Simpson (1989) On the Interaction of Thermal and Haline Fronts: The Islay Front Revisited. *Estuarine, Coastal and Shelf Sciences*, **28**, 495 – 505.

Holt, J. T. and I. D. James (1999) A simulation of the southern North Sea in comparison with measurements from the North Sea Project. Part 1: Temperature. *Continental Shelf Research*, **19**, 1087 – 1112.

Horsburgh, K. J. (1999) *Observations and Modelling of the Western Irish Sea Gyre*. Ph.D. thesis, University of Wales.

Horsburgh, K. J., A. E. Hill, J. Brown, L. Fernand, R. W. Garvine and M. M. P. Angelico (2000) Seasonal evolution of the cold pool gyre in the western Irish Sea. *Progress in Oceanography*, **46**, 1 – 58.

Howarth, M. J. (1998) The Effect of Stratification on Tidal Current Profiles. *Continental Shelf Research*, **18**, 1235 – 1254.

Howarth, M. J. and D. T. Pugh (1983) Observations of Tides over the Continental Shelf of North - West Europe. In B. Johns, editor, *Physical Oceanography of Coastal and Shelf Seas*, volume 35 of *Elsevier Oceanography Series*, pp. 135 – 188. Elsevier Scientific Publishing.

Huntley, D. A. (1980) Tides on the North-West European Continental Shelf. In F. T. Banner, M. B. Collins and K. S. Massie, editors, *The North-West European Shelf Seas: The Sea Bed and the Sea in Motion II. Physical and Chemical Oceanography and Physical Resources*, pp. 301 – 351. Elsevier Scientific Publishing.

Huthnance, J. M. (1973) Tidal Currents Asymmetries over the Norfolk Sandbanks. *Estuarine and Coastal Sciences*, **1**, 89 – 99.

Huthnance, J. M. (1981) Waves and Currents Near the Continental Shelf Edge. *Progress in Oceanography*, **10**, 192 – 226.

Huthnance, J. M. (1986) The Rockall Slope Current and Shelf-Edge Processes. In *Proceedings of the Royal Society of Edinburgh*, volume 88B, pp. 83 –101.

Ip, J. T. C. and D. R. Lynch (1994) Three-Dimensional Shallow Water Hydrodynamics on Finite Elements: Non Linear Time-Stepping Prognostic Models. Technical Report Report NML - 94 - 1, Numerical Methods laboratory, Darthmounth College, Hanover, N. H.

James, I. D. (1977) A model of the annual cycle of temperature in a frontal region of the Celtic Sea. *Estuarine and Coastal Marine Sciences*, **5**, 339 – 353.

James, I. D. (1978) A Note on the Circulation Induced by a Shallow-Sea Front. *Estuarine and Coastal Marine Sciences*, **7**, 197 – 202.

James, I. D. (1987) A general three-dimensional eddy-resolving model for stratified seas. In J. C. J. Nihoul and B. M. Jamart, editors, *Three-dimensional models for marine and estuarine hydrodynamics*, pp. 55 – 72. Elsevier Scientific Publishing.

James, I. D. (1990) Numerical Modelling of Density-Driven Circulation in Shelf Seas. In A. M. Davies, editor, *Modelling Marine Systems*, volume II, pp. 345 – 372. CRC Press.

James, I. D. (1996) Advection schemes for shelf seas models. *Journal of Marine Systems*, **8**, 237 – 254.

Jaw, S. Y. and C. J. Chen (1998) Present Status of Second-Order Closure Turbulence Models. I: Overview. *Journal of Engineering Mechanics (ACSE)*, **124**, 485 – 501.

Jeffrey, D. F., A. Preston and A. K. Steele (1973) Distribution of ^{137}Cs in British Coastal Waters. *Marine Pollution Bulletin*, **4**, 118 – 122.

Jerlov, N. G. (1976) *Marine Optics*, volume 14. Elsevier, Amsterdam, 231 pp.

Jones, E. J. W., R. G. Perry and J. L. Wild (1986) Geology of the Hebridean Margin of the Rockall Trough. In *Proceedings of the Royal Society of Edinburgh*, volume 88B, pp. 27 – 51.

Jones, J. E. and M. J. Howarth (1995) Salinity models of the southern North Sea. *Continental Shelf Research*, **15**, 705–727.

Kliem, N. and J. Pietrzak (1999) On the pressure gradient error in sigma coordinate ocean models: A comparison with a laboratory experiment. *Journal of Geophysical Research*, **104**, 29,781 – 29,800.

Knight, P. J. and M. J. Howarth (1999) The Flow Through the North Channel of the Irish Sea. *Continental Shelf Research*, **19**, 693 – 716.

Kourafalou, V. H., L. Y. Oey, J. D. Wang and T. N. Lee (1996a) The Fate of River Discharge on the Continental Shelf, 1, Modelling the River Plume and The Inner Shelf Coastal Current. *Journal of Physical Oceanography*, **101**, 3415 – 3434.

Kourafalou, V. H., L. Y. Oey, J. D. Wang and T. N. Lee (1996b) The Fate of River Discharge on the Continental Shelf, 2, Transport of coastal low-salinity water under realistic wind and tidal forcing. *Journal of Physical Oceanography*, **101**, 3435 – 3455.

Kowalik, Z. and T. S. Murty (1993) *Numerical Modelling of Ocean Dynamics*, volume 5 of *Series on Ocean Engineering*. World Scientific Publishing Co. Pte. Ltd.

Kundu, P. K. (1990) *Fluid Mechanics*. Academic Press, 628 pp.

Le Févre, J. (1986) Aspects of the Biology of the Frontal Systems. *Advances in Marine Biology*, **23**, 160 – 299.

Levitus, S. (1982) Climatological Atlas of the World. Professional Paper 13, NOAA, U.S. Department of Commerce.

Lwiza, K. M., D. G. Bowers and J. H. Simpson (1991) Residual and Tidal Flow at a Mixing Font in the North Sea. *Continental Shelf Research*, **11**, 1379 – 1395.

Madala, R. V. and S. A. Piacsek (1977) A semi-implicit numerical model for baroclinic oceans. *Journal of Computational Physics*, **23**, 167 – 178.

Maier-Reimer, E. (1977) Residual Circulation in the North-Sea Due to M_2 Tide and Mean Annual Wind Stress. *Deutsche Hydrographische Zeirschrift*, **30**, 69 – 80.

Martin, P. J. (1985) Simulation of the Mixed layer at OWS November and Papa With Several Models. *Journal of Geophysical Research*, **90**, 903 – 916.

McKay, W. A., M. S. Baxter, D. J. Ellett and D. T. Meldrum (1986) Radiocaesium and Circulation Patterns West of Scotland. *Journal of Environmental Radioactivity*, **4**, 205 – 232.

McKinley, I. G., M. S. Baxter, D. J. Ellett and W. Jack (1981) Tracer Applications of the Radiocaesium in the Sea of The Hebrides. *Estuarine, Coastal and Shelf Sciences*, **13**, 69 – 82.

Mellor, G. L. (1991) An equation of state for numerical models of oceans and estuaries. *Journal of Atmospheric and Oceanic Technology*, **8**, 609 – 611.

Mellor, G. L. (1998) Users Guides for a Three-dimensional,Primitive Equation Numerical Ocean Model. Technical report, Program in Atmospheric and Oceanic Sciences, Princeton University.

Mellor, G. L. (2003) Comment on "Stability of algebraic non-equilibrium second-order closure models. *Ocean Modelling*, **5**, 193–194.

Mellor, G. L. and A. F. Blumberg (1985) Modelling Vertical and Horizontal Diffusivities with the Sigma Coordinate System. *Monthly Weather Review*, **113**, 1379 – 1383.

Mellor, G. L., T. Ezer and L. Y. Oey (1994) The Pressure Gradient Conundrum of Sigma Coordinate Ocean Models. *Journal of Atmospheric and Oceanic Technology*, **11**, 1126 – 1134.

Mellor, G. L. and T. Yamada (1982) Development of a Turbulence Closure Model for geophysical Fluid problems. *Reviews of Geophysics and Space Physics*, **20**, 851 – 875.

Minato, S. (1996) Numerical Simulation of Tide and Storm Surges in the Seto Inland Sea Using the Princeton Ocean Model. *Papers in meteorology and Geophysics*, **47**, 103 – 114.

Minato, S. (1998) Storm Surge Simulation using POM and a Revisitation of Dynamics of Sea Surface Elevation Short-Term Variation. *Papers in meteorology and Geophysics*, **48**, 79 – 88.

Mork, M. (1981) Circulation Phenomena and Frontal Dynamics of the Norwegian Coastal Current. *Philosophical Transactions of the Royal Society of London*, **302A**, 635 – 647.

Münchow, A. and R. W. Garvine (1993) Dynamical Properties of a Buoyancy-Driven Coastal Current. *Journal of Geophysical Research*, **98**, 20,062 – 20,077.

Munk, W. H. and E. R. Anderson (1948) Notes on a theory of the thermocline. *Journal of Marine Research*, **7**, 276 – 295.

O'Connor, W. P. (1991) A User's Manual for The Princeton Ocean Model. Technical Report SP-5, Institute for Naval Oceanography.

Oey, L. Y. and P. Chen (1992a) A Model Simulation of Circulation in the Northeast Atlantic Shelves and Seas. *Journal of Geophysical Research*, **97**, 20,087 – 20,115.

Oey, L. Y. and P. Chen (1992b) A Nested-Grid Ocean Model with Application to the Simulation of Meanders and Eddies in the Norwegian Coastal Current. *Journal of Geophysical Research*, **97**, 20,063 – 20,086.

Phillips, N. A. (1957) A coordinate system having some special advantages for numerical forecasting. *Journal of Meteorology*, **14**, 184 – 186.

Pietrzak, J. D. (1995) A comparison of Advection Schemes for Ocean Modelling. Scientific Report 95-8, Danish Meteorological Institute.

Pingree, R. D. and D. K. Griffiths (1978) Tidal Fronts on the Shelf Seas Around The British Isle. *Journal of Geophysical Research*, **83**, 4615 – 4622.

Pingree, R. D. and D. K. Griffiths (1980) Current Driven by a Steady Uniform Wind Stress on the Shelf Seas Around the British Isles. *Oceanologica Acta*, **3**, 227 – 236.

Pingree, R. D. and L. Maddock (1979) Tidal Flow Around An Island With Regularly Sloping Bottom Topography. *Journal of the Marine Biology Association*, **59**, 699 – 710.

Pingree, R. D. and L. Maddock (1980) The Effects of Bottom Friction and Earth's Rotation on an Island's Wake. *Journal of the Marine Biology Association*, **60**, 499 – 508.

Pond, S. and G. L. Pickard (1978) *Introduction to Dynamic Oceanography*. Pergamon Press, 241 pp.

Poodle, T. (1986) Fresh Water Inflow to the Firth of Clyde. In *Proceedings of the Royal Society of Edinburgh*, volume 90B, pp. 55 – 66.

Prandle, D. (1984) A Modelling Study of the Mixing of ^{137}Cs In the Seas of the European Continental Shelf. *Philosophical Transactions of the Royal Society of London*, **310A**, 407 – 436.

Proctor, R. and A. M. Davies (1996) A Three - Dimensional Hydrodynamic Model of Tides Off the North-West Coast of Scotland. *Journal of Marine System*, **7**, 43 – 66.

Pugh, D. T. (1987) *Tides, Surges and Mean Sea-Level*. John Wiley and Sons, Inc., 472 pp.

Ramster, J. W., D. G. Hughes and G. K. Furnes (1978) A 'steadiness' factor for estimating the variability of residual drift in current meter records. *Deutsches Hydrographica*, **31**, 230–236.

Reed, R. K. (1977) On Estimating Insolation over the Ocean. *Journal of Physical Oceanography*, **7**, 482 – 485.

Rippeth, T. P. and J. H. Simpson (1996) The Frequency of Episodes of Complete Vertical Mixing in the Clyde Sea. *Continental Shelf Research*, **16**, 933 – 947.

Robinson, I. S. (1983) Tidally induced residual flow. In B. Johns, editor, *Physical Oceanography of Coastal and Shelf Seas*, volume 35 of *Elsevier Oceanography Series*, pp. 321 – 356. Elsevier Scientific Publishing.

Rosati, A. and K. Miyakoda (1988) A General Circulation Model for Upper Ocean Simulation. *Journal of Physical Oceanography*, **18**, 1601 – 1626.

Sharples, J. and J. H. Simpson (1995) Semi - Diurnal and Longer Period Stability Cycles in the Liverpool Bay ROFI. *Continental Shelf Research*, **15**, 295 – 314.

Simons, T. J. (1974) Verification of numerical models of Lake Ontario, Part I. Circulation in spring and early summer. *Journal of Physical oceanography*, **4**, 507 – 523.

Simpson, J. H. (1981) The Shelf-Sea Fronts: Implications of the Existence and Behaviour. *Philosophical Transactions of the Royal Society of London*, **302A**, 531 – 546.

Simpson, J. H. (1998) Tidal Processes in Shelf Seas. In K. H. Brink and A. R. Robinson, editors, *The Sea*, volume 10, pp. 113 – 150. John Wiley and Sons, Inc.

Simpson, J. H., C. M. Allen and N. C. Morris (1978) Fronts on the Continental Shelf. *Journal of Geophysical Research*, **83**, 4607 – 4614.

Simpson, J. H. and D. G. Bowers (1981) Model of Stratification and Frontal Movement in Shelf Seas. *Deep Sea Research*, **28A**, 727 – 738.

Simpson, J. H., D. J. Edelsten, A. Edwards, N. C. G. Morris and P. B. Tett (1979) The Islay Front: Physical Structure and Phytoplankton Distribution. *Estuarine and Coastal Sciences*, **9**, 713 – 726.

Simpson, J. H. and A. E. Hill (1986) The Scottish Coastal Current. In S. Skreslet, editor, *The Role of Freshwater Outflow in Coastal Marine Ecosystems*, pp. 295 – 308. NATO ASI.

Simpson, J. H. and J. R. Hunter (1974) Fronts in the Irish Sea. *Nature*, **250**, 404 – 406.

Simpson, J. H. and I. D. James (1986) Baroclinic Processes on Continental Shelves. In C. N. K. Mooers, editor, *Coastal and Estuarine Sciences*, pp. 63 – 93. American Geophysical Union.

Simpson, J. H. and A. J. Souza (1995) Semi - Diurnal Switching of Stratification in the Rhine ROFI. *Journal of Geophysical Research*, **100**, 7037 – 7044.

Smagorinski, J. (1963) General circulation experiments with the primitive equations, I. The basic experiment. *Monthly Weather Review*, **91**, 99 – 164.

Smolarkiewicz, P. (1983) A Simple Positive Definite Advection Scheme with Small Implicit Diffusion. *Monthly Weather Review*, **111**, 479 – 486.

Smolarkiewicz, P. (1984) A Fully Multidimensional Positive Definite Advection Transport Algorithm with Small Implicit Diffusion. *Journal of Computational Physics*, **54**, 325 – 362.

Song, Y. and D. B. Haidvogel (1994) A Semi-Implicit Ocean Circulation Model Using a Generalized Topography-Following Coordinate. *Journal of Computational Physics*, **115**, 241 – 267.

Soulsby, R. L. (1990) Tidal - Current boundary layers. In B. le Méhaute and D. M. Hanes, editors, *The Sea*, volume 9A, pp. 523 – 566. John Wiley and Sons, Inc.

Sousa, A. J. and J. H. Simpson (1996) The Modification of Tidal Ellipses by Stratification in the Rhine ROFI. *Continental Shelf Research*, **16**, 997 – 1008.

Taylor, G. I. (1919) Tidal Friction in the Irish Sea. *Philosophical Transactions of the Royal Society of London*, **200A**, 1– 33.

Tee, K. T. (1994) Dynamics of a Two-Dimensional Topographic Rectification Process. *Journal of Physical Oceanography*, **24**, 443 – 465.

Weatherly, G. and P. J. Martin (1978) On the structure and dynamics of the ocean bottom boundary. *Journal of Physical Oceanography*, **14**, 557 – 570.

Xing, J., F. Chen and R. Proctor (1999) A two-dimensional slice model of the shelf edge region off the west coast of Scotland: model response to realistic seasonal forcing and the role of the M_2 tide. *Continental Shelf Research*, **19**, 1353 – 1386.

Xing, J. and A. M. Davies (1995) Application of three dimensional turbulence energy models to the determination of tidal mixing and current in a shallow sea. *Progress in Oceanography*, **35**, 153 – 205.

Xing, J. and A. M. Davies (1996a) Application of a range of turbulence energy models to the determination of M_4 tidal current profiles. *Continental Shelf Research*, **16**, 517 – 547.

Xing, J. and A. M. Davies (1996b) Application of Turbulence Energy Models to the Computation of Tidal Currents and Mixing Intensities in Shelf Regions. *Journal of Physical Oceanography*, **26**, 417 – 447.

Xing, J. and A. M. Davies (1996c) A Numerical Model of the Long Term Flow Along the Malin-Hebrides Shelf. *Journal of Marine Systems*, **8**, 191 – 218.

Xing, J. and A. M. Davies (1999) The Effect of Wind Direction and Mixing Upon the Spreading of a Buoyant Plume in a Non-Tidal Regime. *Continental Shelf Research*, **19**, 1437 – 1483.

Xing, J. and A. M. Davies (2001) The Influence of the Shelf Edge Flows and Wind Upon the Circulation on the Malin Shelf and in the Irish Sea. *Continental Shelf Research*, **21**, 21 – 45.

Young, E. F., J. N. Aldridge and J. Brown (2000) Development and validation of a three-dimensional curvilinear model for the study of fluxes through the North Channel of the Irish Sea. *Continental Shelf Research*, **20**, 997 – 1035.

Young, E. F., J. Brown and J. N. Aldridge (2001) Application of a large area curvilinear model to the study of the wind-forced dynamics of flows through the North Channel of the Irish Sea. *Continental Shelf Research*, **21**, 1403 – 1434.

Zavatarelli, M. and G. L. Mellor (1995) A Numerical Study of the Mediterranean Sea Circulation. *Journal of Physical Oceanography*, **25**, 1384 – 1414.

Appendix A

Comparisons between observed and calculated values for the tidal parameters of the two semi-diurnal constituents M_2 and S_2.

No.	Lat.	Long.	Obs.		Comp.		Δh	Δg	Δhp	Δgp
			amp.(h)	pha.(g)	amp.(h)	pha.(g)				
			cm	deg	cm	deg	cm	deg	%	%
1	58.78	-7.5	104.0	191	95.0	183	9.0	8	9.0	4.3
2	58.45	-5.05	140.0	208	136.0	202	4.0	6	3.1	3.0
3	58.03	-8.58	106.0	178	94.0	173	12.0	5	11.4	3.0
4	57.82	-8.57	107.0	176	97.0	170	10.0	6	9.6	3.7
5	57.77	-7.03	129.0	185	124.0	179	5.0	6	3.7	3.0
6	57.67	-7.48	120.0	177	114.0	169	6.0	8	5.2	4.4
7	57.43	-5.80	153.0	195	147.0	190	6.0	5	3.8	2.7
8	57.30	-7.65	118.0	171	107.0	164	11.0	7	9.3	4.2
9	56.92	-8.58	109.0	168	99.0	161	10.0	7	9.2	4.1
10	56.95	-7.48	113.0	232	106.0	162	7.0	70	6.0	30.2
11	56.50	-6.80	118.0	166	108.0	154	10.0	12	8.6	7.3
12	56.32	-6.38	114.0	165	108.0	149	6.0	16	5.6	9.9
13	56.02	-8.58	112.0	163	98.0	158	14.0	5	12.9	2.9
14	55.38	-7.40	108.0	178	103.0	169	5.0	9	5.0	4.8
15	55.43	-7.23	97.0	175	89.0	175	8.0	0	7.8	0.0
16	55.63	-6.18	16.0	92	21.0	40	-5.0	52	-28.8	56.3
17	55.68	-5.73	19.0	81	31.0	13	-12.0	68	-62.1	84.3
18	55.72	-5.30	107.0	342	119.0	348	-12.0	-6	-11.5	-1.6
19	55.55	-4.68	109.0	340	120.0	346	-11.0	-6	-9.9	-1.7
20	55.47	-6.17	7.0	125	11.0	324	-4.0	161	-63.7	128.8
21	55.32	-5.63	66.0	337	78.0	346	-12.0	-9	-18.6	-2.5
22	55.25	-4.87	105.0	340	117.0	343	-12.0	-3	-11.0	-1.0

Table A.1: Comparison of observed and computed amplitude h (cm) and phase g (degrees) of the M_2 tidal elevation. Last 4 columns give absolute and percentage errors for amplitude and phase.

Error Interval (m)						
-0.15	-0.10	-0.05	0	0.05	0.10	0.15
Number of points						
1	7	7	0	2	5	0

Table A.2: Distribution of errors for amplitude (m) for the elevation of the M_2 tidal constituent. The histogram shows the number of point where the calculated amplitude is above or below the observed value.

Error Interval (degrees)												
-180	-150	-120	-90	-60	-30	0	30	60	90	120	150	180
Number of points												
0	0	0	0	3	1	17	0	0	0	0	1	0

Table A.3: Distribution of errors for phase (degrees) for the M_2 tidal constituent. The histogram shows the number of point where the calculated phase is above or below the observed value.

No.	Lat.	Long.	Obs.		Comp.		Δh	Δg	ht	hc
			amp.(h)	pha.(g)	amp.(h)	pha.(g)				
			cm s^{-1}	deg.	cm s^{-1}	deg.	cm s^{-1}	deg.	m	m
1	59.78	-6.18	27.0	257.4	30.9	240.8	-3.9	16.6	370	250
1	59.78	-6.18	24.5	251.1	30.3	239.7	-5.8	11.4	370	100
1	59.78	-6.18	20.9	244.8	30.8	240.7	-9.9	4.1	370	25
2	59.66	-6.04	23.8	254.4	25.4	232.3	-1.6	22.1	237	150
2	59.66	-6.04	18.8	250.5	23.8	230.7	-5.0	19.9	237	25
3	59.59	-7.25	6.7	213.8	11.9	214.9	-5.2	-1.1	1019	990
3	59.59	-7.25	10.3	231.3	11.8	214.7	-1.5	16.6	1019	549
3	59.59	-7.25	9.5	231.2	11.8	214.8	-2.3	16.4	1019	303
3	59.59	-7.25	8.7	223.1	11.7	214.5	-3.0	8.6	1019	102
3	59.59	-7.25	9.0	189.1	11.8	214.8	-2.8	-25.7	1019	12
4	59.48	-6.35	26.6	225.1	22.8	199.8	3.8	25.3	188	25
5	59.14	-7.71	11.0	210.0	8.7	195.2	2.3	14.8	998	894
5	59.14	-7.71	10.1	211.9	8.6	195.7	1.5	16.2	998	595
5	59.14	-7.71	2.2	156.1	8.5	195.8	-6.3	-39.7	998	47
6	59.09	-7.45	15.2	196.3	11.4	188.6	3.8	7.7	514	399
6	59.09	-7.45	13.7	194.1	11.3	188.6	2.4	5.5	514	248
6	59.09	-7.45	8.1	188.3	11.4	188.6	-3.3	-0.3	514	46
7	59.03	-8.53	7.5	176.1	6.6	186.8	0.9	-10.7	1535	1400
7	59.03	-8.53	6.9	181.5	6.6	186.6	0.3	-5.1	1535	1000
8	58.92	-7.49	17.4	118.0	9.7	159.4	7.7	-41.4	163	130
9	58.78	-7.50	22.0	140.1	10.7	117.7	11.3	22.4	110	25
10	58.72	-5.88	16.3	148.2	20.4	163.4	-4.1	-15.2	114	11
11	58.03	-8.15	3.7	190.8	4.2	186.9	-0.5	3.9	142	75
11	58.03	-8.15	6.6	178	4.5	182.6	2.1	-4.6	142	25
12	58.01	-8.79	9.5	194.2	6.1	196.8	3.4	-2.6	142	28
13	57.99	-8.73	5.4	216.8	6.3	199.7	-0.9	17.2	146	105
13	57.99	-8.73	8.3	194	6.1	196.8	2.2	-2.8	146	25
14	57.94	-8.85	6.8	225.9	6.7	193.9	0.1	32.0	155	100
14	57.94	-8.85	10.2	167.1	6.4	188.9	3.8	-21.9	155	25

No.	Lat.	Long.	Obs.		Comp.		Δh	Δg	ht	hc
			amp.(h)	pha.(g)	amp.(h)	pha.(g)				
			cm s^{-1}	deg.	cm s^{-1}	deg.	cm s^{-1}	deg.	m	m
15	57.93	-8.86	10.1	198.3	6.7	193.9	3.4	4.4	152	100
16	57.60	-8.17	5.7	162.9	6.4	144.1	-0.7	18.8	135	75
16	57.60	-8.17	9.5	144.5	6.5	137.9	3.0	6.6	135	25
17	56.99	-8.94	21.0	139.2	4.8	128.1	16.2	11.1	130	91
17	56.99	-8.94	20.6	136.7	4.7	120.3	15.9	16.4	130	21
18	56.92	-8.58	16.5	113.2	14.7	122.9	1.8	-9.7	126	25
19	56.48	-7.98	11.5	165.7	8.3	119.2	3.2	46.5	170	140
19	56.48	-7.98	15.0	115.6	8.1	117	6.9	-1.4	170	50
20	56.00	-8.57	13.7	140.1	10.2	117.2	3.5	22.9	136	25
21	55.88	-6.56	26.8	90.7	13.4	197.8	13.4	-107.1	44	11
22	55.87	-5.75	15.4	259.9	0.8	300.0	14.6	-40.1	123	81
22	55.87	-5.75	11.4	259.2	0.7	299.1	10.7	-39.9	123	41
23	55.51	-6.85	82.9	234.2	109.8	236.2	-26.9	-2.0	58	39
23	55.51	-6.85	82.2	233.8	109.8	236.2	-27.6	-2.4	58	37
23	55.51	-6.85	69.0	233.3	92.9	235.1	-23.9	-1.8	58	11
24	55.50	-8.01	16.2	168.2	16.5	166.6	-0.3	1.7	73	41
24	55.50	-8.01	12.7	158	15.5	165.0	-2.8	-7.0	73	10
25	55.46	-6.16	46.9	242.4	83.7	244.1	-36.8	-1.7	110	6
26	55.42	-7.51	46.8	201.5	38.5	198.2	8.4	3.3	54	30
26	55.42	-7.51	33.6	192.0	35.6	195.0	-2.0	-3.0	54	11
27	55.34	-5.11	17.6	259.8	21.0	261.4	-3.4	-1.6	52	28
27	55.34	-5.11	17.2	248.0	19.0	257.5	-1.8	-9.5	52	10
28	55.03	-5.32	14.2	198.3	34.7	220.7	-20.5	-22.4	73	60
28	55.03	-5.32	12.3	210.4	32.2	225.7	-19.9	-15.3	73	33
28	55.03	-5.32	9.9	227.5	33.0	224.4	-23.1	3.1	73	5

Table A.4: Comparison of observed and computed amplitude h (cm s^{-1}) and phase g (degrees) for the M_2 East-west tidal velocity component. The 8^{th} and 9^{th} column give absolute errors for amplitude and phase whilst the two last columns give total depth (ht) and height above the bed of the current meter (hc).

No.	Lat.	Long.	Obs.		Comp.		Δh	Δg	ht	hc
			amp.(h)	pha.(g)	amp.(h)	pha.(g)				
			cm s^{-1}	deg.	cm s^{-1}	deg.	cm s^{-1}	deg.	m	m
1	59.78	-6.18	21.3	215.4	20.4	195.8	0.9	19.6	370	250
1	59.78	-6.18	15.8	209.7	19.8	196.0	-4.0	13.7	370	100
1	59.78	-6.18	12.7	214.8	20.3	195.8	-7.6	19.1	370	25
2	59.66	-6.04	22.8	223.7	13.6	196.2	9.2	27.6	237	150
2	59.66	-6.04	18.4	232.0	12.2	203.4	6.2	28.6	237	25
3	59.59	-7.25	10.3	246.4	8.2	213.8	2.1	32.6	1019	990
3	59.59	-7.25	10.1	224.2	8.2	214.1	1.9	10.1	1019	549
3	59.59	-7.25	9.3	228.3	8.2	214.6	1.1	13.7	1019	303
3	59.59	-7.25	7.5	230.2	8.2	214.7	-0.7	15.5	1019	102
3	59.59	-7.25	3.9	256.4	8.2	214.4	-4.3	42.0	1019	12
4	59.48	-6.35	12.5	177.4	5.3	154.5	7.2	22.9	188	25
5	59.14	-7.71	10.0	197.3	9.0	212.1	1.0	-14.8	998	894
5	59.14	-7.71	9.1	203.2	9.1	212.6	0.0	-9.4	998	595
5	59.14	-7.71	10.3	251.0	9.1	212.9	1.2	38.2	998	47
6	59.09	-7.45	9.1	175.4	7.6	204.7	1.5	-29.3	514	399
6	59.09	-7.45	8.5	187.2	7.6	205.7	0.9	-18.6	514	248
6	59.09	-7.45	7.5	217.1	7.6	205.1	-0.1	12.0	514	46
7	59.03	-8.53	3.1	244.3	6.2	207.7	-3.1	36.6	1535	1400
7	59.03	-8.53	4.4	226.5	6.2	207.7	-1.8	18.8	1535	1000
8	58.92	-7.49	8.2	301.0	3.9	254.5	4.3	46.5	163	130
9	58.78	-7.50	8.0	354.5	9.9	280.0	-1.9	74.5	110	25
10	58.72	-5.88	14.8	237.0	13.3	275.2	1.5	-38.2	114	11
11	58.03	-8.15	14.6	194.6	15.9	190.0	-1.3	4.6	142	75
11	58.03	-8.15	12.8	188.5	15.5	189.6	-2.7	-1.1	142	25
12	58.01	-8.79	13.0	171.7	15.0	178.0	-2.0	-6.3	142	28
13	57.99	-8.73	12.6	188.8	15.4	178.0	-2.8	10.8	146	105
13	57.99	-8.73	11.8	176.4	15.0	178.0	-3.2	-1.6	146	25
14	57.94	-8.85	15.4	183.3	14.7	174.6	0.7	8.7	155	100
14	57.94	-8.85	10.2	145.9	14.1	174.8	-3.9	-28.9	155	25
15	57.93	-8.86	14.1	170.6	14.7	174.6	-0.6	-4.0	152	100
16	57.60	-8.17	14.2	159.4	12.2	154.4	2.0	5.0	135	75
16	57.60	-8.17	11.3	147.4	11.8	154.9	-0.5	-7.5	135	25
17	56.99	-8.94	16.9	69.6	5.2	108.0	11.7	-38.4	130	91
17	56.99	-8.94	17.0	69.3	4.8	106.3	12.2	-37.0	130	21
18	56.92	-8.58	11.3	46.0	9.9	67.5	1.4	-21.5	126	25
19	56.48	-7.98	8.8	89.9	9.3	70.5	-0.5	19.4	170	140
19	56.48	-7.98	13.0	41.6	8.9	69.9	4.1	-28.2	170	50
20	56.00	-8.57	7.3	62.6	8	32.6	-0.7	30.0	136	25
21	55.88	-6.56	70.7	69.9	95.7	62.6	-25.0	7.3	44	11

No.	Lat.	Long.	Obs.		Comp.		Δh	Δg	ht	hc
			amp.(h)	pha.(g)	amp.(h)	pha.(g)				
			cm s^{-1}	deg.	cm s^{-1}	deg.	cm s^{-1}	deg.	m	m
22	55.87	-5.75	26.0	18.2	1.2	307.9	24.8	70.3	123	81
22	55.87	-5.75	28.0	358.4	1.2	308.3	26.8	50.1	123	41
23	55.51	-6.85	50.8	76.7	56.3	79.8	-5.5	-3.1	58	39
23	55.51	-6.85	56.1	74.9	56.3	79.8	-0.2	-4.9	58	37
23	55.51	-6.85	41.4	73.2	44.6	73.5	-3.1	-0.3	58	11
24	55.50	-8.01	4.4	75.2	1.4	109.2	3.0	-33.9	73	41
24	55.50	-8.01	2.6	359.4	0.7	185.6	1.9	173.8	73	10
25	55.46	-6.16	31.6	22.0	31.6	43.8	0.0	-21.8	110	6
26	55.42	-7.51	10.1	186.8	16.3	207.1	-6.2	-20.3	54	30
26	55.42	-7.51	10.8	239.3	15.7	211.2	-4.9	28.1	54	11
27	55.34	-5.11	12.8	262.7	5.6	320.9	7.2	-58.2	52	28
27	55.34	-5.11	6.7	271.8	6.4	323.4	0.3	-51.6	52	10
28	55.03	-5.32	45.2	30.1	69.0	51.8	-23.8	-21.7	73	60
28	55.03	-5.32	45.0	34.5	65.2	48.8	-20.2	-14.3	73	33
28	55.03	-5.32	39.0	25.3	66.6	50.0	-27.6	-24.7	73	5

Table A.5: Comparison of observed and computed amplitude h (cm s^{-1}) and phase g (degrees) for the M_2 North-South tidal velocity component. The 8^{th} and 9^{th} column give absolute errors for amplitude and phase whilst the two last columns give total depth (ht) and height above the bed of the current meter (hc).

Error Interval (m s^{-1})												
-0.30	-0.25	-0.20	-0.15	-0.10	-0.05	0	0.05	0.10	0.15	0.20	0.25	0.30
Number of points - u - component												
0	0	0	4	4	9	18	11	1	0	2	1	2
Number of points -v - component												
0	2	0	0	3	6	27	11	1	0	1	2	1

Table A.6: Distribution of amplitude errors (m s^{-1}) for u and v components of the M_2 tidal current. The histogram shows the number of point where the calculated velocity is above or below the observed value.

Error Interval (degrees)												
-90	-75	-60	-45	-30	-15	0	15	30	45	60	75	90
Number of points - u component												
0	0	0	1	3	15	22	7	1	4	0	0	1
Number of points - v component												
0	2	0	4	7	11	11	8	6	3	1	0	0

Table A.7: Distribution of errors for phase (degrees) for u and v components of the M_2 tidal current. The histogram shows the number of point where the calculated phase is above or below the observed value.

N.	R_{max} Obs. cm s^{-1}	R_{max} Mod. cm s^{-1}	R_{min} Obs. m s^{-1}	R_{min} Mod. m s^{-1}	α Obs. deg.	α Mod. deg.	β Obs. deg.	β Mod. deg.	ht m	hc m
1	32.3	34.7	-11.9	-12.8	216	209	62	49	370	250
1	27.6	34.1	-9.2	-12.2	209	209	60	48	370	100
1	23.8	34.6	-5.6	-12.8	210	210	57	49	370	25
2	31.8	27.9	-8.7	-7.3	224	205	60	45	237	150
2	26	26.3	-4.2	-5.1	224	206	62	45	237	25
3	11.9	14.4	3.1	-0.1	239	214	57	34	1019	990
3	14.4	14.4	-0.9	-0.1	224	215	48	34	1019	549
3	13.3	14.3	-0.3	0.0	224	215	50	35	1019	303
3	11.5	14.3	0.7	0.0	221	215	46	35	1019	102
3	9.2	14.4	3.5	0.0	191	215	14	35	1019	12
4	28.1	23.1	-8.8	-3.7	200	190	39	18	188	25
5	14.8	12.4	-1.7	1.8	222	226	24	24	998	894
5	13.6	12.4	-1.0	1.8	222	227	28	25	998	595
5	10.3	12.4	2.2	1.9	271	227	71	25	998	47
6	17.5	13.6	-2.8	1.8	210	213	11	14	514	399
6	16.1	13.5	-0.9	1.9	212	214	12	14	514	248
6	10.7	13.6	2.7	1.8	222	213	22	14	514	46
7	7.6	8.8	2.8	2.2	190	138	0	15	1535	1400
7	7.7	8.9	2.8	1.7	208	223	13	16	1535	1000
8	19.2	9.7	-0.4	3.9	155	178	-62	-22	163	130
9	23	14.4	-4.3	2.2	163	137	-36	-70	110	25
10	16.3	21.3	14.8	11.8	186	160	-26	-28	114	11
11	15.1	16.5	0.2	0.2	256	255	14	10	142	75
11	14.4	16.1	1.1	0.5	243	254	6	9	142	25
12	15.8	16.1	-3.0	-1.8	234	249	-1	0	142	28
13	13.5	16.5	-2.4	-2.2	249	249	13	1	146	105
13	14.3	16.1	-2.1	-1.8	235	249	2	0	146	25

N.	R_{max} Obs. cm s^{-1}	R_{max} Mod. cm s^{-1}	R_{min} Obs. m s^{-1}	R_{min} Mod. m s^{-1}	α Obs. deg.	α Mod. deg.	β Obs. deg.	β Mod. deg.	ht m	hc m
14	16.3	16.0	-4.4	-2	250	246	9	-2	155	100
14	14.2	15.4	-2.6	-1.4	225	246	-24	-3	155	25
15	16.9	16.0	-3.9	-2.0	236	246	0	-2	152	100
16	15.3	13.8	-0.3	1.0	248	242	-20	-28	135	75
16	14.8	13.4	0.4	1.7	230	242	-34	-29	135	25
17	22.6	6.9	-14.8	-1.2	209	227	-61	-63	130	91
17	22.5	6.6	-14.3	-0.8	212	226	-65	-67	130	21
18	17.4	16.1	-9.9	-7.5	202	207	-80	-71	126	25
19	11.9	11.4	-8.2	-5.1	201	230	-29	-89	170	140
19	16.1	11.0	-11.7	-4.8	211	229	-88	-90	170	50
20	13.8	10.3	-7.1	-7.9	189	190	-44	-71	136	25
21	75.1	96.2	-9.0	-9.4	250	96	-108	62	44	11
22	27.3	1.4	12.9	0.1	110	58	28	-54	123	81
22	28.1	1.4	11.2	0.1	94	59	0	-54	123	41
23	95.7	121.7	-16.8	-20.3	150	154	60	61	58	39
23	98.1	121.7	-16.9	-20.3	146	154	60	61	58	37
23	79.5	102.3	-12.2	-12.8	150	155	58	58	58	11
24	16.2	16.5	-4.4	-1.1	179	183	-12	-14	73	41
24	12.9	15.5	-0.9	0.2	169	182	-21	-15	73	10
25	53.6	88.9	17.9	10.3	149	160	51	62	110	6
26	47.8	41.7	-2.5	2.3	192	203	21	20	54	30
26	34.5	38.7	7.8	4.0	193	203	15	18	54	11
27	21.8	21.2	0.5	4.8	216	188	81	83	52	28
27	18.3	19.2	2.5	5.8	200	189	71	80	52	10
28	47.3	77.0	-2.8	-6	107	116	29	50	73	60
28	46.6	72.7	-0.9	-1.6	105	116	34	48	73	33
28	40.1	74.2	3.6	-2.9	103	116	26	49	73	5

Table A.8: Observed and predicted values for the tidal ellipses characteristics for M_2. R_{max} and R_{min} are the semi-major and semi-minor axes and α and β the orientation and the phase. The number in the first column refers to the position of the current meter whilst the two last columns give total depth (ht) and height above the bed of the current meter (hc).

No.	Lat.	Long.	Obs.		Comp.		Δh	Δg	Δhp	Δgp
			amp.(h)	pha.(g)	amp.(h)	pha.(g)				
			cm	deg	cm	deg	cm	deg	%	%
1	56.02	-8.58	42.0	196	39.0	196	3.0	0	7.1	-0.2
2	56.92	-8.58	41.0	202	39.0	201	1.0	1	3.7	0.6
3	58.03	-8.58	40.0	212	38.0	211	2.0	1	5.1	0.3
4	58.78	-7.50	39.0	224	37.0	222	1.0	2	3.2	0.9
5	59.48	-6.35	35.0	238	34.0	237	1.0	1	1.6	0.5
6	58.98	-7.40	38.0	226	36.0	228	2.0	-2	5.0	-1.0
7	59.20	-7.68	36.0	227	34.0	225	2.0	2	4.2	0.7

Table A.9: Comparison of observed and computed amplitude h(cm) and phase g(degrees) of the S_2 tidal elevation. Last 4 columns give absolute and percentage errors for amplitude and phase.

Error Interval (m)						
-0.03	-0.02	-0.01	0	0.01	0.02	0.03
Number of points						
3	3	1	0	0	0	0

Table A.10: Distribution of errors for amplitude (m) for the elevation of the S_2 tidal constituent. The histogram shows the number of point where the calculated amplitude is above or below the observed value.

Error Interval (degrees)												
-180	-150	-120	-90	-60	-30	0	30	60	90	120	150	180
Number of points												
0	0	0	0	0	0	7	0	0	0	0	0	0

Table A.11: Distribution of errors for phase (degrees) for the S_2 tidal constituent. The histogram shows the number of point where the calculated phase is above or below the observed value.

No.	Lat.	Long.	Obs.		Comp.		Δh	Δg	ht	hc
			amp.(h)	pha.(g)	amp.(h)	pha.(g)				
			cm s^{-1}	deg.	cm s^{-1}	deg.	cm s^{-1}	deg.	m	m
1	59.78	-6.18	9.4	296.6	10.2	278.7	-0.8	18	370	250
1	59.78	-6.18	8.8	286.4	10.2	278.7	-1.4	7.7	370	100
1	59.78	-6.18	8.0	284.7	10.2	278.8	-2.2	5.9	370	25
2	59.66	-6.04	7.3	285.8	8.4	266.7	-1.1	19.1	237	150
2	59.66	-6.04	7.1	278.1	8.0	265.6	-0.9	12.4	237	25
3	59.59	-7.25	4.2	227.1	4.0	250.1	0.2	-23.1	1019	990
3	59.59	-7.25	3.8	270.5	4.1	249.7	-0.3	20.8	1019	549
3	59.59	-7.25	3.5	266.0	4.1	249.0	-0.6	17.0	1019	303
3	59.59	-7.25	2.0	292.8	4.0	248.7	-2.0	44.1	1019	102
3	59.59	-7.25	1.6	175.4	4.1	249.3	-2.5	-73.9	1019	12
4	59.48	-6.35	8.2	263.0	7.7	227.7	0.5	35.3	188	25
5	59.14	-7.71	3.2	243.9	2.9	231.2	0.3	12.7	998	894
5	59.14	-7.71	3.8	240.3	2.8	231.9	1.0	8.3	998	595
5	59.14	-7.71	5.1	117.5	2.8	232.6	2.3	-115.1	998	47
6	59.09	-7.45	5.2	230.6	3.4	229.6	1.8	1.1	514	399
6	59.09	-7.45	4.7	231.6	3.4	230.3	1.3	1.3	514	248
6	59.09	-7.45	3.5	215.4	3.4	229.7	0.1	-14.3	514	46
7	59.03	-8.53	3.3	229.8	2.3	220.9	1.0	9.0	1535	1400
7	59.03	-8.53	2.2	224.8	2.3	220.8	-0.1	4.0	1535	1000
8	58.92	-7.49	2.7	223.7	2.3	220.5	0.4	3.2	163	130
9	58.78	-7.50	7.5	168.3	3.5	190.8	4.0	-22.4	110	25
10	58.72	-5.88	7.4	169.2	3.5	149.6	3.9	19.6	114	11
11	58.03	-8.15	5.6	180.8	7.8	191.4	-2.2	-10.6	142	75
11	58.03	-8.15	1.3	12.0	1.6	195.3	-0.3	176.7	142	25
12	58.01	-8.79	3.4	226.6	1.9	182.3	1.5	44.3	142	28
13	57.99	-8.73	3.2	220.6	1.9	207.9	1.3	12.7	146	105
13	57.99	-8.73	2.1	222.5	2.1	215.5	0.0	7.0	146	25
14	57.94	-8.85	2.6	222.3	2.2	211.4	0.4	10.9	155	100
14	57.94	-8.85	2.1	206.7	2.4	202.6	-0.3	4.1	155	25
15	57.93	-8.86	4.2	231.3	2.2	211.4	2.0	19.9	152	100
16	57.60	-8.17	1.7	191.3	2.8	166.8	-1.1	24.5	135	75
16	57.60	-8.17	3.4	155.1	2.7	165.1	0.7	-10.0	135	25
17	56.99	-8.94	8.8	168.0	2.2	161.8	6.6	6.2	130	91
17	56.99	-8.94	6.3	137.5	6.6	146.9	-0.3	-9.4	130	21
18	56.92	-8.58	4.1	190.0	4.4	138.4	-0.3	51.6	126	25
19	56.48	-7.98	6.7	154.3	4.4	134.3	2.3	20	170	140
19	56.48	-7.98	4.3	157.6	4.4	128.7	-0.1	28.9	170	50
20	56.00	-8.57	10.0	120.8	3.5	237.9	6.5	-117.1	136	25
21	55.88	-6.56	5.2	296.7	1.0	29.5	4.2	92.8	44	11

No.	Lat.	Long.	Obs.		Comp.		Δh	Δg	ht	hc
			amp.(h)	pha.(g)	amp.(h)	pha.(g)				
			cm s^{-1}	deg.	cm s^{-1}	deg.	cm s^{-1}	deg.	m	m
22	55.87	-5.75	5.3	299.1	1.0	29.4	4.3	90.3	123	81
22	55.87	-5.75	24.7	268.0	33.3	278.8	-8.6	-10.8	123	41
23	55.51	-6.85	25.3	268.6	33.3	278.8	-8.0	-10.2	58	39
23	55.51	-6.85	21.5	266.8	27.6	277.8	-6.2	-11	58	37
23	55.51	-6.85	6.5	197.9	4.1	185.2	2.4	12.7	58	11
24	55.50	-8.01	2.5	193.8	3.7	179.6	-1.2	14.2	73	41
24	55.50	-8.01	15.8	280.8	27.6	288.5	-11.8	-7.7	73	10
25	55.46	-6.16	11.4	229.2	10.1	235.3	1.3	-6.1	110	6
26	55.42	-7.51	11.2	231.5	10.1	235.3	1.0	-3.8	54	30
26	55.42	-7.51	9.3	226.4	8.9	231.5	0.4	-5.1	54	11
27	55.34	-5.11	5.0	307.7	7.2	321.9	-2.2	-14.2	52	28
27	55.34	-5.11	5.9	291.1	6.3	319.1	-0.4	-28.0	52	10
28	55.03	-5.32	6.2	223.8	11.3	259.2	-5.1	-35.4	73	60
28	55.03	-5.32	4.2	261.6	10.5	266.3	-6.3	-4.7	73	33
28	55.03	-5.32	4.0	268.6	10.6	265.3	-6.6	3.3	73	5

Table A.12: Comparison of observed and computed amplitude h (cm s^{-1}) and phase g (degrees) of the S_2 East-west tidal velocity. The 8^{th} and 9^{th} column give absolute errors for amplitude and phase whilst the two last columns give total depth (ht) and height above the bed of the current meter (hc).

No.	Lat.	Long.	Obs.		Comp.		Δh	Δg	ht	hc
			amp.(h)	pha.(g)	amp.(h)	pha.(g)				
			cm s^{-1}	deg.	cm s^{-1}	deg.	cm s^{-1}	deg.	m	m
1	59.78	-6.18	5.9	259.6	6.8	240.1	-0.9	19.5	370	250
1	59.78	-6.18	5.2	250.0	6.6	240.0	-1.4	10.0	370	100
1	59.78	-6.18	5.2	256.9	6.8	240.0	-1.6	16.9	370	25
2	59.66	-6.04	7.8	263.0	4.3	243.7	3.5	19.3	237	150
2	59.66	-6.04	6.6	265.0	4.0	251.7	2.6	13.3	237	25
3	59.59	-7.25	0.2	249.2	2.9	252.4	-2.7	-3.2	1019	990
3	59.59	-7.25	3.2	258.3	2.9	252.6	0.3	5.7	1019	549
3	59.59	-7.25	2.7	264.4	2.8	253.2	-0.1	11.2	1019	303
3	59.59	-7.25	3.9	285.0	2.8	254.2	1.1	30.7	1019	102
3	59.59	-7.25	4.5	322.8	2.8	253	1.7	69.9	1019	12
4	59.48	-6.35	4.8	234.2	0.9	241.2	3.9	-7.0	188	25
5	59.14	-7.71	3.3	244.1	3.0	245.9	0.3	-1.8	998	894
5	59.14	-7.71	2.9	238.1	3.1	246.8	-0.2	-8.7	998	595
5	59.14	-7.71	6.4	343.1	3.1	246.7	3.3	96.4	998	47
6	59.09	-7.45	3.1	229.1	2.8	241.1	0.3	-12	514	399
6	59.09	-7.45	2.9	225.2	2.8	242.6	0.1	-17.4	514	248
6	59.09	-7.45	2.4	246.7	2.8	241.5	-0.4	5.2	514	46
7	59.03	-8.53	1.4	234.4	2.0	243.2	-0.6	-8.8	1535	1400
7	59.03	-8.53	2.2	259.3	2.0	243.8	0.2	15.6	1535	1000
8	58.92	-7.49	1.7	248.7	2.1	245.0	-0.4	3.8	1535	600
9	58.78	-7.50	2.4	32.9	1.5	297.8	0.9	95.1	163	130
10	58.72	-5.88	3.0	20.3	3.5	315.2	-0.5	65.1	110	25
11	58.03	-8.15	7.5	270.6	6.2	319.8	1.3	-49.2	114	11
11	58.03	-8.15	5.8	245.6	4.9	231.2	0.9	14.4	142	75
12	58.01	-8.79	4.4	203.7	4.5	230.8	-0.1	-27.1	142	25
13	57.99	-8.73	4.2	210.4	4.3	218.7	-0.1	-8.3	142	28
13	57.99	-8.73	3.9	220.7	4.6	217.1	-0.7	3.6	146	105
14	57.94	-8.85	4.0	202.2	4.2	211.2	-0.2	-9	155	100
14	57.94	-8.85	4.2	209.7	4.1	212.4	0.1	-2.7	155	25
15	57.93	-8.86	3.9	204.8	4.2	211.2	-0.3	-6.4	152	100
16	57.60	-8.17	5.3	202.0	3.3	189.7	2	12.3	135	75
16	57.60	-8.17	2.8	180.9	3.4	191.4	-0.6	-10.5	135	25
17	56.99	-8.94	6.9	90.5	2.2	139.1	4.7	-48.6	130	91
17	56.99	-8.94	3.3	67.1	3.4	87.4	-0.1	-20.3	126	25
18	56.92	-8.58	2.5	120.0	3.0	105.7	-0.5	14.3	170	140
19	56.48	-7.98	4.2	78.4	2.7	103.0	1.5	-24.5	170	50
19	56.48	-7.98	2.5	72.5	2.7	60.2	-0.2	12.3	136	25
20	56.00	-8.57	24.1	102.7	31.9	106.6	-7.8	-3.9	44	11
21	55.88	-6.56	8.7	49.5	1.6	30.6	7.1	18.9	123	81

No.	Lat.	Long.	Obs.		Comp.		Δh	Δg	ht	hc
			amp.(h)	pha.(g)	amp.(h)	pha.(g)				
			cm s^{-1}	deg.	cm s^{-1}	deg.	cm s^{-1}	deg.	m	m
22	55.87	-5.75	8.4	35.3	1.6	30.5	6.8	4.8	123	41
22	55.87	-5.75	14.3	111.9	18.3	121.6	-4.0	-9.7	58	39
23	55.51	-6.85	17.3	109.9	18.3	121.6	-1.0	-11.7	58	37
23	55.51	-6.85	13.4	110.5	14.9	119.0	-1.6	-8.5	58	11
23	55.51	-6.85	1.9	93.5	0.5	104.3	1.4	-10.9	73	41
24	55.50	-8.01	0.4	205.3	0.1	284.1	0.3	-78.8	73	10
24	55.50	-8.01	8.9	62.5	10.4	84.0	-1.5	-21.5	110	6
25	55.46	-6.16	2.4	247.3	4.9	250.1	-2.5	-2.8	54	30
26	55.42	-7.51	1.5	245.6	4.9	250.1	-3.4	-4.5	54	28
26	55.42	-7.51	3.8	254.7	4.6	250.5	-0.8	4.2	54	11
27	55.34	-5.11	3.3	318.9	5.2	17.3	-1.9	58.4	52	28
27	55.34	-5.11	2.0	333.1	5.2	15.1	-3.2	42.1	52	10
28	55.03	-5.32	19.2	67.6	25.6	87.5	-6.4	-19.9	73	60
28	55.03	-5.32	15.1	69.2	23.5	82.2	-8.4	-13	73	33
28	55.03	-5.32	13.5	63.7	24.4	84.2	-10.9	-20.5	73	5

Table A.13: Comparison of observed and computed amplitude h (cm s^{-1}) and phase g (degrees) of the S_2 North-South tidal velocity. The 8^{th} and 9^{th} column give absolute errors for amplitude and phase whilst the two last columns give total depth (ht) and height above the bed of the current meter (hc).

Error interval (m s^{-1})												
-0.12	-0.10	-0.08	-0.06	-0.04	-0.02	0	0.02	0.04	0.06	0.08	0.10	0.12
Number of points - u - component												
1	1	2	3	0	12	16	13	4	0	2	0	0
Number of points -v - component												
0	0	2	1	4	8	17	14	5	1	2	0	1

Table A.14: Distribution of errors for amplitude (m s^{-1}) for u and v components of the S_2 tidal current. The histogram shows the number of point where the calculated velocity is above or below the observed value.

Interval (degrees)												
-90	-75	-60	-45	-30	-15	0	15	30	45	60	75	90
Number of points - u component												
3	0	0	3	3	16	13	10	3	0	0	1	2
Number of points - v component												
0	2	2	1	1	12	14	16	22	2	0	1	0

Table A.15: Distribution of errors for phase (degrees) for u and v components of the S_2 tidal current. The histogram shows the number of point where the calculated phase is above or below the observed value.

N.	R_{max} Obs. cm s^{-1}	R_{max} Mod. cm s^{-1}	R_{min} Obs. m s^{-1}	R_{min} Mod. m s^{-1}	α Obs. deg.	α Mod. deg.	β Obs. deg.	β Mod. deg.	ht m	hc m
1	10.6	11.7	-3.1	-3.7	209	211	107	88	370	250
1	9.8	11.6	-2.8	-3.6	208	210	98	88	370	100
1	9.3	11.7	-2.1	-3.7	212	211	97	88	370	25
2	10.5	9.3	-2.1	-1.5	227	206	94	82	237	150
2	9.6	8.9	-1.1	-0.9	223	206	92	83	237	25
3	4.2	5.0	0.1	0.1	182	216	47	71	1019	990
3	4.9	5.0	-0.5	0.1	220	215	85	71	1019	549
3	4.4	4.9	-0.1	0.2	218	215	85	70	1019	303
3	4.4	4.9	-0.2	0.2	243	214	107	70	1019	102
3	4.7	4.9	0.8	0.1	107	215	-34	70	1019	12
4	9.3	7.8	-2.0	0.2	209	186	76	48	188	25
5	4.6	4.2	0.0	0.5	226	226	64	59	998	894
5	4.8	4.2	-0.1	0.5	217	228	60	60	998	595
5	7.6	4.1	-3.1	0.5	126	228	-33	60	998	47
6	6	4.4	-0.1	0.4	211	219	50	54	514	399
6	5.5	4.3	-0.3	0.5	212	219	50	55	514	248
6	4.1	4.4	1.1	0.4	213	219	45	54	514	46
7	3.6	2.6	0.1	1.6	203	143	50	39	1535	1400
7	3	3.0	0.9	0.6	225	221	62	51	1535	1000
8	3.1	3.0	0.6	0.7	211	222	50	52	163	130
9	7.7	3.6	-1.6	1.4	166	172	-9	7	110	25
10	7.8	4.9	-1.5	0.6	160	135	-7	-38	114	11
11	7.5	9.1	5.6	4.2	90	145	-90	-6	142	75
11	5.9	5.1	-1	0.9	278	255	64	48	142	25
12	5.5	4.7	-1.1	1.4	233	253	32	46	142	28
13	5.3	4.7	-0.4	0.3	233	246	34	37	146	105
13	4.4	5.0	-0.1	0.1	242	245	41	37	146	25

N.	R_{max} Obs.	R_{max} Mod.	R_{min} Obs.	R_{min} Mod.	α Obs.	α Mod.	β Obs.	β Mod.	ht	hc
	cm s^{-1}	cm s^{-1}	m s^{-1}	m s^{-1}	deg.	deg.	deg.	deg.	m	m
14	4.7	4.8	-0.8	0.0	238	243	28	31	155	100
14	4.7	4.7	0.1	0.4	244	240	29	30	155	25
15	5.6	4.8	-1.3	0.0	223	243	39	31	152	100
16	5.6	4.2	0.3	0.8	252	231	21	1	135	75
16	4.3	4.2	1.0	1.0	219	232	-15	1	135	25
17	9.1	3.0	-6.5	-0.6	201	226	-27	-30	130	91
17	6.4	6.9	-3.0	-2.8	193	198	-49	-41	130	21
18	4.2	5.2	-2.3	-1.4	197	213	1	-51	126	25
19	6.8	5.0	-4.0	-1.2	193	210	-34	-54	170	140
19	4.3	4.5	-2.5	-2.4	184	198	-25	-61	170	50
20	25.9	31.9	-2.9	-2.6	248	274	-75	-74	136	25
21	9.0	1.9	4.6	0.0	108	58	59	30	44	11
22	8.4	1.9	5.2	0.0	96	57	39	30	123	81
22	28.1	37.5	-5.1	-6.3	151	152	94	104	123	41
23	30.2	37.5	-5.3	-6.3	146	152	95	104	58	39
23	24.9	31	-4.6	-4.8	149	153	93	102	58	37
23	6.5	4.1	-1.8	-0.5	176	181	19	5	58	11
24	2.5	3.7	0.1	0.1	189	180	14	0	73	41
24	17.4	29.2	5.0	4.1	154	161	93	106	73	10
25	11.6	11.2	0.7	1.1	191	205	50	58	110	6
26	11.2	11.2	0.4	1.1	187	205	52	58	54	30
26	9.9	9.9	1.7	1.3	201	206	50	55	54	11
27	6.0	8	0.5	3.8	213	30	131	-23	52	28
27	6.1	7.2	1.3	3.7	195	36	114	-21	52	10
28	20	27.9	-2.4	-1.5	107	114	66	86	73	60
28	15.7	25.7	0.9	0.7	105	114	70	83	73	33
28	14.0	26.6	1.6	0.2	105	113	66	84	73	5

Table A.16: observed and predicted values for the tidal ellipses characteristics for S_2. R_{max} and R_{min} are the semi-major and semi-minor axes and α and β the orientation and the phase. The number in the first column refers to the position of the current meter whilst the two last columns give total depth (ht) and height above the bed of the current meter (hc).